STUDIA UNIVERSITATIS
BABEŞ-BOLYAI

UNIVERSITATEA BABEŞ-BOLYAI
BABEŞ-BOLYAI TUDOMÁNYEGYETEM
BABEŞ-BOLYAI UNIVERSITÄT
BABEŞ-BOLYAI UNIVERSITY
TRADITIO ET EXCELLENTIA

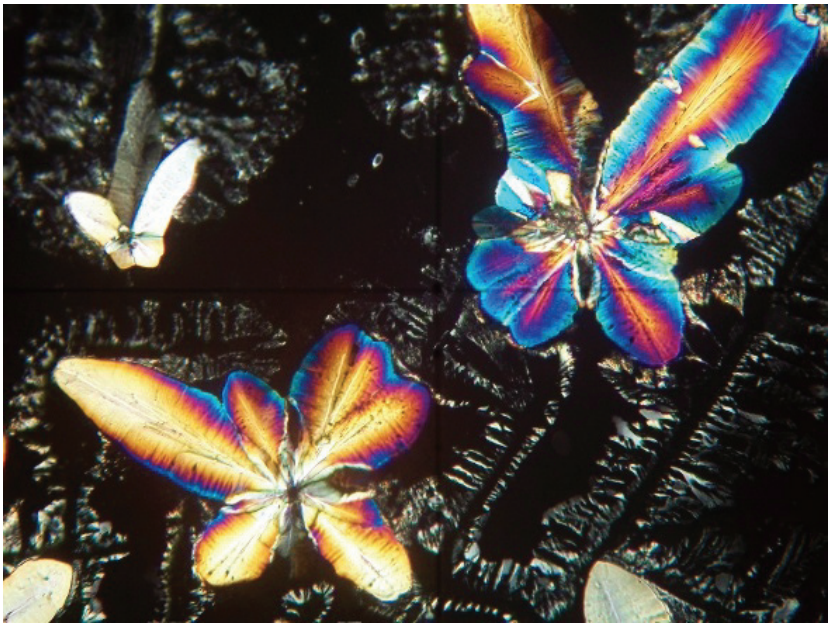

CHEMIA

3/2025

STUDIA UNIVERSITATIS BABEŞ-BOLYAI CHEMIA

3/2025

ISSN (print): 1224-7154;
ISSN (online): 2065-9520; ISSN-L: 1224-7154

Published by Babeş-Bolyai University

https://studia.reviste.ubbcluj.ro/index.php/chemia/
studiachemia@ubbcluj.onmicrosoft.com

YEAR **Volume 70 (LXX) 2025**
MONTH **September**
ISSUE **3**

PUBLISHED ONLINE: 2025-09-24
PUBLISHED PRINT: 2025-10-30
ISSUE DOI: 10.24193/subbchem.2025.3

S T U D I A
UNIVERSITATIS BABEŞ–BOLYAI
CHEMIA

3

CONTENT/ SOMMAIRE/ INHALT/ CUPRINS

Studia Universitatis Babes-Bolyai Chemia has been selected for coverage in Thomson Reuters products and custom information services. Beginning with V. 53 (1) 2008, this publication is indexed and abstracted in the following:

- Science Citation Index Expanded (also known as SciSearch®)
- Chemistry Citation Index®
- Journal Citation Reports/Science Edition

STUDIA UBB CHEMIA, LXX, 3, 2025 (p. 7-20)
(RECOMMENDED CITATION)
DOI:10.24193/subbchem.2025.3.01

ONLINE ELECTROCHEMICAL MONITORING OF PRODUCTS' CONCENTRATIONS DURING THE HBr AND KOH ELECTROSYNTHESIS BY ELECTRODIALYSIS

Gabriele-Mario BOGDAN[a], Sorin-Aurel DORNEANU[a,b,*]

ABSTRACT. In 2022, an estimated 62 billion kg of e-waste was generated, with an approximate value of $91 billion; however, the externalized and process costs of recycling make it economically unattractive. Our previous studies have demonstrated the possibility of electrochemically producing and regenerating the main reagents required for the Br_2/Br^- leaching system used in metals recovery from waste printed circuit boards. To facilitate the optimization of these processes, in this study, mathematical models were developed that enabled us to calculate concentration of KOH, H_2SO_4 and KBr from temperature and conductivity data and to determine the fitting parameters over the required concentration and temperature ranges using MATLAB's Curve Fitting Toolbox. The developed models were compared against pre-existing ones and literature data and were validated using experimental data gathered using a complex computer-controlled setup. For KOH and KBr, the adapted models provide an almost perfect fit between the obtained calibration surfaces and literature and experimental data. Contrarily, for H_2SO_4, a more complex 10-parameter model was developed to properly fit data in the desired range of temperature and concentration. Using the obtained fitting parameters, the possibility of online and in situ monitoring of target electrolyte concentrations using inexpensive conductivity and temperature sensors was confirmed.

Keywords: *mathematical model; conductivity; concentration monitoring; electrochemical sensors; WPCBs recycling process.*

[a] *Department of Chemical Engineering, Faculty of Chemistry and Chemical Engineering, Babeş-Bolyai University, 11 Arany Janos Street, RO-400028, Cluj-Napoca, Romania*
[b] *Interdisciplinary Research Institute on Bio Nano Sciences, Babeş-Bolyai University, 42 Treboniu Laurian Street, RO-400271, Cluj-Napoca, Romania*
[*] *Corresponding author: sorin.dorneanu@ubbcluj.ro*

INTRODUCTION

Technological progress and consumerism have turned e-waste into one of the largest pollution-related issues in modern times, with more than 62 billion kg generated in 2022. One of the most valuable components of e-waste are waste printed circuit boards (WPCBs) which — due to their high content of valuable metals — represent an extremely important resource for recycling, with an approximate value of $91 billion. Insufficiently ecological recycling processes, however, have led to an estimated externalized cost (the cost of bad societal outcomes related to pollution) of e-waste recycling of around $78 billion, with another $10 billion in operational costs [1]. Consequently, the development of more environmentally friendly and economically viable recycling processes is crucial for successful long-term and sustainable implementations of WPCB recycling technologies [2–5]. Though WPCB recycling technologies are very diverse [6], pyrometallurgical and mechanical recycling technologies can be very polluting, releasing heavy-metal containing particulate matter, greenhouse and toxic gases all of which can be very detrimental to human and environmental health [5,7]. As of 2024, approximately 46% of the global energy production capacity comes from renewable sources [8], meaning hydrometallurgical processes combined with electrochemical techniques present the highest potential in regards to sustainability and pollution reduction compared to pyrometallurgical or physical methods. Electrochemistry can be applied at almost every stage of the recycling process, starting from dissolving the metals using electrochemically regenerable leaching systems like $H_2SO_4/CuSO_4/NaCl$ [9] or Fe^{3+}/Fe^{2+} [10], followed by selective electroextraction of metals from solution [11,12] and electrochemical regeneration of reagents [13], allowing for a very sustainable, low-cost recycling system.

Our previous studies have demonstrated the feasibility of implementing the electrochemically regenerable Br_2/Br^- leaching system for complete metals recovery from WPCBs [14,15]. A flowchart of the proposed recycling process was developed during author Bogdan's Bachelor Thesis [16]. The main takeaway from the proposed flowchart is that, after the recycling process is concluded, the resulting secondary fluxes consist of two clean KBr solutions of concentration smaller than 2 M, one of which contains an unknown amount of HBr. Provided these KBr solutions are reconcentrated up to process requirements, which could be achieved through electrodialysis, they can be used as raw materials for the electrochemical reagent preparation and regeneration process. In this context, we previously demonstrated the possibility of profitably producing, by electrodialysis, KOH and HBr solutions at the required process concentrations using a 2 M KBr and a four-compartment filter press electrochemical reactor. During the electrosynthesis tests, solutions of 2 M KBr, 2 M H_2SO_4 and 0.1 M KOH were used in the reactor's compartments' flow

circuits, with final concentrations of HBr and KOH of 0.768 and 0.893 M respectively. Consequently, for the complete monitoring of reagent concentrations in this process, in order to optimize the operating parameters and increase its profitability, this research focuses exclusively on adapting, improving and testing the viability of the mathematical model around the operating concentrations of products and reagents. Additionally, our preliminary results proved the possibility of using low-cost conductivity sensors for the online and in-situ monitoring of KOH concentrations between 0.1 ÷ 1 M [13]. Building on these promising results, the aims of this study are (i) to develop mathematical relationships that will allow the computation of, using real-time sensor data, reagent concentrations in all four electrodialysis reactor compartments using simple and inexpensive electrochemical sensors and (ii) to acquire conductivity data for KBr, H_2SO_4 solutions between 1.25 ÷ 2.5 M, and KOH solutions between 0.5 ÷ 1 M, for temperatures between 23 ÷ 40°C in order to validate the proposed mathematical model. The temperature and concentration ranges were chosen based on prior electrosynthesis efficiency and performance data [13]. Exceeding 40°C indicates excessive energy loss as heat, thus, this value was chosen to be the upper limit for this study.

Developing robust mathematical models able to accurately compute concentration using sensor data would help eliminate the labor-intensive processes of samples extraction and manual determination of solute concentrations that is currently required, thus reducing process labor, materials and operational costs through advanced automation, resulting in further reductions of recycling process costs.

RESULTS AND DISCUSSION

Mathematical modelling of calibration surfaces

Even if many commercially available concentration sensors are based on electrical conductivity (EC) and temperature (T) data, the subject is not very well treated in literature. For example, Shahid et al. [17] proposed a mathematical relationship for determining concentration of NaCl, methylene blue (MB) and methyl violet 2b as a function of measured T and EC reproduced below:

$$C_{xx} = \frac{EC_{xx}}{a + b \cdot EC_{xx} + c \cdot EC_{xx}^2 + d \cdot EC \cdot T_{xx} + e \cdot T_{xx}} \quad (1)$$

where a ÷ e represent the fitting coefficients, xx represents the species for which the fitting was performed (xx=KOH, H_2SO_4, KBr), EC is the electrical conductivity (in mS/cm), T is the temperature (in K) and C is the electrolyte concentration (in mol/L).

This model was implemented inside MATLAB's Curve Fitting Toolbox, which allowed the input of a custom equation and to choose the Levenberg – Marquardt algorithm for estimating the fitting coefficients based on available (EC, T, C) literature data for KOH [18], H_2SO_4 [19] and KBr [20]. The fitted coefficients obtained, the corresponding R^2 value (computed by MATLAB) and the applicable temperature, concentration and conductivity ranges are presented in Table 1.

Conductivity values must be constrained in order to remain within the model's applicable range using a first order equation EC=f(T), which was determined through linear regression in Excel for the upper concentration limit of each substance. For a wider range of temperatures or concentrations, higher degree polynomials might need to be determined and implemented for each substance.

Table 1. Fitted coefficients a÷e of equation (1) obtained for KOH, H_2SO_4, KBr and applicable for specified concentration, temperature and conductivity ranges.

Subst.	**KOH**	**H_2SO_4**	**KBr**
a	-0.566	-0.589	-0.505
b	-0.861	-0.828	0.159
$c \cdot 10^3$	2.599	2.660	0.591
$d \cdot 10^2$	-17.24	-19.10	-4.77
$e \cdot 10^3$	2.711	3.460	2.111
R^2	0.9999	0.9983	0.9999
T range [K]	273 ÷ 323	300 ÷ 344	288 ÷ 328
C range [M]	0 ÷ 1	0 ÷ 3.05	0 ÷ 3.18
EC range [mS]	$0 \div (2.82 \cdot 10^{-3} \cdot T - 0.62)$	$0 \div (5.05 \cdot 10^{-3} \cdot T - 1.16)$	$0 \div (1.09 \cdot 10^{-3} \cdot T - 2.45)$

The R^2 values indicate that Shahid's model could be successfully implemented for calculating KBr and KOH concentrations within the specified ranges, however the marginally lower value for H_2SO_4, combined with the narrower temperature range warrants further investigation. A visual comparison between the obtained surface and the literature data reveals a very large discrepancy between the two for temperatures under 300 K, with residuals reaching up to 1.2 M at 273 K. Including data from 273 – 300 K reduces the R^2 value to 0.938. Unfortunately, despite extensive adjustments to the many fitting options available in MATLAB's Curve Fitting Toolbox, no further improvement of the fitting was observed. In conclusion, Shahid's mathematical model is not suitable for determining H_2SO_4 concentration under the given conditions.

Further inspection of the fit between the surface obtained through the mathematical model and the literature data reveals that Shahid's model is unable to properly compensate for the strong curvature present at lower temperatures,

which is absent in the case of KBr and KOH at the specified concentration range. Existing models for conductivity as a function of concentration contain exponential or logarithmic terms in the form of $a \cdot C^n \cdot e^{b \cdot C}$ or $a \cdot C \cdot \log C$ respectively, terms which introduce an inflection point at one or more local maximums for specific concentrations and temperatures [21,22]. In the case of KOH the inflection point occurs at high concentrations, greater than 5 M [18], and in the case of KBr, above 15°C, conductivity varies monotonously over the entire concentration range [21,23], meaning that the exponential/logarithmic term is not very significant. In contrast, the EC = f(C) dependency of H_2SO_4 exhibits an inflection point at concentrations much closer to our range of interest, starting at around 3.5 M at 0°C, gradually shifting towards higher concentrations at elevated temperatures. A visual representation of the EC=f(C) dependency for KOH and H_2SO_4 at 25 °C superimposed with the target concentration ranges of this study is presented in Figure 1.

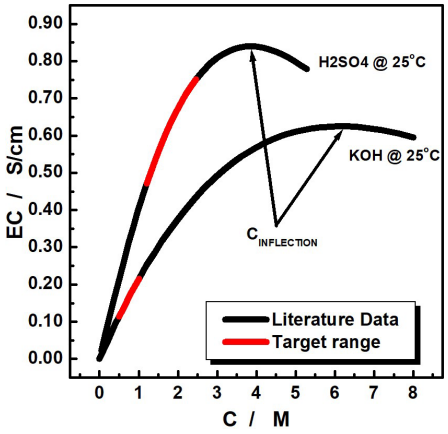

Figure 1. Dependency between conductivity and concentration for KOH and H_2SO_4 (black) superimposed with the target concentration ranges of this study (red).

This can be explained by two main factors, (i) the lower mobility of the HSO_4^- and SO_4^{2-} anions compared to OH^- or Br^- and (ii) the high dissociation factor of the second proton of H_2SO_4 at low concentrations and it's reassociation at higher concentrations respectively. It's widely accepted that, up to around 80 wt%, the first proton of sulfuric acid is completely dissociated, meaning that the dissociation factor of the second proton will play an important role towards changes in conductivity of sulfuric acid solutions. Spectroscopic investigations of sulfuric acid over a wide range of temperature and composition have shown that the dissociation factor of the second proton rises quickly between 10 ÷ 20% wt% H_2SO_4/H_2O, however its increase slows down and plateaus around 27 wt% H_2SO_4/H_2O at 290 K, decreasing at higher concentrations [24]. This behavior is consistent with the variation of conductivity

with concentration observed for H_2SO_4. Consequently, this behavior influences the allure of the EC = f(C) plot, resulting in a strongly exponential character of the C = f(EC) relationship around the studied concentration range.

Using these insights, an enhanced mathematical model that extends Shahid's model to be able to accurately determine concentrations for conductivity values close to the inflection point of the EC = f(C) relationship was proposed. This was done by first expanding the polynomial equation under the fraction to a complete linear combination of second order EC and T terms followed by the addition of the exponential $k \cdot T^n$ term which should be able to compensate for the strong curvature present near the inflection point, alongside other additional terms which were needed in order to obtain a better fit for portions where the exponential term's influence is not as large. Our proposed mathematical model is presented in equation (2):

$$C_{xx} = \frac{a \cdot EC_{xx} + b \cdot T_{xx}}{c + d \cdot EC_{xx} + e \cdot EC_{xx}^2 + f \cdot EC_{xx} \cdot T_{xx} + g \cdot T_{xx} + h \cdot T_{xx}^2 + k \cdot T_{xx}^n} \quad (2)$$

where EC, T, C and xx have the same meaning as described for equation (1). Using the same method described above, fitting coefficients were re-evaluated for all three substances and presented in Table 2.

Table 2. Fitted coefficients a÷n of equation (2) obtained for KOH, H_2SO_4, KBr.

Subst.	a	$b \cdot 10^5$	c	d	e	$f \cdot 10^3$	$g \cdot 10^2$	$h \cdot 10^5$	k	n	R^2
KOH	4.727	0.051	-0.411	-2.306	-0.267	5.794	-0.347	2.926	-	-	1.0000
H_2SO_4	1.927	8.619	0.360	-2.041	-0.185	5.419	16.87	-11.75	-0.853	0.672	0.9985
KBr	19.11	-6.298	-1.605	4.535	-1.442	-15.01	-1.376	8.984	-	-	1.0000

In the case of KOH and KBr, where the target concentrations are not close to an inflection point, the exponential term $k \cdot T^n$ is negligible and thus can be ignored in order to allow for simpler and faster calculation. An improvement in the R^2 value can be observed for all three substances, with a perfect fit ($R^2 = 1.0000$) for KOH and KBr. The applicable temperature range for H_2SO_4 increased from 300 ÷ 344 K to 278 ÷ 366 K, showing the great improvement of the model. Critically, because n takes a value below 1, the $k \cdot T^n$ term grows slower than the first and second order polynomial terms, meaning that its influence will diminish at higher temperatures. This is consistent with the real behavior of electrolyte solutions, where the inflection points of the EC = f(C) plot moves to higher concentrations at elevated temperatures, sometimes moving past the electrolyte's saturation limit. Though this study only validates

the model for H_2SO_4, we believe it could be successfully implemented for other electrolytes which exhibit an inflection point close to the target concentration range. Also, it is very important to note that, by inverting the EC = f(C) relationship, the resulting C = f(EC) function is bijective only up to the concentration $C_{inflection}$, where the derivative dEC/dC is equal to 0. If concentration needs to be calculated for the entire range up to the saturation point, fitting coefficients need to be determined for points pre/post $C_{inflection}$, and another property of the solution which varies monotonously with concentration up to the saturation point (such as density) must be used in order to determine which side of the inflection point you are on and, consequently, which of the equations to use.

Using the fitted coefficients and equation (2), calibration surfaces, presented in Figure 2, were generated for concentration and conductivity ranges mentioned in Table 1, covering a temperature range of 293 ÷ 323 K. These surfaces enable real-time concentration estimation from sensor data within the studied ranges.

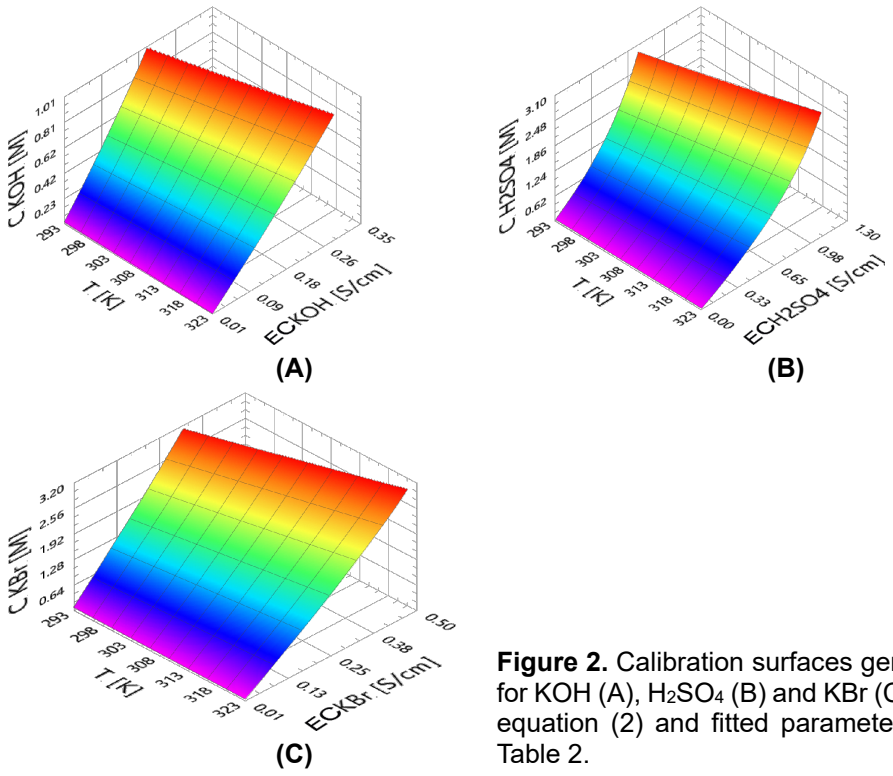

Figure 2. Calibration surfaces generated for KOH (A), H_2SO_4 (B) and KBr (C) using equation (2) and fitted parameters from Table 2.

Validation of calibration surfaces

In order to validate our mathematical model, conductivity measurements were performed for KOH, H_2SO_4 and KBr at 11 concentrations and 3 temperatures using a complex computer-controlled experimental setup (see Experimental Section), resulting in 3 sets of 33 (EC, T, C) points per substance to be used for comparison. Experimental temperature and conductivity data were input into our and Shahid's models and corresponding concentrations were computed. A comparison between (i) experimental data, (ii) Shahid's model and (iii) our model against reference literature data is presented in Figure 3.

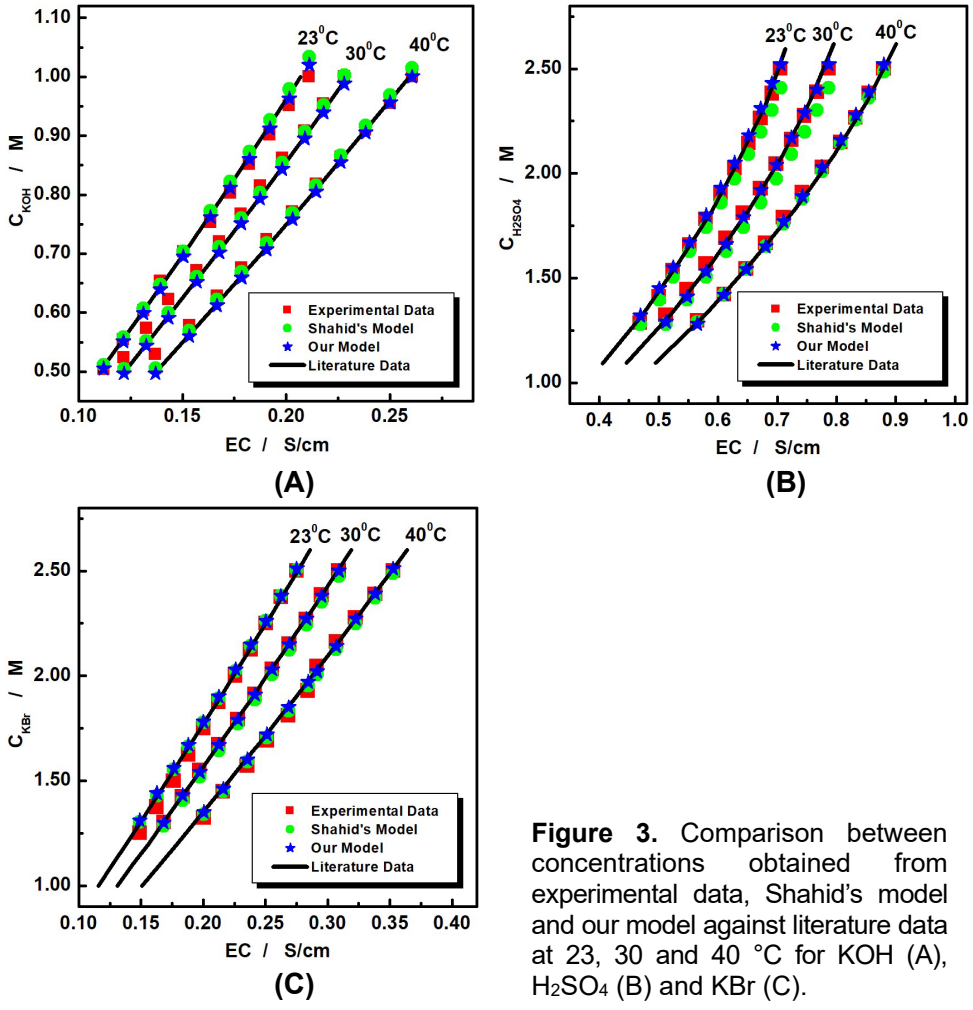

Figure 3. Comparison between concentrations obtained from experimental data, Shahid's model and our model against literature data at 23, 30 and 40 °C for KOH (A), H_2SO_4 (B) and KBr (C).

For a quantitative comparison of the model's performance and experimental accuracy, three statistical metrics, R^2, R (accuracy rate) and SSE (sum of squares error), were evaluated against reference literature data using the following equations:

$$R^2 = 1 - \frac{\sum_1^i (y_{i,d} - f_{i,lit})^2}{\sum_1^i (y_{i,d} - \overline{y_{i,lit}})^2} \quad (3)$$

$$R = \frac{1}{11} \cdot \sum_1^i \frac{1 - \left| y_{i,d} - f_{i,lit} \right|}{y_{i,d}} \quad (4)$$

$$SSE = \sum_1^i (y_{i,d} - f_{i,lit})^2 \quad (5)$$

where i represents the index of the data point, $y_{i,d}$ represents the i-th concentration value of the considered dataset d (experimental, Shahid's model, our model), $f_{i,lit}$ represents the concentration calculated for the i-th measured conductivity through polynomial regression on literature data and $\overline{y_{i,lit}}$ is the mean of the literature concentration values used for comparison. The calculated R^2, R and SSE values are presented in Table 3.

Table 3. Values of relevant statistical metrics evaluated by comparing experimental and model data against literature data for KOH, H_2SO_4 and KBr at 23, 30 and 40°C.

Subst.	Temp.	Experimental data			Shahid's model			Our model		
		R	R^2	SSE·10^2	R	R^2	SSE·10^2	R	R^2	SSE·10^2
KOH	23°C	0.993	0.986	0.199	0.999	0.993	0.037	0.999	0.993	0.035
	30°C	0.985	0.975	0.371	0.998	0.991	0.053	1.000	0.996	0.011
	40°C	0.992	0.983	0.198	0.998	0.990	0.055	0.999	0.995	0.017
H_2SO_4	23°C	0.997	0.991	0.520	0.964	0.972	5.116	0.998	0.990	0.419
	30°C	0.992	0.983	1.219	0.951	0.968	6.943	0.999	0.994	0.240
	40°C	0.998	0.992	0.349	0.999	0.996	0.083	0.999	0.994	0.190
KBr	23°C	0.995	0.985	0.932	0.999	0.995	0.093	0.999	0.993	0.190
	30°C	1.000	0.997	0.043	0.994	0.986	0.884	1.000	0.998	0.032
	40°C	0.995	0.986	0.867	0.997	0.989	0.487	1.000	0.998	0.022

As anticipated, our model demonstrates only marginal improvements over Shahid's model for KOH and KBr, since the studied concentration intervals are far away from the inflection point. A substantial improvement in

the fit is observed for H_2SO_4, with R^2 values very close to 1, and SSE values more than 10 to 30 times lower at 23 and 30°C respectively. These results confirm that our additional terms effectively compensate for the pronounced curvature present near the inflection point.

CONCLUSIONS

This study successfully developed enhanced mathematical models for real-time concentration determination in solutions of KOH, H_2SO_4 and KBr used in the Br_2/Br^- metals recovery system from WPCBs through temperature and conductivity measurements. The equation parameters required to calculate concentrations based on temperature and conductivity data for KOH, H_2SO_4 and KBr were determined by building upon a model proposed by Shahid et al, improving it by expanding its viability for concentrations close to the inflection point of the EC = f(C) dependency. Literature and experimental data acquired through a complex experimental setup were used to successfully validate the fitted parameters we obtained for our models, thus proving the possibility of implementing electrochemical sensors for online monitoring and control of certain inorganic electrosynthesis processes. Further developments and improvements to these models should focus on testing the possibility of using them to monitor other electrolytes' concentrations and finding other solution properties which could be used to determine the measurement's position in regards to the inflection point, thus widening the applicable operating range of the models. These new models will gain significant relevance for potential industrial applications concerning the electrochemical monitoring of inorganic reagents concentrations obtained by electrosynthesis.

EXPERIMENTAL SETUP

Reagents

All chemicals were of analytical grade (purity >99%) unless otherwise specified. Solid KBr, KOH and methylene blue (MB) used in the preparation of stock 2.5 M KBr, 1 M KOH and 400 μM MB were purchased from Merck, Germany. The 2.5 M H_2SO_4 stock solution was prepared using 98% H_2SO_4 from Chempur, Germany. All solutions were prepared using double distilled water produced by a laboratory-grade water distillation system.

Equipment

The experimental setup used the following commercial equipment: one SP10T pH/T combined sensor (Consort, Belgium), one LM35 semiconductor-based temperature sensor, one SK23T conductivity sensor (Consort, Belgium), two Reglo Digital MS-2/8 peristaltic pumps called P.P.1 and P.P.2 (ISMATECH, Switzerland), one NI PCI-6259M data acquisition board (National Instruments, USA) inside of a pre-built computer, one USB4000 modular UV-VIS diode array spectrophotometer, two QP600-025-SR UV optical fibers, a FIA-Z-SMA-PEEK flow spectrophotometric cell with 10 mm optical path, a UV-VIS-NIR DT-MINI-2-GS light source all from Ocean Optics, USA, one Thermomix UB thermostat (B. Braun, Germany) and auxiliary equipment such as tubes, stirrers, etc.

Besides commercial equipment, proprietary equipment developed by author S.-A. Dorneanu was integrated in the experimental setup. Our custom equipment was able to interface with the sensors and the computer, allowing for the simultaneous acquisition of conductivity, pH, spectral and temperature data.

Experimental setup

A simplified schematic of the experimental setup employed is presented in Figure 4. The setup consists of a 75 mL double-walled mixing cell connected to a thermostatically controlled water bath and equipped with a lid which had holes for sensors and tubes. Conductivity, pH and T sensors were placed in the appropriate holes, alongside the connecting tubes of P.P.1 and P.P.2. The tubes were positioned inside of the cell such that it allowed for the bidirectional flow of liquid pumped by P.P.2, yet allowed only unidirectional flow from the tank of water dyed with methylene blue (T-W+MB) towards the mixing cell for P.P.1. The EC, pH and T sensors were connected to our proprietary equipment, which was then connected to the data acquisition board using a 68-pin cable. The pumps, magnetic stirrer, light source and spectrophotometer were controlled using a dedicated LabVIEW application. Thermoregulation required manual temperature adjustments between measurements because of the thermostat's limited interface capabilities.

To begin the experiment, 25 mL of stock solution of the target substance was transferred into the dry mixing cell using a calibrated pipette, after which it was given time to reach the target temperature under stirring. Meanwhile, pump P.P.2 was vehiculating the solution through the Z-cell, in order for the external fluid channels to reach thermal equilibrium with the solution inside the mixing cell. Once the desired temperature was reached, using the LabVIEW application, the black (baseline) and blank signals were acquired simultaneously with the conductivity and temperature values at the time when the spectroscopic measurement was taken. In order to improve measurement accuracy, each data

point represented the average of 10 measurements taken over the course of 3 seconds. After the first measurement, P.P.1 starts pumping a pre-determined volume of water dyed with methylene blue, which was calculated such that, after 10 additions, the concentration of the solution will be halved and the concentration values would be evenly distributed across the test range. After each dyed water addition, the software waited for the solution to reach the desired temperature and repeated the acquisition steps from the first measurement, except registering the black signal. The tube used for the peristaltic pump P.P.1 was calibrated before and after each experiment by running it at maximum speed for 1 minute and reading the volume pumped on the graduated pipette.

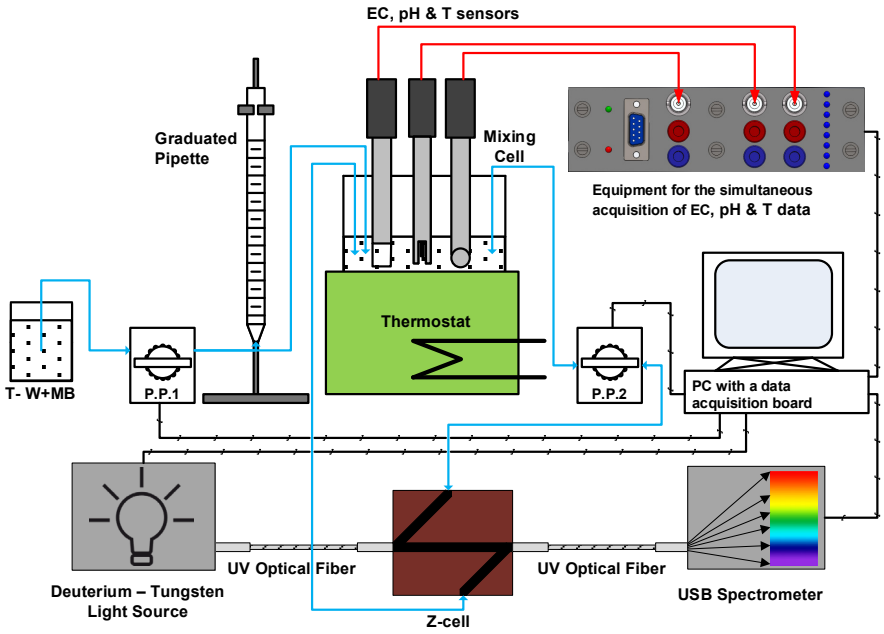

Figure 4. Simplified schematic of the experimental setup used for the acquisition of temperature, conductivity, pH and spectral data for KOH, H_2SO_4 and KBr.

Experimental concentrations after each addition were calculated based on pumping speed, pumping time and the tube calibration constant. In order to validate this approach, we implemented an innovative verification method utilizing methylene blue as a spectroscopic tracer. By measuring absorption at well-defined peaks, we calculated concentrations using the Lambert-Beer law and compared the concentrations obtained spectrophotometrically with

those obtained based on pumping parameters. Consequently, we prepared a 20 μM MB solution by diluting 50 mL of the 400 μM stock solution in 1 L of distilled water, which was then used for the dilution of the electrolyte solutions inside of the mixing cell, resulting in a range of MB concentrations between 0 ÷ 10 μM over the course of the experiments, range for which MB has a linear absorption characteristic.

Some of the key advantages of this method are that it can provide real-time validation of dilution accuracy, it enables the detection of potential systematic errors and it confirms the proper working of the entire experimental setup The concentrations calculated from the pumping parameters and the ones calculated using the Lambert-Beer law agree within 1%, proving that there were no major errors in the dilution setup.

ACKNOWLEDGEMENTS

Author Gabriele-Mario Bogdan is grateful to Babeș-Bolyai University for the Special Scholarship for Scientific Activity (2024-2025), contract number 35809/28.11.2024.

REFERENCES

1. C. P. Baldé; R. Kuehr; T. Yamamoto; R. McDonald; S. Althaf; G. Bel; O. Deubzer; E. Fernandez-Cubillo; V. Forti; V. Gray; S. Herat; S. Honda; G. Iattoni; D. S. Khetriwal; V. Luda di Cortemiglia; Y. Lobuntsova; I. Nnorom; N. Pralat; M. Wagner; *The Global E-waste Monitor 2024*, ITU & UNITAR, Geneva/Bonn, **2024**.
2. J. Lee; H. Choi; J. Kim; *Chem. Eng. J.*, **2024,** *494*, 152917.
3. A. M. Elgarahy; M. G. Eloffy; A. K. Priya; A. Hammad; M. Zahran; A. Maged; K. Z. Elwakeel; *Sustain. Chem. Environ.*, **2024**, *7*.
4. F. Cucchiella; I. D'Adamo; S. C. Lenny Koh; P. Rosa; *Renewable Sustainable Energy Rev.*, **2016**, *64*, 749–760.
5. R. Wang; Q. Zhang; L. Zhan; Z. Xu; *Environ. Pollut.*, **2022**, *308*, 119704.
6. H. Vermeșan; A.-E. Tiuc; M. Purcar; *Sustain.*, **2019**, *12*, 74.
7. S. Udayakumar; M. I. B. A. Razak; S. Ismail; *Mat. Today: Proc.*, **2022**, *66*, 3062–3070.
8. J. Prime; I. A. Ahmed; A. Dennis; N. Elhassan; Y. Melnikov; A. Whiteman; *Renewable capacity statistics 2025*, International Renewable Energy Agency, Abu Dhabi, **2025**.
9. C. Cocchiara; S.-A. Dorneanu; R. Inguanta; C. Sunseri; P. Ilea; *J. Cleaner Prod.*, **2019**, *230*, 170–179.
10. S. Fogarasi; F. Imre-Lucaci; A. Egedy; Á. Imre-Lucaci; P. Ilea; *Waste Manage.*, **2015**, *40*, 136–143.

11. M.-I. Frîncu; E. Covaci; S.-A. Dorneanu; P. Ilea; *Studia UBB Chemia*, **2020**, *65*, 33–44.
12. M. I. Frîncu; E. Covaci; S. A. Dorneanu; P. Ilea; *Studia UBB Chemia*, **2021**, *66*, 137–149.
13. G.-M. Bogdan; M. I. Frîncu; S.-A. Dorneanu; *Studia UBB Chemia*, **2024**, *69*, 177–191.
14. S. Varvara; S.-A. Dorneanu; A. Okos; L. M. Muresan; R. Bostan; M. Popa; D. Marconi; P. Ilea; *Mater.*, **2020**, *13*, 3630.
15. M.-I. Frîncu; G.-M. Bogdan; S.-A. Dorneanu; *Studia UBB Chemia*, **2025**, *70*, 7–22.
16. G.-M. Bogdan; *FCIC*, **2024**.
17. E. S. Shahid; S. H. Afzali; N. Talebbeydokhti; M. Rastegar; *Desalin. Water Treat.*, **2020**, *175*, 255–262.
18. R. J. Gilliam; J. W. Graydon; D. W. Kirk; S. J. Thorpe; *Int. J. Hydrogen Energy*, **2007**, *32*, 359–364.
19. H. E. Darling; *J. Chem. Eng. Data*, **1964**, *9*, 421–426.
20. T. Isono; *J. Chem. Eng. Data*, **1984**, *29*, 45–52.
21. B. B. Owen; H. Zeldes; *J. Chem. Phys.*, **1950**, *18*, 1083–1085.
22. S. Naseri Boroujeni; X. Liang; B. Maribo-Mogensen; G. M. Kontogeorgis; *Ind. Eng. Chem. Res.*, **2022**, *61*, 3168–3185.
23. H. E. Gunning; A. R. Gordon; *J. Chem. Phys.*, **1943**, *11*, 18–20.
24. C. E. Lund Myhre; D. H. Christensen; F. M. Nicolaisen; C. J. Nielsen; *J. Phys. Chem. A*, **2003**, *107*, 1979–1991.

STUDIA UBB CHEMIA, LXX, 3, 2025 (p. 21-33)
(RECOMMENDED CITATION)
DOI:10.24193/subbchem.2025.3.02

MOLYBDENUM FLAT COIL FILAMENT FOR SAMPLE INTRODUCTION AND MULTIELEMENTAL DETERMINATION BY SMALL-SIZED ELECTROTHERMAL VAPORIZATION CAPACITIVELY COUPLED MICROPLASMA OPTICAL EMISSION SPECTROMETRY

Sergiu CADAR[a], Adrian-Ioan DUDU[b,c], Dorin PETREUS[d], Simion Bogdan ANGYUS[a], Maria FRENTIU[a], Eniko COVACI[b,e,*]

ABSTRACT. A novel small-sized electrothermal vaporization device including a molybdenum flat coil filament was studied for sample introduction into a capacitively coupled microplasma (SSETV-μCCP-OES) for the simultaneous multielemental determination of Cu, Zn, Pb, Cd, Hg, Se, Te, Sb and Bi by optical emission spectrometry. The limits of detection, obtained by this experimental setup were 2–25 times lower than those previously obtained using a Rh coil filament, ranging from 0.16 μg L^{-1} for Cd to 10.7 μg L^{-1} for Se. This improvement was primarily attributed to the more efficient heating of the Mo flat coil filament compared to the Rh coil filament, considering that Rh has a lower melting point and therefore must be heated more gradually. Consequently, in the transient spectra recorded using the Mo flat coil filament the maximum signal intensities were observed earlier, ranging from 1.5 s for Hg to 3.3 s for Zn, compared to those obtained with the Rh coil filament, which

[a] *National Institute for Research and Development of Optoelectronics INOE 2000 INCD Bucharest, Research Institute for Analytical Instrumentation, Donath 67, 400293 Cluj-Napoca, Romania.*
[b] *Babeş-Bolyai University, Faculty of Chemistry and Chemical Engineering, 11 Arany Janos str., RO-400028, Cluj-Napoca, Romania.*
[c] *Enzymology and Applied Biocatalysis Research Center, Arany Janos 11, 400028 Cluj-Napoca, Romania.*
[d] *Technical University of Cluj-Napoca, Faculty of Electronics, Telecommunications and Information Technology, Gheorghe Baritiu 26-28, 400027 Cluj-Napoca, Romania.*
[e] *Babeş-Bolyai University, Research Center for Advanced Analysis, Instrumentation and Chemometrics, Arany Janos 11, 400028 Cluj-Napoca, Romania.*
[*] *Corresponding author: eniko.covaci@ubbcluj.ro*

ranged from 2.4 s for Hg to 5.3 s for Cu. The results demonstrate the strong analytical potential of the SSETV device with the Mo flat coil filament, for the simultaneous multielemental trace metal analysis.

Keywords: *electrothermal vaporization, molybdenum flat coil filament, capacitively coupled microsplasma optical emission spectrometry.*

INTRODUCTION

The development of innovative analytical techniques is increasingly steered by the principles of Green Analytical Chemistry, with emphasis on miniaturization and improved sensitivity [1-4]. This approach is closely aligned with lab-on-a-chip paradigms and responds to the growing demand for portable, field-deployable instrumentation across environmental, clinical, and forensic domains [5]. A central challenge in trace elemental analysis lies in the efficient sample introduction techniques into plasma sources [6]. Conventional pneumatic nebulization techniques are often constrained by low analyte transport efficiency, susceptibility to matrix effects, and limited compatibility with microplasma sources [7].

Electrothermal vaporization (ETV) presents a compelling alternative, offering direct analyte vaporization from electrically heated tubes, boats, or filaments [6, 8]. ETV significantly enhances analyte transport efficiency and facilitates temporal separation of analyte from matrix by selective vaporization, and thereby reducing spectral interferences and improving signal-to-noise ratio [6, 9]. Moreover, ETV requires for analysis only microgram-level sample quantities. Collectively, these attributes position ETV as a highly versatile and efficient sample introduction technique for trace elemental and speciation analysis across a wide range of application areas [9-11].

Common heating substrates are commonly made of metals filaments such as W [12-14], Ta [7, 15], Mo [12], Re [5] and Rh [16, 17], as well as composite systems like rhodium-coated tungsten [18], graphite tubes, and emerging metal–ceramic heaters [19]. Compared to graphite furnace used in atomic absorption spectrometry (AAS), metal filaments offer faster heating, lower-power requirements, and reduced memory effects, especially when coated with modifiers like rhodium to enhance durability [8]. Tungsten is most commonly used due to its high melting point, but is prone to oxidation, and they frequently require the presence of hydrogen [18, 20, 21].

Tungsten-based ETV devices have been integrated with a wide range of spectrometric detection techniques, such as atomic absorption spectrometry (AAS) [22], inductively coupled plasma optical emission spectrometry (ICP-

OES) [23], mass spectrometry (ICP-MS) [13], dielectric barrier discharge optical emission spectrometry (DBD-OES) [12] and atmospheric pressure glow discharge atomic emission spectrometry (APGD-AES) [20] for multielemental determination in environmental, food and biological samples. Rhenium and Ta filaments have been applied in ETV systems coupled with AAS, AES, and atomic fluorescence spectrometry (AFS) for trace metal determination, such as Pb, Cu, Mn, Cd, K, Na and Li [5, 7].

Molybdenum on the other hand, has previously been explored for ETV coupled with AAS, ICP-MS, and more recently with dielectric barrier discharge optical emission spectrometry (DBD-OES) for the determination of Zn, Pb, Ag, Cd, Au, Cu, Mn, Fe, Cr and As in various environmental samples [24, 25]. In these studies, only tubular and wire-based filament geometries were employed, in combination with conventional benchtop instruments. Microplasma based configurations remain largely unexplored, and no prior studies have reported of such filament.

Until now, the capacitively coupled microplasma torch has been coupled with a miniaturized sample introduction system based on electrothermal vaporization from a Rh coil filament. Although rhodium offers several important advantages, such as ease of manual handling, high chemical resistance to oxygen and acids used for sample digestion, and the fact that it does not require the presence of hydrogen in the electrothermal vaporization atmosphere, its relatively low melting point of approximately 1963 °C limits the rate of analyte evaporation, which in turn negatively affects the sensitivity of the analysis [16, 17]. Thus, the aim of this study was to design and characterize a novel Mo flat coil filament as sample introduction device for the simultaneous multielemental determination of Cu, Zn, Pb, Cd, Hg, Se, Te, Sb and Bi by small-sized electrothermal vaporization capacitively coupled microplasma optical emission spectrometry (SSETV-μCCP-OES). Limits of detection (LOD) were evaluated based on signal-to-background ratio and relative standard deviation of the background signal (SBR-RSDB) [26, 27] by comparison with those previously obtained with a Rh coil filament.

RESULTS AND DISCUSSION

Figure 1 and 2 illustrate the novel SSETV sample introduction system with a Mo flat coil filament developed for the simultaneous multielemental determination of Cu, Zn, Pb, Cd, Hg, Se, Te, Sb and Bi by μCCP-OES. The system operates in two sequential stages. In the first stage, the filament is heated in air to 80 °C for 180 s to dry the microsample previously pipetted onto its surface, while in the second stage, the filament is heated in Ar flow to 1500 °C

for 10 s to vaporize the sample and introduce it into the microplasma for excitation. Simultaneously with the vaporization step, the emission signals were recorded using the Maya2000 Pro microspectrometer (Ocean Optics, Dunedin, USA) as 100 episodic spectra with 100 ms integration time. A detailed description of the construction and operation of the SSETV device is provided in the Experimental section.

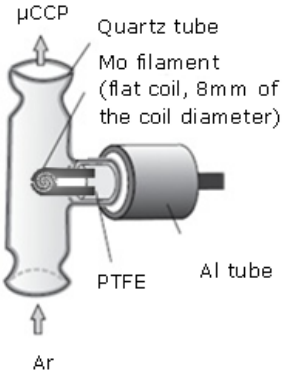

Figure 1. Scheme of the Mo flat coil filament installed in the vaporization chamber

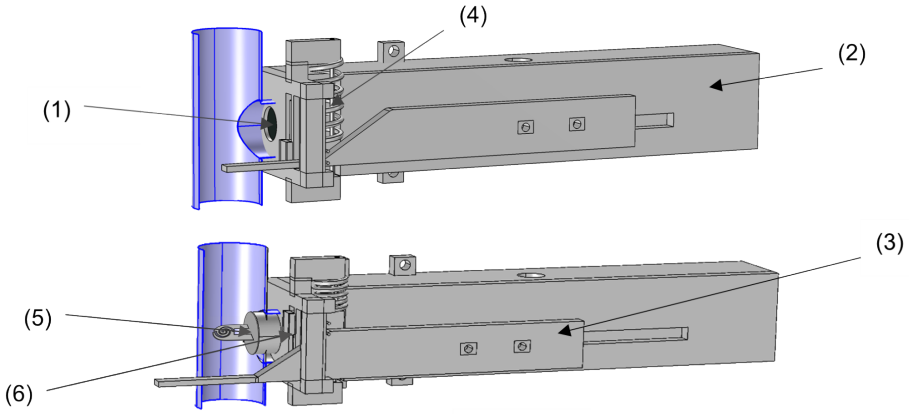

Figure 2. Filament introduction system in sample drying (top) and vaporization (bottom) positions (1 – iris type mechanism; 2 – piston support; 3 – lever; 4 – spring; 5 – Mo flat coil filament fixed on a PTFE piston with the aid of epoxy resin; 6 – iris actuator slider)

An initial study on the excitation capability of the μCCP indicated an optimal operating power of 15 W and an argon consumption rate of 150 mL min^{-1}.

For spectroscopic observation of the plasma, a height of 0.8 mm above the molybdenum tip microelectrode was selected, as previously determined to be optimal for achieving maximum emission signal intensity and enabling simultaneous multielement detection of transient emission spectra [17, 28, 29]. It was also previously observed that a temperature of 1500 °C is sufficient for the evaporation of a significant number of elements from the Rh coil filament, which can be vaporized and excited at resonance lines with excitation energies of up to 7.5 eV [28]. This temperature was also selected for the Mo filament in the present study. A sample volume of 10 µL was employed in all measurements, consistent with those used in previous studies. The optimal operating conditions for the SSETV-µCCP-OES tandem for the simultaneous determination of Cu, Zn, Pb, Cd, Hg, Se, Te, Sb, and Bi using both the Mo flat coil filament and the Rh coil filament are presented in Table 1.

Table 1. The optimal operating conditions of the SSETV-µCCP-OES tandem for the simultaneous determination of Cu, Zn, Pb, Cd, Hg, Se, Te, Sb, and Bi using the Mo flat coil filament and the Rh coil filament

Parameter	**Working conditions**	
	Rh coil filament	**Mo flat coil filament**
Microplasma power	15 W	
Ar flow rate	150 mL min^{-1}	
Observation height	0.8 mm	
Sample drying	80 °C for 180 s (0.25 V, 1.93 A)	80 °C for 180 s (0.1 V, 3.6 A)
Sample vaporization	1500 °C for 10 s (1.62 V, 4.32 A)	1500 °C for 10 s (1.20 V, 12 A)
Spectra registration	100 episodic spectra with 100 ms integration time	

The temperature control of the filaments was verified by optical pyrometry using the Optris 3ML and Optris 1MH1-CF3 IR detectors from Optris GmbH (Berlin, Germany). In contrast to the Rh coil filament, which has a melting point of 1963 °C and needs a current limit of 5 A, the Mo flat coil filament, due to its higher electrical resistance, is characterized by a higher melting point (2620 °C) and can be operated at higher currents of up to 12 A, enabling faster heating. The filament temperature during the vaporization stage was controlled with a precision better than 2% and a bias of +20 °C relative to the target temperature. The power source used for the filaments heating enabled microsecond-level temperature control, resulting in highly reproducible operating temperatures. Under these operating conditions, the evaporation of elements is expected to occur more rapidly with the Mo flat coil filament compared to the Rh coil filament, with a higher instantaneous

analyte flux, resulting in an earlier appearance of the analytical signals and within fewer episodic spectra. Accordingly, based on the higher sensitivity, expressed as signal-to-background ratio (SBR), improved limits of detection are expected to be obtained for the Mo flat coil filament compared to the Rh coil filament.

Figure 3 presents the 3D emission spectra of the elements obtained using the Mo flat coil filament under the optimal operating conditions of the SSETV-μCCP-OES setup.

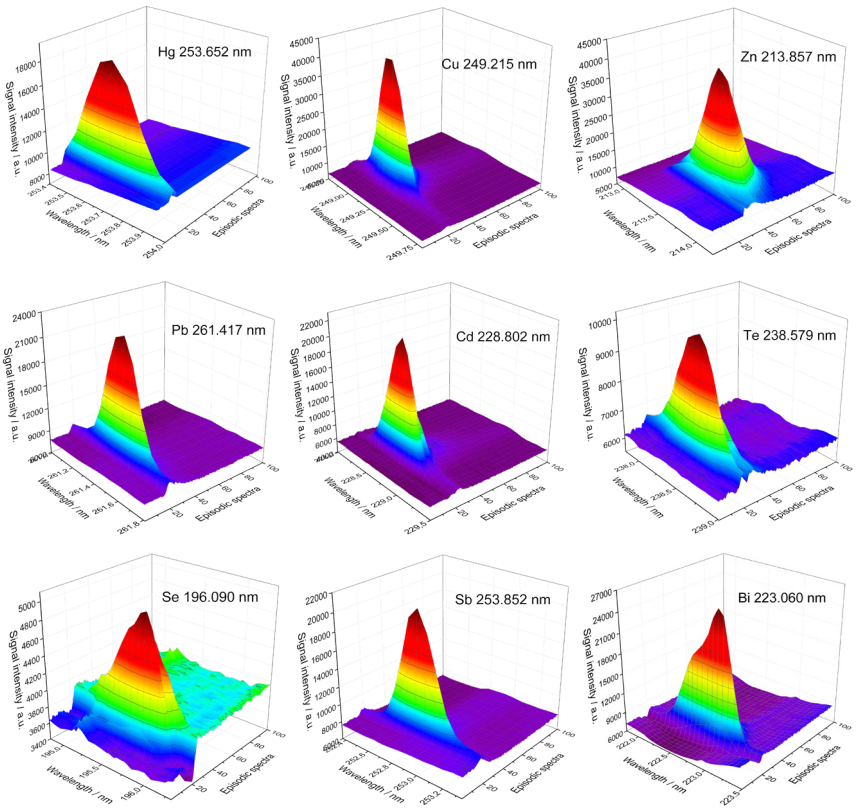

Figure 3. 3D emission spectra (signal intensity, wavelength, time) of Hg, Cu, Zn, Pb, Cd, Te, Se, Sb and Bi recorded by ETV-μCCP-OES using the Mo flat coil filament in measurement conditions: plasma observation height: 0.8 mm above the Mo tip electrode; plasma power: 15 W; Ar flow rate: 150 mL min^{-1}; sample volume: 10 μL; elements concentration: 1 mg L^{-1} Cu, Pb, Te, Se, Sb and Bi and 0.1 mg L^{-1} Cd, Zn and Hg multielement standard solution in 2% (v/v) HNO_3, vaporization: 1500 °C for 10 s

Figure 4 presents the transient net emission signals of elements, along with the times at which maximum signal intensities occurred, obtained by SSETV-μCCP-OES using the Mo flat coil filament under optimized working conditions. It was observed that, except for Zn, all elements reached maximum vaporization between 1.5 s (Hg) and 2.2 s (Cu and Bi). In contrast, previously reported data using a Rh coil filament showed delayed vaporization maxima, with maximum emission signals at 2.4 s Hg; 5.3 s Cu; 4.9 s Zn; 5.2 s Pb; 4 s Te; 3.5 s Se; 4.3 s Sb and 4 s Bi [28, 29]. These findings demonstrate that the Mo flat coil filament provides a more efficient vaporization of the microsample compared to the Rh coil counterpart.

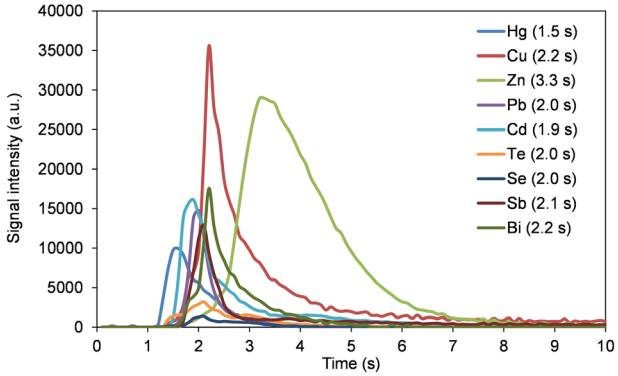

Figure 4. Transient net emission signals of elements at their most sensitive lines recorded by SSETV-μCCP-OES using the Mo flat coil filament in measurement conditions: plasma observation height: 0.8 mm above the Mo tip electrode; sample volume: 10 μL; elements concentration: 1 mg L^{-1} Cu, Pb, Te, Se, Sb and Bi and 0.1 mg L^{-1} Cd, Zn and Hg multielement standard solution in 2% (v/v) HNO_3

The limits of detection obtained using the SBR–RSDB approach [26, 27] for the SSETV-μCCP-OES method, employing both the Mo flat coil and Rh coil filament under optimized working conditions, are presented in Table 2. Signal-to-background ratio values were determined using emission signals recorded using a multielement solution containing 1 mg L^{-1} of Cu, Pb, Te, Se, Sb, and Bi, and 0.1 mg L^{-1} of Cd, Zn, and Hg. Although the concentrations were selected arbitrary, they do not affect the calculated limits of detection, as they fall within the linear dynamic range of the method. Previous work using the same experimental setup with a Rh coiled filament demonstrated linear calibration curves up to concentrations of 5 mg L^{-1}. [28] The RSDB values ranged from 0.5% to 1.5% for the Mo flat coil filament, similar to those obtained with the Rh coil filament, which ranged from 0.8% to 1.9%. Significantly better LODs were achieved using the Mo flat coil filament ranging from 0.16 μg L^{-1} for Cd to 10.7 μg L^{-1} L for Se, compared with the range of 0.28 μg L^{-1} for Cd –

22.6 μg L^{-1} Se for the Rh coil filament. Thus, improvements in the limits of detection (LODs) by factors of 2 to 25 were achieved for the majority of elements, with the exception of copper. This enhancement can be attributed to the faster heating of the Mo flat coil filament, as expected, compared to the Rh filament, which is limited to a current of 5 A, in contrast to 12 A for the Mo filament. A comparison between the LODs obtained by SSETV-μCCP-OES using the Mo flat coil filament and those reported for other microplasma sources equipped with metallic electrothermal vaporization devices used in optical emission spectrometry is presented in Table 3.

Table 2. Analytical figures of merit of the SSETV-μCCP-OES method using the Rh coil and Mo flat coil filaments

Element	λ (nm)[a]	Rh coil filament			Mo flat coil filament		
		RSDB (%)	SBR[b]	LOD[c](μg L^{-1})	RSDB (%)	SBR[b]	LOD[c] (μg L^{-1})
Hg	253.652	1.1	2.2	1.50	1.2	18.0	0.20
Cu	249.215	1.0	5.0	0.61	1.0	4.0	0.74
Zn	213.857	1.9	1.1	5.06	1.5	22.5	0.20
Pb	261.417	1.2	0.4	8.60	1.0	1.2	2.40
Cd	228.802	0.8	8.6	0.28	1.2	22.5	0.16
Te	238.579	1.6	0.4	4.86	1.1	2.1	1.60
Se	196.090	1.0	0.1	22.6	1.5	0.4	10.7
Sb	253.852	1.6	0.2	19.0	0.5	1.4	1.10
Bi	223.060	1.2	0.6	5.60	0.7	1.9	1.09

[a] Wavelengths correspond to values listed in the NIST Atomic Spectra Database;
[b] SBR is the Signal-to-Background ratio for 1 mg L^{-1} Cu, Pb, Te, Se, Sb and Bi and 0.1 mg L^{-1} Cd, Zn and Hg [b] LOD was calculated according to the SBR-RSDB approach [26, 27];

Table 3. Comparison of LODs for the Mo flat coil filament SSETV-μCCP-OES method with other ETV-based microanalytical systems

Element	SSETV-μCCP-OES (Mo flat coil)	ETV-DBD-OES (Mo coil) [24][a]	ETV-DBD-OES (W coil) [12][b]	ETV-DBD-OES (W coil) [14][c]	ETV-PD-OES[f] (Re coil) [30][d]	ETV-PD-OES[f] (W coil) [21][e]
Hg	0.20	0.40	-	-	-	-
Cu	0.74	7.94	-	-	1.5	15
Zn	0.17	1.89	24	-	20	5
Pb	2.40	8.95	-	7.7	20	8
Cd	0.16	0.65	0.8	-	20	0.08
Te	1.60	-	-	-	-	-
Se	10.7	-	-	-	-	-
Sb	1.10	-	-	-	-	41
Bi	1.09	-	-	-	-	40

[a] Sample volume: 3 μL, plasma power: 37 W;
[b] Sample volume: 10 μL, plasma power: 2 W;
[c] Sample volume: 20 μL, plasma power: 30 W;
[d] Sample volume: 3 μL, plasma power: 4 W;
[e] Sample volume: 10 μL, plasma power: 0.8–3.2 W;
[f] ETV-PD-OES – electrothermal vaporization point discharge optical emission spectrometry

A comparison between various analytical systems, including those based on optical emission spectrometry using microplasma sources, is challenging without considering the characteristics of the micro sample introduction device, the sample volume, and the operating conditions of the microplasma, particularly the power. Therefore, in miniaturized systems employing electrothermal evaporation, the emission signal is directly proportional to both the micro sample volume and the microplasma power at a given analyte concentration. Thus, the LODs for Hg, Cu, Zn, Pb, and Cd obtained using the SSETV-μCCP-OES experimental setup with the Mo flat coil filament were superior to those reported by Li et al. [24] using ETV-DBD-OES with a Mo coil, primarily due to the use of a 10 μL sample volume in our study, compared to only 3 μL in the DBD microplasma system. A similar trend was observed for Zn and Cd, compared to those reported using the ETV-DBD-OES system with a W filament. This enhancement is attributed to the higher microplasma power employed in our setup (15 W), in contrast to the 2 W used in the DBD microplasma configuration. Compared to the ETV-DBD-OES setup with a W filament, the achieved LOD for Pb using our experimental configuration was superior, despite using only half the micro-sample volume and a plasma power two times lower than those employed in the DBD microplasma system [14]. This is likely due to a lower spectral background of the capacitively coupled microplasma and an improved signal-to-background ratio. Compared to the experimental ETV-MPD-OES system with a Re filament [30], in which a volume of 3 μL sample and a microplasma power of 4 W was employed, our limits of detection for Cu, Pb, Zn, and Cd were also superior, as a result of the aforementioned considerations. In the case of the ETV-PD-OES system [21], which employed a W filament, a sample volume of 10 μL, and an operating power of up to 3.2 W, the limits of detection for Cu, Zn, Pb, Sb, and Bi were also superior to those obtained with our SSETV-μCCP-OES setup using the Mo flat coil filament. These findings highlight that the Mo flat coil filament, designed and fabricated in our laboratory, is a promising device for use in a miniaturized ETV configuration coupled with microplasma-based optical emission spectrometry for trace metal analysis. By using a faster heating rate, the LODs were substantially improved, and the method can be applied to food, environmental, and polymeric material samples subjected to acid digestion; however, further studies are needed to evaluate potential matrix effects caused by the presence of concomitant elements in the sample matrix.

CONCLUSIONS

A novel SSETV device based on innovative molybdenum flat coil filament was successfully used for microsample introduction in a capacitively coupled microplasma for the simultaneous multielemental determination of Cu, Zn, Pb, Cd, Hg, Se, Te, Sb, and Bi by optical emission spectrometry. The Mo flat coil filament allowed better limits of detection to those previously obtained by the same SSETV-μCCP-OES equipped with a Rh coil filament. This was attributed to a faster vaporization process and an improved signal-to-background ratio (SBR). Furthermore, the comparative data obtained using the SSETV-μCCP-OES setup with the Mo flat coil filament, in relation to other miniaturized microplasma-based analytical systems reported in the literature, confirmed its analytical capabilities required for multielement trace metals analysis in liquid microsamples.

EXPERIMENTAL SECTION

Reagents and solutions

Single element ICP standard solutions of Cu, Zn, Pb, Cd, Te, Se, Sb, Bi and Hg of 1000 mg L^{-1} in HNO_3, purchased from Merck (Darmstadt, Germany), were used for the preparation of 1 mg L^{-1} Cu, Pb, Te, Se, Sb and Bi and 0.1 mg L^{-1} Cd, Zn and Hg multielement-standard solution by serial dilution with 2% (v/v) HNO_3. Nitric acid 65% (m/m) for analysis (max 0.005 mg L^{-1} Hg) was purchased from Merck (Darmstadt, Germany). A solution of 5% (v/v) HNO_3 was used for decontamination of glassware by immersion overnight, followed by rinsing with ultrapure water (18 MΩ cm), obtained using a Milli-Q water purification system (Millipore, Bedford, USA).

Instrumentation

The μCCP-OES instrumentation was similar to that previously used, with the exception of the Rh coil filament, which was replaced by a small-sized electrothermal vaporization device based on Mo flat coil filament [17]. The SSETV-μCCP-OES setup used in this study consisted of the following components: (1) a home-made capacitively coupled microplasma (μCCP-OES) as excitation source (2); a miniaturized RF generator of 13.56 MHz (Technical University, Cluj-Napoca, Romania), operated at low power (15 W) and low Ar flow rate (150 mL min^{-1}); (3) a Maya2000 Pro CCD spectrometer with a spectral range of 165–309 nm and a Full Width at Half Maximum (FWHM) of 0.35 nm, Ocean Optics (Dunedin, USA); (4) a home-made Mo

flat coil filament as sample introduction system powered from a TENMA 72-13360 (TENMA Inc. China). The heating of the Mo filament was controlled by an application developed in Labview (National Instruments, USA) for sample drying at 80 °C for 180 s and vaporization at 1500 °C for 10 s. Simultaneously with the evaporation of a volume of 10 µL microsample, the transient emission spectrum was recorded over a period of 10 s with an integration time of 100 ms per episode for all elements. The Mo flat coil filament, the SSETV setup was incorporated in a 3D printed sample introduction system from polyacrylamide using the Creality K1 3D equipment (Shenzhen Creality 3D Technology Co., Ltd., China) (Figures 1 and 2). The 3D printing conditions were: 0.4 mm nozzle diameter, 230 °C nozzle temperature, 45 °C platform temperature, 8–15% sparse infill density, diamond infill pattern, 2 mm s^{-1} printing speed, 0–15% internal fill density of support material and diamond infill pattern of support material. The Mo flat coil filament was manufactured from a 0.13 mm thick Mo sheet, with a purity of 99.9% (JSflline Material Store, China), cut into a coil geometric form using a laser cutting equipment (Fiber laser MOPA 30w, China).

The Mo flat coil filament is installed and fixed on a PTFE piston with the aid of epoxy resin (Figure 2, (5)), using a set of two cables soldered to its two terminals and passed through the piston body in the middle for connection to the power supply. The piston support (2) includes a cover with a cutout for attaching the lever and couplings, and at the end of the piston support, the mount with the iris-type mechanism (1) is installed, which includes a shaft and a spring to guide the iris actuator slider (6). The lever (3) is attached to the rod and inserted through a channel of the iris-type mechanism. When the piston is moved, the lever is also engaged, which in turn moves the iris actuator slider, namely opening it during forward motion and closing it during retraction. This mechanism converts the horizontal movement of the piston into a vertical movement of the slider. The iris opening and closing zones are correlated with the slope on the lever, and the positioning of the lever on the piston determines the moment at which the iris begins to open or close, ensuring that the orifice remains open for the shortest possible time. Since it is crucial to have the slider in a position where the iris is closed when extracting the filament, and a gravitational solution was neither sufficient nor reliable, a spring (4) was chosen to act on the slider, ensuring it moves downward and keeps the iris closed. The heating of the filament was ensured by connecting the 4 wires to the power source, of which 2 served for voltage supply, while the other 2 were connected to the regulation loop (Sense) of the power supply. This ensured that the power source maintained the set voltage applied to the filament, eliminating voltage drops across the supply cables and the contacts at the power terminals.

Method figures of merit

The figures of merit of the SSETV-μCCP-OES method, were evaluated in terms of relative standard deviation of the background signal (RSDB,%), signal-to-background ratio (SBR), and limit of detection (LOD). Instrumental LODs were calculated using the SBR-RSDB approach [26, 27], previously developed by Boumans, according to equation (1)

$$\mathrm{LOD} = 3 \times 0.01 \times \mathrm{RSDB} \times \frac{c_0}{\mathrm{SBR}} \quad (1)$$

where, RSDB – is the relative standard deviation of the background signal from 10 episodic spectra (100 ms integration time) before micro sample introduction; c_0 – is the analyte concentration; and SBR – the signal-to-background ratio.

The analyte signal was obtained by time integration, using the signal generated by the pixel corresponding to the analytical line. The number of spectra in which the analytical signal appeared ranged from 15–64, depending on the temporal evaporation kinetics of the element.

ACKNOWLEDGMENTS

This work was supported by a grant of the Romanian Ministry of Research Innovation and Digitization through the Core Program within the National Research Development and Innovation Plan 2022–2027, carried out with the support of MCID, project no. PN 23 05. This work was also supported by a grant of the Romanian Ministry of Research, Innovation and Digitization, CNCS/CCCDI-UEFISCDI, contract nr. 15PED/2025, project number PN-IV-P7-7.1-PED-2024-0091, within PNCDI IV.

REFERENCES

1. T. Matusiak; K. Swiderski; J. Macioszczyk; P. Jamroz; P. Pohl; L. Golonka; *Sensor Rev.,* **2020**, *40*, 437–444.
2. D. A. Agrawal; R. Keçili; F. Ghorbani-Bidkorpeh; C. M. Hussain; *TrAC - Trends Anal. Chem.,* **2021**, *143*, 116383.
3. Y. Zhang; J. Liu; X. Mao; G. Chen; D. Tian; *TrAC - Trends Anal. Chem.,* **2021**, *144*, 116437.
4. A. Galuszka; Z. Migaszewski; J. Namieśnik; *TrAC - Trends Anal. Chem.,* **2013**, *50*, 78–84.
5. H. R. Badiei; C. Liu; V. Karanassios; *Microchem. J.,* **2013**, *108*, 131–136.

6. D. C. Gregoire; *Electrothermal vaporization sample introduction for inductively coupled plasma-mass spectrometry* in *Comprehensive Analytical Chemistry*, Elsevier, **2000**, *Vol. 34*, pp. 347–444.
7. Y.-I. Lee; J.-K. Kim; K.-H. Kim; Y.-J. Yoo; G.-H. Back; S.-C. Lee; *Microchem. J.,* **1998**, *60*, 231–241.
8. L. Huang; D. Beauchemin; *Electrothermal vaporization* in *Sample Introduction Systems in ICPMS and ICPOES*, ed. by D. Beauchemin, Elsevier, Amsterdam, **2020**, pp. 411–467.
9. M. Aramendía; M. Resano; F. Vanhaecke; *Anal. Chim. Acta.,* **2009**, *648*, 23–44.
10. M. Resano; F. Vanhaecke; M. T. C. de Loos-Vollebregt; *J. Anal. At. Spectrom.,* **2008**, *23*, 1450–1475.
11. G. C. Y. Chan; G. M. Hieftje; N. Omenetto; O. Axner; A. Bengtson, et al.; *Appl. Spectrosc.,* **2024**, *79*, 481–735.
12. X. Jiang; Y. Chen; C. Zheng; X. Hou; *Anal. Chem.,* **2014**, *86*, 5220–5224.
13. N. H. Bings; Z. Stefanka; *J. Anal. At. Spectrom.,* **2003**, *18*, 1088–1096.
14. H. Zheng; J. Ma; Z. Zhu; Z. Tang; S. Hu; *Talanta,* **2015**, *132*, 106–111.
15. Q. Jin; H. Zhang; W. Yang; Q. Jin; Y. Shi; *Talanta,* **1997**, *44*, 1605–1614.
16. T. Frentiu; E. Darvasi; S. Butaciu; M. Ponta; D. Petreus; R. Etz; M. Frentiu; *Microchem. J.,* **2015**, *121*, 192–198.
17. T. Frentiu; E. Darvasi; S. Butaciu; M. Ponta; D. Petreus; A. I. Mihaltan; M. Frentiu; *Talanta,* **2014**, *129*, 72–78.
18. P. J. Parsons; Y. Zhou; C. D. Palmer; K. M. Aldous; P. Brockman; *J. Anal. At. Spectrom.,* **2003**, *18*, 4–10.
19. G. Lan; X. Li; J. Yao; X. Yu; Q. Liu; C. Qiu; X. Mao; *Front. Nutr.,* **2023**, *10*, 1201801.
20. L. Qian; Z. Lei; X. Peng; G. Yang; Z. Wang; *Anal. Chim. Acta.,* **2021**, *1162*, 338495.
21. Y. Deng; J. Hu; M. Li; L. He; K. Li; X. Hou; X. Jiang; *Anal. Chim. Acta.,* **2021**, *1163*, 338502.
22. S. N. Hanna; K. Joseph; C. J. C. P.; B. T. and Jones; *Instrum. Sci. Technol.,* **2011**, *39*, 345–356.
23. A. C. Davis; C. P. Calloway; B. T. Jones; *Talanta,* **2007**, *71*, 1144–1149.
24. N. Li; Z. Wu; Y. Wang; J. Zhang; X. Zhang; H. Zhang; W. Wu; J. Gao; J. Jiang; *Anal. Chem.,* **2017**, *89*, 2205–2210.
25. J. A. Rust; G. L. Donati; M. T. Afonso; J. A. Nóbrega; B. T. Jones; *Spectrochim. Acta B.,* **2009**, *64*, 191–198.
26. P. W. J. M. Boumans; *Spectrochim. Acta B.,* **1991**, *46*, 431–445.
27. P. W. J. M. Boumans; J. C. Ivaldi; W. Slavin; *Spectrochim. Acta B.,* **1991**, *46*, 641–665.
28. S. B. Angyus; E. Levei; D. Petreus; R. Etz; E. Covaci; O. T. Moldovan; M. Ponta; E. Darvasi; T. Frentiu; *Molecules,* **2021**, *26*, 2642.
29. S. B. Angyus; M. Senila; T. Frentiu; M. Ponta; M. Frentiu; E. Covaci; *Talanta,* **2023**, *259*, 124551.
30. S. Weagant; V. Chen; V. Karanassios; *Anal. Bioanal. Chem.,* **2011**, *401*, 2865–2880.

STUDIA UBB CHEMIA, LXX, 3, 2025 (p. 35-53)
(RECOMMENDED CITATION)
DOI:10.24193/subbchem.2025.3.03

PHYSICOCHEMICAL INVESTIGATION OF SOME GEOTHERMAL WATERS FROM SALAJ COUNTY ROMANIA

Simona Elena AVRAM[a], Cristian MANDIUC[a], Ioan PETEAN[b,*], Lucian Barbu TUDORAN[c,d], Gheorghe BORODI[d,*]

ABSTRACT. Geothermal waters solve minerals from the geological layers due to their increased temperature. These minerals affect water hardness and salinity. Therefore, thermal water samples were collected from spa pools springs in Salaj County Romania: Broscarie (Simleul Silvaniei), Jibou, and Boghis. The physicochemical measurement reveal that Jibou water has higher electrical conductivity of 10580 µSi/cm caused by the higher value of total dissolved solids (TDS) of 5264 mg/l, it is followed by Broscarie water having an electrical conductivity of 1949 µSi/cm related to TDS of 1023 mg/l. The weaker mineralization was found in Boghis water around of 619 mg/l corresponding to an electrical conductivity of 1200 µSi/cm. Water hardness is related to $CaCO_3$ amount. Boghis water is the harder containing 356 mg/l followed by Broscarie having 178 mg/l. Jibou water is the softer having $CaCO_3$ about 106.8 mg/l. The mineral distribution was assessed by mineralogical optical microscopy (MOM) and X ray diffraction (XRD). It results that NaCl crystallized as halite is responsible for the samples salinity while aragonite, magnesian calcite and calcite are the minerals which causes the water hardness. Hard thermal water containing Ca and Mg are effective for rheumatoid symptoms amelioration while salted water is optimal for skin care.

Keywords: *Thermal water, mineral content, hardness, salinity.*

[a] *Faculty of Materials and Environmental Engineering, Technical University of Cluj-Napoca, 103-105 Muncii Bd., RO-400641, Cluj-Napoca, Romania.*
[b] *Faculty of Chemistry and Chemical Engineering, Babes-Bolyai University, 11 Arany Janos Street, 400028 Cluj-Napoca, Romania.*
[c] *Faculty of Biology and Geology, Babes-Bolyai University, 44 Gheorghe Bilaşcu Street, 400015 Cluj-Napoca, Romania.*
[d] *National Institute for Research and Development of Isotopic and Molecular Technologies, 65-103 Donath Street, 400293 Cluj-Napoca, Romania.*
[*] *Correspondent authors:* ioan.petean@ubbcluj.ro*;* borodi@itim-cj.ro

INTRODUCTION

Geothermal waters are formed into the deeper geological formation heated by the magma layer. They are most likely occur through the tectonic faults which facilitates the water infiltration and it's subsequently lift as hot springs [1, 2]. The increased temperature facilitates minerals dissolution enriching water is specific ions depending on the geological layers composition [3]. The dominant mineral imposes the geothermal characteristic as: carbonated when CO_2 interacts with Ca and Mg from sedimentary rocks, sulphurated geothermal water contains S from the rocks interaction with H_2S or from biogenic sources like sulfur bacteria [4, 5]. On the other hand, salted water are formed by the water interaction with Halite evaporite deposits (NaCl crystallized in cubic system), without need of thermal energy [6, 7]. High temperature of the geothermal water increases the Halite solubility in water and therefore it is often found in geothermal and mineral waters in various ratios depending on its occurrence on the geological layers.

Salaj County is situated in northwestern side of Romania and is affected by the North Transylvanian fault influencing the sedimentary layers [8]. For instance, Simleul Silvaniei is influenced by the Badenian deposits including yellow sand, crystalline conglomerates, sandstone and evaporite deposits. Krezsek and Bally reports sedimentary layers of sandstone, limestone with crystalline conglomerates formed in Eocene period [8]. Thus, Jibou Formations includes Lower Variegated Red Shales and Rona limestone interfered with some evaporitic salt deposits [9, 10]. Similar sedimentary conditions are reported in literature for Boghis area influencing the geothermal water mineral content [11]. The local tectonic rift and the geological layers interaction with water deposits facilitate its emergence to the surface as hot geothermal springs in Simleul Silvaniei, Jibou and Boghis. These springs were collected directly from the source and the water is currently used for spa pools.

Sandstone is a pressed conglomerate formed by quartz sand and clay fine fractions as granular filler and calcium carbonate as mineral binder. This binder most likely occurs as calcite crystallized in Trigonal system and less crystallized in orthorhombic system as aragonite as occurs in limestone [12, 13]. Calcium carbonate has a limited solubility in water of about 13 mg/l at 25 °C and increases with temperature, therefore the geothermal water are enriched in Ca^{2+} ions [13].

Sandstone and limestone might contain $CaMg(CO_3)_2$ crystallized in Trigonal system having ordered successive layers of Mg and Ca atoms and consist in a major source of magnesium within geothermal water [14]. The other source of magnesium within the geothermal water is magnesian clays mineral such as palygorskite, sepiolite and kerolite but it might occurs as

impurities in red clays like Muscovite and Biotite replacing some of the Fe atoms in their structure. Water, especially at high temperature, penetrates the clay interplanar layers solving some of their mineral content [15, 16].

Badenian evaporite deposits within the Transylvanian Basin are formed mainly by NaCl crystallized in cubic system as halite. However they might be accompanied by moderate amounts of calcium sulfate crystallized as gypsum or anhydrite [17, 18]. Halite has an extremely high solubility in water around of 360 g/L at 25 °C, compared to calcite and dolomite and strongly increases with the temperature [19]. Thus, the evaporitic deposits are quickly dissolved by the hot water while carbonaceous rocks take longer. Larger geothermal water deposits have long interaction with the geological layers until burst out from the ground as hot springs collecting the specific mineral amount. A complete investigation regarding their mineralization mechanism would require detailed geological drillings for accurate establishing of each stone layer's composition. Hence, the geological drillings are very expensive and require a lot of work on the field, relevant information regarding the water mineralization can be obtained through their in vitro crystallization.

One of our previous studies reveals successfully the mineralization within the public springs in Borsec [20]. Water physicochemical properties like pH, turbidity, of total dissolved solids (TDS), salinity, electrical conductivity and chloride content were correlated with the specific mineral crystallization. These aspects were reveled with some targeted investigation: minerals formation and crystallization was investigated by X-ray diffraction (XRD) coupled with optical mineralogical microscopy (MOM), morphological aspects were correlated with the elemental composition through the SEM – EDX analysis. It was found that pre-existent solid particles dispersed in the water samples (samples with high turbidity) acts as germination seeds while in the clear water samples crystallization germs precipitates through the homogeneous germination under concentration gradient induced by the water evaporation. Such behavior was also reported in literature for the Pharmacolite ($CaHAsO_4 \cdot 2H_2O$) along with carbonates [21]. It is expected that a competitive behavior will occur between the crystallization of carbonates and halides when the collected water samples are dried.

The aim of present research is to discover a sustainable approach of these geothermal waters based on their physicochemical properties correlation with the crystallization of mineral content during the natural drying.

RESULTS AND DISCUSSION

The mineral charge has a strong influence on the physicochemical characteristics of the water samples. It results that all investigated springs have slightly alkaline pH around 8, Figure 1a, forming a single relevant statistical group.

It indicates a balance between carbonated and salted mineralization which is proper for curative baths. The constant ph values for the waters collected from all 3 investigated sites rely on the similar sedimentary geological formations interacting with hot water.

Turbidity represents another general physical characteristic of the water samples revealing the presence or absence of the solid particles dispersed within. Figure 1b reveal that samples from Broscarie and Boghis are clear having turbidity below the detection limit and thus forms a relevant statistical group. It might be a characteristic favored by their temperature of about 40 ˚C at collection moment. Water samples collected from Jibou has a turbidity of about 6 FTU which is a low value according to the Directive (EU) 2020/2184. However the statistical analysis indicates that Jibou sample forms the second statistical relevant group. Statistical comparing of these two groups reveals statistical differences $p < 0.05$. It might influence the crystallization process through the solid dispersoids acting as heterogeneous crystallization germs.

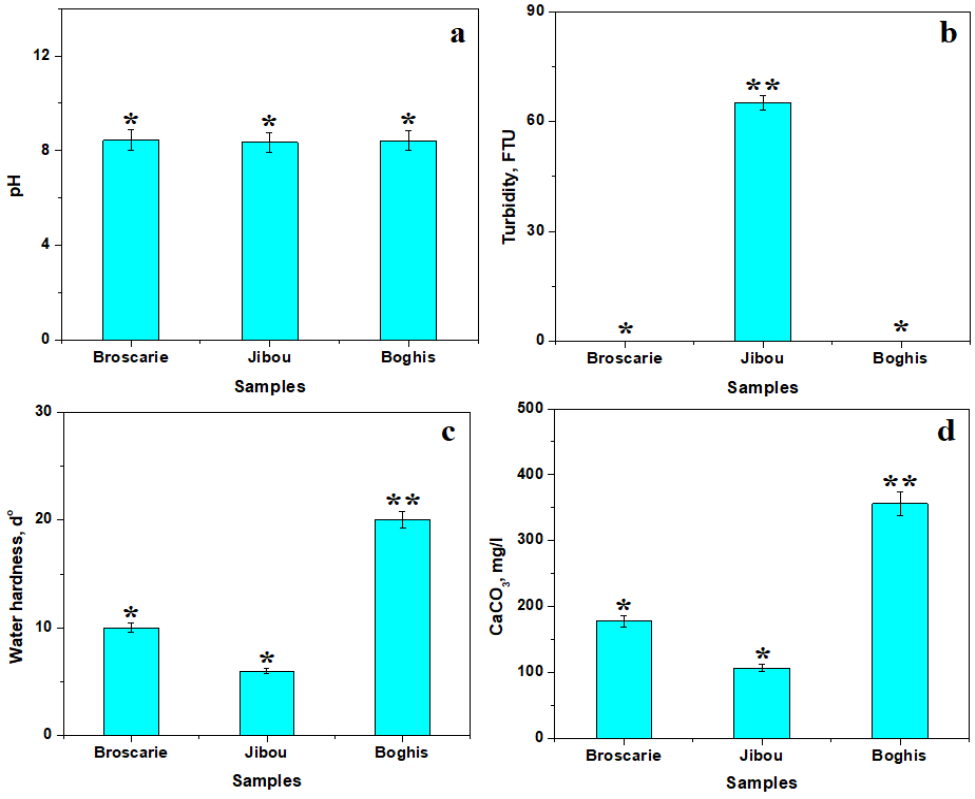

Figure 1. General physicochemical parameters of the water samples: a) pH, b) Turbidity, c) Hardness and d) $CaCO_3$ amount.

Water hardness is a measure of the carbonate mineralization which are dissolved from the sedimentary deposits, Figure 1c. The samples collected from Broscarie and Jibou have hardness below 10 dH˚ indicating a moderate carbonation, therefore forms a relevant statistical group. Boghis water has almost double hardness indicating a more carbonated nature, thus it forms the second relevant statistical group. There are statistical differences between the observed groups. Calcium carbonate amount was determined based on the hardness results, Figure 1d. It results that Broscarie water has calcium carbonate about of 178 mg/l followed by Jibou sample with 106.8 mg/l. The water sample collected from Boghis has a more enhanced carbonated characteristic having dissolved $CaCO_3$ about of 356 mg/l. These values are very important for understanding the crystallization process.

Total dissolved solids (TDS) comprises both dissolved carbonates but are prone affected by the halite dissolution as observed in literature [6, 7]. Figure 2a reveal that Broscarie and Boghis samples have relatively low TDS below 2000 mg/l forming a relevant statistical group totally different regarding Jibou sample having high TDS value of about 5000 mg/l. TDS also influences the electrical conduction by providing mobile ions ensuring the electrical charge movement thus the water samples collected from Broscarie and Boghis have moderate electrical conductivity while Jibou water has a high electrical conductivity. It certainly prove the statistical difference between observed groups $p < 0.05$, Figure 2b.

Salinity represents a specific measure of the dissolved sodium chloride, Figure 2c, and strongly relates with the values of the total Cl, Figure 2d. Thus, sample collected from Broscarie has a salinity of 1.17 PSU which agrees the total Cl of 0.15 mg/l while Boghis water has a lower salinity of only 0.69 PSU related to slightly lower amount of total Cl of about 0.1 mg/l. On the other hand, Jibou sample has increased salinity of about 6.7 PSU which is confirmed by high amount of total Cl which is about 3.5 mg/l. The statistical analysis indicates that Broscarie and Boghis waters are less salted than Jibou water and the salty behavior is given by the dissolved halite.

TDS values variation indicates a strong mineralization within the investigated samples which should promote a particularized crystallization of each sample. The long time crystallization process developed in Petri dishes is developed by the progressive evaporation of the water inducing a concentration gradient that facilitate crystals formation and their subsequently growth. The mineral crusts formed in the Petri dishes were optically inspected in reflected light, Figure 1.

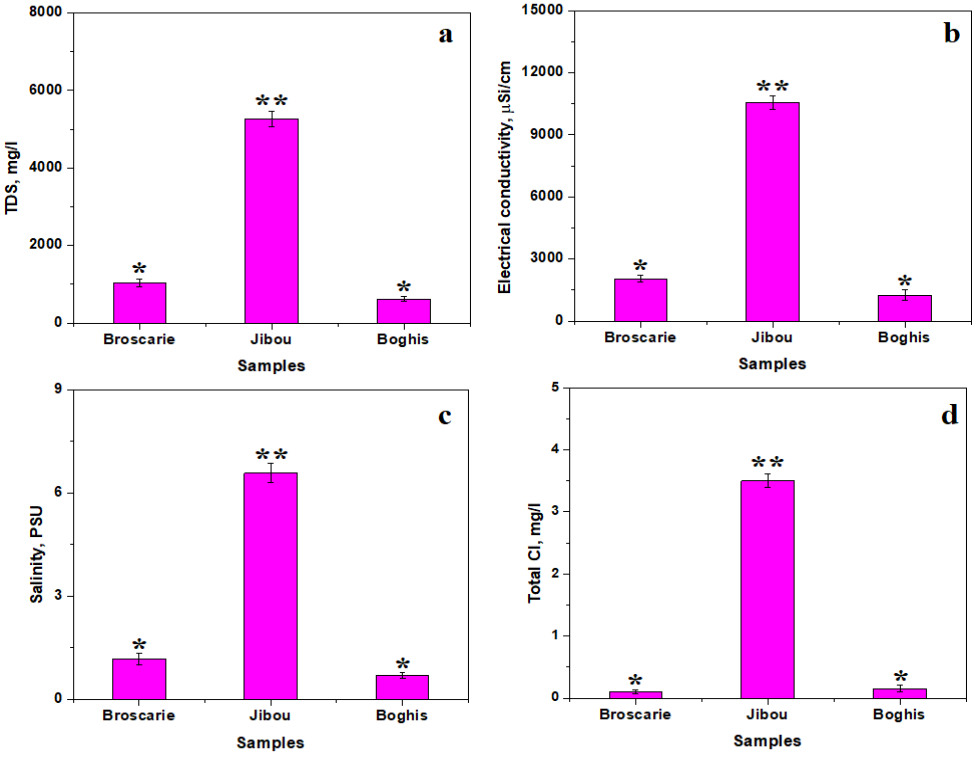

Figure 2. Specific physicochemical parameters of the water samples:
a) TDS, b) Electrical conductivity, c) Salinity and d) Total Cl.

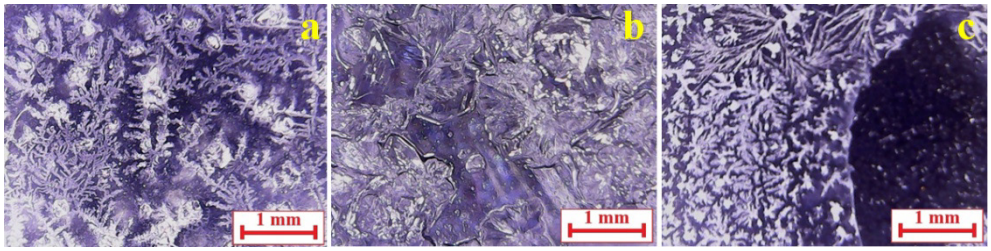

Figure 3. Optical microstructure observed in reflected light:
a) Broscarie, b) Jibou, and c) Boghis.

Sample collected from Broscarie has a moderate mineralization directly related to the TDS amount and reveal relatively equiaxed crystal clusters ranging from about 300 – 800 µm in diameter most likely belonging to the calcium carbonate formation, Figure 3a. These are surrounded in a dense manner by the NaCl dendrites.

The sample collected from Jibou has a high salinity and moderate carbonate content, fact influencing the microstructural aspect of the crystallized crust, Figure 3b. It has well defined carbonate clusters disposed in local nests with diameters ranging from 500 to 900 μm interlaced with large cubic crystals of NaCl and a dense structure of fine dendrites.

Physicochemical measurements reveal that Boghis sample has an increased hardness and lower salinity indicating that carbonates are the main crystalline components in the formed crust, Figure 3c. There is fine carbonate clusters promoting a branched structure imitating bushes embedded in a tiny mineral crust which might be related with the lower amounts of NaCl. The general optical inspection is not sufficient for a proper assessment of the crystallization process. Therefore the mineral crusts formed in the Petri dishes were subjected to the optical mineralogical microscopy and afterwards erased and transformed in powder which was subjected to the X ray diffraction (XRD) resulting the patterns presented in Figure 3.

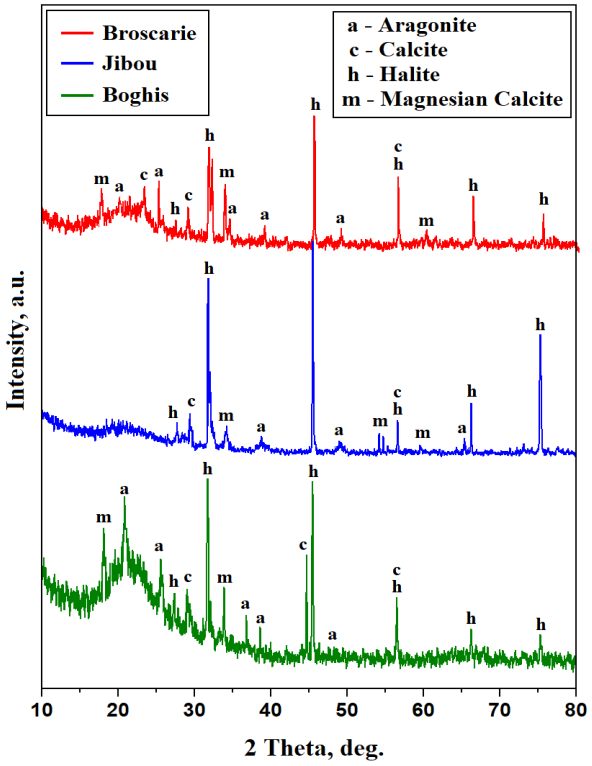

Figure 4. The XRD patterns for the crystallized minerals: aragonite PDF 71-2396; calcite PDF 86-2339; halite 77-2064; magnesian calcite PDF 89-1305.

The XRD patterns in figure 4 are well developed having narrow aspect and strong intensities corresponding to the high degree of crystallinity of the investigated powders. NaCl crystallized as halite has a very ordered crystal structure within face centered cubic system (FCC) having alternant atoms of Na and Cl centering each other cubic faces [22]. Therefore it exhibits more intense peaks regarding Trigonal and orthorhombic crystals of carbonate minerals. This difference is quantified by the Corundum Factor. Thus, apparently Halite dominates all samples but we observe strong and well developed peaks for carbonate minerals such Aragonite, Calcite and magnesian calcite in samples from Boghis and Broscarie. Each mineral amount can be calculated using the Relative Intensity Ratio (RIR) method previously described in literature [23, 24]. The obtained amounts are centralized in Table 1.

Table 1. Samples mineral characteristics revealed by XRD and MOM

Component	**Aragonite**	**Calcite**	**Magnesian Calcite**	**Halite**
Formula	$CaCO_3$	$CaCO_3$	$CaMg(CO_3)2$	NaCl
Crystal system	Orthorombic	Trigonal	Trigonal	Cubic
Color in cross polarized light	blue-violet	white -brown	white - yellow	transparent pale blue
Particle shape	rhombic	pseudo hexagonal	columnar	cubic rectangular
Broscarie				
Amount, wt.%	22	13	37	28
Particle size range, μm	200 - 400	50 - 150	200 - 600	10 - 200
Jibou				
Amount, wt.%	8	14	26	52
Particle size range, μm	50 - 150	50 - 600	200 - 600	10 - 300
Boghis				
Amount, wt.%	19	28	35	18
Particle size range, μm	100 - 250	50 - 600	200 - 800	-

The crystals size ranges were measured after the long time crystallization in Petri dishes.

It results that sample collected from Broscarie is dominated by the magnesian calcite and followed by halite. Significant amounts of aragonite were found and only moderate amounts of pure calcite. Jibou sample is clearly dominated by halite amounts followed by carbonated minerals. Magnesian Calcite is the most representative carbonated mineral followed by the pure Calcite wile Aragonite occurs almost as traces. On the other hand, Boghis sample is completely dominated by the carbonated minerals such as: magnesian calcite, pure calcite and aragonite and only small amounts of Halite were found.

XRD allow the proper identification of the crystallized minerals and their amounts but lacks in evidencing their distribution which should be followed under cross polarized light inspection through the mineralogical microscopy. The literature data reveal that aragonite specific colors ranges from blue to violet depending on the crystal position regarding the microscope optical axis. Magnesian calcite has predominantly pale yellow color while pure calcite is prone white. Halite crystals are mostly transparent and therefore it features a pale blue hue at the contact interface with other developed minerals [20, 22]. Thus, MOM investigation has the benefit of observing the crystallization process directly on the glass slide revealing the incipient crystals evolution up to the complete evaporation of the water.

Broscarie water has turbidity below detecting limit proving that there are no solid dispersed particles to facilitate crystals precipitation. Water evaporation induces a concentration gradient. The first germination seeds start precipitating when the liquid sample reaches the calcium carbonate supersaturating limit of 13 mg/l. In consequence, we found calcite crystallization centers having pseudo-hexagonal shapes and sizes of 10 – 15 μm appearing as small white spots randomly dispersed on the observation field within Figure 5a. The magnesian calcite forms columnar crystals of about 25 – 50 μm in length and about 5 μm widths disposed radially around the germination seed. The sodium chloride is still solved into the remnant liquid. The final stage of crystallization on the glass slide occurs after 24 hours after the drops deposition. The precipitated calcite has almost no changes in shape, size and distribution but magnesian calcite crystals strongly increases to about 300 μm in length keeping their radial disposal, Figure 5b. All carbonate crystal is surrounded by fine network of halite dendrites having pale blue nuance, but these are less visible due to the relative quick crystallization on the glass lamella. The long time crystallization (about 1 week) takes place in to the Petri dish. All crystals are better grown having bigger sizes and are better represented including the halite dendrites, Figure 5c.

Several microstructural details were taken on the best specimens of each crystals formed by drying of Broscarie water. Thus, Figure 5d reveal two aragonite clusters having rhombic crystals ranging from 50 to 100 μm associated each other resembling butterflies, the specific blue – violet color is better observed on their sides. The best specimen of magnesian calcite is observed in Figure 5e where 6 crystals grow radially around the germination seed having different lengths (shorter on the base having length of 150 μm and longer on the top having about 650 μm) displaying a flowery look. Halite dendrites are better observed in Figure 5f having a squared stem and lateral branched formed by small cubic crystals. The dendrite length is longer than 800 μm. Some pseudo-hexagonal calcite crystals having white appearance can be observed in the right lower side of Figure 5f.

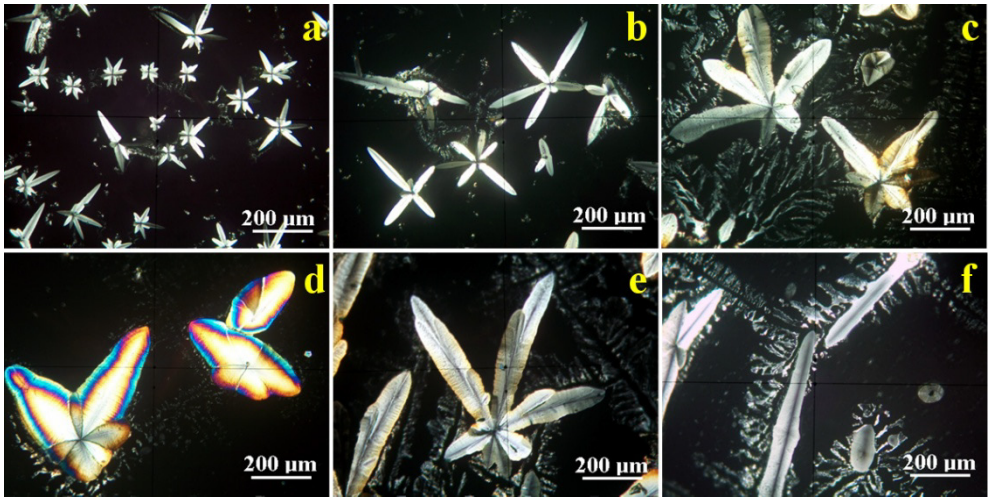

Figure 5. Crystals development in Broscarie sample observed by mineralogical optical microscopy: a) initial crystallization stage on glass slide, b) final crystallization stage on glass slide, c) long time crystallization in Petri dish. Microstructural details on specific crystals: d) aragonite, e) magnesium calcite and f) halite dendrites embedding calcite.

Jibou water very salty of about 6.7 PSU but also has a significant turbidity about 6 FTU indicating the presence of solid particles dispersed within. Several small yellow dots are observed floating in the liquid during the initial stage of crystallization, Figure 6a. These have strong resemblance to sulfur according to the literature [25] and most likely occur as organo-synthesis made by the sulfur bacteria [26]. These small dots act as heterogeneous crystallization germs facilitating appearance of small magnesian calcite radial clusters and some white pseudo – hexagonal Calcite particles. It fits the usual crystallization pattern but the most notable difference is the occurrence of well defined halite crystals beginning to form dendrites.

The end stage of crystallization on the glass slide, Figure 6b, reveal the carbonate crystals overwhelmed by the halite formation with two strong dendrites having over 800 µm length and lateral branches of about 100 – 150 µm. The inter-dendritic spaces also contain well developed halite crystals growth on [100] and [110] directions having cubic or rectangular shape. The long term crystallization in Petri dish allow a regrouping of the carbonate crystals into some “composite leaf” with the base attached onto central large square pyramidal halite crystal growth on the [220] with octahedral resemblance. Leafs looks palmate and contains a mixture of magnesian calcite, aragonite and

calcite, Figure 6c. Specific details found on some of leafs gathering into their structure only Calcite crystals, Figure 6d and magnesian calcite in Figure 6e. These formations are surrounded by the halite dendrites. Figure 6f reveal an interesting morphology centered on two Aragonite crystals having rhombic aspect and specific blue – violet nuance. These are partly covered by a dense cloud of fine yellow particles which resemble to the sulfur clusters.

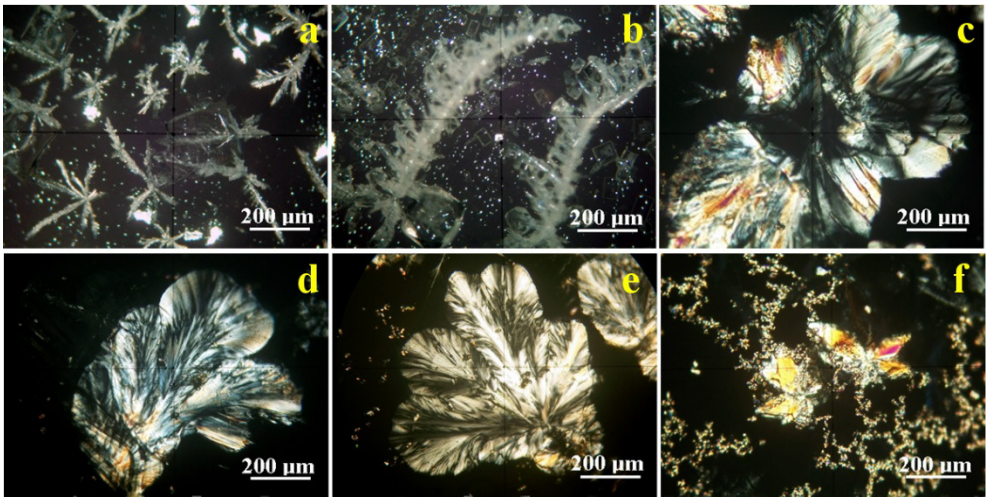

Figure 6. Crystals development in Jibou sample observed by mineralogical optical microscopy: a) initial crystallization stage on glass slide, b) final crystallization stage on glass slide, c) long time crystallization in Petri dish. Microstructural details on specific crystals: d) calcite surrounded by halite dendrites, e) magnesium calcite and f) aragonite surrounded by small S clusters.

The mineral amount within Boghis water is lower than in the other investigated samples having TDS only 619 mg/l correlated with relatively high hardness characteristic indicate a strong carbonated behavior. Therefore, the initial stage of crystallization is dominated by formation of radial clusters of mixed magnesian calcite and calcite while aragonite is less observed, Figure 7a.

The radial clusters progressively grow and reorganize their positions forming calcified branches consolidated by the precipitation of newest formed crystallites until the final stage of crystallization on the glass slide, Figure 7b. Their length is greater than 2 µm but they are still thin because of the shorter crystallization time (10 – 35 µm). The lower amount of chlorine within Boghis water reduces considerably the halite amount which forms thin crusts between the calcified branches inducing a blue hue over their sides.

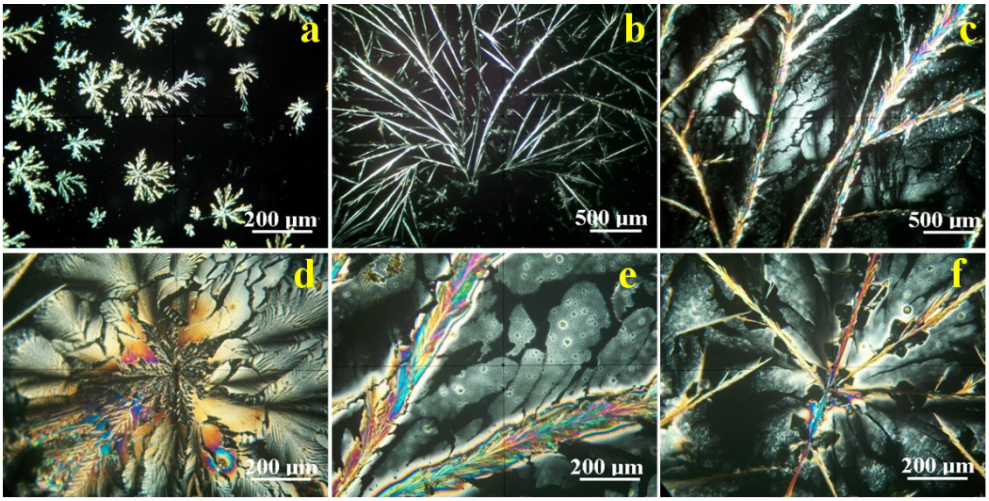

Figure 7. Crystals development in Boghis sample observed by mineralogical optical microscopy: a) initial crystallization stage on glass slide, b) final crystallization stage on glass slide, c) long time crystallization in Petri dish. Microstructural details on specific crystals: d) aragonite and magnesium calcite, e, f) Calcified branches surrounded by halite crusts.

The long term crystallization allow a massive regrouping of the carbonate crystals in more developed branches as observed in Figure 7c. Their length seems to be the same but the thickness increases to about 50 – 200 µm depending on their position regarding the initial crystallization center. The halite crusts are more evident having pale blue nuance filling inter-dendritic space. Microstructural detail in Figure 7d reveals a radial distribution of the carbonate minerals around a crystallization center. The inner area is characterized by the predominantly yellow white nuance characteristic for magnesian calcite with small iridescent aragonite crystallite. The outer area of the formation contains predominantly calcite crystallites grouped in compact areas. On the other hand, the microstructural aspect of the branches derived from the central formations, Figure 7e reveal a complex mixture of magnesian calcite, calcite and aragonite while halite crusts fill the adjacent space, Figures 7e and f.

The crystallization experiments reveal that the sodium chloride amount within the water samples play a key role in the shape and size of the calcium carbonate crystals size and shape. Higher NaCl concentration (Jibou sample) lead to large formations of the carbonate crystals individualized or mixed in complex structure resembling to leaf aspect. Moderate amount of sodium chloride as observed in Broscarie water ensure a coherent deposition of the

newly precipitate crystalline matter over the formed crystals facilitating their size growth. It looks that lower sodium chloride amount facilitates the branch crystallization through the concentration gradient during the slow drying in the Petri dish.

The powder examined by XRD was subjected to SEM investigation and the elemental distribution was revealed, Figure 8. The broken crystals within Broscarie sample reveal pseudo-hexagonal and rhombic particles colored in light green nuance due to the yellow label assigned to C, green label assigned to Ca and light blue assigned to O. Their size ranges from 5 to 10 μm in good agreement with MOM observation. The central side of Figure 8a reveal a Magnesian Calcite fragment broken from a large acicular crystal, its specific footprint is given by the pink spots over its green surface indicating the random presence of Mg atoms within $CaMg(CO_3)_2$ structure. The halite crust traces are revealed by local violet hue associated with Na atoms.

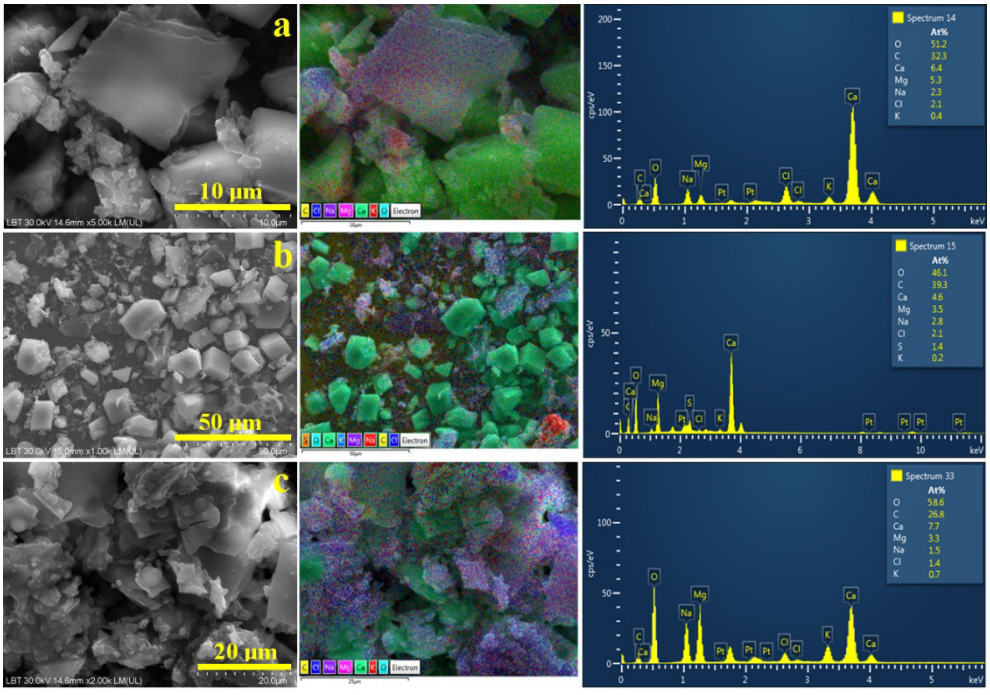

Figure 8. SEM secondary electron images (SEI) of the mineral powder crystallized from the water samples: a) Broscarie, b) Jibou, and c) Boghis. The equivalent backscattered electron image featuring elemental distribution map and the EDS spectrum are presented in the right side of each SEI image.

Jibou powder sample reveals broken pseudo-hexagonal calcite and rhombic aragonite crystals along with fine sand resulted from the broken magnesian calcite crystals. The large amount of crystallized NaCl generates well individualized Halite particles having red appearance because of red label of Na atoms (the lower right side of Figure 8b).

Boghis water, Figure 8c, looks rich in Magnesian Calcite particles mixed up with Calcite and Aragonite broken crystals. There are mostly finest particles below 5 μm resulted from the broken calcified branches. Na distribution is poorly observed only as marginal deposits because of low Halite content of the sample. The elemental composition of the mineral powder crystallized from the water samples is centralized in Table 2.

Table 2. Crystal powder elemental composition

Element	Elemental composition, at.%							
	O	C	Ca	Mg	Na	Cl	K	S
Broscarie	51.2	32.3	6.4	5.3	2.3	2.1	0.4	-
Jibou	46.1	39.3	4.6	3.5	2.8	2.1	0.2	1.4
Boghis	58.6	26.8	7.7	3.3	1.5	1.4	0.7	-

The elemental composition is dominated by O and C in all samples proving their rich carbonaceous nature. Boghis water is richest in Ca while Jibou sample has the lower amount, fact in good agreement with water hardness measurements. Na and Cl amounts are almost identical in Broscarie and Jibou samples while Boghis sample has lower values proving its low salinity. Sulfur was not detected in Broscarie and Boghis water but we found significant amount of 1.4 at.% in Jibou water confirming that the small yellow dots observed by mineralogical optical microscopy in Figure 6f are indeed sulfur clusters.

The elevated temperature of about 40 °C within Broscarie and Boghis water combined with their significant content in Ca^{2+} and Mg^{2+} ions prove to be effective for amelioration of rheumatic symptoms because of their anti-inflammatory effect. For instance, Verhagen et.al evidence the pain relief induced by Ca^{2+} and Mg^{2+} ions during the balneotherapy cures mainly due to the physicochemical effects on the inflamed areas because of their penetration through skin which avoid dietary metabolic flow [27]. The benefit of carbonaceous geothermal waters on rheumatic affection alleviation is also confirmed by Romay-Barrero indicating a Ca content of 432.7 mg/l and Mg of about 88.5 mg/l related to a HCO_3^- of 109.8 mg/l [28]. It clearly indicate that Boghis water perfectly fits the requirements for alleviating rheumatic symptoms followed closely by Broscarie water which is slightly less mineralized with Ca and Mg.

Saline and sulfur geothermal water are renowned for skin care treatments since antiquity their efficacy being reported for various skin diseases such as dermatitis and moderate fungal infections but also alleviate symptoms regarding psoriasis and atopic dermatitis [29, 30]. Jibou water best fits this application field because of the high salinity and the other proactive minerals, and is closely followed by Broscarie water which has significant salinity beside its carbonated characteristic. The significant amount of sulfur detected in Jibou water makes it proactive for treatment of moderate fungal infections beside its tendency to forms scales deposits on the spa installation pipes because facilitation of carbonate mineral precipitation as observed in our sample by MOM microscopy [31].

Literature data reports the successfully mixing of such geothermal waters with peloid particles like clays [32, 33]. On the other hand natural peloids (medicinal muds) containing geothermal water and clay soil particles were tested for potential toxicological effects against white mustard and Eisenia worms. It was found that targeted peloids have no acute toxicity but reduces the growth of Eisenia worms while white mustard remains unaffected [34]. Volcanic associated geothermal systems combined with local clays generate sulfur based peloid like the unique one formed Copahue volcano in Argentina [35]. The peloid is based mainly on beidelite and kaolinite mixed up with solute ions of $S0_4^{2-}$ and S^{2-} becoming so called clayey–sulphurous mud having therapeutic action skin affections [35]. Thus, present article opens a research path regarding the targeted water samples. It can be the start point for more detailed investigations which allows finding of specific application in spa therapy. One of the potential direction would be the development of advanced peloid based on this geothermal waters as dispersion environment for specific sorts of clays.

CONCLUSIONS

The conducted investigations on the targeted geothermal water reveal useful conclusions regarding their physicochemical behavior. The crystal formation is strongly influenced by the samples salinity which has a strong influence on the carbonate mineral precipitation and crystal growth. The higher salinity determines coalescence of small carbonate crystals and their further fusion into larger crystals at longer evaporation times.

Magnesian calcite is the dominant carbonated mineral followed by aragonite and calcite. The prevalence of calcite is favored by increased salinity in Jibou water while relative lower salinity favored prevalence of aragonite in Broscarie and Boghis waters.

The carbonated minerals are formed during the early crystallization stage due to their low solubility in water while sodium chloride crystallizes as halite in the later crystallization stages forming dendrites and well individualized crystals in Broscarie and Jibou waters and weak pellicle between carbonated branches in Boghis waters.

The physicochemical characteristics of the investigated samples and the crystallized content indicate that Boghis water is more useful for rheumatic symptoms alleviation while Jibou water is more useful for skin care benefits. Broscarie water has an equilibrate balance of salt and carbonated mineralization at moderate level indicating them as suitable for wellness and relaxation spa.

EXPERIMENTAL SECTION

Samples collection

Water samples were collected from the geothermal springs supplying system from: Broscarie spa pool in Simleul Silvaniei (measured temperature 39 °C), curing bath spa pool in Jibou (measured temperature 25 °C) and from the carbonated spring from Boghis spa (measured temperature 42 °C) in June 2025 following procedures described in standards: SR EN ISO 5667-5/2017, SR EN ISO 5667-1 /2007. Water was taken into glass recipients of 1 l hermetically closed with the gasket cap. They attend naturally the environmental temperature of about 25°C and afterwards stored in cooling case at 4 ˚C during transport to the laboratory where analyzed.

Measurement of water physicochemical properties

Physicochemical properties of the water samples were investigated according to the standard provisions: SR EN ISO 5667-3/2018 using a Hanna HI9829 multimeter measuring: pH, electrical conductivity, totals dissolved solids (TDS), and salinity. Turbidity was measured with Hanna 93703 turbidimeter with a sensitivity of 0-1000 FTU at a resolution of ± 5%. Chloride amount was measured by a Hanna HI 96711 photo-colorimeter with a resolution of 0.01 mg/l. Water total hardness was measured with Supleco MQuant test strips purchased from Sigma Aldrich, the obtained values being expressed in German degrees at a conversion rate of 1 °d= 17.8 mg/l of dissolved calcium carbonate (e.g. calcite). The measurements were effectuated in triplicate and the obtained mean values were statistically analyzed using Anova method followed by Tukey post hoc test effectuated with Origin Microcal software (Amherst, MA, USA).

Crystalline samples preparation and investigation methods

There were prepared two kind of crystallized samples: the first type was made by putting a few water drops onto glass slide to monitories the crystallization process by observation of the initial crystallization stage after 12 hours of natural drying and the final stage occurring after 24 hours. These samples reveal the crystallization process with great accuracy but cannot provide enough material for XRD investigation. The second type was made by water natural evaporation in Petri dishes followed by slow and progressive crystallization during long time (about 7 days). The crystalline formations were investigated by reflected light microscopy and mineral optical microscopy and afterward erased from the Petri dishes resulting in a white- yellow powders' which were subjected to XRD and SEM investigations.

Reflected light microscopy was effectuated using a Ulefone uSmart C01 microscope equipped with an integrated computer aided image acquiring system working on the Windows platform using png high resolution output format 720 x 1080 pixels.

Mineralogical optical microscopy (MOM) was effectuated using cross polarized light imaging performed on a Laboval 2 microscope (Carl Zeiss, Oberkochen, Germany). The images were digitally acquired through a Samsung digital system having a resolution of 10 MPx (Samsung, Hangul, Republic of Korea).

X ray diffraction (XRD) was performed with a Bruker D8 Advance diffractometer with Cu kα monochromatic radiation having a wavelength of 1.540562 Å. The patterns were registered at a speed of 1°/min. in the range of 10 – 80°. Crystal phase identification was made upon the XRD peaks using Match 1.0 software (Crystal Impact Company, Bonn, Germany).

Scanning Electron Microscopy (SEM) was done with Hitachi SU8230 operated in high vacuum mode at an acceleration voltage of 30 kV. The samples were coated with a thin layer of Pt to ensure a proper electrical conductivity. The elemental analysis was effectuated with the Energy Dispersive Spectroscopy (EDS) detector X-Max 1160 EDX (Oxford Instruments, Oxford, UK). The Pt component was subtracted from the EDS results.

REFERENCES

1. X. Shi, X. Bai, Z. Sun, J. Liu, H. Ye, L. Pang, G. Chen, H. Yan, *Geothermics*, **2025**, 131, 103402. https://doi.org/10.1016/j.geothermics.2025.103402
2. Y. Zheng, D. Nan, Z. Liu, C. Pubu, M. Zhu, H. Zhao, Y. Xing, S. Han, Q. Zeng, L. Zhang, *Geothermics*, **2025**, 131, 103374. https://doi.org/10.1016/j.geothermics.2025.103374

3. L. Yuan, P. Shen, J. Zhang, J. Yang, X. Kong, *Geothermics*, **2025**, 128, 103273. https://doi.org/10.1016/j.geothermics.2025.103273
4. Y. Jia, K. Li, L. Du, C. Zhu, F. Gao, L. Cui, Y. Shen, H. Fu, *Water,* **2025**, *17*, 1677. https://doi.org/10.3390/w17111677
5. B. Li, Q. Kong, F. Liao, G. Wang, F. Liu, L. Guo, C. Liu, Z. Shi, *Geothermics*, **2024**, 119, 102931. https://doi.org/10.1016/j.geothermics.2024.102931
6. S.E. Avram, L. Rus, V. Micle, S.S. Hola, *Water*, **2022**, 14(15), 2366. https://doi.org/10.3390/w14152366
7. L. Rus, S.E. Avram, V. Micle, *Studia UBB Chemia*, **2020**, 65(2), 257. DOI:10.24193/subbchem.2020.2.21
8. C. Krézsek, A.W. Bally, *Marine and Petroleum Geology*, **2006**, 23(4), 405-442. https://doi.org/10.1016/j.marpetgeo.2006.03.003
9. M. Venczel, I. Sabău, V. Codrea, *Nymphaea*, **2022**, 48. 77-108.
10. V. Codrea, A. Hosu, The Paleocene-Eocene formations and the Eocene/ Oligocene boundary in the Jibou area, Field Trip Guide the 4th regional meeting of IFAA, **2001**, 93-107.
11. M. Antics, M. Rosca, *Geothermics*, **2003**, 32(4-6), 361-370. https://doi.org/10.1016/S0375-6505(03)00047-6
12. M. Zhong, B. Liu, J. Chen, G. Yan, *Journal of Petroleum Science and Engineering*, **2022**, 218, 111040. https://doi.org/10.1016/j.petrol.2022.111040
13. J. Rohleder, E. Kroker, Calcium Carbonate: From the Cretaceous Period into the 21st Centruy, Springer Publishing House, **2001**.
14. H. Xue, H., J. Qian, W. Xu, *Minerals,* **2025**, *15*, 717. https://doi.org/10.3390/min15070717
15. F. Armijo, F. Maraver, M. Pozo, M.I. Carretero, O. Armijo, M.A. Fernández-Torán, M.V. Fernández-González, I. Corvillo, *Applied Clay Science*, **2016**, 126, 50-56, https://doi.org/10.1016/j.clay.2016.02.020
16. J. Walter, R. Chesnaux, V. Cloutier, D. Gaboury, *Journal of Hydrology: Regional Studies*, **2017**, 13, 168-188. https://doi.org/10.1016/j.ejrh.2017.07.004
17. T.M. Peryt, *Sedimentary Geology*, **2006**, 188–189, 379-396. https://doi.org/10.1016/j.sedgeo.2006.03.014
18. O. Gelencsér, A. Szakács, A., Gál, A. Szabo, Z. Dankházi, T. Tóth, D. Breitner, Zs. Szabó-Krausz, Cs. Szabó, Gy. Falus, *Acta Geod Geophys*, **2024**, 59, 343–365. https://doi.org/10.1007/s40328-024-00436-z
19. R.Yuan, W. Zhang, H.Gan, F. Liu, S. Wei, L. Liu, Water 2022, 14, 2235. https://doi.org/10.3390/w14142235
20. S.E. Avram, D.V. Platon, L.B. Tudoran, G. Borodi, I. Petean, *Appl. Sci.*, **2024**, 14, 10806. https://doi.org/10.3390/app142310806
21. X. Zhu, P. Chang, J. Zhang, Y. Wang, S. Li, X. Lu, R. Wang, C-Q. Liu, H.H. Teng, *Geochimica et Cosmochimica Acta*, **2022**, 339, 70-79. https://doi.org/10.1016/j.gca.2022.10.039
22. I. Petean, G. Arghir, R.F. Câmpean, M. Bărăian, A.G. Hosu Prack, *Acta Technica Napocensis Series: Matematica Aplicata si Mecanica*, **2011**, 54, 2011,193 – 200.
23. S.E. Avram, B.V. Birle, L.B. Tudoran, G. Borodi, I. Petean, *Water*, **2024**, 16, 1027. https://doi.org/10.3390/w16071027

24. S.E. Avram, B.V. Birle, C. Cosma, L.B. Tudoran, M. Moldovan, S.Cuc, G. Borodi, I. Petean, *Materials*, **2025**, 18, 1715. https://doi.org/10.3390/ma18081715
25. M. Li, X. Wang, J. You, Y. Wang, M. Zhao, P. Sun, J. Fu, Y. Yu, K. Mao, *Sustainability* **2025**, 17, 5988. https://doi.org/10.3390/su17135988
26. S. Paskucza, R. Carpa, A. Remizovschi, T. Rusu, *Scientific Papers. Series E. Land Reclamation, Earth Observation & Surveying, Environmental Engineering*, **2018**, 7, 240-246.
27. A.P. Verhagen, S.M. Bierma-Zeinstra, M. Boers, J.R. Cardoso, J. Lambeck, R. de Bie, H.C. de Vet, *Cochrane Database Syst Rev.*, **2015**, 11 (4), CD000518. https://doi.org/10.1002/14651858.CD000518.pub2
28. H. Romay-Barrero,J. Herrero-López, J.A. Llorente-González, G. MelgarDel Corral, R. Palomo-Carrión, I. Martínez-Galán, *Balneo and PRM Research Journal*, **2022**, 13(4): 527. https://doi.org/10.12680/balneo.2022.527
29. A. Huang, S. Seité, T. Adar, *Clinics in Dermatology*, **2018**, 36, 363-368. https://doi.org/10.1016/j.clindermatol.2018.03.010
30. V. Milanković, J. Djuriš, A. Tubić, J. Agbaba, S. Forkapić, M. Lukić, *RSC Advances*, **2025**, 15, 17755-17775. https://doi.org/10.1039/d5ra01252j
31. K. Wątor, *Water Resources and Industry*, **2024**, 31, 100248. https://doi.org/10.1016/j.wri.2024.100248
32. M.V. Fernández-González, M.I. Carretero, J.M. Martín-García, A. Molinero-García, R. Delgado, *Applied Clay Science*, **2021**, 202, 105969. https://doi.org/10.1016/j.clay.2020.105969
33. T. Barhoumi, I. Bekri-Abbes, E. Srasra, *Comptes Rendus Chimie*, **2019**, 22, 126-131. https://doi.org/10.1016/j.crci.2018.11.006
34. G. Gerencsér, E. Murányi, K. Szendi, C. Varga, *Applied Clay Science*, **2010**, 50, 47-50. https://doi.org/10.1016/j.clay.2010.06.022
35. M.T. Baschini, G.R. Pettinari, J.M. Vallés, C. Aguzzi, P. Cerezo, A. López-Galindo, M. Setti, C. Viseras, *Applied Clay Science*, **2010**, 49, 205-212. https://doi.org/10.1016/j.clay.2010.05.008

STUDIA UBB CHEMIA, LXX, 3, 2025 (p. 55-64)
(RECOMMENDED CITATION)
DOI:10.24193/subbchem.2025.3.04

SALT TEMPLATE-ASSISTED SYNTHESIS OF β-CYCLODEXTRIN DERIVED 3D CARBON NANOCORALS

Jinyan HUANG[a], Ye XING[b], Haichao LI[b,c,*]

ABSTRACT. Carbon nanomaterials have great scientific importance due to their unique physicochemical properties. They show great promise in the fields of catalysis, energy storage and environmental treatment. However, the traditional synthesis methods are characterized by cumbersome steps, difficult template removal and high environmental costs. In this study, a salt template-assisted strategy was innovatively employed with β-cyclodextrin (β-CD) as a renewable carbon source and NaCl as a dynamic separation template. Controlled preparation of 3D carbon nanocorals (CNCs) has been achieved for the first time by regulating the self-assembly and carbonization process. XRD and Raman spectroscopy showed that the graphite microcrystalline ordering of the material increased significantly with increasing concentration, and the graphite layer spacing was reduced from 0.453 nm to 0.443 nm. In addition, the NaCl template has a recovery rate of over 90% after washing. Meanwhile the sodium chloride can be reused after recycling. It is in line with the concept of green chemistry. This strategy provides a new idea for the precise construction of complex carbon nanostructures.

Keywords: *3D Carbon Nanocorals, Salt Template-assisted, β-Cyclodextrin, Carbon nanomaterial.*

[a] *Qinghai Institute for Advanced Study, Qinghai University, Xining, 810016, Qinghai, China.*
[b] *School of Chemistry and Materials Science, Qinghai Minzu University, Xining, 810007, Qinghai, China.*
[c] *Qinghai Institute for Advanced Study, Qinghai Minzu University, Xining, 810007, Qinghai, China.*
[*] *Corresponding author: lihaichao@vip.163.com*

INTRODUCTION

Carbon nanomaterials, due to their unique physicochemical properties, show broad application prospects in the fields of catalysis, energy storage, biomedical and environmental treatment [1-3]. In recent years, researchers have devoted themselves to the development of structurally novel carbon nanomaterials to break through the limitations of conventional materials in terms of specific surface area, mass transfer efficiency and stability. The 3D porous carbon materials have become a research hotspot due to their high specific surface area, rich pore structure and excellent electron transport properties [4]. However, the existing synthesis methods such as hard template method and hydrothermal method still face the problems of cumbersome steps, difficult template removal, high cost and environmental burden [5,6]. The traditional hard template method requires the use of corrosive reagent HF to remove silica templates, which is not only dangerous to operate, but also limits the large-scale production of the material [7]. Therefore, the development of green, efficient and structurally controllable synthesis strategies has become an important challenge in the field of carbon nanomaterials.

In recent years, the salt template method has attracted much attention due to its advantages such as environmental friendliness, easy operation and template recyclability [8,9]. Literature data reveals that salt lakes represents special environmental systems proving the green approach of the chosen method [10]. Du et al. successfully prepared size-tunable carbon nanoframes using the DTAB @ NaCl self-assembly strategy and achieved precise control of the structure by modulating the surfactant concentration [11]. Lin et al. further extended the method by synthesizing carbon nanoframes and hollow carbon nanocubes using the SB3-12 @ NaCl system, revealing the key role of salt templates in morphology modulation [12]. These studies provide an important reference for the application of the salt template method in the design of carbon nanostructures. However, the existing results are still limited to simple geometric forms such as frames or hollow spheres. There is no breakthrough yet in constructing complex 3D network structures.

Cyclodextrins as a renewable biomass carbon source, show unique potential in nanomaterial synthesis due to their unique ring-like cavity structure and tunable self-assembly properties [13]. Xing et al. developed hollow carbon nanospheres based on a salt separation strategy of α-cyclodextrin and NaCl, with a shell thickness that can be flexibly adjusted by the precursor concentration [14]. Compared to α-cyclodextrin, β-cyclodextrin has a larger cavity size and stronger hydrophobic interactions, making it easier

to form multilayered supramolecular assemblies. By modulating the cyclodextrin concentration, the aggregates may take the shape of rods, disks, oblong spheres, globules, bilayers, vesicles, or reversible micelles [15]. However, the aggregation of cyclodextrins in NaCl solution has been rarely reported.

In this study, a salt template-assisted strategy using β-cyclodextrin as a carbon source and NaCl as a dynamic template is reported. We demonstrate that β-cyclodextrin can form 3D carbon nanocoral structures under NaCl assistance, with the template recovered by water washing for green chemistry compliance. This work provides a new approach for controllable synthesis of complex carbon nanostructures and expands the application of cyclodextrin-based functional materials.

RESULTS AND DISCUSSION

The 3D CNCs prepared at different concentrations have similar morphology. For example, Figure 1 shows SEM images of CNCs prepared at 10 mM at different magnifications. The formation of carbon nanocorals (CNCs) from β-CD assisted by NaCl template is mainly due to the self-assembly property of β-CD and the dynamic domain-limiting effect of NaCl template. β-CD has a unique cyclic cavity structure and a tunable self-assembly ability. β-CD molecules spontaneously form dispersed, small-sized aggregates through hydrogen bonding and hydrophobic interactions. This self-assembly behavior was further modulated in NaCl solution. The addition of NaCl enhanced the intermolecular interactions between β-CD molecules, possibly through an electrostatic shielding effect or by changing the solvent polarity, thus promoting the formation of coral-like structures. NaCl provides a dynamic template during high-temperature carbonization. Through the domain-limiting effect of its crystal structure, it guides the formation of specific 3D network structures of β-CD derived carbon precursors during pyrolysis. The facile nature of NaCl in water allows the final product to retain the coral-like morphology formed by the template [16]. The formation of coral-like structures by β-CD assisted by the NaCl template is the result of a combination of self-assembly behavior, dynamic template domain-limiting effects, and concentration-dependent interactions. This strategy provides a new idea for the controlled synthesis of complex 3D carbon nanostructures.

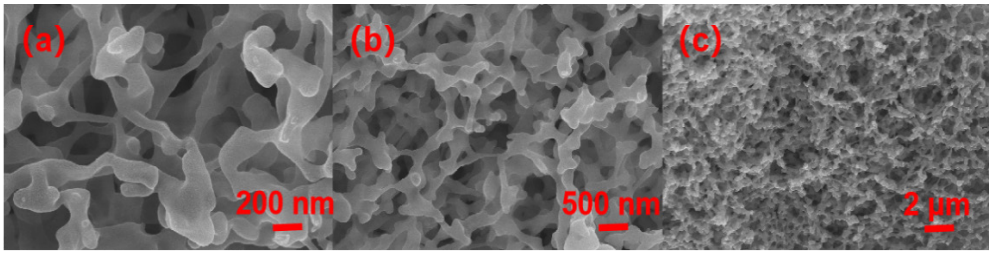

Figure 1. SEM images of CNCs at different magnifications

The degree of graphitization reflects the degree of ordering of carbon atoms to form hexagonal graphite crystals and is an important indicator of the quality of graphite materials. The degree of graphitization of the synthesized CNCs at concentrations of 5 mM, 10 mM and 20 mM increased significantly with increasing concentration as detected by XRD. As shown in Figure 2, the structures were analyzed by XRD, and all samples with (002) crystalline facets at 2θ = 26° had characteristic diffraction curves of carbon, with no crystallographic Bragg peaks detected, which is characteristic of amorphous structures [17, 18]. As the concentration increases, the (002) peak at 2θ ≈ 26.5° (assigned to hexagonal graphite, PDF#41-1487) becomes sharper and more intense, indicating microcrystalline growth. This assignment is validated by matching the peak position to the standard graphite phase (a=2.461 Å, c=6.708 Å, ICDD PDF#41-1487). The peak shift to higher Bragg angles (evident in Figure XRD) corresponds to a decrease in d_{002} spacing from 0.453 nm (5 mM) to 0.443 nm (20 mM) as calculated by Bragg's law (Table 1). This narrowing of interlayer spacing aligns with the increased peak intensity, both indicators of improved graphitic ordering. While the 20 mM sample shows a d_{002} value (0.443 nm) slightly larger than fully graphitized carbon (0.335 nm), the trend confirms enhanced local crystallinity with concentration [19]. The apparent (104) crystal surfaces in the Figure 2 are from $CaCO_3$ and $CaMg(CO_3)_2$, and since Ca and Mg are not added to the raw materials, it is hypothesized that they may be due to the abundance of minerals in the tap water in the Qinghai region. Indeed the natural water can contain significant amounts of $CaCO_3$ crystallized as calcite and micro dispersoids of $CaMg(CO_3)_2$ crystallized as dolomite occurring form the shore rocks, but dissolved Ca^{2+} and Mg^{2+} ions re-crystallizes as pseudo-dolomite. The diffraction peak in Figure 2 at about 29.3° belongs to calcite and the peak of about 30.98° belongs to dolomite [20, 21]. At the same time the work of the ultrapure water machine at high altitude is affected, resulting in some of the ions not being removed cleanly.

Table 1. XRD parameters of 5 mM, 10 mM and 20 mM

	5 mM	**10 mM**	**20 mM**
$2\theta_{(002)}$/(°)	19.58	19.90	20.02
d_{002}/nm	0.453	0.445	0.443

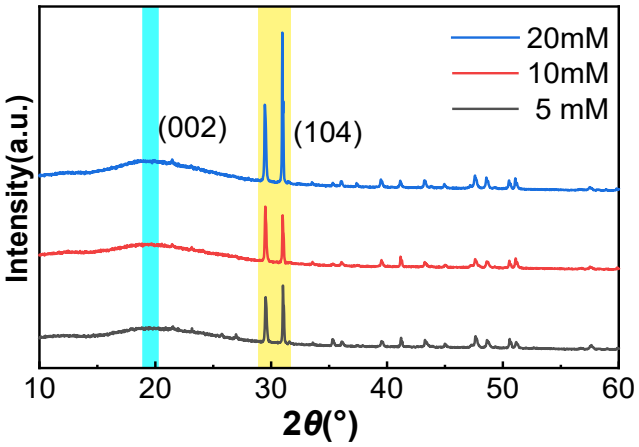

Figure 2. XRD patterns of CNCs at different concentrations

Raman spectroscopy can provide information about the graphite crystal structure and structural defects in graphite, and the data can be used to complement XRD data. As shown in Figure 3, at concentrations of 5 mM, 10 mM and 20 mM, D bond, G bond and D+G bond appeared simultaneously in the samples, which is a typical feature of amorphous carbon. The intensity ratio of the D and G bonds (I_D/I_G) is another key parameter to analyze the degree of graphitization [22]. The intensity ratios of carbon nanomaterials (I_D/I_G) were 0.931, 0.862 and 0.736 at concentrations of 5 mM, 10 mM and 20 mM. The height difference between the D and G bonds decreased significantly with increasing concentration. This suggests a gradual reduction of microcrystalline defects within the CNCs as they transform from a graphite disordered layer structure to an ordered structure [23]. The broad and weak D+G bonds near 2700 cm^{-1} also indicate again that there are some defects in the prepared CNCs graphite layer structure. Raman spectroscopy again verifies that the concentration increase can effectively induce the evolution of carbon nanomaterials towards ordered structures.

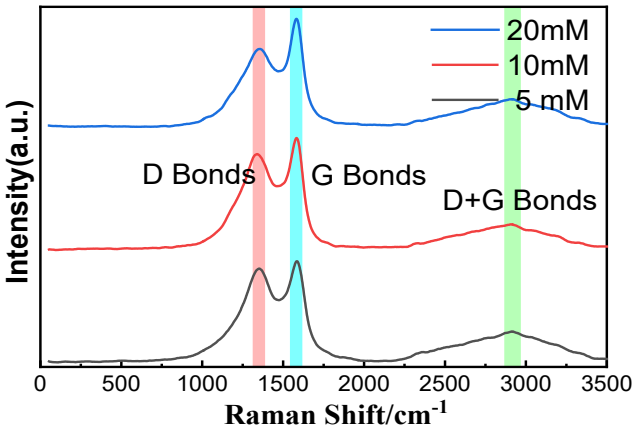

Figure 3. Raman spectra of CNCs at different concentrations

The elemental test composition of carbon nanomaterial XPS is shown in Table 2. There is no significant change in the elemental content, which is mainly composed of C and O elements, and most of them are carbon elements. As the β-CD concentration increased to 10 mM, the carbon content of CNCs reached its maximum. The carbon content of CNCs decreased when the β-CD concentration increased to 20 mM. Due to the change in concentration that the structure of β-CD aggregates changed, which is beneficial to the overflow of small molecule hydrocarbons during thermolysis. XPS is commonly used to characterize the chemical structure of material surfaces. Figure 4 show the full XPS spectra of the different samples, verifying that the main components of the prepared CNCs are the elements C and O. Figures (5, 6, 7) show the split peaks of C1s and O1s, with the C1s spectrum splitting into three peaks. The results show that in combination with elemental analysis, there are three possible bonding forms of C, C=C (284.8 eV), C-O (286.4 eV) and C-O (288.4 eV). O1s splits into 2 peaks, C-O (530.8 eV) and C=O (529.5 eV). XPS data showed that the prepared CNCs were all amorphous carbon with similar surface chemical structure [17].

Table 2. Elemental analysis of CNCs at different concentrations

Sample	C (at.%)	O (at.%)
5 mM	72.26	26.28
10 mM	87.14	12.15
20 mM	85.04	14.33

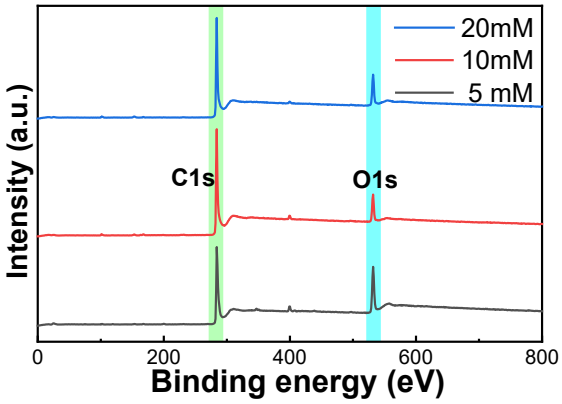

Figure 4. Full XPS spectra of CNCs at different concentrations

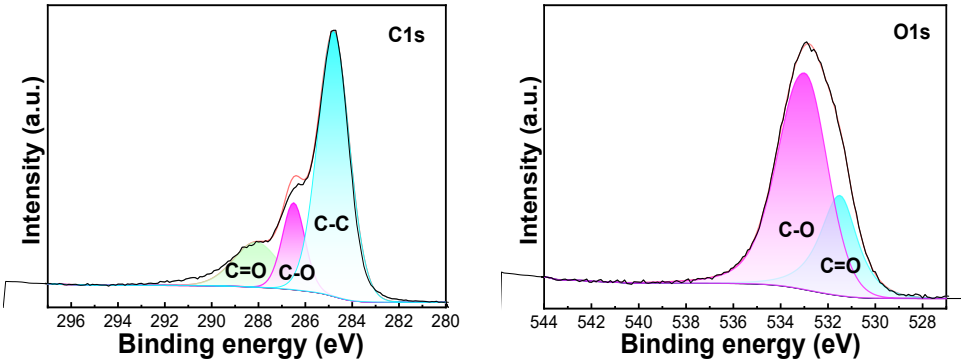

Figure 5. C1s and O1s XPS spectra of CNCs at 5 mM

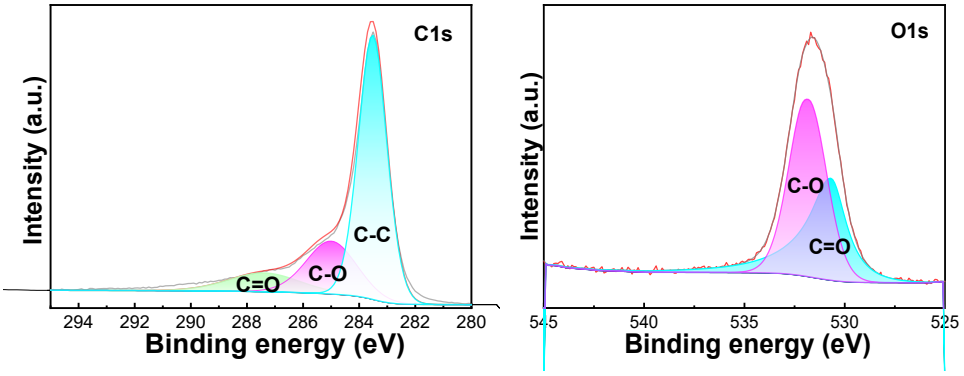

Figure 6. C1s and O1s XPS spectra of CNCs at 10 mM

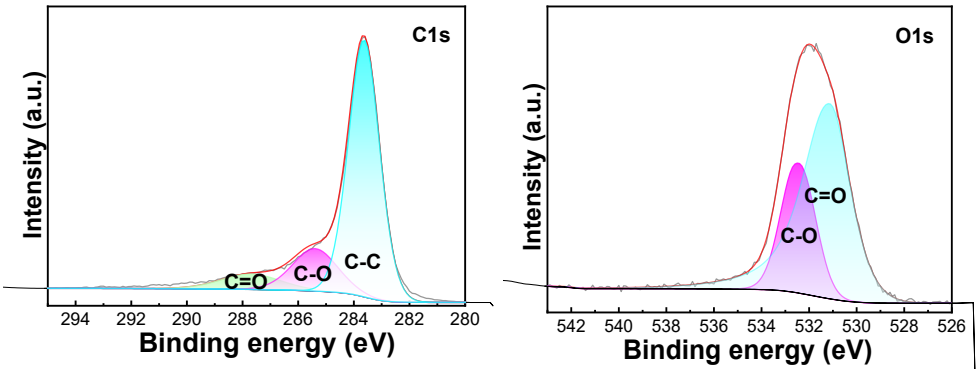

Figure 7. XPS spectra of C1s and O1s of CNCs at 20 mM

CONCLUSIONS

In this study, a novel synthesis method of 3D carbon nanocorals (CNCs) based on a salt template-assisted strategy was successfully developed. By using β-Cyclodextrin (β-CD), a renewable carbon source, combined with the domain-limiting effect of NaCl dynamic templates. Controllable preparation of coral-like carbon 3D networks was realized for the first time. The unique self-assembly behavior of β-CD, driven by hydrogen bonding and hydrophobic interactions, combined with the dynamic domain-limiting effect of NaCl, enabled the formation of well-defined 3D coral-like carbon nanostructures. The NaCl template not only guided the morphology but also facilitated the creation of network. The method efficiently recovers NaCl templates by water washing, avoiding the dependence on corrosive reagents such as HF in the traditional hard template method. This is in line with the concept of green chemistry. This study not only provides new ideas for the controllable synthesis of complex carbon nanostructures, but also expands the boundary for the application of cyclodextrin-based functional materials in energy and environmental fields.

EXPERIMENTAL SECTION

β-Cyclodextrin (β-CD) and NaCl, all the chemicals used were analytically pure reagents purchased from Aladdin Biochemical Technology Co., Ltd. in Shanghai, China, and the water used in the experiments was ultrapure water.

Solutions of β-CD at 5 mM, 10 mM and 20 mM were prepared in a crucible and allowed to stand for 48 hours to fully form the aggregates. The aggregates of β-CD were segregated by adding an appropriate amount of salt to the crucible

and the mixture was referred to as the β-CD @ NaCl system. The prepared β-CD @ NaCl system was carbonized in a muffle furnace. The temperature was increased to 700°C at a rate of 5°C/min. Samples were left at the highest temperature for 2 h to ensure complete carbonization. At the end of the carbonization process, wait for natural cooling to room temperature, remove the samples, and place the carbonization products extracted from the muffle furnace in a 1000 mL beaker with excess boiling water. After complete dissolution in NaCl, the target product, carbon nanocorals (CNCs), was obtained by filtration through a 200 nm microporous filtration membrane. After rough calculations, the NaCl recovery reached more than 90%.

The morphology of CNHCs was observed by SEM (ZEISS GeminiSEM 500, Germany). The crystalline structure parameters of the samples were determined using a D/MAX-B type X-ray diffractometer from RIKEN, Japan. Cu target radiation (λ = 0.154056 nm) and scanned the sample at a scanning speed of 4° min^{-1} in the range of 2θ=10°-80°. Surface functional groups were analysed by X-ray photoelectron spectroscopy with the ESCALAB 250XI model from Thermo Fisher Scientific, USA. Each photoelectron spectral region was scanned several times to obtain a good signal ratio. The C1s peak was set to 284.6 eV and used as an internal standard for the other peaks.

ACKNOWLEDGMENTS

This work was supported by the Key R&D and Transformation Program of Qinghai (2022-QY-210), and Research Teams of Kunlun Scholars Project of Qinghai Province.

REFERENCES

1. Q. Xu; H. Cai; W. Li; M. Wu; Y. Wu; X. Gong; *J. Mater. Chem. A,* **2022**, 10, 14709-14731.
2. D. G. Saini; J. Kaushik; R. Aggarwal; K.M. Tripathi; S.K. Sonkar; *ACS Appl. Nano Mater.,* **2021**, 4, 12825-12844.
3. Y. Yin; X. Hou; B. Wu; J. Dong; M. Yao; *Adv. Funct. Mater.,* **2024**, 34, 2411472.
4. C. Jiang; H. Liu; J. Ye; N. Wang; Y. Tang; C. He; H. Zhang; B. Chen; *Batteries & Supercaps,* **2025**, 8, e202400563.
5. V. Malgras; J. Tang; J. Wang; J. Kim; N.L. Torad; S. Dutta; K. Ariga; M.S.A. Hossain; Y. Yamauchi; K.C. Wu; *J Nanosci. Nanotechno.,* **2019**, 19, 3673-3685.
6. H. Liang; R. Sun; B. Song; Q. Sun; P. Peng; D. She; *J. Hazard. Mater.,* **2020**, 387, 121987.

7. Y. Chen; L. Tong; G. Lin; W. Zhang; Q. Zeng; X. Liu; *J. Mater. Sci-Mater.* El., **2021**, 32, 2774-2783.
8. Q. Chen; H. Li; *Nanomaterials*, **2022**, 12, 1652.
9. X. Kang; H. Li; X. Yang; Z. Lin; *RSC Adv.*, **2024**, 14, 28215-28223.
10. L., Rus; S.E. Avram; V Micle, Romania. *Studia UBB Chemia,* **2020**, 65, 257–268.
11. B. Du; H. Li; C. Zhang; Q. Ji; Adv. Mater. Int., **2024**, 11, 2300832.
12. Z. Lin; B. Du; C. Zhang; Q. Ji; X. Yang; H. Li; *Adv. Mater. Int.*, **2024**, 11, 2400509.
13. A. Ryzhakov; T. Do Thi; J. Stappaerts; L. Bertoletti; K. Kimpe; A.R.S. Couto; P. Saokham; V. Mooter; G., Augustijns; P. Somsen; *J. Phar. Sci.,* **2016**, 105, 2556-2569.
14. Y. Xing; Y.N. Wang; H. Li; *Fuller Nanotub. Car. N.,* **2024**, 32, 1135-1139.
15. D. Duchene; A. Bochot; *Int J Pharmaceut.*, **2016**, 514, 58-72.
16. S. Hao; Q. Zhang; Y. Shi; Q. Guo; P. Li; J. Huang; *Biomass. Convers. Bior.,* **2024**, 14, 9581-9594.
17. Y. Guangzhi; Y. Binbin; S. Shen; T. Zhihong; Y. Dengguang; Y. Junhe; *RSC Adv.,* **2017**, 7, 16341-16347.
18. J. Tu; H. Li; J. Zou; S. Zeng; Q. Zhang; L. Yu; X. Zeng; *Dalton T.*, **2018**, 47, 16909-16917.
19. H. Wei; W. Liu; T. Liu; Q. Li; H. Li; *Mater. Res. Express,* **2019**, 6, 0950b8.
20. A. Tamas; L. Cocheci; L. Lupa; *Studia UBB Chemia,* **2025**, 70, 147–158.
21. S.E. Avram; D.V. Platon; L.B. Tudoran; G. Borodi; I. Petean; *Appl. Sci.,* **2024**, 14,10806.
22. Y. Gong; L. Xie; H. Li; Y. Wang; *Chem. Commun*., **2014**, 50, 12633-12636.
23. H. Nishihara; T. Kyotani; *Adv. Mater.,* **2012**, 24, 4473-4498.

STUDIA UBB CHEMIA, LXX, 3, 2025 (p. 65-84)
(RECOMMENDED CITATION)
DOI:10.24193/subbchem.2025.3.05

NANO-STRUCTURED Nd-Fe-B THIN FILMS DEPOSITED ON GLASS SUBSTRATE BY FLASH EVAPORATION METHOD

Ana-Maria POPESCU[a]*, Mihai ANASTASESCU[a], Jose CALDERON MORENO[a], Elena Ionela NEACSU[a], Olga DEMIDENKO MINCHUKOVA[b], Kazimir YANUSHKEVICH[b(†)], Virgil CONSTANTIN[a]*

ABSTRACT. Nd-Fe-B nanostructured thin layers have been growth on the glass substrate by the "flash" evaporation (FE) method. The microscopic and surface structure analysis of the Nd-Fe-B thin films investigated by X-ray diffraction (XRD), scanning electron microscopy (SEM), atomic force microscopy (AFM) and X-ray photoelectron spectroscopy (XPS) demonstrate these thin films to be nanostructured.The temperature dependence of the specific magnetization of the films in the 80 ≤ T ≤ 800 K range, measured by the ponderomotive method showed that the magnetization of the Nd-Fe-B nanostructured thin films before corrosion did not exceed 85 $A \cdot m^2 \cdot kg^{-1}$ at 77 K. In such Nd-Fe-B nano thin films the long-range structural order is destroyed. After corrosive action on the thin films, their specific magnetization value increased to 140-155 $A \cdot m^2 \cdot kg^{-1}$, most probably because of the formation of Fe_3O_4 (iron oxide) and the presence of free iron ions on the surface of the nanometric Nd-Fe-B layer upon heating the samples to 1050 K. XPS spectra confirmed the presence of Fe_3O_4, FeOOH and $Nd(OH)_3$.

Keywords: *nanostructured thin film, NdFeB thin films; microstructure; characterization of thin films; thin film surface analysis; nanomagnetic properties of NdFeB thin films.*

[a] *Romanian Academy, "Ilie Murgulescu" Institute of Physical Chemistry, Laboratory of Electrochemistry and Corrosion, 202 Splaiul Independentei, 060021, Bucharest, Romania*
[b] *Scientific-Practical Materials Research Center NAS, P. Broski Str.19, Minsk, Belarus*
* *Corresponding authors: popescuamj@yahoo.com, virgilconstantin@yahoo.com*

INTRODUCTION

Permanent Nd-Fe-B magnets and products based on them are currently widely used in the development of many industries [1-7]. Application of this class of magnets opens the perspective of creating products with fundamentally new technical capabilities. It is already known that, Nd-Fe-B magnets span a wide range of magnetic properties and application requirements due to large values of the coercive force and residual magnetization. A highly sought-after target of present work is to provide transparent nano-magnets based on quenched Nd-Fe-B permanent magnets for some miniature engineering products. The structural and magnetic properties of Nd-Fe-B thin films represent a subject of growing scientific interest due to the wide range of applications especially on MEMS (micro-mechanical systems), MES (micro-electronical systems) and MMD (micro-magnetic devices). There are a lot of studies on Nd-Fe-B thin films [8-12]. This interest determines the relevance of studying the properties of Nd-Fe-B nanocrystalline thin films [13-15]. In this paper we will present the structure, morphology, surface chemistry and magnetic properties of Nd-Fe-B nano-structured thin films evaporated on glass substrate by the “flash” method (FM). The motivation of this investigation is based on the challenge to analyze information on the nano-structured Nd-Fe-B film sample deposited by FM on glass, as we did not found any other study in the literature.

RESULTS AND DISCUSSION

1.Thin film characterization

The X-ray analysis of precursor powder used for thin film production from the permanent magnets showed that their crystal structure corresponds to the tetragonal $R4_2/mnm$ space group of $Nd_2Fe_{14}B$ compound (Fig. 1) [16]. Results of the crystal structure study of Nd-Fe-B nanolayers in CuK_α-radiation revealed that for all the three prepared samples (Fig. 1 a, b, c), their structure is nano-crystalline. The film thickness of sample (0.2 mg) is too small and Bragg peaks related with the film cannot be detected. Increasing a film thickness, intensity of the strongest Bragg peak increases however the peak are much wider then for precursor materials. It might indicate on small crystalline size and stress in film as well. Origins of (physical) line broadening are numerous. In general any lattice imperfections will cause additional line broadening, which can be dependent and independent on the reflection order: if a crystal is broken into smaller incoherently diffracting domains by dislocation arrays (small-angle boundaries), stacking faults, twins, or other extended imperfections, then size broadening occurs; dislocations, vacancies, interstitials, substitutionals, and similar defects lead to microstrain broadening. From the nature of the lattice

imperfections noted above follows, that both effects are interconnected. For example dislocations cause lattice strain but also arrange into boundaries between incoherently diffracting domains resulting in crystallite size broadening. This is one of the reasons why any interpretation of the underlaying physics of broadening is difficult. XRD data that was introduced in the analysis software program TOPAS 5 and crystallite size was calculated. So, calculation give a crystallite size of about 1.203 nm for sample 0.2 mg, 2.85 nm for sample 0.3 mg and 2.95 nm for sample 0.7 mg. For sample 0.2mg (Fig.1 b) it is difficult to apply Scherrer formula on the XRD pattern, but for the other samples (Fig.1 c, d) which are clearly nanocrystalline we calculate the crystallite size (D) for the peak at 28° and the obtained values are: 2.04 nm for sample 0.3mg and 2.73 nm for sample 0.7mg. Those results are of the same order of magnitude with thedata obtained by TOPAS 5 calculation.

The thickness of these nano-films calculated from the density and film area were as follows: 0.2 mg (sample 1) – 110 ± 5 nm, 0.3 mg (sample 2) – 150 ± 5 nm and 0.7 mg (sample 3) – 360 ± 5 nm. For density value we used a literature one for $Nd_2Fe_{14}B$ constant magnet (7.4 g/cm^3). In our case the process the thin films formation can be described as follows. $Nd_2Fe_{14}B$ vaporized mass is the only one variable of the deposition process influencing the films thickness and nano-structures shape and size. The alloy vapours in contact with the glass slide forms germination spots and the nanoparticles grew through homogeneous crystallization. In consequence:

- low density vapours (0.2 mg vaporized material) generates a lot of small germination spots which further grows as numerous small nanoparticles;
- mean density vapours (0.3 mg vaporized material) generates a lot of germination spots which grows developing numerous nanoparticles slightly bigger than previous ones. A small fusion between two adjacent germination spots might occur explaining the appearance of bigger formations;
- high density vapours (0.7 mg vaporized material) generates a lot of germination spots. The higher vapour density facilitates the faster homogeneous growth developing strong nano-particles that partly fuses each other becoming nano-structural clusters.

The XRD pattern of a NdFeB magnet corroded in a NaCl solution will show the disappearance of the original $Nd_2Fe_{14}B$ phase peaks, replaced by peaks associated with corrosion products like iron and neodymium oxides and hydroxides. The corrosion process in NaCl solution preferentially attacks the Nd-rich phases, leading to the formation of these corrosion products. In fact corrosion can only change the surface of the sample. In Fig. 1 e is depicted XRD patterns of the corrosion product after 10 minutes in aq. solution 3.5 wt. % NaCl. The analysis shows that corrosion product contains Lepidocrocite [17], Goethite [18] and $Nd(OH)_3$ [19]. The average size of crystallite (D), calculated with Sherrer formula for the main peaks in Fig.1 e were 7.68 nm for FeOOH and 4.68 nm for $Nd(OH)_3$.

In fact XRD probes deeper than the surface layer (~1–10 μm), but corrosion products form in an ultra-thin surface layer (~10–100 nm). Corrosion products (Nd_2O_3, Fe_2O_3, B_2O_3) are often poorly crystalline or amorphous in early-stage corrosion. Surface roughening may slightly broaden XRD peaks, but not always enough to shift or replace them [20]. In fact **XRD isn't suitable** for detecting surface-limited corrosion on $Nd_2Fe_{14}B$ thin film magnets exposed to 3.5 wt. % NaCl and that is why we choosed the XPS experiments for surface study.

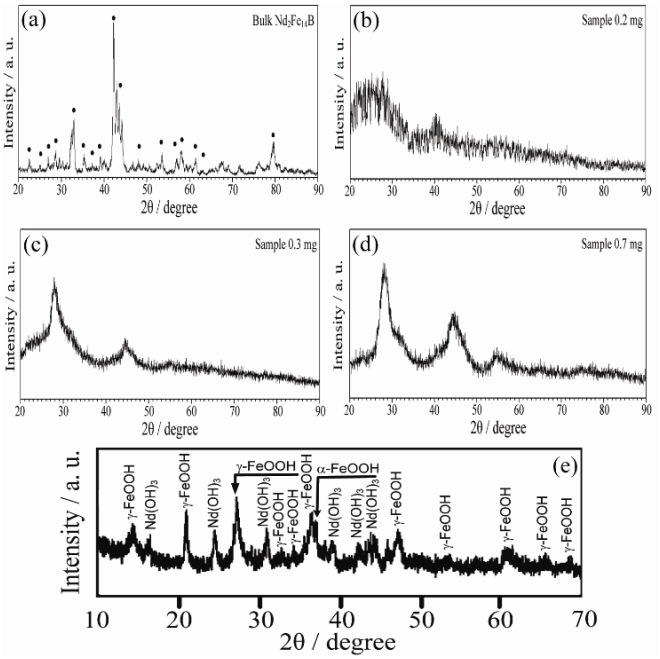

Figure 1. a) XRD pattern of bulk Nd-Fe-B; b-d) XRD pattern of as-deposited Nd-Fe-B thin films, e) XRD patterns of the corrosion product after 10 minutes in aq. solution 3.5 wt. % NaCl.

SEM micrographs obtained on the three Nd-Fe-B thin films on glass (Fig. 2) revealed homogeneous and dense films with a granulated surface texture, indicating a polycrystalline structure of equiaxed nanosized grains. The isolated grains sticking out of the film give a good indication of the particle size. Sample 0.2 mg (Fig. 2 a-b) show grains sized 50-80 nm, sample 0.3 mg (Fig. 2 c-d) show bigger grains of 70-120 nm. Sample 0.7 mg (Fig. 2e) shows a distinct feature that is the formation of columnar agglomerates of hundreds of nms or even micron-size, about one order of magnitude higher than the isolated particles observed in samples 1 and 2 corresponding to deposition of 0.2 and 0.3 mg, respectively.

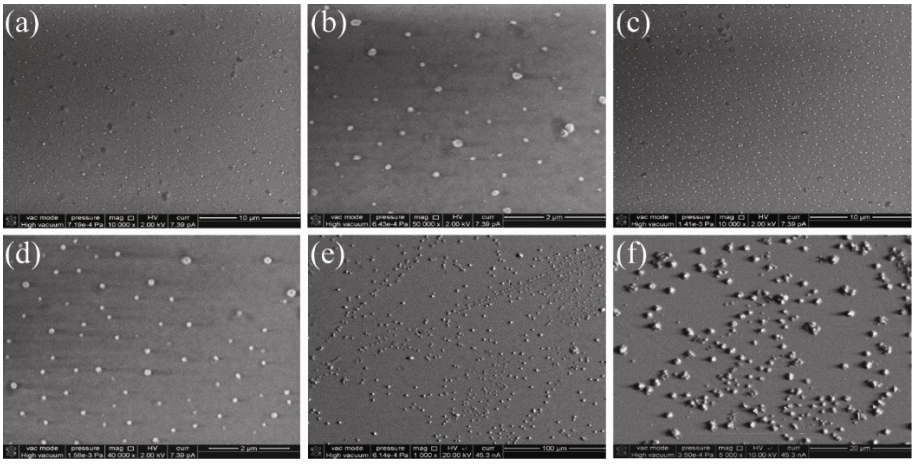

Figure 2. SEM micrographs of different magnifications of the nanostructured thin films in sample 1 (0.2 mg): a) 10 000 x b) 50 000 x; sample 2 (0.3 mg): c) 10 000 x d) 40 000 x; sample 3 (0.7 mg): e) 1 000 x f) 5 000 x.

Atomic force microscopy (AFM) measurements were used to study the surface microstructure of the Nd-Fe-B thin films in higher details, before and after corrosion tests, and the results are shown in Fig. 3.

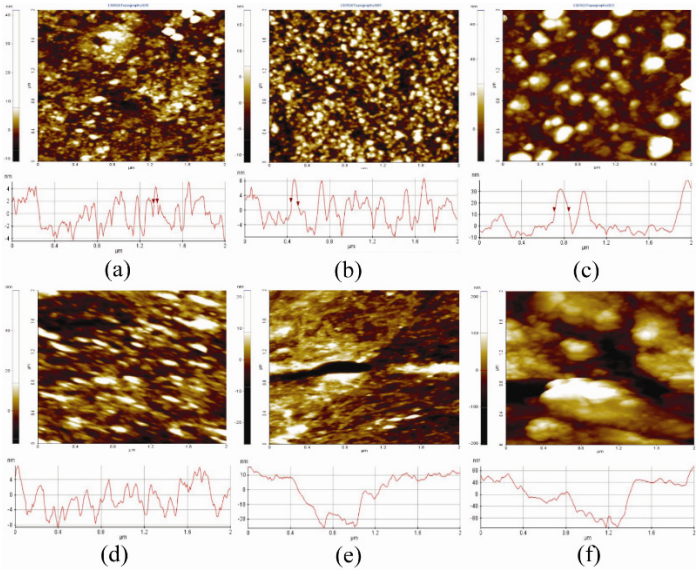

Figure 3. 2D AFM images (2x2 μm^2) and line profiles of NdFeB nanostructured thin films, before: a) sample 1-0.2 mg; b) sample 2-0.3 mg; c) sample 3-0.7 mg and after corrosion tests: d) sample 1-0.2 mg; e) sample 2-0.3 mg; f) sample 3-0.7 mg

While SEM images were scanned over larger areas (Fig. 2), details on the morphology of the sample at nanometric scale, were obtained from the AFM images taken over 2×2 μm^2. Taking into considerations the microstructural aspects reveal by both SEM and AFM, it can be observed that sample 1 exhibit the beginning of a particles structure formation, which due to thelow density vapours (0.2 mg vaporized material) generates random small particles growth sites, further leading to a random appearance of distinct surface particles (Fig. 3 a). Fig. 3b exhibit a homogeneous structure of individual surface particles, well defined, due to the increased vapours density (0.3 mg vaporized material) which generates a large number of germination sites, which further develop a uniform structure of nanoparticles, with diameters slightly bigger. The highest vapour density in this series (0.7 mg vaporized material) leads to a fast interaction between the particles (high diffusion rate) favouring the particles fusion, explaining the appearance of large particles – Fig 3c (in form of material clusters at larger scales). The information regarding the films microstructure (thickness and grains dimensions) is summarized in Fig 4a.

AFM measurements were also performed after corrosion experiments and the images recorded for samples 1, 2 and 3 with 0.2 mg, 0.3 mg and 0.7 mg deposition weights, are presented in Fig 3 d-f. It can be noticed the appearance of the distinctive marks of the corrosion process as pits and ditches, and the distortion of the previously formed particles.

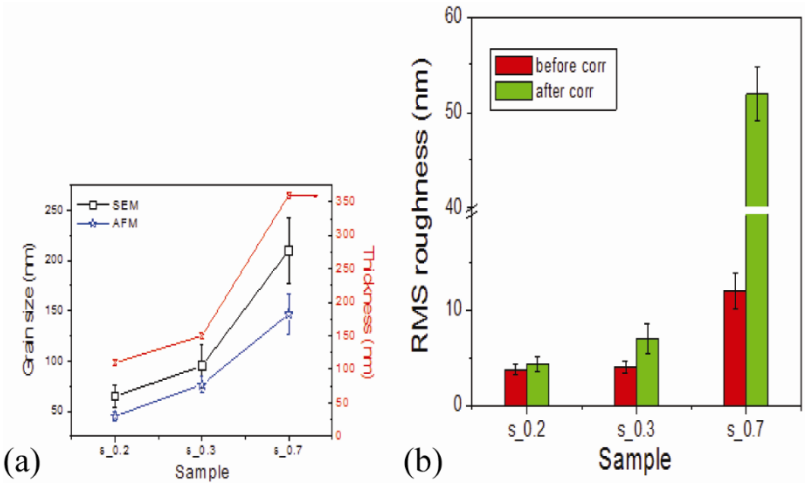

Figure 4. Thickness and grains size from SEM and AFM (a) Roughness histograms for the sample 1- 0.2 mg, sample 2- 0.3 mg and sample 3- 0.7 mg (at the scale of 2x2 μm^2) before and after corrosion tests (b).

In line with the results obtained before corrosion experiments, and with the SEM observations, a similar trend in roughness behavior (before and after corrosion tests) could be observed in Fig. 4b, in which lower value of roughness are found for samples 0.2 and 0.3 mg in comparison with sample 0.7. However, typical pattern of corrosion could be observed on sample 0.7, in agreement with SEM (as shown later), in forms of deep cracks of hundred of nm (as well as in the AFM image recorded at the scale of 8x8 microns).

A comparison between XRD and AFM measurements shows that a 33 % increase in crystallite size for the samples 0.3 mg and 0.7 mg (from 2.05 to 2.73 nm) corresponds to a 175% increase in surface roughness (from 4.45 to 12.25 nm). This indicates that even modest increases in crystallite size can result in significant changes in surface morphology, likely due to grain coalescence and emerging surface topography. Thus, while crystallite size and roughness are distinct properties, their evolution may be linked under certain processing or environmental conditions.

In order to obtain surface chemistry information, X-ray photoelectron spectroscopy (XPS) was performed on Nd-Fe-B nanostructured thin films that had been exposed to atmosphere. The survey spectra were collected over a binding energy range of 0-1200 eV. Depth profile XPS was aquired using an Ar ion gun operated at 2 KeV (2x2)mm scaning area for 1 minute and 5 minutes time sputtering. Referring to Fig. 5, elemental analysis of characteristic binding energies confirms the presence of neodymium (Nd4d, 3d5), praseodymium (Pr3d), oxygen (O2s, 1s), sodium (Na2s,1s, KLL), carbon (C1s), iron (Fe3s, 2p,LMM) and boron (B1s). It is already known that rare earth metals can not be completely separated, so Pr is an impurity of Nd. The presence of a peak corresponding to C on the XPS spectra is due to environmental contamination or handling of the samples, while that of Na peak is due to the glass substrate because the Nd-Fe-B are very thin (nano films). The thickness of the deposited film was estimated at ~25nm by theory, into account the sputter rate [20] and the inelastic mean free path (imfp) ~ 5 nm for Fe 2p transition. This, calculation leads us to an overall thicken of ~ 25 nm. As for the O peak, this might results from the adsorbed oxygen during air exposure. The Na(KLL), Fe(LMM), Fe(LMM1) and Fe(LMM2) lines represent Auger transitions.

It has already been shown by Mao et al [21] that the peaks of Fe and Nd are present in the XPS spectrum of Nd-Fe-B in the Nd-rich phase. All XPS spectral peaks were fitted with PhI Multipack 9.1.0.9. software using Gaussian-Lorentian line shapes. Deconvolution of the peaks is necessary in order to identify correctly all the peaks present and to obtain quantitative data pertaining to relative concentrations. However, this step is quite challenging and nearly impossible considering the number of constituents present within the alloy and the amount of overlapping that occurs between characteristic binding energies.

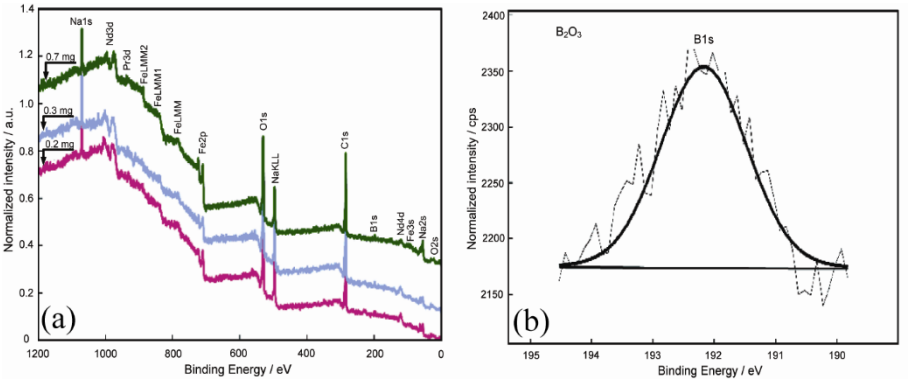

Figure 5. a) Wide scan XPS spectra for the Nd-Fe-B nano-structured thin films: sample 1-0.2 mg (bottom spectrum); sample 2-0.3 mg (middle spectrum); sample 3-0.7 mg (top spectrum); b) B1s deconvoluted spectrum.

To further determine the film components, high-resolution XPS spectra of C1s, O1s, B1s, Nd 3d, Nd 4d and Fe 2p regions were recorded. The spectra were fitted using Gaussian-Lorentzian curves modified by a tail function, after back subtraction following the Shirley procedure [22]. The concentrations of Nd, Fe and B in the three studied samples were quantified using high-resolution spectra of O2s, C1s, Nd3d, Nd4d, Fe2p and B1s.

The obtained results are presented in Table 1. It is appropriate to note here that all the calculations were performed assuming that the samples were homogeneous within the XPS detected volume. We have to emphasize that the errors in our quantitative analysis (relative concentrations) were estimated to be in the range of ± 10 %, while the accuracy for Binding Energies (BEs) assignments was found to be ± 0.2 eV. The accuray of the quantitative analysis (rel.conc. or values the BEs) was estimated by manufacture Company (ULVAC-PHI) [23].

The high-resolution spectra of B1s are very noisy (see Fig. 5b) because concentration of B in the alloy is very low. However, XPS analysis identified the oxidized state, namely B_2O_3. The dotted spectrum is the experimental curve, the line spectrum is the theoretical deconvolution.

The deconvoluted spectra for the $Nd3d_{5/2}$, indicates the presence of stable neodymium oxide, Nd_2O_3 at a binding energy of 982.5 eV (Fig. 6a). The Nd 4d transition indicates that the volume of the “nano film” gives the signal (Fig. 6b). The presence of a number of oxidation states in transition metals can give several transitions corresponding to a particular element as seen in this case for Nd.

Table 1. The relative elemental composition of Nd, Fe, B, C and O in wt.% in the three thin film Nd-Fe-B samples quantified by using high-resolution spectra of O2s, C1s, Nd3d, Nd4d, Fe2p and B1s (see Section 1).

Deposited wt.	Element composition* (wt.%)				
	C	O	Nd	Fe	B
1 (0.2 mg)	1.47	10.47	35.28	52.59	0.18
2 (0.3 mg)	0.48	10.91	38.21	49.78	0.60
3 (0.7 mg)	0.28	30.51	31.56	37.55	0.08

* Estimated errors in the reported values of relative elemental concentrations in the three Nd-Fe-B thin films are ± 10 %

In the case of iron oxides (FeO, Fe_2O_3), the Fe_2O_3 (Fig.6c inset) could be reduced to Fe_3O_4 by Ar^+ sputtering in XPS analysis, or by oxidation during a corrosion process [24-26]. So one can see from the high resolution spectra (Fig.5b and Fig. 6) that all elements (Nd, Fe, B) of the nano-films are present in their oxidized form (B_2O_3, Nd_2O_3, Fe_2O_3) in the Nd-Fe-B nano-films. Table 2 summarizes the corresponding binding energies determined from the XPS spectra.

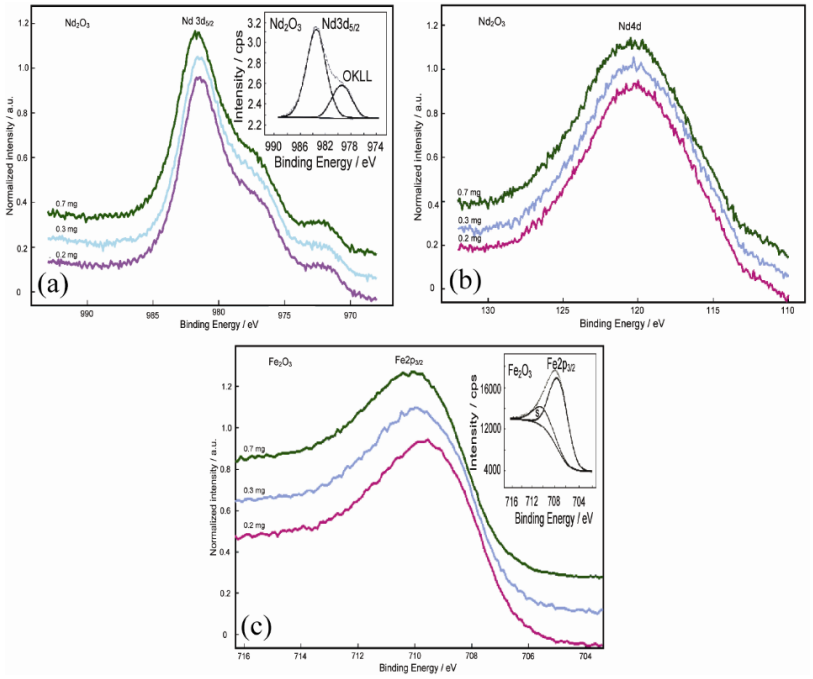

Figure 6. High resolution XPS spectra for: a) Nd3d (inset - the deconvoluted spectrum); b) Nd4d; c) Fe2p (inset - the deconvoluted spectrum).

Table 2. Calculated binding energies from XPS spectra for the initial Nd-Fe-B nanostructured thin films.

Deposited wt.	Binding energies* - B.E. (eV)			
	Nd $3d_{5/2}$	Nd 4d	Fe $2p_{3/2}$	B 1s
1 (0.2 mg)	983.4	121.2	709.5	192.1
2 (0.3 mg)	982.5	122.0	710.0	192.3
3 (0.7 mg)	982.8	122.3	710.2	192.0

* Estimated uncertainties in the reported calculated values of binding energies in the three Nd-Fe-B thin films are ± 0.2 eV.

2. Magnetic properties

Results of average specific magnetization (σ) measured as a function of temperature for three transparent films with d < 100 nm thickness are presented in Fig. 7. This figure shows that at ~ 100 K the nano-films specific magnetization is 85 ± 0.005 $A \cdot m^2 \cdot kg^{-1}$. Films heating to T ~ 750 K during the specific magnetization measurement changes the magnetic state of the films, leading to a decrease in the specific magnetization as seen in Fig. 7. Continuous reduction in the specific magnetization of nanostructured films from 77 K to 750K may be caused by the changing chemical composition of the thin films. The Curie temperature of all studied thin films is almost the same as the initial powders (about 580 K). The Curie temperature is determined from extrapolation of the linear part of $\sigma^2 = f(T)$ dependence to x axis.

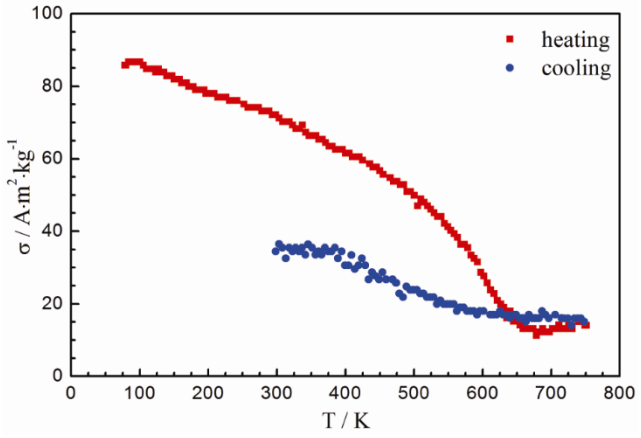

Figure 7. Temperature dependence of average specific magnetization before corrosion action of Nd-Fe-B nanostructured thin films of thickness, d < 100 nm.

3. Morphology, magnetic and surface properties of the nano-structured thin films after the corrosion test

It was established that the corrosion action most noticeably changes the magnetic state of nanoscale films.

Even if the samples were so thin (nanostructed) which do not justify subjecting them to a corrosion study, we performed rapid potentiodynamic corrosion tests in a 3.5 wt. % NaCl aerated solution at 25±0.5° C. By the open circuit potential test (OCP), zero current potentials were determined as follows: for sample 1 (0.2 mg deposition weight), E_{OCP}= -0.425 V; for sample 2 (0.3 mg deposition weight), E_{OCP}= -0.045 V; and for sample 3 (0.7 mg deposition weight), E_{OCP}= -0.397 V. But we observed the rapid dissolution of the samples (too thin) and so neither Tafel plots, nor the calculated kinetic parameters of corrosion process could not be measured. In this case, we limited ourselves to establishing the morphology and surface condition of the nano-structured Nd-Fe-B films after the corrosion process.

SEM measurements of the samples after corrosion in 3.5 wt.% NaCl revealed very significant morphological changes and confirmed the destruction of films, as can be seen in Fig. 8.

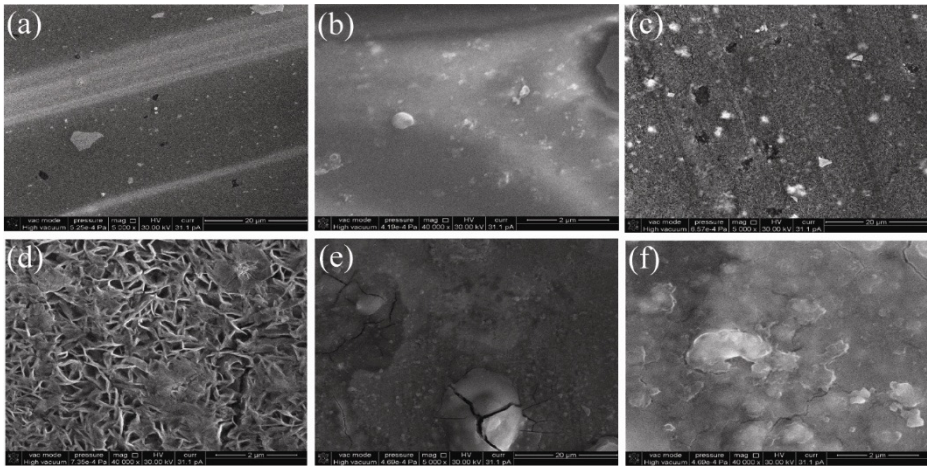

Figure 8. SEM images of different magnification of the Nd-Fe-B films after corrosion process in 3.5 wt. % NaCl. Sample 1 (0.2 mg): a) 5 000 x and b) 40 000 x; sample 2 (0.3 mg): c) 5 000 x and d) 40 000 x; sample 3 (0.7 mg): e) 5 000 x and f) 40 000 x.

Corrosion process leads to the disappearance of the 0.2 mg nanostructured film and to formation of cracks and delaminated surface in the 0.7 mg film. Surprisingly however, sample 2 (0.3 mg) showed the formation

of novel characteristic microstructures of intersecting nanowalls, with thickness of around 50 nm, growing perpendicularly to the plane of the film as can be seen from the structure shown at a higher magnification of 100 000 x in Fig. 9. In this figure both acicular grains and tabular scales are observed and as γ – FeOOH (Lepidocrocite) forms flattened scales (tabular crystals), this confirms the XRD data from Figure 1e.

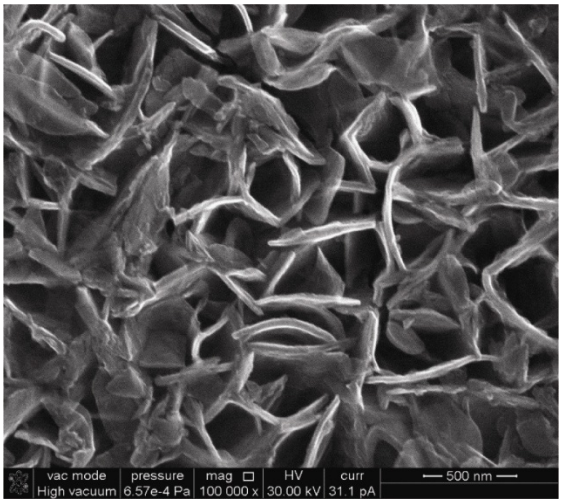

Figure 9. SEM imagesat a higher magnification of 100 000 x providing detail of the nanowalls grown perpendicularly to the sample 2- 0.3 mg after corrosion.

By analyzing the σ = f (T) temperature dependence of Nd-Fe-B nanoscale films after exposure to oxidative processes (Fig. 10), it can be seen that the corrosion processes lead to an increase in the specific magnetization of up to 140 - 155 $A \cdot m^2 \cdot kg^{-1}$, and the transition temperature to the paramagnetic state to 840-1010 K. Most likely, this may be due to the intensive formation of Fe_3O_4 iron oxide on the surface of Nd-Fe-B thin layers, and even the presence of free iron ions upon heating the samples up to 1000 K during the specific magnetization measurements. This fact was demonstrated by the specific magnetization measurement and the accuracy of this measurement is very high. The presence of a free iron and Fe_3O_4 iron oxide is proveded by temperature dependences of specific magnetization. The determined from them Curie points of corroded films is about 1000 K, and as it is known that the transition temperature to the paramagnetic state of Fe_3O_4 oxide is in the range T_C ~ 820-860 K and of iron T_C ~ 1030 K. Only the release of these ions from the Nd-Fe-B thin layers may increase the specific magnetization value in comparison with non-corroded samples.

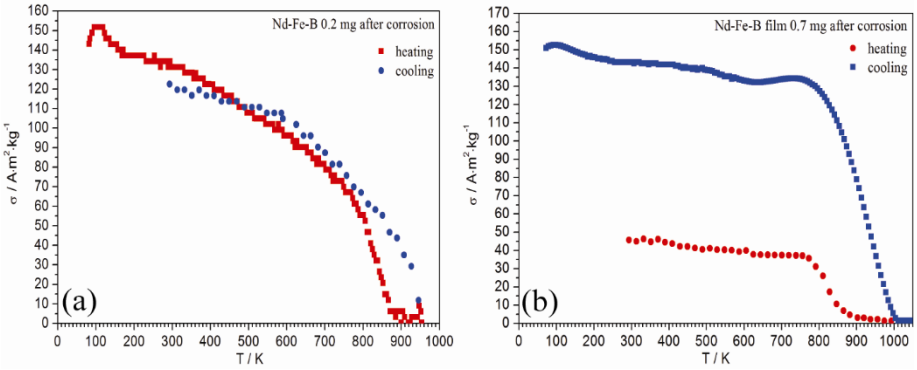

Figure 10. Temperature dependence of specific magnetization after corrosion action on Nd-Fe-B nanostructured thin films a) sample 1- 0.2 mg (sample 2- 0.3 mg has almost the same behaviour); b) sample 3- 0.7 mg.

In fact we can assume that $Nd_2Fe_{14}B$ is a rare-earth permanent magnet with a tetragonal structure. When exposed to NaCl solution (especially 3.5% NaCl, simulating seawater), it undergoes electrochemical corrosion, driven by the difference in electrochemical potential between the constituents: Nd (rare earth) is highly electropositive and oxidizes easily; Fe is moderately reactive; B is more inert but forms oxides slowly; Cl^- ions in NaCl solution accelerate corrosion by destabilizing protective oxide films. Neodymium ions dissolve into the electrolyte. These ions can react with water and hydroxide ions to form: Nd_2O_3 or $Nd(OH)_3$, which can precipitate locally as corrosion products. Iron in the lattice can also oxidized and form: Fe^{2+}/Fe^{3+}. Dissolved oxygen in NaCl solution reacts with water and electrons and generate OH^- and so the possibility of hydroxide formation. Chloride ions (Cl^-) are not directly oxidize, but destabilize oxides, facilitating Nd and Fe dissolution.

XPS measurements on all corroded nano-structured thin films (Fig. 11) proved the formation of those 2 species $Fe^{2+}(Fe_3O_4)$ and $Fe^{3+}(FeOOH)$. Decovolution data of Fe $2p_{3/2}$ spectra for the three studied samples, after oxidation during corrosion process, lead to a mixture of the oxides: Fe^{2+} (Fe_3O_4 with B.E. at 709.8, 710.2, 710.3 eV for the corresponding 3 samples 1, 2 and 3 respectively) and Fe $^{3+}$ (with BE at 711.2, 711.0, 711.2 eV for the corresponding 3 samples 1, 2 and 3 respectively). It has been previously reported that $Fe2p_{3/2}$ for Fe_3O_4 does not have a satellite peak [27, 28], and this is what we also observed in this study (Fig. 11a). Also, the very week satellite presented indicates the presence of an oxidized for of iron. It is absolutely possible (and common) for XPS peaks of Fe_2O_3, Fe_3O_4, and FeOOH to overlap, especially in the Fe 2p region. This overlap arises because all three compounds contain

Fe^{3+}, and their Fe $2p_3/_2$ binding energies fall in a narrow range: Fe_2O_3 710.6-711.2 eV, Fe_3O_4 709.5-710.6 eV and FeOOH 710.8-711.5 eV. So peak shapes can be nearly identical in typical lab-resolution XPS spectra and FeOOH [α (Lepidocrocite) or γ (Goethite)] can "hide" beneath the Fe_2O_3 signal. Using O1s high-resolution spectrum we could interpreting changes during Fe→FeOOH oxidation. In Fig. 11b the following peaks can be observed: Fe-O at 529.7 eV, Fe-OH at 531.7 eV and some absorbed species H_2O/-OH at 532.5-533 eV. The corroded surface shows oxide hydroxides that are very small in size and hydroxides that overlap in the XPS spectra over the oxides (see the very close binding energies) .So this proved that during corrosion of NdFeB in NaCl aqueous solution the oxidation can generate not only iron oxides but also hydroxide as presented in the XRD pattern (Fig.1e). Our results are in agreement with former publications [29,30]

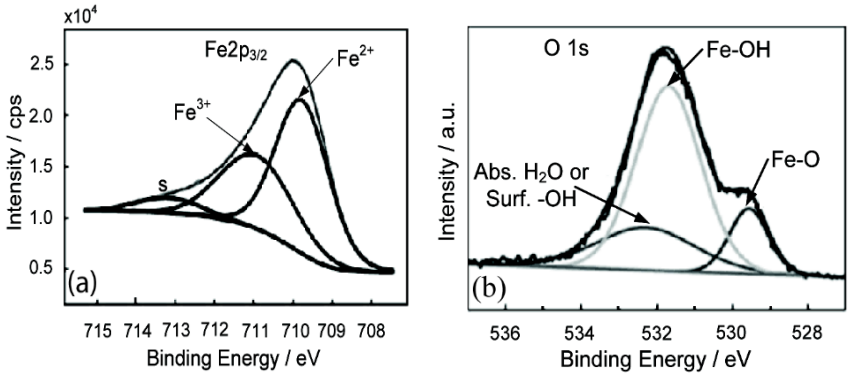

Figure 11. a) simulated XPS Fe2p3/2 spectra for Fe oxides and oxyhydroxides; b) simulated XPS spectra for O1s for Fe oxides/Oxihydroxides.

In Figure 12 are presented the XPS spectra: a) for the 3 NdFeB nano-samples after corrosion in 3.5 wt. % NaCl; b) high resolution spectra for Nd3d; c)deconvoluted spectrum for Nd3d.The presence of an oxygen phase (O at ~970 eV) is observed, which is due to the existence of the corrosion product $Nd(OH)_3$ [31]. On the overal spectra XPS the the Nd3d XPS peaks for Nd_2O_3 and $Nd(OH)_3$ can significantly overlap, because both compounds contain Nd in the +3 oxidation state. The main Nd peaks overlap within ~0.1–0.3 eV (982.4-982.5 eV for Nd_2O_3 and 982.5-982.7 eV for $Nd(OH)_3$, which is often within the instrumental resolution, especially in standard-resolution XPS. By capturing high-resolution Nd 3d and O 1s spectra, especially focusing on binding energies shifts, O-environment peaks, and satellite shapes, one can

confidently differentiate $Nd(OH)_3$ from Nd_2O_3. On the deconvoluted spectrum of $Nd3d_{5/2}$ (Fig.12 c) multiple split are observed. The peak at 980.7 eV confirms the presence of Nd^{3+} in hydroxide environment, similar to the values tabulated for $Nd(OH)_3$. This peak is smaller than the one corresponding to Nd_2O_3 (~983 eV) which proved that only some part of neodin oxide is transformed into hydroxide.

Also we have to take in account the spectrum of O1s from Fig. 11b which proved the existence of oxide and hydroxides after corrosion. The main peak between 530–531 eV, proved the metallic oxygen (Nd–O) while the shoulder at about 532 eV is due to hydroxyl groups, i.e. the OH in $Nd(OH)_3$.

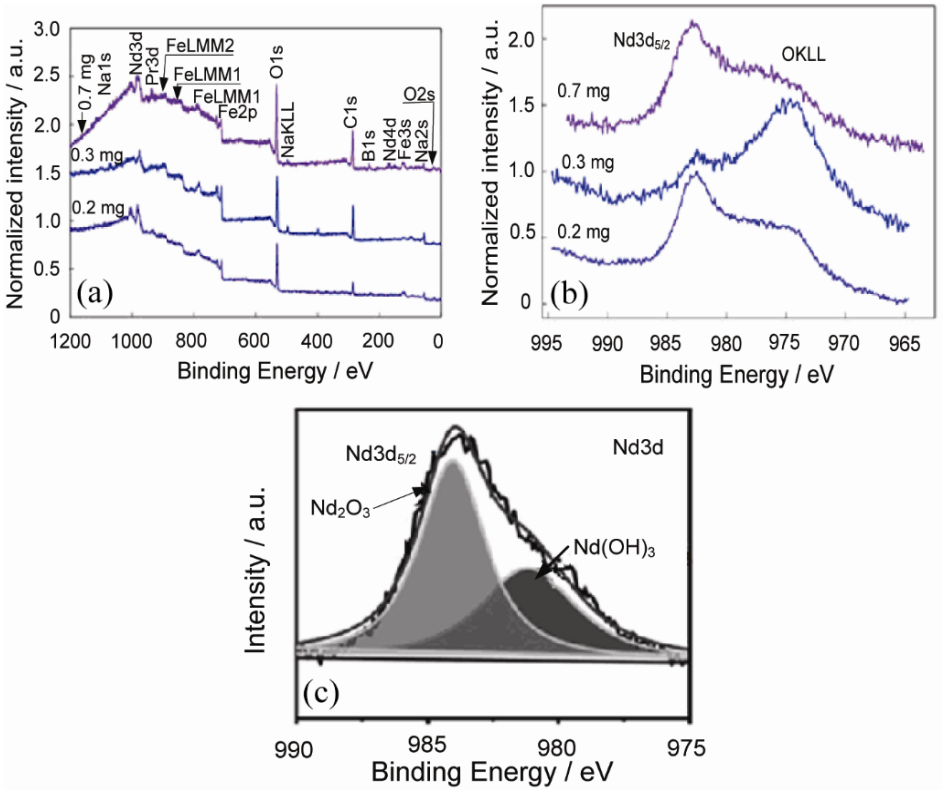

Figure 12. The XPS spectra obtained after corrosion of NdFeB thin films: a) the general spectra of the 3 films; b) the high-resolution spectrum of Nd3d; c) the deconvolution spectrum for Nd3d.

CONCLUSIONS

A method of producing $Nd_2Fe_{14}B$ thin films of different thicknesses at a nanoscale is developed.

X-ray diffraction study showed that synthesized films are nano-crystalline. SEM micrographs obtained on the Nd-Fe-B thin films deposited on glass revealed these films to be homogeneous and dense with a granulated surface texture, indicating a polycrystalline structure of equiaxed nanosized grains. The AFM images which measured the presence of Nd-Fe-B grains on the three thin films (with deposition weights of 0.2, 0.3 and 0.7 mg and and thicknesses of 40 nm,130 nm and 70 nm respectively) confirmed SEM observations that those samples are nano-structurated.

High-resolution XPS spectra showed that all elements constituting the nano-films are present in their oxidized forms (B_2O_3, Nd_2O_3, Fe_2O_3). SEM and AFM measurements of the samples after quick corrosion in a 3.5 wt. % NaCl solution revealed very significant morphological changes and confirmed the destruction of nano-films. The $\sigma = f(T)$ temperature dependences of specific magnetization revealed that after corrosion action on the thin films, their specific magnetization increases from 85 to 140 - 155 $A \cdot m^2 \cdot kg^{-1}$, and the transition temperature to the paramagnetic state increases from 620 to 840-1010 K. This behaviour could be explained by the intensive formation of Fe^{2+} oxide and presence of free iron ions on the surface of Nd-Fe-B thin layers. On a macro level, therefore, the magnetic properties of the thin Nd-Fe-B layers were determined not only by corrosion action on $Nd_2Fe_{14}B$ composition, but also by the formation of the Fe compositions and by free iron appearance. XPS analysis confirmed the presence of Fe_3O_4/FeOOH and of $Nd(OH)_3$ on the surface of the corroded samples.

EXPERIMENTAL SECTION

1. Thin film deposition of Nd-Fe-B

A powders, received from bulk commercially available Nd-Fe-B constant magnets (alloy MQP-B) (Magnequench Technology Center, SG, Singapore, Korea), was used as precursor in deposition of the samples. $Nd_2Fe_{14}B$ thin films were obtained by thermal evaporation (flash method) in a standard sputtering installation UHV-71R-2 type on 1 × 1 cm^2 glass substrates.The type of glass used was sodium-calcium-silicate (60-70% SiO_2, 12% Na_2O, 13% CaO, 2.8-4% MgO, 0.6-2% Al_2O_3); preliminarily a glass substrates were purified by liquid etching method. a special device based on shock vibration for a strictly dosed spilling powder charge into the evaporation zone is applied.

During deposition the powder grains fall on an tantalum evaporator, heated to a temperature significantly above the $Nd_2Fe_{14}B$ melting point (~ 1723 K – 1740 K), in this case, ~ 2773 K. Rapid evaporation and subsequent cooling of the substance deposited on the substrate maintains its composition and structure. By using this method, we obtained three different nanoscale films on glass substrate. Additionally, the films composition is confirmed by XPS analysis method. The thickness of received films is determinated by mass of the evaporated substance and by time of deposition, as following: 0.2 mg for 90 s (sample 1), 0.3 mg for 120 s (sample 2) and 0.7 mg for 300 s (sample 3). The films thickness will be specified below. All received films were transparent.

2.Thin film characterization

The crystalline structure of the as-deposited alloy thin films was characterized by X-ray diffraction (XRD) using an X-ray diffractometer (model DRON-2, Russia) WITH CU-Kα-radiation (λ = 0.154056 nm). X-ray patterns were obtained by the automatic recording of reflection intensities using a 0.03° scanning step and 2-3 s exposition time per step.

The morphology of the obtained thin films was analyzed before and after the corrosion process by scanning electron microscopy (SEM) using a 3d FEG apparatus equipped with an energy dispersive X-ray spectrometer (EDS). Atomic force microscopy (AFM) measurements were carried out in the non-contact mode with a XE-100 apparatus from Park Systems equipped with flexure-guided, cross-talked eliminated scanners, using sharp tips (<8 nm tip radius; Si material - PPP-NCLR type from NanosensorsTM) of app. 225 mm length, 38 mm width and 48 N/m nominal spring constant/~190 kHz nominal resonance frequency. The topographical 3D AFM images were obtained by scanning the AFM tip over areas of 8×8 μm^2 and 2×2 μm^2. XEI (v1.8.0) software program was used for displaying the images and subsequent statistical data analysis, including the calculation of the root mean square (RMS) roughness.

Surface analysis of the samples was performed by X-ray photoelectron spectroscopy (XPS) and was carried out on a Quantera SXM equipment, with a base pressure in the analysis chamber of 10-9 Torr. The X-ray source was Al K_α radiation (1486.6eV, monochromatized) operating at 350 W and the overall energy resolution is estimated at 0.65 eV by the full width at half maximum (FWHM) of the Au4f7/2 line. In order to take into account the charging effect on the measured Binding Energies (BEs), the spectra were calibrated using the C1s line (BE = 284.8 eV, C-C (CH)n bondings) of the adsorbed hydrocarbon on the sample surface.

The specific magnetization of Nd-Fe-B alloy thin films were measured by ponderomotive method in 0.86 T magnetic field and 80 - 720 K temperature range [32]. The method is based on, measurement of the sample force of retraction in magnetic field.

3. Corrosion assembly test

Electrochemical measurements of the thin Nd-Fe-B films magnets was studied experimentally by the potentiodynamic polarisation technique and using a potentiostat/gavanostat model PARSTAT 2273 (Princeton Applied Research, Oak Ridge, USA), with a “Power Corr” Software. For the electrochemical tests we used open circuit potential (OCP), linear polarization (LPR) and Tafel polarization measurements. These tests were performed in a 3.5 wt. % NaCl aerated aqueous solution under ambient conditions, (25 ± 2)° C and without stirring. All electrochemical tests were performed using a 100 cm^3 thermostatic glass cell with a standard three-electrode system, with the steel samples as the working electrode (WE), the Ag/AgCl reference electrode (saturated with 0.3 M KCl), and a platinum plate with area of 1 cm^2 as counter electrode, both produced by Radiometer (Radiometer Medical ApS., Denmark). The cell assembly was placed in a Faraday cage to prevent electrical interference.

ACKNOWLEDGEMENTS

This research was financed by Romanian Academy and Belarus Academy of Science bilateral project 2011-2013, no.F12RA-007 within the research programme “electrode processes, corrosion and materials for electrochemical systems” of the “Ilie Murgulescu” Institute of Physical Chemistry and by “EU(ERDF)-Romanian government” that allowed for acquisition of the research infrastructure under POS-CEEO 2.2.1 INFRANANOCHEM project nr.19 /01.03.2009. The authors thank prof. K. Yanushkevich[2(†)] for his guidance and help in the magnetism experiments. Authors also express sincere regret for prof. K. Yanushkevich passing into existence in 2023.

REFERENCES

1. *J. Thiel*sch; *D. Hinz;* L. Schultz*;* O.Gutfleisch; *J. Magn. Magn. Mat*., **2010**, *322*(20), 3208-3213. https://doi.org/10.1016/j.jmmm.2010.05.064
2. R. Sueptitz; K. Tschulik; M. Uhlemann; M. Katter; L. Schultz; A Gebert; *Corr. Sci*., **2011**, *53*(9), 2843-2852. https://doi.org/10.1016/j.corsci.2011.05.022

3. H. Sepehri-Amin; Y. Une; T. Ohkubo; K. Hono; M. Sagawa; *Scripta Mater.*, **2011**, *65*(5), 396-399. https://doi.org/10.1016/j.scriptamat.2011.05.006
4. W.F. Li; H. Sepehri-Amin; T. Ohkubo; N. Hase; K. Hono; *Acta Mater.*, **2011**, *59*(8), 3061-3069. https://doi.org/10.1016/j.actamat.2011.01.046
5. W.B. Cui; Y.K. Takahashi; K. Hono; *Acta Mater.*, **2011**, *59*(20), 7768-7775. https://doi.org/10.1016/j.actamat.2011.09.006
6. V.V. Ovchinnokov; *Mössbauer Analysis of the Atomic and Magnetic Structure of Alloys*, Cambridge International Science Publishers: UK, **2006**. ISBN: 1-904602-13-4
7. P. Gutlich; E. Bill; A.X. Trautwein; *Mössbauer Spectroscopy and Transition Metal Chemistry: Fundamentals and Applications,* Springer-Verlag: Berlin, Heidelberg, **2011**. ISBN: 978-3-540-88427-9
8. L.K.E.B Serrona; A. Sugimura; R. Fujisaki; T. Okuda; N. Adachi; H. Ohsato;I. Sakamoto; A. Nakanishi; M. Motokawa*; Mater. Sci. Eng.: B*, **2003**, *97*(1), 59-63. https://doi.org/10.1016/S0921-5107(02)00401-4
9. Y.G. Ma;Z. Yang;M. Matsumoto;A. Morisako;S. Takei; *J. Magn. Magn. Mater.*, **2003**, 267(3), 341-346. https://doi.org/10.1016/S0304-8853(03)00402-5
10. C. Constantinescu; N. Scarisoreanu; A. Moldovan; M. Dinescu; L. Petrescu; G. Epureanu;*Appl. Surf. Sci.*, **2007**, 253(19), 8192-8196. https://doi.org/10.1016/j.apsusc.2007.02.165
11. M. Ştefan; E.J. Popovici; I. Baldea; A. Mesaros; L. Muresan; R. Grecu; *Studia UBB Chemia*, **2006**, LI, 2, 147-151.
12. E. Burzo, *Studia UBB Chemia*, **2021**, LXVI, 3, 63-72. https://doi.org/10.24193/subbchem.2021.3.02
13. J.M. Song; *J. Korean Phys. Soc.*, **2001**, *39*, 314-317.
14. L.K.E.B. Serrona; A. Sugimura; N. Adachi; T. Okuda; H. Osato; I. Sakamoto; A. Nakanishi; M. Motokawa; D.H. Ping; K. Hono; *Appl. Phys. Lett.,* **2003**, *82*, 1751-1753. https://doi.org/10.1063/1.1561576
15. S.N. Piramanayagam; M. Matsumoto; A. Morisako; *J. Magn. Magn. Mater.*, **2000**, *212*(1-2), 12-16. https://doi.org/10.1016/S0304-8853(99)00597-1
16. PCPDFWIN, Joint Committee on Powder Diffraction Standards, International Centre for Diffraction Data, JCPDS-ICDD, v. 2.01, # 88-2285; 1998.
17. PCPDFWIN, Joint Committee on Powder Diffraction Standards, International Centre for Diffraction Data, JCPDS-ICDD, v. 2.01, # 74-1877; 1998.
18. PCPDFWIN, Joint Committee on Powder Diffraction Standards, International Centre for Diffraction Data, JCPDS-ICDD, v. 2.01, # 74-2195; 1998.
19. PCPDFWIN, Joint Committee on Powder Diffraction Standards, International Centre for Diffraction Data, JCPDS-ICDD, v. 2.01, # 83-2035; 1998.
20. A.M. Popescu; J. Calderon Moreno; K. Yanushkevich;A. Aplevich; O. Demidenko; E.I. Neacsu; V. Constantin; *J. Braz. Chem. Soc.* **2024**, 35, 1, e-20230089, 1-12. https://dx.doi.org/10.21577/0103-5053.20230089
21. S. Mao; H. Yang; Z. Song; J. Li; H. Ying; K. Sun; *Corros. Sci.*, **2011**, *53*(5), 1887-1894. https://doi.org/10.1016/j.corsci.2011.02.006
22. D.A. Shirley; *Phys. Rev. B,* **1972**, *5*, 4709-4714. https://doi.org/10.1103/PhysRevB.5.4709

23. J.F. Moulder; W.F. Stickle; P.E. Sobol; K.D. Bomben; *Handbook of X-ray Photoelectron Spectroscopy,* Physical Electronics USA, Inc., Chamhassen, **1995**.
24. R.J. Lad; V.E. Henrich; *Surf. Sci*., **1988**, *193*(1-2*)*, 81-93. https://doi.org/10.1016/0039-6028(88)90324-X
25. E. Paparazzo; *Appl. Surf. Sci*., **1986**, 259(1-2), 1-12. https://doi.org/10.1016/0169-4332(86)90021-8
26. P. Mills; J.L. Sullivan; *J. Phys. D-Appl. Phys.,***1983**, *16*(5), 723-732. https://doi.org/10.1088/0022-3727/16/5/005
27. D.D. Hawn; B.M. DeKoven; *Surf. Interface Anal.,***1987**, *10*(2-3), 63-74. https://doi.org/10.1002/sia.740100203
28. M. Muhler; R.Schlogl; G. Ertl; *J. Catal.,***1992**, *138*(2), 413-444. https://doi.org/10.1016/0021-9517(92)90295-S
29. A.P. Grosvenor; B.A. Kobe; M.C. Biesinger;N.S. McIntyre; *Surf. Interface Anal*. **2004**; 36: 1564–1574.DOI: 10.1002/sia.1984
30. C. Lyu;·L. Ju; X. Yang; L. Song; N. Liu; *J. Mater. Sci*., **2020**, *31,* 4797-4807. https://doi.org/10.1007/s10854-020-03041-2
31. S. Lasek; M. Kursa; K. Konecna; Proceeding of Metall Conference, **2011**, Brno, Cehia, p.1-5.
32. K.I. Yanushkevich; *Methods of specific magnetization and magnetic susceptibility measurement,* Assurance system of measurement uniformity of the Republic of Belarus, MVI. MN 3128-2009, BelSIM: Minsk, **2009**.

STUDIA UBB CHEMIA, LXX, 3, 2025 (p. 85-106)
(RECOMMENDED CITATION)
DOI:10.24193/subbchem.2025.3.06

GREEN SYNTHESIS AND ANTIBACTERIAL EVALUATION OF SILVER NANOPARTICLES USING NEEM (AZADIRACHTA INDICA) LEAF EXTRACT

Syeda Farheen ANDERABI[a], Jahanzeb SHEIKH[b,c], Sania TANVIR[c], Rehana KOUSER[a], Iftikhar Ahmed CHANNA[f], Tanzeela IKRAM[a], Sidra Abid SYED[c], Ali Dad CHANDIO[f], Tan Tian SWEE[b], Jose-Javier SERRANO OLMEDO[d], Rashid KHAN[e], Muhammad FAIZAN[f], Madeeha SADIA[a, b, *]

ABSTRACT. The synthesis of silver nanoparticles (AgNPs) using traditional physical and chemical methods often involves toxic reagents, high energy consumption, and poor biocompatibility, making them unsuitable for many biomedical applications. Moreover, existing green synthesis approaches frequently lack control over nanoparticle size, shape, and stability, limiting their reproducibility and scalability. To address these limitations, this study employed a green synthesis route using Azadirachta indica (Neem) leaf extract as a natural reducing and stabilizing agent. Silver nitrate ($AgNO_3$) solutions of varying concentrations (1 mM, 5 mM, and 10 mM) were reacted with the Neem extract under ambient conditions. UV–Visible spectroscopy confirmed the formation of AgNPs with a characteristic surface plasmon resonance peak at 402 nm. Scanning Electron Microscopy (SEM) showed that the 5 mM $AgNO_3$

[a] *Department of Biomedical Engineering, NED University of Engineering & Technology, Karachi, Pakistan.*
[b] *Department of Biomedical Engineering and Health Sciences, Universiti Teknologi Malaysia, Johor Bahru 81310, Johor, Malaysia.*
[c] *Department of Biomedical Engineering, Sir Syed University of Engineering and Technology, Karachi, Pakistan.*
[d] *Centre for Biomedical Technology Madrid, Universidad Politécnica de Madrid, Madrid, Spain.*
[e] *Mechanical Engineering Department, College of Engineering, Al Imam Muhammad Ibn Saud Islamic University, Riyadh, Saudi Arabia.*
[f] *Department of Metallurgy, NED University of Engineering & Technology, Karachi, Pakistan.*
[*] *Corresponding author: madeehaoz@neduet.edu.pk*

concentration produced the most desirable morphology, uniformly spherical nanoparticles with an average size of 98 nm. Energy Dispersive X-ray (EDX) analysis further confirmed the presence of pure elemental silver with no silver compounds. Moreover, antibacterial testing, conducted against Total Coliform bacteria and Propionibacterium acnes, revealed that the synthesized AgNPs, particularly in powder form, effectively inhibited bacterial growth over extended incubation periods. In conclusion, this study demonstrates that Neem-mediated synthesis is a viable, sustainable, and efficient approach for producing biologically active silver nanoparticles.

Keywords: *Silver nanoparticles; Green synthesis; Azadirachta indica (Neem); Antibacterial activity; SEM characterization; Plant-based nanomaterials.*

INTRODUCTION

Nanotechnology has revolutionized material science by enabling the manipulation of matter at the atomic and molecular scale, typically within 1–100 nm [1]. Among the diverse applications, the synthesis of metallic nanoparticles, particularly silver nanoparticles (AgNPs), has garnered significant attention due to their exceptional antimicrobial, anti-inflammatory, and optical properties [2]. Silver, a noble metal known historically for its antimicrobial efficacy [3], becomes remarkably more reactive at the nanoscale due to an increased surface area-to-volume ratio [4].

Traditionally, AgNPs have been synthesized using physical and chemical methods [5], such as evaporation-condensation [6] and chemical reduction using agents like sodium borohydride and citrate [7]. While these methods are efficient and scalable, they often involve high energy consumption [8], toxic reagents [9], and hazardous by-products [10], limiting their suitability for biomedical applications. For example, tube furnace-based evaporation methods consume significant energy and produce environmental heat pollution [11]. Similarly, chemical synthesis can lead to nanoparticle agglomeration [12] due to insufficient capping agents, and the residual chemicals may remain on particle surfaces, posing cytotoxic risks [13].

To overcome these drawbacks, green synthesis using biological systems such as bacteria [14], fungi [15], and plant extracts [15 – 17] has emerged as a safer and more sustainable approach [18]. Microbial synthesis, though effective, often requires complex culturing conditions and longer synthesis times [19]. Fungal methods, while yielding higher nanoparticle quantities, involve risk of contamination [20] and require precise control over pH and temperature [21]. Furthermore, both microbial and fungal synthesis approaches may involve challenges in downstream processing and scale- up.

Among plant-based green synthesis methods, the use of Azadirachta indica (Neem) has shown great promise [22, 23]. Neem is a medicinally valuable plant known for its antibacterial, antifungal, and anti-inflammatory properties [24]. Moreover, Research has established that limonoid compounds extracted from neem seeds exhibit minimum inhibitory concentrations (MICs) ranging from 32 µg/ml to 128 µg/ml against *Pseudomonas aeruginosa* (*P. aeruginosa*) and *Staphylococcus epidermidis* (*S. epidermidis*), an opportunistic skin pathogen [25]. Its extract contains various phytochemicals such as flavonoids, terpenoids, and phenolics, which serve as both reducing and stabilizing agents during nanoparticle formation. For instance, Zanjage [26] and Ghazali [27] demonstrated the rapid biosynthesis of AgNPs using aqueous Neem extracts. However, the limitations included poor reproducibility, lack of control over particle size, and agglomeration due to unstable phytochemical profiles in extracts. Moreover, the influence of synthesis parameters such as extract concentration, reaction time, temperature, and pH were not rigorously optimized in many prior studies.

In terms of characterization, studies employing UV-Vis spectroscopy, Scanning Electron Microscopy (SEM), and Energy Dispersive X-ray (EDX) analysis have confirmed the successful formation and elemental composition of Neem-derived AgNPs [28, 29]. However, gaps remain in detailed structure-property correlation, and many works lack thorough antibacterial efficacy validation against clinically relevant strains. Therefore, in this research, we addressed the limitations of conventional AgNP synthesis methods by developing a green, eco-friendly approach using Neem leaf extract. This method eliminated the need for toxic chemicals and high energy input. The study involved optimizing critical synthesis parameters to achieve controlled particle size and minimize agglomeration. Additionally, detailed characterization using UV-Vis spectroscopy, SEM, and EDX was conducted to verify the successful synthesis and purity of the silver nanoparticles. Antibacterial activity was further evaluated against *Total Coliform* and *Propionibacterium acnes* to confirm their potential for biomedical applications.

RESULTS AND DISCUSSION

Visual Confirmation of Silver Nanoparticle Formation

The initial visual indicator of silver nanoparticle (AgNP) formation was the change in color of the Neem extract and silver nitrate solution mixture. Upon mixing, the solution exhibited a rapid transition from pale yellow to dark brown within five minutes, which is characteristic of silver nanoparticle synthesis due to surface plasmon resonance (SPR). The color intensity increased with incubation time, confirming nanoparticle growth [32].

The SPR peak at 402 nm observed in this study aligns with previous reports on Neem-mediated AgNP synthesis, where similar peaks (400–420 nm) have been linked to spherical particle morphology and stable colloidal dispersion [33, 34]. However, unlike some earlier studies that reported broader peaks due to polydispersity, the sharp peak at 5 mM $AgNO_3$ suggests a relatively narrow size distribution, indicative of improved synthesis control in our method [35].

UV–Visible Spectroscopy

UV–Visible (UV-Vis) spectroscopy was employed to confirm the formation of silver nanoparticles and to study their optical properties at three different silver nitrate concentrations: 1 mM, 5 mM, and 10 mM (Figure 3.1). All samples exhibited a characteristic surface plasmon resonance (SPR) peak at 402 nm, which is indicative of the presence of silver nanoparticles and corresponds to their spherical morphology.

At 1 mM concentration (Figure 1a), a sharp absorption peak was observed at 402 nm with an absorbance value of 1.6, indicating successful synthesis but with moderate nanoparticle yield. Increasing the concentration to 5 mM resulted in a more intense absorption peak at the same wavelength (Figure 1b), with a maximum absorbance of 1.8, suggesting a higher nanoparticle concentration and improved synthesis efficiency. However, at 10 mM, the absorbance decreased to 1.4, even though the SPR peak remained at 402 nm (Figure 1c). This decline may be attributed to agglomeration or particle over-saturation, which can occur when the silver ion concentration exceeds the optimal threshold for stable nanoparticle formation.

The results demonstrate a clear correlation between silver ion concentration and nanoparticle formation efficiency. Specifically, absorbance increased from 1 mM to 5 mM, reflecting a greater number of nanoparticles, but declined at 10 mM, likely due to particle instability and clustering. Moreover, since smaller nanoparticles typically exhibit higher absorbance due to greater surface area-to-volume ratio, the findings also support the conclusion that 5 mM $AgNO_3$ yields smaller, more stable nanoparticles compared to the other concentrations. Based on the combination of peak intensity and stability, 5 mM was identified as the optimal concentration, and samples from this condition were used for further characterization.

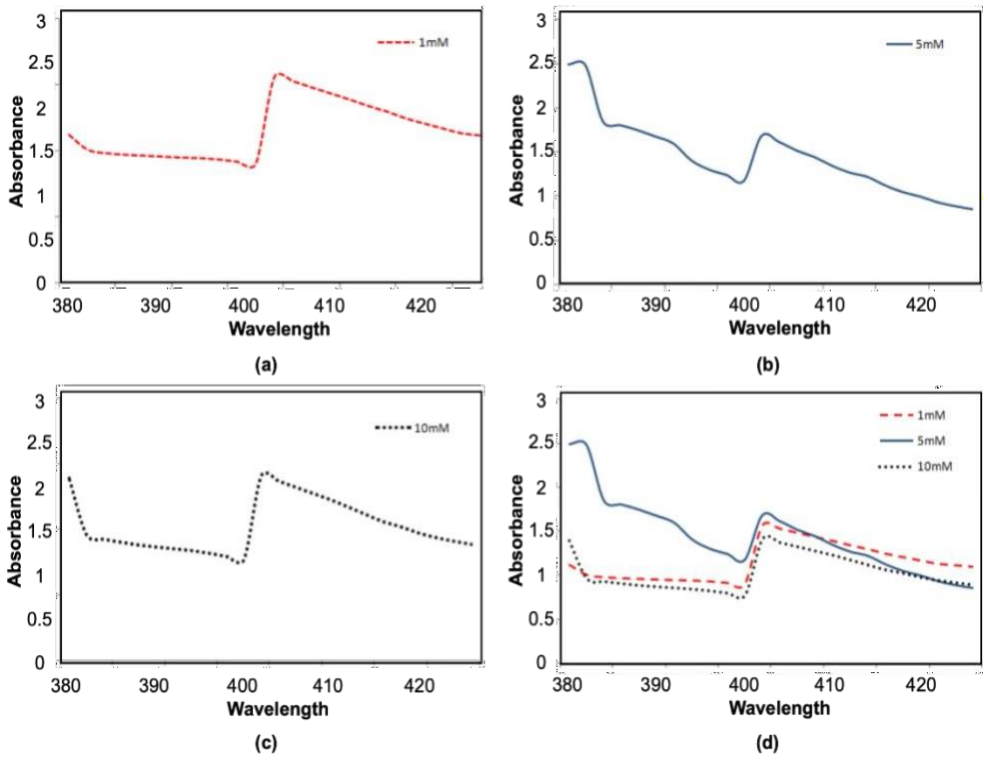

Figure 1. The UV-VIS spectroscopy spectrum of: (a) 1mM, (b) 5mM, (c) 10mM

Moreover, SEM analysis was carried out to investigate the morphology and size of silver nanoparticles synthesized using different concentrations of silver nitrate (1 mM, 5 mM, and 10 mM). At 1 mM, the nanoparticles predominantly exhibited a spherical shape, though some rod- like structures were also observed Figure 2. The presence of rod-shaped particles, while uncommon in green synthesis, suggests minor deviation in nucleation or growth dynamics under lower precursor concentration. The particle sizes ranged from 109.2 nm (Figure 2a) to 289.8 nm (Figure 2b), with an average diameter of approximately 325.1 nm. The irregularity in shape and relatively large size at this concentration indicates suboptimal synthesis conditions.

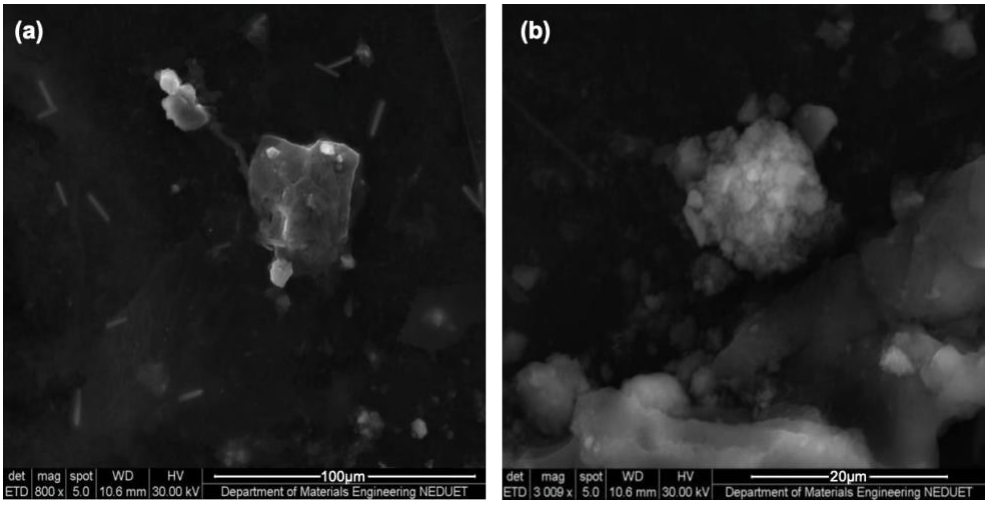

Figure 2. SEM analysis of silver nanoparticles synthesized using different concentrations of silver nitrate, (a–b) SEM images for 1 mM $AgNO_3$ showing primarily spherical nanoparticles with some rod-shaped structures at magnifications of 800X and 3009X, respectively.

The 5 mM sample produced the most desirable results, with SEM images (Figures 3a and 3b) showing uniformly distributed, spherical nanoparticles. The particles had diameters of 96 nm and 100 nm, with an average size of 98 nm. Some clustering was observed, likely due to the presence of biomolecules from the Neem extract acting as natural capping agents. Additional SEM images (Figures 3c and Figure 3d) confirmed the consistency of spherical morphology and narrow size distribution, reinforcing that 5 mM $AgNO_3$ is the optimal concentration for producing stable, monodispersed silver nanoparticles using green synthesis. Overall, the SEM results demonstrate that 5 mM silver nitrate yields the best combination of controlled shape, smaller particle size, and uniform morphology, making it the most suitable condition for further applications.

Earlier studies from demonstrated the impact of bacterial morphology on various disinfection efficacies [61-62], which aligns with the present investigation into morphology-dependent antibacterial responses to AgNPs. The SEM micrographs revealed that only the 5 mM $AgNO_3$ concentration yielded predominantly spherical nanoparticles (~98 nm), a morphology often associated with enhanced antibacterial efficacy due to higher surface energy [36, 37]. The absence of dendritic structures at this concentration contrasts with the

morphological deviations observed in other plant-mediated syntheses, where excess precursor concentration (>10 mM) accelerates nucleation and disrupts uniform growth [38, 39].

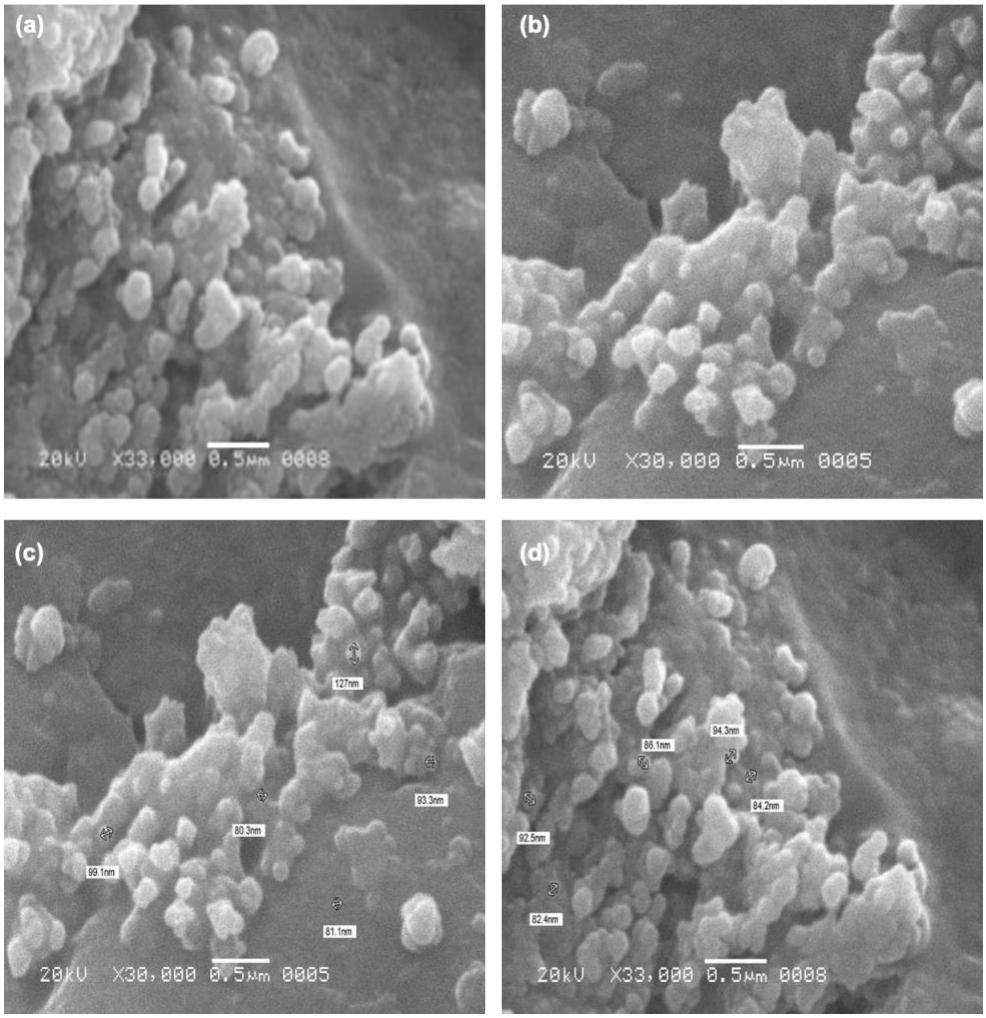

Figure 3. SEM analysis of silver nanoparticles synthesized using different concentrations of silver nitrate, SEM images for 5 mM $AgNO_3$ illustrating uniformly spherical nanoparticles with minimal agglomeration at higher magnifications (a) 33000X, (b) 30000X, (c) 30000X and (d) 33000X, with average particle sizes of 96.1 nm and 87.9 nm (a-d), respectively.

In the case of 10 mM, the nanoparticles exhibited dendritic and rod-shaped morphologies, as shown in Figure 4a and Figure 4b. These complex structures are typically associated with physical or chemical synthesis methods and are rarely observed in green synthesis. The particle diameters recorded were 195.3 nm and 146.4 nm, respectively, resulting in an average size of around 174 nm. The formation of such unusual structures at higher precursor concentrations may be due to rapid nucleation and uncontrolled particle growth.

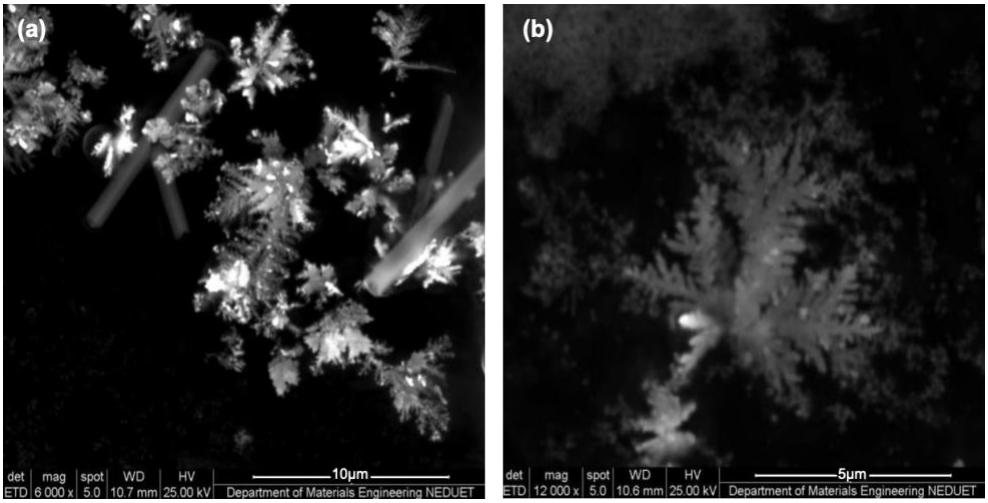

Figure 4. SEM images for 10 mM $AgNO_3$ displaying dendritic and rod-shaped nanoparticles at (a) 6000X and (b) 12000X magnification, indicating morphological changes at higher precursor concentration

Energy Dispersive X-ray (EDX) Analysis

EDX spectroscopy confirmed the elemental composition of the synthesized nanoparticles (Figure 5). A strong characteristic peak for silver was observed at 2.98 keV, affirming the successful reduction of silver ions to elemental silver. The analysis showed the presence of 100% pure silver with no significant contamination from other elements, validating the efficacy of the green synthesis method.

The EDX spectra confirming 100% elemental silver purity are noteworthy, as many plant-based syntheses report minor impurities from plant metabolites or environmental contaminants [40, 41]. This high purity underscores the efficiency of Neem phytochemicals as both reducing and capping agents, minimizing

unwanted secondary phases [42, 43]. The EDS spectrum (Figure 5) confirms the presence of Ag through its characteristic peak, while minor peaks of C, O, Na, S, and Cl originate from residual plant phytochemicals due to analysis over the full BSE image. This representative spectrum is considered adequate for elemental confirmation at this proof-of- concept stage, with spot EDS planned in future studies for refined compositional profiling.

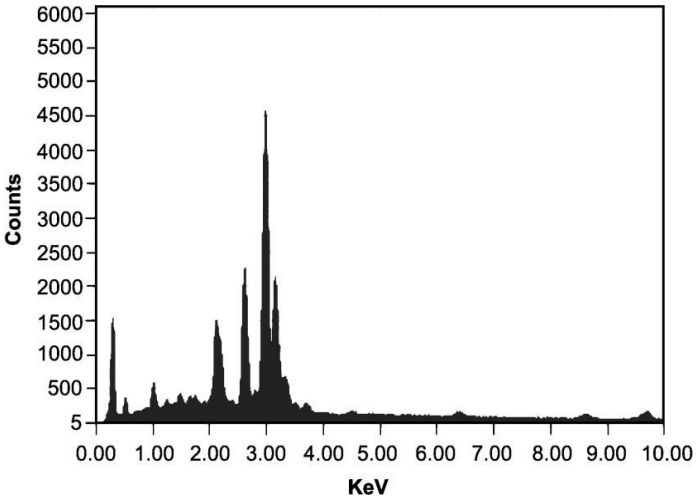

Figure 5. Energy-dispersive X-ray spectroscopy (EDS) spectrum of the synthesized Ag nanoparticles, showing a prominent Ag peak confirming their successful formation. Additional peaks corresponding to C, O, Na, S, and Cl are attributed to residual phytochemicals from the plant extract, as the spectrum was acquired over the entire BSE image.

Antibacterial Assay Results

By selecting one environmental bacterium (*T. coliform*) and one skin-associated opportunistic pathogen (*P. acnes*), the study assessed the broad-spectrum antibacterial potential of Neem- synthesized silver nanoparticles for skin wound care. This combination simulates real-world wound contamination scenarios: Environmental exposure (dirt, water, surfaces) tested with *T. Coliform* [44]. Endogenous skin bacteria turning pathogenic tested with *P. acnes* [45]. Testing against this bacterium assesses whether the antibacterial properties of the plant leaf extract attributed to its phytochemical compounds along with silver nanoparticles can synergistically prevent or treat infections that develop directly in skin and wound tissues [47, 48].

The results showed that silver nanoparticles, particularly in powdered form [49], effectively inhibited both bacteria, meaning they could help protect wounds from contamination and infection during the healing process. Neem extract alone also showed antibacterial activity, but the nanoparticles were more effective and longer lasting in their protection [23, 50].

Powdered synthesized silver nanoparticles (AgNPs) and neem (Azadirachta indica) based formulations typically outperform simple AgNP solutions against both Gram-positive and Gram-negative bacteria because they (i) maintain higher colloidal/surface stability, (ii) provide sustained and localized Ag^+ release at the cell–material interface, and (iii) add polyphenolic/terpenoid phytochemicals from neem that yield true multi-target synergy and reduce aggregation [51, 52].

AgNP solutions are prone to aggregation and oxidative changes in typical media (ionic strength, proteins), which reduces bioactive surface area and bactericidal performance; repeated bacterial exposure can even drive NP aggregation as a resistance strategy. Dry (powdered) AgNPs or solid-state/biocomposite formats preserve particle dispersion until contact with moisture, limiting pre-exposure aggregation and enabling higher effective surface contact on cells [51, 53, 54].

Therefore, powdered AgNPs has better stability. They are more consistent to cell-wall contact and ROS/protein–thiol interactions, especially on surfaces and in gels/agar, than the same particles stored and aged in liquid [54].

Bactericidal action correlates with controlled Ag^+ dissolution at the microbe material interface. Powdered/solid matrices (including coatings, composites, solid-state, green-synthesized powders) typically meter Ag^+ over time, maintaining inhibitory levels without rapid bulk dilution or scavenging that occurs in free colloids. Several recent studies on solid carriers/coatings show tunable, long-lasting Ag^+ release with superior inhibition zones compared with freely dispersed AgNPs [52, 55, 56]

Hence powdered synthesized AgNPs Sustained release helps maintain activity across growth phases in both Gram-positive and Gram-negative bacteria while limiting one-shot spikes that are neutralized by broth constituents [57].

Neem leaves/bark provide flavonoids, terpenoids (e.g., nimbin), tannins and quercetin-like polyphenols that (a) reduce and cap AgNPs (smaller, more stable particles), (b) perturb membranes/enzymes/DNA directly, and (c) inhibit biofilm and efflux, thereby potentiating silver. Green-synthesized or neem-infused AgNPs repeatedly show broader and stronger activity than either AgNPs or neem alone [18, 58]

Silver's multi-site mechanism (membrane disruption, metabolic/protein thiol binding, ROS, DNA damage) is not wall-type specific; neem's phytochemicals add outer-membrane permeabilization and quorum/biofilm interference helpful for Gram-negatives with lipopolysacchride barriers and for Gram-positives with thick peptidoglycan. Contemporary reviews confirm broad-spectrum efficacy and enhanced performance when AgNPs are combined with bio-actives [59].

Table 1 show that synthesized powdered (dry) silver nanoparticles, diluted silver nanoparticles, and Neem extract all showing bacterial inhibition properties. But powdered silver nanoparticles show better bacterial inhibition growth.

Table 1. Comparative antibacterial activity of synthesized powdered (dry) silver nanoparticles, diluted silver nanoparticles, and Neem extract.

Bacterial Assays	Time (Hrs)	Time Days	Powdered Silver Nanoparticles	Silver Nanoparticles solution + distilled water	Neem extract
T. cloriform (Gram-Negative)	0	0	-	-	-
	24	1	-	-	-
	48	2	-	-	-
	96	4	+++	+	+++
P. acne (Gram-Positive)	0	0	-	-	-
	24	1	-	-	-
	48	2	-	-	-
	96	4	-	-	-
	168	7	+++	+	++

"+++" = Clear inhibition zone observed (High antibacterial activity present)
"++" = Inhibition zone observed (Medium antibacterial activity present)
"+" = Inhibition zone observed (Minimum antibacterial activity present)
"–" = inhibition zone observed (no antibacterial activity)

Against *Total Coliform* Bacteria

The antibacterial activity of the synthesized silver nanoparticles against Total Coliform bacteria was assessed using the disc diffusion method (Figure 6). Observations were recorded at 24, 48, and 96 hours of incubation. At 24 and 48 hours, all three discs, containing silver nanoparticle powder (Disc 1), silver nanoparticle solution (Disc 2), and Neem extract (Disc 3), showed limited or no visible bacterial growth around the treated areas. By 96 hours, Disc 1 (silver nanoparticle powder) exhibited complete inhibition of bacterial growth, with a clear and well-defined zone of inhibition. Disc 2 (silver nanoparticle solution) showed slight bacterial regrowth, indicating moderate antibacterial activity. Disc 3 (Neem extract) also exhibited no bacterial

growth, suggesting that the plant extract retained antibacterial potential, though likely milder than nanoparticle treatments. These results confirm that silver nanoparticles, particularly in powdered form, have a strong inhibitory effect on Total Coliform bacteria, maintaining clear zones of inhibition over a 96-hour period.

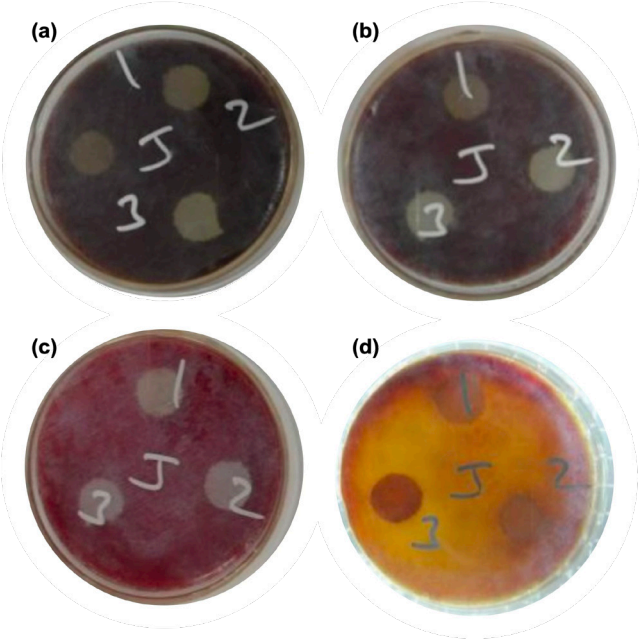

Figure 6. Antibacterial activity of silver nanoparticles and Neem extract against Total Coliform bacteria observed at different incubation times. (a) At 0 minutes showing initial placement of discs: 1 (silver nanoparticle powder), 2 (silver nanoparticle solution), 3 (Neem extract). (b) At 24 hours, showing early signs of bacterial inhibition. (c) At 48 hours, indicating progressive bacterial suppression around the treated discs. (d) At 96 hours, with clear zones of inhibition, particularly around Disc 1 (AgNP powder), confirming strong antibacterial efficacy.

Against Propionibacterium acnes

The antibacterial effect against *P. acnes* was evaluated over a similar incubation period (Figure 7), and up to 7 days, due to the slow-growing nature of this bacterium. At 24 and 48 hours, initial signs of inhibition were observed, but no significant difference between treatments was apparent. By 96 hours and especially at 7 days, Disc 1 (silver nanoparticle powder) and Disc 2 (silver nanoparticle solution) both demonstrated complete inhibition of

bacterial growth, as evidenced by clear zones around the discs. Disc 3 (Neem extract) also showed no bacterial growth after 7 days, although its inhibitory effect appeared delayed compared to the nanoparticle treatments. These findings indicate that both forms of synthesized silver nanoparticles exhibit effective antibacterial activity against *P. acnes*, with the powdered form showing slightly superior performance. Neem extracts also showed potential antimicrobial properties, though its activity may be slower or less potent.

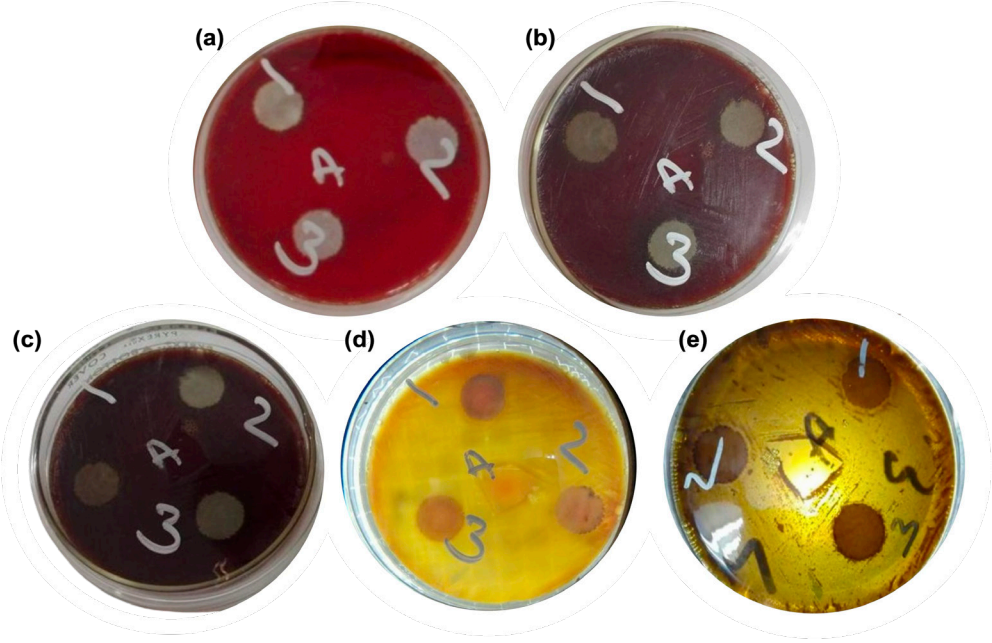

Figure 7. Antibacterial activity of silver nanoparticles and Neem extract against Propionibacterium acnes observed over time. (a) At 0 minutes showing placement of discs 1 (silver nanoparticle powder), 2 (silver nanoparticle solution), 3 (Neem extract), (b) At 24 hours with initial bacterial inhibition beginning to appear, (c) At 48 hours showing increased suppression around nanoparticle discs, (d) At 96 hours with clearer zones of inhibition, especially around Disc 1 and Disc 2, (e) After 7 days, exhibiting complete bacterial growth inhibition around all discs, confirming strong antimicrobial efficacy, particularly of the powdered silver nanoparticles.

The superior antibacterial performance of AgNP powder against *Total Coliform* and *P. acnes* can be attributed to its higher surface contact and potential for sustained ion release compared to colloidal forms, as supported by previous work demonstrating enhanced bacterial membrane disruption

with increased nanoparticle–cell wall interactions [3, 9, 32]. Furthermore, the slower yet observable inhibition by Neem extract alone reaffirms its intrinsic antimicrobial activity, likely driven by limonoids and flavonoids [60, 50], which may also synergistically enhance the bioactivity of the synthesized AgNPs. While earlier Neem-based AgNP syntheses have faced challenges in reproducibility and particle agglomeration due to fluctuating phytochemical profiles [27], our optimization of precursor concentration and reaction conditions resulted in monodispersed particles with stable morphology. This improvement addresses a key limitation highlighted in recent reviews, where the need for process standardization is emphasized for clinical translation of phytofabricated nanoparticles [23, 45].

These findings hold promise for developing biocompatible, non-toxic antimicrobial agents for wound healing and dermatological applications, areas where both AgNPs and Neem phytochemicals have demonstrated complementary bioactivities [3, 29]. The ability to produce high-purity, optimally sized particles through an eco-friendly route further strengthens the case for scaling up this approach for biomedical device coatings and environmental disinfection systems [5, 28].

CONCLUSIONS

The present study successfully demonstrated the green synthesis of silver nanoparticles using Azadirachta indica (Neem) leaf extract as a natural reducing and stabilizing agent. This eco-friendly and cost-effective method proved to be efficient in terms of reaction time, stability, and reproducibility, offering a cleaner and safer alternative to conventional chemical and physical synthesis techniques. The formation of silver nanoparticles was confirmed through UV–Visible spectroscopy, which showed a consistent SPR peak at 402 nm. SEM analysis revealed that the morphology and size of the nanoparticles were highly dependent on the silver nitrate concentration, with the most desirable spherical and uniformly distributed nanoparticles observed at 5 mM concentration, averaging 98 nm in diameter. EDX analysis further validated the presence of pure elemental silver with no detectable silver compounds, confirming complete reduction by the phytochemicals in the Neem extract. Antibacterial testing showed that the synthesized silver nanoparticles exhibited strong inhibitory effects against both Total Coliform bacteria and *P. acnes*, particularly in powdered form. Neem extract alone also demonstrated antimicrobial potential, though the nanoparticles were significantly more effective in inhibiting bacterial growth over extended incubation periods. Overall, the study confirms that Neem leaf extract is a powerful and sustainable agent

for the green synthesis of silver nanoparticles with excellent antibacterial properties. These findings highlight the potential of this method for biomedical and environmental applications where non- toxic, biocompatible nanomaterials are essential.

MATERIALS AND METHOD

Preparation of Neem Leaf Extract

Fresh Azadirachta indica (Neem) leaves were collected (Figure 8a), washed thoroughly with distilled water to eliminate any surface impurities, and then air-dried under sunlight. A total of 25 grams of the dried leaves were chopped into smaller pieces and boiled in 100 mL of distilled water for 15 minutes [30] (Figure 8b). The boiling process resulted in a yellow-colored solution, indicating the extraction of bioactive compounds [31]. After cooling to room temperature, the mixture was filtered using standard filter paper. The resulting filtrate, rich in phytochemicals, was stored at 6 °C and used as a reducing and stabilizing agent in the synthesis of silver nanoparticles

Green Synthesis of Silver Nanoparticles

Silver Nitrate Solution was prepared of 1mM, 5mM, and 10mM concentrations where 1mM Silver Nitrate solution contains 0.1699g of AgNO3 in 1000ml of distilled water. These solutions were each mixed with the Neem extract in a 1:6 ratio (extract to silver nitrate solution). Upon mixing, a rapid color change from pale yellow to dark brown was observed within five minutes (Figure 8c), indicating the reduction of silver ions and the formation of silver nanoparticles. To ensure complete synthesis and prevent photoactivation, the mixtures were incubated in the dark at room temperature for 24 hours.

Collection and Drying of Nanoparticles

After incubation for 24 hours, the silver nanoparticles were collected by centrifugation at 4000 rpm for 15 minutes. The supernatant was discarded, and the solid pellet was dried in a laboratory oven set at 50 °C. The supernatant was discarded and the solid mass was kept in an oven to dry, at 50 degree Celsius. The resulting dried product was a black powder, which was carefully collected using spatula and stored in airtight containers for further characterization and testing (Figure 8d).

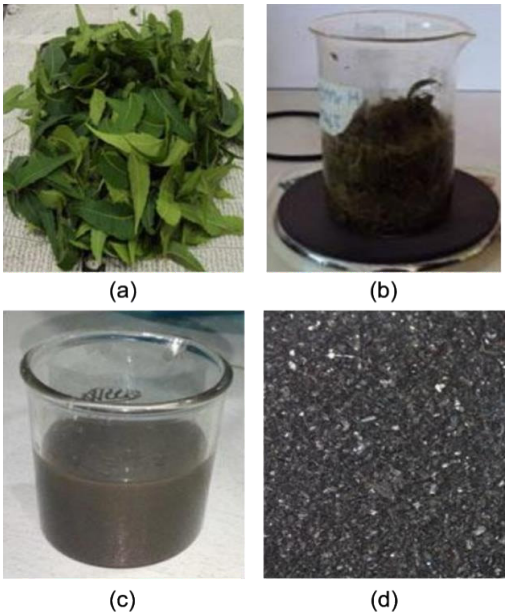

Figure 8. Visual representation of the green synthesis process of silver nanoparticles using Azadirachta indica (Neem) leaf extract, including (a) Collection phase, (b) Boiling phase, (c) Visualization of color change, (d) Stereo optical microscope image of black colored powder at 30X

Characterization of Silver Nanoparticles

The synthesized silver nanoparticles were characterized using three analytical techniques. UV–Visible spectroscopy (UV-Vis) was used to confirm nanoparticle formation by detecting the surface plasmon resonance (SPR) peak, typically centered around 402 nm. The UV–Vis absorption spectra were recorded using a Spectrum Lab 22 PC spectrophotometer operating in the range of 340–1000 nm with a spectral band width 6nm. Scanning Electron Microscopy (SEM) was employed to examine the morphology, size, and distribution of the nanoparticles, confirming their predominantly spherical shape with average diameters around 98 nm. The morphological analysis of the nanoparticles was performed using a JSM-6380A JEOL (JEOL Ltd., Japan) operated at an accelerating voltage of 5–15 kV under high-vacuum mode**.** In addition, Energy Dispersive X-ray (EDX) analysis verified the elemental composition of the samples, showing a distinct silver peak, which confirmed the presence and purity of the nanoparticles without contamination from other metals or compounds. Elemental composition was determined using JEOL Japan model number EX-54175JMU attached to the SEM, operating at 15 kV.

Antibacterial Testing

The antibacterial activity of the synthesized silver nanoparticles was evaluated using the disc diffusion method on blood agar medium. Two bacterial strains were selected for testing: *T. Coliform* and *P. acnes*. To prepare the blood agar, nutrient agar powder was dissolved in distilled water and heated until completely dissolved. The mixture was then autoclaved for 15 minutes. Once cooled to approximately 50 °C, 5% warm sheep blood was added to the medium, which was gently mixed to avoid air bubble formation. The prepared blood agar was poured into sterile petri dishes and allowed to solidify under aseptic conditions. For the antibacterial assay, each solidified agar plate was uniformly inoculated with one of the bacterial strains using sterile cotton swabs. Three types of discs were prepared for testing: one impregnated with silver nanoparticle powder, another with silver nanoparticle solution, and a third with Neem leaf extract. These were labeled as 1 (AgNP powder), 2 (AgNP solution), and 3 (Neem extract), respectively. The discs were gently pressed onto the agar surface to ensure firm contact. All plates were incubated at 37 °C under aerobic conditions, and bacterial growth inhibition was monitored at regular intervals. In this study, the antibacterial activity was assessed using the disc diffusion method. The evaluation was qualitative and based on the extent of clear inhibition zones observed around the discs impregnated with AgNP powder, AgNP solution, and Neem extract. To provide a comparative interpretation of the results, the inhibition zones were categorized into four levels: “+++” indicating high antibacterial activity with a prominent and clear zone; “++” indicating medium activity with a moderately visible zone; “+” indicating minimum activity with a faint inhibition zone; and “–” indicating no observable antibacterial activity. This scale was adopted in place of direct zone measurements (in mm) because the primary aim was comparative evaluation of treatment effectiveness rather than precise quantification. The formation of clear zones around the discs indicated antibacterial activity, allowing for comparative evaluation of the effectiveness of each treatment.

ACKNOWLEDGMENTS

The authors gratefully acknowledge the funding support provided by NED University of Engineering and Technology for this final year project. They also extend their sincere appreciation to the Department of Biomedical Engineering at Sir Syed University of Engineering and Technology and Universiti Teknologi Malaysia for their valuable guidance and assistance in refining the research and manuscript preparation

REFERENCES

1. Bayda, S., Adeel, M., Tuccinardi, T., Cordani, M., & Rizzolio, F. (2019). The history of nanoscience and nanotechnology: from chemical–physical applications to nanomedicine. *Molecules*, 25(1), 112.
2. Sati, A., Ranade, T. N., Mali, S. N., Ahmad Yasin, H. K., & Pratap, A. (2025). Silver nanoparticles (AgNPs): comprehensive insights into bio/synthesis, key influencing factors, multifaceted applications, and toxicity─ a 2024 update. *ACS omega*, 10(8), 7549-7582.
3. Aswathy Waliaveettil, F., & Anila, E. I. (2024). A Comprehensive Review on Antibacterial, Anti-Inflammatory and Analgesic Properties of Noble Metal Nanoparticles. *Particle & Particle Systems Characterization,* 41(5), 2300162.
4. Sadasivuni, K. K., Rattan, S., Waseem, S., Brahme, S. K., Kondawar, S. B., Ghosh, S., & Mazumdar, P. (2019). Silver nanoparticles and its polymer nanocomposites—Synthesis, optimization, biomedical usage, and its various applications. *Polymer nanocomposites in biomedical engineering,* 331-373.
5. Nguyen, N. P. U., Dang, N. T., Doan, L., & Nguyen, T. T. H. (2023). Synthesis of silver nanoparticles: from conventional to 'modern'methods—a review. *Processes*, 11(9), 2617.
6. Abbas, R., Luo, J., Qi, X., Naz, A., Khan, I. A., Liu, H., ... & Wei, J. (2024). Silver nanoparticles: Synthesis, structure, properties and applications. *Nanomaterials*, 14(17), 1425.
7. Zahoor, M., Nazir, N., Iftikhar, M., Naz, S., Zekker, I., Burlakovs, J., & Ali Khan, F. dsynthesis, and their potential roles in biomedical applications and water treatment. *Water*, 13(16), 2216.
8. Tourinho, P. S., Silva, A. R. R., Santos, C. S., Prodana, M., Ferreira, V., Habibullah, G., & Loureiro, S. (2022). Microplastic fibers increase sublethal effects of AgNP and AgNO3 in Daphnia magna by changing cellular energy allocation. *Environmental toxicology and chemistry,* 41(4), 896-904.
9. Xu, L., Wang, Y. Y., Huang, J., Chen, C. Y., Wang, Z. X., & Xie, H. (2020). Silver nanoparticles: Synthesis, medical applications and biosafety. *Theranostics*, 10(20), 8996.
10. David, L., & Moldovan, B. (2020). Green synthesis of biogenic silver nanoparticles for efficient catalytic removal of harmful organic dyes. *Nanomaterials*, 10(2), 2020.
11. Zhao, J., Ma, L., Zayed, M. E., Elsheikh, A. H., Li, W., Yan, Q., & Wang, J. (2021). Industrial reheating furnaces: A review of energy efficiency assessments, waste heat recovery potentials, heating process characteristics and perspectives for steel industry. *Process Safety and Environmental Protection,* 147, 1209-1228.
12. Szczyglewska, P., Feliczak-Guzik, A., & Nowak, I. (2023). Nanotechnology–general aspects: A chemical reduction approach to the synthesis of nanoparticles. *Molecules*, 28(13), 4932.

13. Sun, H., Jiang, C., Wu, L., Bai, X., & Zhai, S. (2019). Cytotoxicity-related bioeffects induced by nanoparticles: the role of surface chemistry. *Frontiers in Bioengineering and Biotechnology,* 7, 414.
14. Tsekhmistrenko, S. I., Bityutskyy, V. S., Tsekhmistrenko, O. S., Horalskyi, L. P., Tymoshok, N. O., & Spivak, M. Y. (2020). Bacterial synthesis of nanoparticles: A green approach. *Biosystems Diversity*, 28(1), 9-17.
15. Salem, S. S., & Fouda, A. (2021). Green synthesis of metallic nanoparticles and their prospective biotechnological applications: an overview. *Biological trace element research,* 199(1), 344-370.
16. Ullah, A., & Lim, S. I. (2022). Plant extract-based synthesis of metallic nanomaterials, their applications, and safety concerns. *Biotechnology and Bioengineering,* 119(9), 2273-2304.
17. Hano, C., & Abbasi, B. H. (2021). Plant-based green synthesis of nanoparticles: Production, characterization and applications. *Biomolecules*, 12(1), 31.
18. Alsaiari, N. S., Alzahrani, F. M., Amari, A., Osman, H., Harharah, H. N., Elboughdiri, N., & Tahoon, M. A. (2023). Plant and microbial approaches as green methods for the synthesis of nanomaterials: synthesis, applications, and future perspectives. *Molecules*, *28*(1), 463.
19. Wehrs, M., Tanjore, D., Eng, T., Lievense, J., Pray, T. R., & Mukhopadhyay, A. (2019). Engineering robust production microbes for large-scale cultivation. *Trends in microbiology*, 27(6), 524-537.
20. Sardella, D., Gatt, R., & Valdramidis, V. P. (2019). Metal nanoparticles for controlling fungal proliferation: quantitative analysis and applications. *Current Opinion in Food Science,* 30, 49-59.
21. Mateo, E. M., Mateo, F., Tarazona, A., & Jiménez, M. (2025). Engineered Metal Nanoparticles: A Possible Small Solution to Big Problems Associated with Toxigenic Fungi and Mycotoxins. *Toxins*, 17(8), 378.
22. Kumari, P., Devi, L., Kadian, R., Waziri, A., & Alam, M. S. (2025). Eco-friendly Synthesis of Azadirachta indica-based Metallic Nanoparticles for Biomedical Application & Future Prospective. *Pharmaceutical Nanotechnology,* 13(3), 448-464.
23. Kumari, P., Devi, L., Kadian, R., Waziri, A., & Alam, M. S. (2025). Eco-friendly synthesis of Azadirachta indica-based metallic nanoparticles for biomedical application & future prospective. *Pharmaceutical Nanotechnology*, 13(3), 448- 464.
24. Singh, V., Roy, M., Garg, N., Kumar, A., Arora, S., & Malik, D. S. (2021). An insight into the dermatological applications of neem: a review on traditional and modern aspect. *Recent Advances in Anti-Infective Drug Discovery* (Formerly *Recent Patents on Anti-Infective Drug Discovery*), 16(2), 94-121.
25. Lu, X. F., Lin, P. C., Zi, J. C., and Fan, X. N. (2019). Limonoids from Seeds of Azadirachta indica and Their Antibacterial Activity. *Zhongguo Zhong Yao Za Zhi* 44 (22), 4864–4873. doi:10.19540/j.cnki.cjcmm.20190813.202
26. Zanjage, A., & Khan, S. A. (2021). Ultra-fast synthesis of antibacterial and photo catalyst silver nanoparticles using neem leaves. *JCIS Open,* 3, 100015.
27. Ghazali, S. Z., Mohamed Noor, N. R., & Mustaffa, K. M. F. (2022). Anti-plasmodial activity of aqueous neem leaf extract mediated green synthesis-based silver nitrate nanoparticles. *Preparative Biochemistry & Biotechnology,* 52(1), 99-107.

28. Noor, A., Pant, K. K., Malik, A., Moyle, P. M., & Ziora, Z. M. (2025). Green Encapsulation of Metal Oxide and Noble Metal ZnO@ Ag for Efficient Antibacterial and Catalytic Performance. *Industrial & Engineering Chemistry Research*, 64(21), 10360-10372.
29. Suresh, N., Thomas, N. G., Mauramo, M., Waltimo, T., Sorsa, T., & Anil, S. (2025). Phytonanoparticles as novel drug carriers for enhanced osteogenesis and osseointegration. *Discover Nano*, 20(1), 11.
30. Sejali, S. N. F., & Anuar, M. S. (2011). Effect of drying methods on phenolic contents of neem (Azadirachta indica) leaf powder. *Journal of Herbs, Spices & Medicinal Plants,* 17(2), 119-131.
31. Ofongo, R. T., Ohimain, E. I., & Iyayi, E. A. (2021). Qualitative and quantitative phytochemical screening of bitter and neem leaves and their potential as antimicrobial growth promoter in poultry feed. *European Journal of Medicinal Plants,* 38-49.
32. Kim, D. H., Park, J. C., Jeon, G. E., Kim, C. S., & Seo, J. H. (2017). Effect of the size and shape of silver nanoparticles on bacterial growth and metabolism by monitoring optical density and fluorescence intensity. *Biotechnology and Bioprocess Engineering,* 22, 210-217.
33. Zanjage, A., & Khan, S. A. (2021). Ultra-fast synthesis of antibacterial and photocatalyst silver nanoparticles using neem leaves. *JCIS Open*, 3, 100015.
34. Ghazali, S. Z., Mohamed Noor, N. R., & Mustaffa, K. M. F. (2022). Anti-plasmodial activity of aqueous neem leaf extract mediated green synthesis-based silver nitrate nanoparticles. *Preparative Biochemistry & Biotechnology,* 52(1), 99-107.
35. Noor, A., Pant, K. K., Malik, A., Moyle, P. M., & Ziora, Z. M. (2025). Green Encapsulation of Metal Oxide and Noble Metal ZnO@Ag for Efficient Antibacterial and Catalytic Performance. *Industrial & Engineering Chemistry Research*, 64(21), 10360-10372.
36. Sati, A., Ranade, T. N., Mali, S. N., Ahmad Yasin, H. K., & Pratap, A. (2025). Silver nanoparticles (AgNPs): comprehensive insights into bio/synthesis, key influencing factors, multifaceted applications, and toxicity– a 2024 update. *ACS Omega*, 10(8), 7549-7582
37. Kim, D. H., Park, J. C., Jeon, G. E., Kim, C. S., & Seo, J. H. (2017). Effect of the size and shape of silver nanoparticles on bacterial growth and metabolism by monitoring optical density and fluorescence intensity. *Biotechnology and Bioprocess Engineering,* 22, 210-217.
38. Restrepo, C. V., & Villa, C. C. (2021). Synthesis of silver nanoparticles, influence of capping agents, and dependence on size and shape: A review. *Environmental Nanotechnology, Monitoring & Management,* 15, 100428.
39. Ullah, A., & Lim, S. I. (2022). Plant extract-based synthesis of metallic nanomaterials, their applications, and safety concerns. *Biotechnology and Bioengineering,* 119(9), 2273-2304.
40. Salem, S. S., & Fouda, A. (2021). Green synthesis of metallic nanoparticles and their prospective biotechnological applications: an overview. *Biological Trace Element Research*, 199(1), 344-370.

41. Guilger-Casagrande, M., & Lima, R. D. (2019). Synthesis of silver nanoparticles mediated by fungi: a review. *Frontiers in Bioengineering and Biotechnology*, 7, 87/
42. Kumari, P., Devi, L., Kadian, R., Waziri, A., & Alam, M. S. (2025). Eco-friendly synthesis of Azadirachta indica-based metallic nanoparticles for biomedical application & future prospective. *Pharmaceutical Nanotechnology*, 13(3), 448-464.
43. Zainurin, M. A. N., & Zainol, I. (2022). Biogenic synthesis of silver nanoparticles using neem leaf extract as reducing agent and hydrolyzed collagen as stabilizing agent. *Malaysian Journal of Microscopy*, 18(1).
44. Bai, V. R., Kit, A. C., Kangadharan, G., Gopinath, R., Varadarajan, P., & Hao, A. J. (2022). Experimental study on total coliform violations in the complied NH2CL, O3, and UV treated municipal water supply system. *The European Physical Journal Plus*, *137*(6), 689.
45. Perry, A., & Lambert, P. (2011). Propionibacterium acnes: infection beyond the skin. *Expert Review of Anti-Infective Therapy,* 9(12), 1149–1156. https://doi.org/10.1586/eri.11.137
46. Sadia, Fazilah Abd Manan, Norjihada Izzah Ismail, Saravana Kumar Jaganathan, Syafiqah Saidin; *Extraction of bioactive compounds from Moringa oleifera leaves using different organic solvents.* AIP Conf. Proc. 2 June 2023; 2601 (1): 020046. https://doi.org/10.1063/5.0129684
47. Sadia, F. A. M., Ismail, N. I., Jaganathan, S. K., & Saidin, S. (2023). *Extraction of bioactive compounds from Moringa oleifera leaves using different organic solvents.* AIP Conference Proceedings, 2601(1), 020046. https://doi.org/10.1063/5.0129684
48. Andreica, A.M, Vlassa, M.C, R. Carpa, I. Petean, Green Synthesis of Silver Nanoparticles Using Galium Verum L. Aqueous Extract and Evaluation of its Antimicrobial Activity, *Studia UBB Chemia,* 2025, 70 (1), 87-100. https://doi.org/10.24193/subbchem.2025.1.06
49. Sadia, M., Mohd Zaki, M.A., Jaganathan, S.K. et al. Blending of Moringa oleifera into Biodegradable Polycaprolactone/Silver Electrospun Membrane for Hemocompatibility Improvement. *Arab J Sci Eng*, 48, 7323–7336 (2023). https://doi.org/10.1007/s13369-023-07736-6
50. Wylie, M. R., & Merrell, D. S. (2022). The antimicrobial potential of the neem tree Azadirachta indica. *Frontiers in Pharmacology*, 13, 891535.
51. Ershov VA, Ershov BG. (2024). Oxidative Dissolution and the Aggregation of Silver Nanoparticles in Drinking and Natural Waters: The Influence of the Medium on the Process Development. *Toxics*, Oct 18; 12(10):757. doi: 10.3390/toxics12100757
52. Kara, I. (2024). Use of geopolymers as tunable and sustained silver ion release mediums. *Sci Rep,* 14, 8606. https://doi.org/10.1038/s41598-024-59310-1
53. Hochvaldová, L., Panáček, D., Válková, L. et al. (2024). E. coli and S. aureus resist silver nanoparticles via an identical mechanism, but through different pathways. *Commun Biol*, 7, 1552. https://doi.org/10.1038/s42003-024-07266-3
54. Roberto Vazquez-Muñoz, Nina Bogdanchikova, and Alejandro Huerta-Saquero. (2020). Beyond the Nanomaterials Approach: Influence of Culture Conditions on the Stability and Antimicrobial Activity of Silver Nanoparticles, *ACS Omega,* 5 (44), 28441-28451, DOI: 10.1021/acsomega.0c02007

55. Liu, J., Sonshine, D. A., Shervani, S., & Hurt, R. H. (2010). Controlled release of biologically active silver from nanosilver surfaces. *ACS Nano*, 4(11), 6903–6913. https://doi.org/10.1021/nn102272n
56. Dube, E., & Okuthe, G. E. (2025). Silver nanoparticle-based antimicrobial coatings: Sustainable strategies for microbial contamination control. *Microbiology Research*, 16(6), 110. https://doi.org/10.3390/microbiolres16060110
57. Wang, L., Periyasami, G., Aldalbahi, A., & Fogliano, V. (2021). The antimicrobial activity of silver nanoparticles biocomposite films depends on the silver ions release behaviour. *Food Chemistry,* 359, 129859. https://doi.org/10.1016/j.foodchem.2021.129859
58. Barik, B., Satapathy, B. S., Pattnaik, G., Bhavrao, D. V., & Shetty, K. P. (2024). Sustainable synthesis of silver nanoparticles from Azadirachta indica: Antimicrobial, antioxidant and in silico analysis for periodontal treatment. *Frontiers in Chemistry*, 12, 1489253. https://doi.org/10.3389/fchem.2024.1489253
59. Rodrigues, A. S., Batista, J. G., Rodrigues, M. Á., Thipe, V. C., Minarini, L. A., Lopes, P. S., & Lugão, A. B. (2024). Advances in silver nanoparticles: A comprehensive review on their potential as antimicrobial agents and their mechanisms of action elucidated by proteomics. *Frontiers in Microbiology*, 15, 1440065. https://doi.org/10.3389/fmicb.2024.1440065
60. Lu, X. F., Lin, P. C., Zi, J. C., & Fan, X. N. (2019). Limonoids from Seeds of Azadirachta indica and Their Antibacterial Activity. *Zhongguo Zhong Yao Za Zhi*, 44(22), 4864–4873.
61. Sheikh, J., Tan, T. S., Saidin, S., Ahmed, S., & Chua, L. S. (2024). Bacterial morphology and microscopic advancements: navigating from basics to breakthroughs. *Microbiol Immunol Commun*, 3, 03-41.
62. Swee, T., Sheikh, J., Saidin, S., Serrano Olmedo, J., Agha, S. & Salim, M. (2025). Chamber design and intensity-modulated ultraviolet-C LEDs for advanced pulsed photonic disinfection. *Biomedical Engineering / Biomedizinische Technik.* https://doi.org/10.1515/bmt-2025-0070

STUDIA UBB CHEMIA, LXX, 3, 2025 (p. 107-114)
(RECOMMENDED CITATION)
DOI:10.24193/subbchem.2025.3.07

INFLUENCE OF DIFFERENT SWEETENERS ON THE TOTAL ANTHOCYANIN CONTENT OF HOMEMADE FOREST FRUIT JAM

Bianca MOLDOVAN[a], Luminița DAVID[a, *]

ABSTRACT. Anthocyanins, natural water-soluble pigments, responsible for the red, purple and blue colors in many fruits, are valued for their nutritional properties in fruit-based food products such as jams. However, their stability during storage is influenced by various factors among which the type of sweetener used to obtain these jams plays an important role. The present study aims to evaluate the impact of different sweeteners – sucrose, fructose, xylitol and aspartame – on anthocyanins' degradation in homemade forest fruit jams during storage. Results indicate that xylitol offers the highest anthocyanins retention, the rate constant of the degradation process of the investigated pigments being k = 0.0124 days^{-1}. Sucrose and fructose demonstrated a similar protective effect presenting comparable values of the degradation process of anthocyanins in their presence ($k_{sucrose}$ = 0.0184 days^{-1} and $k_{fructose}$ = 0.0196 days^{-1}). The use of aspartame, a non-caloric sweetener, was associated with significantly higher degradation rate of anthocyanins over time. Overall, the choice of sweetener plays the critical role in preserving anthocyanins content in the homemade forest fruit jam with important implications for product quality, shelf-life and nutritional value.

Keywords: *forest fruits, sweeteners, anthocyanins, antioxidant activity.*

INTRODUCTION

Forest fruits, such as blueberries, raspberries, blackberries, blackcurrants and strawberries, are highly valued for their rich content of anthocyanins and other antioxidant compounds which contribute to their vibrant colour and well

[a] *Babeş-Bolyai University, Faculty of Chemistry and Chemical Engineering, 11 Arany Janos Str., RO-400028, Cluj-Napoca, Romania*
* *Corresponding author: luminita.david@ubbcluj.ro*

documented health benefits, making them valuable for their functional potential in health promoting foods. Jams made from forest fruits are a popular way to preserve these seasonal products but the heat treatment and formulation involved in jam production can lead to significant degradation of their bioactive compounds. Various factors, including pH, temperature, light and the type of sweetener can influence the preservation of anthocyanins and other antioxidant compounds [1].

Anthocyanins, a subgroup of flavonoids, are potent natural antioxidants associated with a range of biological activities including anti-inflammatory, cardioprotective and neuroprotective effects [2]. These compounds are particularly sensitive to processing and storage conditions, making their stability a critical factor in the development of functional food products such as jams.

Sweeteners are among the most influential formulation variables in jam production, not only affecting taste and texture but also potentially altering the chemical composition of the food matrix containing antioxidant compounds. While sucrose (table sugar) is widely used as the standard sweetener in jam making, increasing consumer demand for healthier, low calorie alternatives has led to the use of artificial or natural sugar substitutes, such as aspartame, polyols or other monosaccharides like fructose or tagatose. These sweeteners differ in chemical structure, sweetness intensity, metabolic impact and interaction with other components of the food matrix and can influence the stability of anthocyanins and the overall antioxidant potential of the final product during processing or storage. For example, fructose is known to participate in Maillard reaction that can degrade antioxidants [3] whereas sugar alcohols like xylitol may offer a more stable environment. Artificial sweeteners, such as aspartame, despite their low caloric profile, may also impact the thermal and chemical stability of phenolic compounds.

The present study aimed to evaluate the influence of four commonly used sweeteners (sucrose, aspartame, fructose and xylitol) on the stability of anthocyanins and antioxidant activity of forest fruit jam during storage. By evaluating changes of total anthocyanins content and antioxidant capacity of the investigated jam, this research seeks to provide a better understanding of how sweeteners choice can affect the nutritional and functional properties of fruit preserves, providing relevant information both for industrial food formulations and consumers who are constantly looking for healthier and functional food options.

RESULTS AND DISCUSSION

Anthocyanins are water soluble flavonoid pigments responsible for the red, purple and blue hues in various forest fruits [4]. Their stability is crucial for maintaining the colour and the nutritional quality of fruit-based products, such as jams. Understanding their degradation pathways and kinetics during processing and storage is essential for optimizing the preservation methods of these highly-consumed fruit derived food products. Storage conditions, including temperature, duration and composition of the food matrix significantly affect the stability of these high valued bioactive compounds present in fruits [5].

The composition of jams typically includes a blend of fruits, sweetener (sucrose or alternatives) and, depending on natural pectin fruit level, a gelling agent. As the sweetener is the main additive in these fruit derived products, the stability of anthocyanins in forest fruit jams is significantly influenced by the type and concentration of this ingredient. Anthocyanins' degradation kinetics in various food products, such as beverages and jams, typically follows a first order kinetic model, the rate of degradation being proportional to the anthocyanin concentration [6].

In order to evaluate the influence of different sweeteners on the variation of total anthocyanin content of homemade forest fruits jam, the total anthocyanin content of an alcoholic extract obtained from jams stored at room temperature was spectrophotometrically monitored at 520 nm for 56 days.

The obtained data were successfully fitted to a first order kinetic model (Figure 1), enabling us to calculate the degradation kinetic parameters, rate constants and half-lives, of the anthocyanins in the investigated jams.

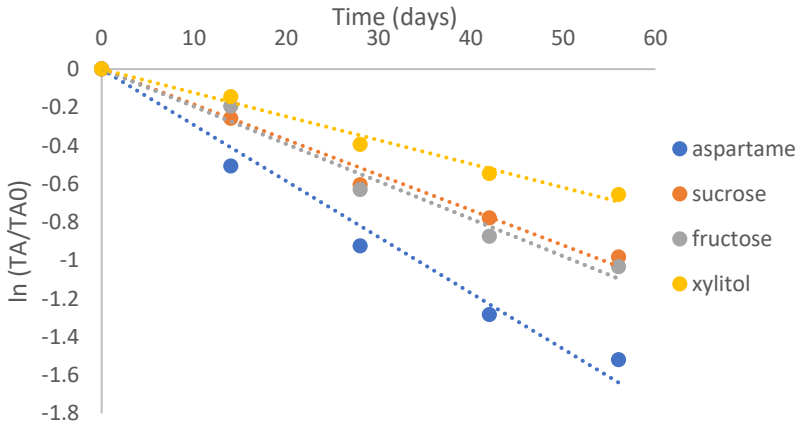

Figure 1. Degradation plots of anthocyanins from forest fruit jam in the presence of various sweeteners

Anthocyanins present in the forest fruit jam prepared with xylitol presented the highest stability over time. After 56 days of storage, the xylitol sweetened forest fruit jam lost 48% of its total anthocyanin content. The rate constant of the degradation of anthocyanins in the presence of this sweetener was ~1.5 fold lower than that obtained for sucrose (Table 1), recommending xylitol as a suitable sweetener in functional and low-calorie food products. Our results were in accordance with those obtained in previous studies concerning anthocyanins stability in blackberry jam [7], which demonstrated that anthocyanins degrade more slowly in the presence of xylitol compared to other sweeteners. Unlike reducing sugars, such as fructose, xylitol does not participate in Maillard reaction, which can degrade phenolics and reduce antioxidant levels and does not generate pro-oxidative intermediates during storage. Its non-reducing nature and chemical stability make it a favourable alternative to sucrose or fructose in the production of functional, low-sugar jams.

Using aspartame as sweetener for the forest fruit jam resulted in an accelerate anthocyanins degradation, the loss of total anthocyanin content being of 78% after 56 days (Table 1), demonstrating that aspartame was not able to preserve the colour intensity of the jam as well as carbohydrates and polyols. Aspartame tends to accelerate anthocyanin degradation, especially in acidic environments, being unstable in low pH overtime, especially below pH = 4, the typically pH of the forest fruit jams [8], acidic pH where anthocyanins are more stable. During heat processing, applied by jam preparation, aspartame degrades into aspartic acid, phenylalanine and methanol, which will further affect anthocyanins' stability [9]. Unlike sucrose or xylitol, aspartame does not reduce water activity [10] or significantly interact with anthocyanins, via hydrogen bonding, to protect their structure.

Compared to sucrose (non-reducing sugar) or xylitol (a sugar alcohol), fructose led to a faster degradation process of the anthocyanins in forest fruits jam (Table 1). Being a reducing sugar, fructose participates in Maillard reaction especially during thermal processing, Maillard intermediates degrading anthocyanins [11,12]. Unlike polyols, such as xylitol, fructose lacks the molecular structure to stack for co-pigmentation reactions of anthocyanins, process that also enhance the stability of these health promoting compounds [13].

Anthocyanins' degradation involves several pathways including hydrolysis, oxidation and condensation. Numerous degradation studies have identified the formation of various degradation products such as phenolic acids, which can contribute to changes in antioxidant properties of the anthocyanins containing food products during processing and storage [14, 15].

Table 1. Kinetic parameters of anthocyanins' degradation in the presence of various sweeteners

Sweetener	k (days^{-1})*	$t_{1/2}$ (days)	$t_{1/2}$ / $t_{1/2\ sucrose}$
Sucrose	0.0184 (0.9834)	37.66	1
Fructose	0.0196 (0.9745)	35.35	0.94
Xylitol	0.0124 (0.9828)	55.88	1.48
Aspartame	0.0293 (0.9745)	23.65	0.63

* Numbers in parentheses are the correlation coefficients.

CONCLUSIONS

The present study reports the influence of different caloric and non-caloric sweeteners (sucrose, fructose, xylitol and aspartame) on the variation of total anthocyanin content of homemade forest fruit jam during storage for 56 days at room temperature. In all cases, the degradation process of anthocyanins follows mainly a first order kinetics (but other paths might also interfere). Among the tested sweeteners significant differences were observed in the rate of anthocyanin degradation, confirming the sensitivity of these pigments to the jam matrix components. The most deleterious effect on anthocyanin stability was noticed for aspartame ($t_{1/2}$ = 23.65 days), while xylitol presented the best stabilizing effect on these dyes ($t_{1/2}$ = 55.88 days). Overall, the results indicate that the choice of sweetener plays a critical role in the long-term anthocyanin retention in fruit-based products. For low-caloric jam formulations aiming to maximize color and nutritional properties stability, xylitol can be used as an effective sweetener while aspartame should be used cautiously in anthocyanin rich food products.

EXPERIMENTAL SECTION

Chemicals and reagents

All chemicals and reagents were purchased from Merck (Darmstadt, Germany), not needing purification.

Preparation of jams

A mixture of frozen forest fruits (blueberries, strawberries, black currants, raspberry and blackberries) was purchased from a local supermarket and stored at -18°C until used for jam preparation.

In order to obtain the fruit purees necessary for making jams, 900 g of frozen berries were crushed for 2 minutes in a 2L blender at 3.500 rpm. The obtained mixture was further boiled for approximately 30 minutes together with the sweetener and the gelling agent (pectin with added citric acid to correct the acidity). Four sweeteners were used to obtain various jam formulations given in Table 2:

Table 2. Formulations of the forest fruit jams

Formulation	**1**	**2**	**3**	**4**
Fruit puree (g)	200	200	200	200
Sucrose (g)	100	-	-	-
Fructose (g)	-	75	-	-
Aspartame (g)	-	-	0.5	-
Xylitol (g)	-	-	-	100
Pectin (g)	4	4	4	4

The amount of added sweetener was chosen in such a way as to maintain the same intensity of the sweet taste of the obtained jam in all cases (regardless of the sweetener used in the preparation of the jam).

Sample storage conditions

Jams were stored in sealed glass jars at ambient temperature (22±2 °C) and protected from direct light. Over a 56-days period, samples were collected at designated time intervals (day 0, 14, 28, 42 and 56) to monitor anthocyanins degradation.

Extraction of anthocyanins from forest fruit jams

At each time point, 5 g of each jam formulation were mixed with 20 ml ethanol and stirred for 1 hour at room temperature. The obtained extract resulted after vacuum filtration of the mixture was further used to evaluate the total anthocyanin content of the investigated jams.

Evaluation of total anthocyanin content

Determination of the total anthocyanin content was conducted according to the pH-differential method of Giusti and Wrolstad [4]. Briefly, 0.5 mL of extract were mixed with 3.5 mL of buffer solution (pH = 1 potassium chloride/HCl and pH = 4.5 sodium acetate/acetic acid). After 15 minutes, the samples were spectrophotometrically analyzed and absorbances were read

in triplicate, against a buffer blank, at 520 and 700 nm, using a Perkin Elmer Lambda 25 UV-Vis spectrophotometer. The total anthocyanin content was calculated and expressed as mg cyanidin-3-O-glucoside/L of extract.

Changes in anthocyanin concentration over time were use to determine the kinetic parameters of the degradation process of these pigments during storage.

Kinetic analysis

Anthocyanins' degradation was modeled as a first order kinetic process. The natural logarithm of the relative anthocyanin concentration, at each time point, was plotted against storage time in days. The rate constant k (days^{-1}) was calculated from the slope of the linear regression, according to eq. 1. A minimum correlation coefficient of 0.95 was considered acceptable for confirming the first order kinetics.

$$\ln[TA/TA_0] = -kt \qquad \text{(eq. 1)}$$

The degradation half-life $t_{1/2}$ in days was calculated using eq. 2:

$$t_{1/2} = -\ln 0.5/k \qquad \text{(eq. 2)}$$

where: $t_{1/2}$ = half-life (days); k = reaction rate constant (days^{-1}).

REFERENCES

1. R. N.Cavalcanti, D.T. Santos,M. A.A. Meireles, *Food Research International*, **2011**, *44*, 499-509
2. H. Xue, Y. Sang, Y. Gao, Y. Zeng, J. Liao, J. Tan, *Antioxidants*, **2022**, *12*, 3
3. C. Buvé, H. T. T. Pham, M. Hendrickx, T. Grauwet, A. Van Loey, *Comprehensive Reviews in Food Science and Food Safety*, **2021**, *20*, 5698-5721
4. B. Moldovan, A. Hosu, L. David, C. Cimpoiu, *Acta Chimica Slovenica*, **2016**, *63*, 213-219
5. B. Moldovan, L. David, *Foods*, **2020**, 1266
6. L.G. Santos, V. H. Martins, *Journal of Food Processing and Preservation*, **2022**, *46*, e17161
7. C. Benedek, Z. Bodor, V. T. Merrill, Z. Kokai, A. Gere, Z. Kovacs, I. Dalmadi, L. Abranko, *European Food Research and Technology*, **2020**, *246*, 2187-2204
8. M. S. Rana, F. Yeasmin, M. J. Khan, M. H. Riad, *Food Research*, **2021**, *5*, 225-231
9. J. Trawinski, R. Skibinski, *Food Research International*, **2023**, *173*, 113365

10. M. F. Gliemmo, A. M. Calvino, O. Tamasi, L. N. Gherschon, C. A. Campos, *LWT-Food Science and Technology*, **2008**, *41*, 611-619
11. A. Shakoor, C. Zhang, J. Xie, X. Yang, *Food Chemistry*, **2022**, *393*, 133416
12. D. B. Rodriguez-Amaya, J. Amaya-Farfan, *Vitamins and Hormones*, **2024**, *125*, 149-182
13. W. Pang, H. Zhao, D. Li, Y. Li, C. Liu, R. Yu, *International Journal of Food Science and Technology*, **2024**, *59*, 1299-1313
14. J. Dong, S. Li, J. Zhang, A. Liu, J. Ren, *Food Chemistry*, **2022**, *370*, 131018
15. K. Keppler, C.-U. Humpf, *Bioorganic & Medicinal Chemistry*, **2005**, *13*, 5195-5205

STUDIA UBB CHEMIA, LXX, 3, 2025 (p. 115-127)
(RECOMMENDED CITATION)
DOI:10.24193/subbchem.2025.3.08

ASYMMETRIC, WATER-SOLUBLE CYANINE DYES: SYNTHESIS AND FLUORESCENT PROBE FOR THE Fe^{3+} ION

Xinyu DUAN[a], Weijian LI[a], Yanan NIU[a], Aihong HAN[a,*]

ABSTRACT. Two known symmetric and four novel asymmetric water-soluble pentamethyl cyanine dyes were synthesized and fully characterized by IR, MS and NMR. These dyes exhibited good water solubility and possessed good stability at different pH environment. On the basis of investigation toward the change of U-vis absorption spectra under heat or illumination, these results indicated that the asymmetric cyanine dyes have better photo-thermal stability than that of symmetric dyes under the state of solution, which was also proved by the results of thermogravimetric analysis (TGA). Meanwhile, the researches on the fluorescent probes for metal ions detection demonstrated that the dyes can be considered as a fluorescent probe for detection of Fe^{3+} ion, and the anti-interference experiments displayed that the dye exhibits excellent selectivity towards Fe^{3+} ion over other common metal cations (Cr^{3+}, Zn^{2+}, Ni^{2+}, Al^{3+}, Mg^{2+}, Cu^{2+}).

Keywords: *chemical sensor, ferric ion, fluorescent probe, cyanine dyes, near-infrared dyes.*

INTRODUCTION

Owing to the unique optical properties and the easy chemical modification of their molecular structures of cyanine dyes, it has been attracting the researcher's development interest [1-5], which leads to its diversity of molecular structure, and the new application fields have been developing besides for traditional application. Especially in recent years, a lot of breakthroughs are

[a] *College of Chemistry and Chemical Engineering, Shenyang Normal University, Shenyang, 110034, China*
* *Corresponding author: hanhong@hotmail.com*

reported in the field of medicine [6-10] and fluorescent probes [11, 12], which puts forward specific requirements for the structure and performance of cyanine dyes under the consideration of application, because the solubility and stability is especially critical, so it becomes a research hot point for the preparation of water-soluble cyanine dyes, and their photo-thermal stability is also improved on the basis of the structural modification [13, 14]. In order to apply as fluorescent probe for detection of metal ions in aqueous media, in the paper, four novel asymmetric cyanine dyes with the better water solubility and stability are designed and synthesized, the hydrophilic character of dyes are enhanced through introducing sulfonate groups, while the photo-thermal stability of the dye can be improved due to the design of asymmetric structure. As known, the component containing the nitrogen hetero-cycle has more influence toward its properties in the molecular structure of cyanine dyes, and the cyanine dye with indole cycle is the most stability [15, 16], therefore, in this study, 2,3,3-trimethylindolenine was selected as a raw material. Firstly, the hydrophilic sulfonate group is introduced through the reaction with sulfophactone, and then the intermediate was further reacted with different modified indolium salts under the presence of malonaldehyde dianilide hydrochloride, two known symmetric and four novel asymmetric water soluble cyanine dyes were successfully synthesized (as illustrated in Scheme 1).

Many researches have proved that it is an effective method to detect the cations and anions utilizing fluorescent probes technique [17, 18], and a variety of NIR dyes have been utilized as a sensor for the detection of the Fe^{3+} ion[19-21]. However, because of poor selectivity and solubility in aqueous media for present chemical sensor, their application scope is restricted. Herein, a novel cyanine dyes were investigated as the fluorescent probe for the detection of Fe^{3+} ion, and it exhibited the notable characters of highly sensitive, selective sensing under the aqueous environment.

RESULTS AND DISCUSSION

The Synthesis of Cyanine Dyes

As shown in Scheme 1, through the reaction of the two sultones (1,3-propanesultone or 1,4-butanesultone) with 2,3,3-trimethylindolenine, the two intermediates of indolium quaternary salts were conveniently prepared under the condition of 1,2-dichlorobenzene solvent and high temperature(150℃), after purification, further condensation with hemi-molar quantity of malonaldehyde dianilide hydrochloride in the presence of sodium acetate and acetic anhydride,

two known symmetric, water soluble cyanine dyes (**Ia** and **IIa**) were synthesized [22, 23], and while three components of malonaldehyde dianilide hydrochloride, *N*-alkylindolium and sulfonated indolium[24] was mixed at equimolar quantity, four novel asymmetric, water soluble cyanine dyes with different chain lengths were obtained (seeing supplementary information in detail), their maximum absorption wavelength was observed at about 650 nm (in DMF), and their spectroscopic data are summarized in Table 1.

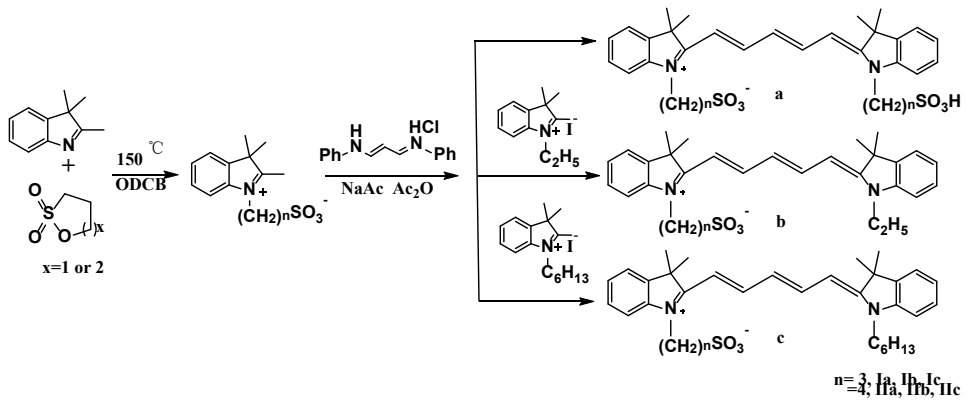

Scheme 1. The synthesis route of cyanine dyes

Table 1. Spectroscopic data of six prepared dyes in methanol

Dye	**Ia**	**Ib**	**Ic**	**IIa**	**IIb**	**IIc**
λ_{ab} (nm)	642	642	642	642	642	642
λ_{em} (nm)	721	722	726	718	721	718
Stokes shift (nm)	79	80	76	74	79	74

The measurement results show that the all six dyes exhibit almost same maximum absorption and emission wavelength, which indicates that the structural differences do not affect the spectral performance, meanwhile, the highest value of Stokes shift was also summarized in Table 1. And the larger the Stokes shift, the more favorable the reducing interference of background fluorescence, it indicates that these cyanine dyes have great potential applications in fluorescence labeling and multi-color imaging.

As a functional material, the stability is the important parameter under the consideration for its application, meanwhile, in order to assess the effect of molecular structure on the stability, the photo-thermal stability of six cyanine dyes were investigated at the state of solution and solid by analyzing the

UV-Vis-NIR spectroscopy and thermogravimetric analysis (TGA). Firstly, through measuring the changes of absorption spectra under the condition of illumination or heat, on the basis of relationship between absorbance intensity (A) and time (T), a linear fitting relationship is hypothesized between A and T, when the dye completely disappears, the A is zero, and the time referred as decomposition time is calculated through the linear equation hypothesized. Here, the summary of these results are displayed in Table 2 (seeing supplementary information in detail).

According to analytical results (Table 2), we can find that the decomposition time of the asymmetric dyes are longer than that of corresponding to symmetric dyes regardless illumination or heat at solution, meanwhile, the analytical results also indicate the longer alkyl chain is advantageous for increasing the decomposition time, and the same conclusion is also confirmed by the results of TGA. The excellent material among the six compounds prepared is the **IIc** with long alkyl chain (butyl sulfonate group and hexyl group), it displays the highest decomposition temperature. But on the consideration of hydrophilic character, the suitable alkyl length must be chosen[25], and the present research results clarify the structure-effect relationship about the stability of cyanine dyes designed.

Table 2. The decomposition time of six dyes in solution[a] and TGA

Compound	Illumination[b](h) (Increase ratio)	Heat[c](h) (Increase multiple)	Thermal decomposition temperature[d](℃)
Ia	12.2	9.8	220
Ib	16.6(36.1%)	37.8(2.9)	315
Ic	24.9(104.1%)	43.6(3.4)	320
IIa	13.6(11.5%)	12.9(0.3)	240
IIb	15.7(15.4%)	21.0(0.6)	340
IIc	17.7(30.1%)	31.6(1.4)	360

[a] Estimated by linear relationship between absorption (A) and the time (t), when A=0 (the dye is completely decomposed), the time is calculated.The value in bracket represents the rate or multiple of change.
[b] Illuminated wavelength between 400 nm and 750 nm.
[c] At 70 ℃ without light.
[d] Decomposition 5% (lost weight).

Application as Fluorescent Probe

1. The pH Dependence

Because the stability of free probe is an important reference index under different pH conditions[26], and in order to decide where the prepared dyes are suitable for fluorescent probe, the effect of pH toward the stability

was investigated, and two cyanine dyes (**Ia** and **IIb**) were selected to analyze the changes of UV spectrum under different pH value, the results are shown in Figure 1.

The results (Figure 1) displayed that no significant change in either the absorption intensity or wavelength of **Ia** and **IIb** was observed in different pH environment, which indicates that these dyes are stable between pH 0.95 and 13.53. We guess that the reason is attributed to the special structure of dyes containing alkyl sulfony ammonium inner salt, which is stable under acid or base condition owing to its intramolecular acid-base equilibrium. And the good stability at different pH value can expand its application field.

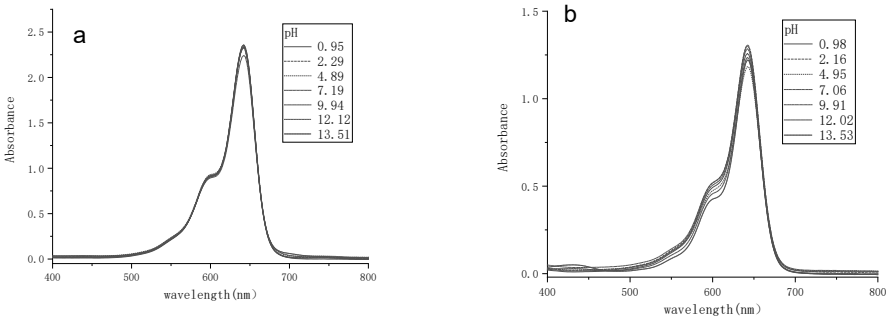

Figure 1. The UV-Vis spectra of dye **Ia** (a) and **IIb** (b) in aqueous solution of different pH

2. Sensitivity and Selectivity Study of Probe

Further, on the basis of investigation of fluorescent spectra of dyes, the researches on the fluorescent probes for metal ions in aqueous solution were implemented. Many metal ions (Cr^{3+}, Zn^{2+}, Ni^{2+}, Al^{3+}, Mg^{2+}, Cu^{2+} and Fe^{3+}) were chosen as targets, through utilizing the fluorescence spectrum and analyzing the change of spectra after adding metal ions, the detectability of dyes toward metal ions was determined. The dye **IIb** was used as a example of probe (other results can be found in the supplementary materials), the analytical results are displayed in Figure 2.

According to the results shown in Figure 2, the fluorescence quenching phenomenon was observed while adding Fe^{3+} ion to the aqueous of dye **IIb**, and adding other metal ions (Cr^{3+}, Zn^{2+}, Ni^{2+}, Al^{3+}, Mg^{2+}, Cu^{2+}) only slightly reduce the fluorescence intensity, which indicates that the series of dyes prepared can be used as a fluorescent probe to recognize and capture the

Fe^{3+} ion. But the complexity of real sample maybe present a great challenge to detection of probe for metal ion in detection selectivity, in order to effectively apply in practical environment detection conditions of co-existence of Fe^{3+} with other metal ions, it's necessary to investigate the specific and selective detection of probe when other interfering metal ions also exist, thus, the selectivity studies were carried out to evaluate the performance of probe, the anti-interference experiments were implemented under the conditions of co-existence of Fe^{3+} with other metal ions, the results are shown in Figure 3.

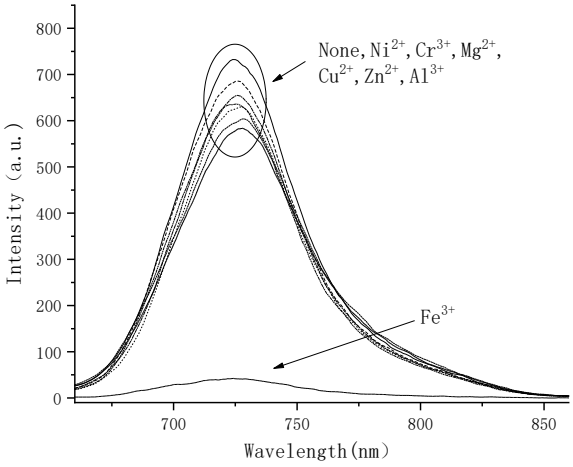

Figure 2. Fluorescence spectra change of **IIb** (2.0×10^{-4} mol/L) after adding different metal ions in aqueous solution (5.0×10^{-4} mol/L)

The blank box in Figure 3 depicts the fluorescence intensity of probe **IIb** in the presence of the different metal ions, it displays that the used metal ions hardly change the fluorescence intensity of **IIb** (seeing the Figure 2). Subsequently, the Fe^{3+} ion (5.0×10^{-4} mol/L) was added to the above solutions to form a co-existence mixture of two metal ions, then its fluorescence spectra were measured again, and the fluctuation of the fluorescence intensity was recorded as a stripe box in Figure 3.

The fluorescence quenching phenomenon induced by adding Fe^{3+} ion was almost observed in the presence of various competitive metal ions. The results show that dye **IIb** has anti-interference ability for other metal ions (Cr^{3+}, Zn^{2+}, Ni^{2+}, Al^{3+}, Mg^{2+}, Cu^{2+}) while detecting Fe^{3+} ions, which demonstrates that probe **IIb** is quite selective in detecting Fe^{3+} ion even if the conditions of co-existence of other metal ions.

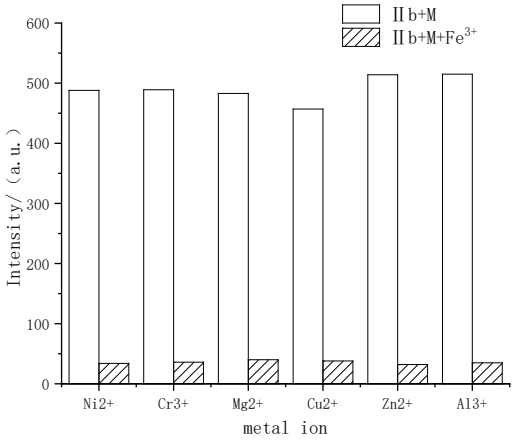

Figure 3. Effect of other metal ions on the recognition of Fe^{3+} (5.0×10^{-4} mol/L) by probe **IIb** (2.0×10^{-4} mol/L)

In brief, investigation results illustrated in Figure 2 and Figure 3 indicate that dye **IIb** possesses strong anti-interference capability and superior selectivity for Fe^{3+} over other coexisting metal ions.

3. Limit of Detection

In order to further investigate the recognition ability for Fe^{3+} by probe **IIb**, the limit of detection (LOD) was calculated through fluorescence titration. The titration results are shown in Figure 4, on the basis of the titrations of the probe **IIb** with different concentration of Fe^{3+}, the Job's plot was obtained [27].

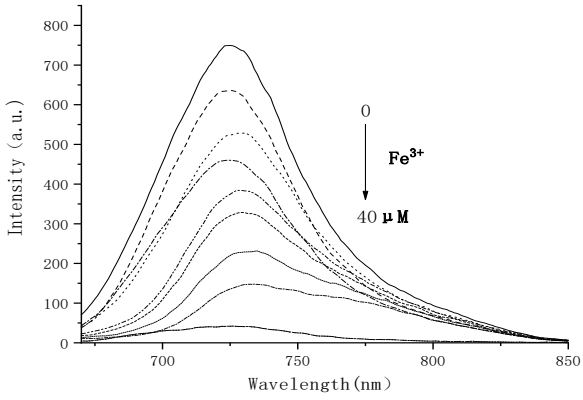

Figure 4. Fluorescence response of **IIb** to various concentration of Fe^{3+} in aqueous solution

As shown in Figure 5, the quenching efficiency (I_0/I) disclosed a good linear relationship (R^2=0.9691) versus the concentration of Fe^{3+}. The LOD is then calculated through the equation: limit of detection =3δ/k [28], where δ is the standard deviation of blank measurements; k is the slope between intensity versus sample concentration. The limit of detection was measured to be 6.8μM, which indicates that probe **IIb** can be applied as an efficient fluorescent probe for Fe^{3+} detection. The structure of the probe **IIb** and Fe^{3+} coordination compound was determined by using the Job's plot. A distinct inflection point at the Job's plot was observed when the ratio of [Fe^{3+}]/([Fe^{3+}]+[**IIb**]) was 0.494, indicating a 1:1 binding stoichiometry between dye **IIb** and Fe^{3+} (Figure 6).

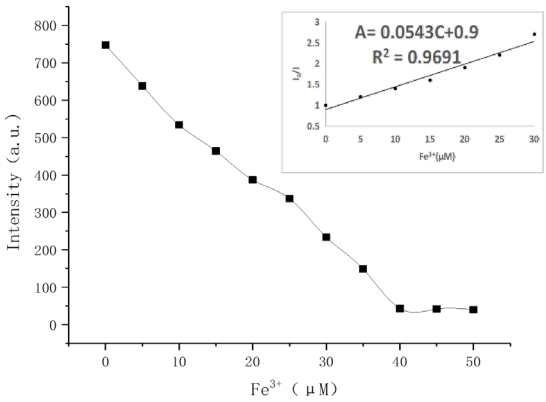

Figure 5. Plot of relative fluorescence intensity of **IIb** and concentration of Fe^{3+}, inset: linear relationship between A (I_0/I) and C (concentration of Fe^{3+})

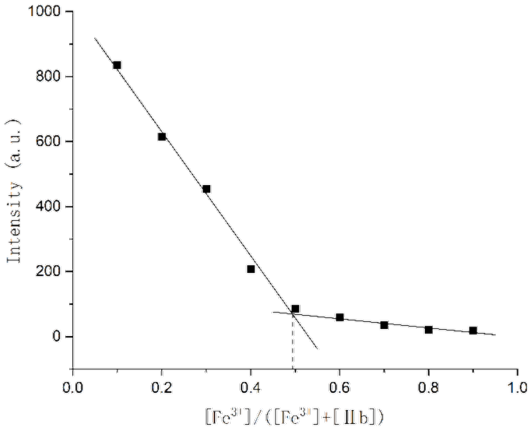

Figure 6. Job plot for the determination of the dye IIb and Fe^{3+} in the complex, the excitation wavelength was set at 721 nm

CONCLUSION

In summary, four novel asymmetric and two known symmetric water-soluble pentamethyl cyanine dyes were synthesized and fully characterized by IR, MS and NMR, and their spectroscopic properties were analysed. On the basis of investigation on Uv-vis spectra and TGA, photo-thermal stability of six cyanine dyes were compared, and the effect factors toward the stability of dyes prepared was also analyzed, which simply give the structure- effect relationship about the stability of cyanine dye. A lot of investigations about fluorescence spectra indicate that these dyes can be considered as a fluorescent probe for detection of Fe^{3+} ion, and exhibits excellent selectivity and anti-interference capability towards Fe^{3+} over other common metal cations，and **IIb** possesses a limit of detection of 6.8μM for the detection of Fe^{3+} ion, meanwhile, Job's plot analysis reflects the 1:1 complexation of dye **IIb** and Fe^{3+} complexes. Notably, this probe can be applied in aqueous media, which expands their application scope.

EXPERIMENTAL SECTION

Chemical Reagents

2,3,3-trimethylindole, 1,3-propanesultone, 1,4-butane sultone, malonaldehyde dianilide hydrochloride, methanol, dichloromethane, sodium acetate, acetic anhydride were commercially purchased and used directly without treatment. The two N-alkyl indolium salts (1-ethyl-2,3,3-trimethyl-3H-indol-1-ium iodide and 1-hexyl-2,3,3-trimethyl-3H-indol-1-ium iodide) were prepared by our lab. The stock solutions of metal ions were prepared from $Cr(NO_3)_3 \cdot 9H_2O$, $FeCl_3 \cdot 6H_2O$, $Ni(NO_3)_2 \cdot 6H_2O$, $Cu(NO_3)_2 \cdot 3H_2O$, $Zn(NO_3)_2 \cdot 6H_2O$, $Al(NO_3)_3 \cdot 9H_2O$ with distilled water.

Instrumentation

The NMR of the dyes were measured with a AC-400 Nuclear magnetic resonance apparatus. The Ms of the dyes were measured with a Waters UPLC-Quattro Micro LC-MS. The functional groups of the dyes were measured with a NICOLET 380 Fourier infrared spectrometer. UV-vis absorption spectra were measured with a Optizen 2120 spectrophotometer. Emission spectra were taken on a VARIAN fluorescence spectrophotometer.

The Synthesis of Six Cyanine Dyes

1. Intermediate of Indoline

Under nitrogen atmosphere, 1,3-propanesultone (9.22g, 0.76mol), 2,3,3-trimethyl-indole (10.22g, 0.64mol) and 5ml 1,2-dichlorobenzene (ODCB) was added into a two-necked bottle, the reaction mixture was heated for 4 h at 150℃, after cooling to r.t., pouring the upper liquid, then washing with acetone for 3 times, the resulting residue was recrystallized with methanol, the intermediate of 3-(2,3,3-trimethyl-3H-indol-1-ium-1-yl)propane-1-sulfonate (12.27g) was obtained, which was purple solid with a yield of 68%. IR(KBr) (cm^{-1}) 3044-3019 (Ar-H), 2995~2920(-CH_3, -CH_2), 1659 (C=N), 1480 (C=C), 1199 (S-O); ESI-MS: $[M+H]^+$: m/z= 282.06 (observ.), 282.10 (calc.).

The same procedure, the intermediate of 4-(2,3,3-trimethyl-3H-indol-1-ium-1-yl)butane-1-sulfonate was also prepared.

2. The symmetric Cyanine dye (Ia)

In a two-necked bottle, 3-(2,3,3-trimethyl-3H-indol-1-ium-1-yl)propane-1-sulfonate (0.97g, 3.45mmol), malonaldehyde dianilide hydrochloride (0.30g, 1.15mmol), sodium acetate (0.11g, 1.29mmol) and 10ml acetic anhydride was added, then heated for 2h at 120℃ under N_2 atmosphere, after cooling to r.t., the solvent was removed at reduce pressure, the residue was isolated by silica gel column eluted with mixed solvent of dichloromethane / methanol (v/v =4/1), the product with a metallic luster (0.43g) was obtained, yield is about 62%. IR(KBr) (cm^{-1}) 3065-3019 (Ar-H), 2995-2925 (-CH_3, -CH_2), 1659 (C=N), 1465 (C=C), 1189 (S-O); UV-Vis: λ_{ab}= 642nm, FI: λ_{em}=721nm (CH_3OH); ESI-HRMS: $[M+H]^+$: m/z= 599.2240 (observ.), 599.2205 (calc.);
^{1}H-NMR (400 MHz, CD_3OD) δ 8.29(t, J = 12.0 Hz, 2H), 7.48(d, J = 7.5 Hz, 2H), 7.40(d, J = 4.2 Hz, 4H), 7.25(dt, J = 8.0, 4.2 Hz, 2H), 6.68(s, 2H), 6.40(d, J=13.7 Hz, 2H), 4.33(t, J=7.9 Hz, 4H), 3.01(t, J = 7.0 Hz, 4H), 2.26(t, J = 7.8 Hz, 4H), 1.72(s, 12H).
^{13}C-NMR(101 MHz, CD_3OD) δ 174.7, 155.7, 143.5, 142.6, 129.8, 127.4, 126.2, 123.4, 112.1, 104.6, 51.7, 50.6, 43.9, 28.5, 28.0, 24.1.

3. The asymmetric Cyanine dye (Ib)

In a two-necked bottle, 3-(2,3,3-trimethyl-3H-indol-1-ium-1-yl)propane-1-sulfonate (0.26g, 1.27mmol), malonaldehyde dianilide hydrochloride (0.30g, 1.15mmol), sodium acetate (0.11g, 1.29mmol) and 5ml acetic anhydride was added, then heated for 2h at 120℃ under N_2 atmosphere, after cooling to r.t., 1-ethyl-2,3,3-trimethyl-3H-indol-1-ium iodide (0.38, 1.22mmol) was added into the reaction mixture, and then afer further reacting for 30 min at 120℃, the solvent was removed at reduce pressure, the residue was isolated by

silica gel column eluted with mixed solvent of dichloromethane / methanol (v/v =8/1), the product with a metallic luster (0.21g) was obtained, yield is about 36%. IR(KBr) (cm^{-1}) 3053-3015 (Ar-H), 2965-2905 (-CH_3, -CH_2), 1660 (C=N), 1485 (C=C), 1209 (S-O); UV-Vis: λ_{ab}= 642nm, FI: λ_{em}= 722nm (CH_3OH); ESI-MS: $[M+H]^+$: m/z=505.41 (observ.), 505.42 (calc.);
^{1}H-NMR (400 MHz, $CDCl_3$) δ 8.01 (s, 2H), 7.31 – 7.28 (m, 2H), 7.21 (d, J = 7.3 Hz, 2H), 7.13 (t, J = 7.5 Hz, 2H), 7.05 (d, J = 8.3 Hz, 2H), 7.01 (d, J = 7.6 Hz, 1H), 6.68 (d, J = 12.7 Hz, 1H), 6.10 (d, J = 13.5 Hz, 1H), 4.47 (s, 2H), 4.05 (d, J = 7.6 Hz, 2H), 3.22 (d, J = 7.1 Hz, 2H), 2.32 (s, 2H), 1.60 (s, 6H), 1.54 (s, 6H), 1.36 – 1.32 (m, 3H).
^{13}C-NMR (101 MHz, $CDCl_3$) δ 173.9, 172.7, 142.5, 141.8, 128.9, 128.6, 127.7, 126.4, 125.1, 125.1, 122.4, 122.2, 121.5, 111.3, 110.3, 105.0, 102.9, 49.5, 48.1, 39.4, 28.0, 23.4, 12.6.

4. The asymmetric Cyanine dye (Ic)

The same as procedure of **Ib** preparation except for replacing the 1-ethyl-2,3,3-trimethyl-3H-indol-1-ium iodide using 1-hexyl-2,3,3-trimethyl-3H-indol-1-ium iodide, the Ic also was obtained at the yield of 32%. IR(KBr) (cm^{-1}) 3044-3019 (Ar-H), 2965-2925 (-CH_3, -CH_2), 1659 (C=N), 1480 (C=C), 1195 (S-O); UV-Vis: λ_{ab}= 642nm, FI: λ_{em}= 726nm (CH_3OH); HRMS: $[M+H]^+$: m/z= 561.3144 (observ.), 561.3106 (calc.);
^{1}H- NMR (400 MHz, $CDCl_3$) δ 8.21 (t, J = 13.1 Hz, 1H), 7.64 (d, J = 8.0 Hz, 1H), 7.38 (d, J = 2.4 Hz, 1H), 7.36 (d, J = 1.9 Hz, 2H), 7.34 (d, J = 1.5 Hz, 2H), 7.23 (d, J = 3.3 Hz, 1H), 7.21 (d, J = 3.3 Hz, 1H), 7.15 (d, J = 7.8 Hz, 1H), 7.02 (d, J = 8.1 Hz, 1H), 6.25 (d, J = 13.6 Hz, 1H), 6.03 (d, J = 13.6 Hz, 1H), 4.54 (s, 2H), 3.91 (t, J = 7.7 Hz, 2H), 3.11 (d, J = 6.4 Hz, 2H), 2.34 (d, J = 8.7 Hz, 2H), 2.10 (s, 2H), 1.78 (s, 12H), 1.34 (q, J = 4.8 Hz, 6H), 0.90 – 0.87 (m, 3H).
^{13}C- NMR (101 MHz, $CDCl_3$) δ 174.0, 173.2, 142.2, 141.6, 128.9, 128.9, 128.6, 128.5, 126.7, 125.1, 123.8, 122.6, 122.5, 122.4, 120.0, 110.6, 110.2, 103.7, 103.0, 49.6, 49.5, 47.7, 44.3, 31.5, 28.3, 28.0, 27.8, 27.5, 27.4, 26.8, 24.8, 22.6, 21.2, 14.1.

5. The Cyanine dye (II)

According to the preparation procedure of I, three cyanines (**II**) were also synthesized, the analytical data were displayed as following:

IIa: Yield was 46%. IR(KBr) (cm^{-1}) 3064-3025 (Ar-H), 2956-2887 (-CH_3, -CH_2), 1659 (C=N), 1485 (C=C), 1158 (S-O); UV-Vis: λ_{ab}= 642nm, FI: λ_{em}= 718nm (CH_3OH); ESI-MS: $[M+H]^+$: m/z=626.21 (observ.), 626.25 (calc.);
^{1}H- NMR (600 MHz, DMSO-D6) δ 8.33 (t, J = 13.1 Hz, 2H), 7.61 (d, J = 7.4 Hz, 2H), 7.42 (d, J = 8.0 Hz, 2H), 7.38 (t, J = 7.6 Hz, 2H), 7.23 (t, J = 7.3 Hz,

2H), 6.60 (t, J = 12.4 Hz, 1H), 6.36 (d, J = 13.8 Hz, 2H), 4.10 (t, J = 7.5 Hz, 4H), 2.48 (d, J = 7.4 Hz, 4H), 1.77 (d, J = 15.0, 7.1 Hz, 4H), 1.70 (s, 6H), 1.69 (s, 2H), 1.68 (s, 6H), 1.24 (d, J = 11.7 Hz, 2H).
^{13}C- NMR (101 MHz, DMSO-D6) δ 176.51, 172.50, 154.03, 142.06, 141.11, 128.42, 125.74, 124.60, 122.37, 111.17, 103.31, 50.68, 48.85, 27.19, 26.02, 24.20, 22.42.

IIb: Yield was 29%. IR(KBr) (cm^{-1}) 3062-3017 (Ar-H), 2965-2915 (CH_2-H, C-H), 1660 (C=N), 1482 (C=C), 1197 (S-O); UV-Vis: λ_{ab}= 642nm, FI: λ_{em}= 721nm (In CH_3OH); ESI-MS: $[M+H]^+$: m/z=626.21 (observ.), 626.25 (calc.);
^{1}H- NMR (400 MHz, $CDCl_3$) δ 8.36 (d, J = 14.9 Hz, 1H), 7.92 (t, J = 13.0 Hz, 2H), 7.62 (d, J = 7.9 Hz, 1H), 7.35 (d, J = 7.6 Hz, 1H), 7.22 (d, J = 7.1 Hz, 2H), 7.13 (t, J = 7.5 Hz, 1H), 7.04 (d, J = 7.7 Hz, 2H), 6.75 (t, J = 12.4 Hz, 1H), 6.40 (d, J = 13.6 Hz, 1H), 6.19 (d, J = 13.4 Hz, 1H), 4.13 (s, 2H), 4.04 (d, J = 7.1 Hz, 2H), 3.07 (d, J = 7.6 Hz, 2H), 1.91 (s, 2H), 1.62 (s, 6H), 1.59 (s, 6H), 1.31 (t, J = 7.0 Hz, 5H).
^{13}C- NMR (101 MHz, $CDCl_3$) δ 173.0, 171.8, 142.1, 141.8, 141.3, 141.2, 129.2, 128.9, 128.7, 126.9, 125.2, 123.9, 122.7, 120.1, 112.0, 110.4, 103.1, 50.4, 49.4, 49.3, 28.5, 28.2, 12.6.

IIc: Yield was 36%. IR(KBr) (cm^{-1}) 3044-3025 (Ar-H), 2956-2887 (-CH_3, -CH_2), 1659 (C=N), 1485 (C=C), 1158 (S-O); UV-Vis: λ_{ab}= 642nm, FI: λ_{em}= 718nm (CH_3OH);
^{1}H- NMR (400 MHz, $CDCl_3$) δ 7.90 (s, 2H), 7.40 (d, J = 7.7 Hz, 1H), 7.37 (d, J = 1.5 Hz, 1H), 7.36 – 7.33 (m, 2H), 7.22 (d, J = 6.0 Hz, 1H), 7.19 (d, J = 7.5 Hz, 1H), 7.14 (d, J = 8.0 Hz, 1H), 7.02 (d, J = 8.1 Hz, 1H), 6.74 (t, J = 12.5 Hz, 2H), 6.09 (d, J = 13.5 Hz, 1H), 4.21 (t, J = 8.1 Hz, 2H), 3.93 (t, J = 7.7 Hz, 2H), 3.06 (t, J = 6.2 Hz, 2H), 2.19 – 2.12 (m, 2H), 1.78 (t, J = 7.7 Hz, 2H), 1.72 (s, 6H), 1.64 (s, 6H), 1.44 (d, J = 7.8 Hz, 2H), 1.34 (q, J = 3.8 Hz, 4H), 1.25 (s, 2H), 0.91 – 0.87 (m, 3H).
^{13}C- NMR (101 MHz, $CDCl_3$) δ 173.8, 154.0, 142.4, 141.1, 129.0, 128.7, 126.9, 125.5, 124.9, 122.4, 122.3, 111.1, 110.2, 102.9, 49.5, 44.4, 31.6, 28.3, 28.1, 27.4, 26.8, 22.9, 22.6, 14.1.

REFERENCES

1. W. Sun; S. Guo; C. Hu; J. Fan; *Chem. Rev.*, **2016**, *116(14)*, 7768-7817.
2. A. Mishra; R. K. Behera; P. K. Behera; B. K. Mishra; G. B. Behera; *Chem. Rev.*, **2000**, *100(6)*, 1973-2012.
3. H. A. Shindy; *Dyes Pigm.*, **2017**, *145*, 505-513.
4. H. Mustroph; *Phys. Sci. Rev.*, **2020**, *5(5)*, 20190145.

5. G. S. Gopika; P. H. Prasad; A. G. Lekshmi; S. Lekshmypriya; S. Sreesaila; C. Arunima; ... & Z. S.Pillai; *Mater. Today: Proc.*, **2021**, *46*, 3102-3108.
6. X. Yang; J. Bai; Y. Qian; *Spectrochim. Acta, Part A*, **2020**, *228*, 117702.
7. P. G. Pronkin; A. S. Tatikolov; *Chemosensors*, **2023**, *11(5)*, 280.
8. Y. Li; Y. Zhou; X. Yue; Z. Dai; *Adv. Healthcare Mater.*, **2020**, *9(22)*, 2001327.
9. Z. Guo; S. Park; J. Yoon; I. Shin; *Chem. Soc. Rev.*, **2014**, *43*, 16-29.
10. C. Zhang; Y. T. Sun; S. Y. Gan; A. M. Ren; S. Milaneh; D. J. Xiang; W. L. Wang; *Mater. Chem. C*, **2023**, *11*, 16859-16889.
11. E. M. S. Stennett; M. A. Ciuba; M. Levitus; *Chem. Soc. Rev.*, **2014**, *43*, 1057-1075.
12. P. Kaur; K. Singh; *The Chem. Rec.*, **2023**, *23(1)*, e202200184.
13. J. Cao; T. Wu; C. Hu; T. Liu; W. Sun; J. Fan; X. Peng; *Phys. Chem. Chem. Phys.*, **2012**, *14(39)*, 13702-13708.
14. J. L. Serrano; A. Maia; A. O. Santos; E. Lima; L. V. Reis; M. J. Nunes; ... & P. Almeida; *Molecules*, **2022**, *27(18)*, 5779.
15. J. Yuan; H. Yang; W. Huang; S. Liu; H. Zhang; X. Zhang; X. Peng; *Chem. Soc. Rev.*, **2025**，*54*，341-366.
16. X. Zhao; J. Du; W. Sun; J. Fan; X. Peng; *Acc. Chem. Res.*, **2024**, *57*, 2582−2593.
17. X. Tang; B. Zhou; Z. Su; R. Wu; X. Qiu; L. Liu; *Spectrochim. Acta, Part A*, **2024,** *322*, 124826.
18. B. Li; X. Gu; M. Wang; X. Liu; K. Xu; *Dyes Pigm.*, **2021**, *194*, 109637.
19. C. Sun; W. Du; B. Wang; B. Dong; B. Wang. *BMC chem.*, **2020**, *14*, 1-28.
20. S. Li; D. Zhang; S. Ma; Y. Liu; Z. Xu; ... & Y. Ye; *Sens. Actuators, B*, **2016**, *224*, 661-667.
21. K. Vijay; C. Nandi; S. D. Samant; *RSC Adv.*, **2016**, *6(55)*, 49724-49729.
22. T. V. S. Rao; J. B. Huff; C. Bieniarz. Tetrahedron, **1998**, *54(36)*, 10627-10634.
23. V. E. Kuznetsova; V. A. Vasiliskov; A. S. Zasedatelev; A. V. Chudinov. *Mendeleev Commun.*, **2008**, *18(3)*, 138-140.
24. C. Pardal; S. S. Ramos; P. F. Santos; L. V. Reis; P. Almeida; *Molecules*, **2002**, *7*, 320-330.
25. M. Zhu; C. Shi; X. Xu; Z. Guo; W. Zhu; *RSC Adv.*, **2016**, *6(103)*, 100759–100764.
26. S. Pal; N. Chatterjee; P. K. Bharadwaj; *RSC Adv.*, **2014**, *4*, 26585–26620.
27. S. K. Sahoo; D. Sharma; R. K. Bera; G. Crisponi; J. F. Callan; *Chem. Soc. Rev.*, **2012**, *41*, 7195–7227.
28. J. H. Ye; Y. Zhang; Q. Zhu; Z. Chang; W. He; *Luminescence,* **2024**, *39*, e70024.

STUDIA UBB CHEMIA, LXX, 3, 2025 (p. 129-140)
(RECOMMENDED CITATION)
DOI:10.24193/subbchem.2025.3.09

SYNTHESIS AND SPECTROSCOPIC INVESTIGATIONS OF A NEW *γ*-*L*-GLUTAMYL AMIDE AS POTENTIAL LIGAND FOR TRANSITION METAL COMPLEXES

Carmen SACALIS[a,*], Maria HATAGAN[b], Emese GAL[c]

ABSTRACT. Considering the important chemical and biochemical application of L-glutamyl amides, this research reports a new compound namely (*S*)-2-amino-5-((4-(octyloxy)phenyl)amino)-5-oxopentanoic acid, as a potential ligand for transition metal complexes or for biological tests. This derivative was synthesized by a regioselective acylation of 4-(octyloxy)aniline using *N*-phthaloyl-L-glutamic anhydride, followed by hydrolysis of phthaloyl group with hydrazine hydrate. The mild conditions under which the reactions took place prevented the final synthetic product from being racemized. The identity of the glutamyl amide as well as the synthesis intermediates have been confirmed by spectral analyses such as ^{1}H-NMR, ^{13}C-NMR, HRMS and FT-IR in the solid state.

Keywords: *L-glutamic acid, L-glutamyl-amides, 4-(octyloxy)aniline derivatives, spectroscopic studies*

INTRODUCTION

Due to the great importance of L-glutamic acid in a lot of biochemical reaction such as the biosynthesis of other amino acids through a transamination process, or as a key excitatory neurotransmitter in the central nervous

[a] *Babeş-Bolyai University, Faculty of Chemistry and Chemical Engineering, Department of Chemistry, 11 Arany Janos str., RO-400028, Cluj-Napoca, Romania.*
[b] *Utrecht University, Utrecht Institute of Pharmaceutical Sciences, Department of Pharmaceutics, Universiteitsweg 99, 3584 CG, Ultrecht, Netherlands.*
[c] *Babeş-Bolyai University, Faculty of Chemistry and Chemical Engineering, Department of Chemistry and Chemical Engineering, Hungarian Line of Study, 11 Arany Janos str., RO-400028, Cluj-Napoca, Romania.*
[*] *Corresponding author: carmen.sacalis@ubbcluj.ro*

system, playing a vital role in nerve signaling, learning, and memory, can be considered a vital amino acid with far-reaching effects on brain function, energy metabolism, and overall health. An excellent substrate for determination of γ-glutamyl transpeptidase (GGT) proved to be γ-L-glutamyl-*p*-nitroanilide which has been used successfully in the diagnosis of liver, pancreas, kidney diseases and recently as a prognostic tool for heart failures [1,2].

For this reason, other glutamyl amide derivatives have also been successfully tested as substrate for GGT with satisfactory results [3,4].

Another application for L-glutamide derivatives was reported as organogelator. A new organogelator was created by attaching L-glutamide derivatives to a cyclotriphosphazene core, resulting in an improved gelation ability, chirality, and thixotropic properties compared to a similar organogelator without the core. This new organogel sensor was developed using a cyclotriphosphazene core and L-glutamide derivatives, showing improved self-assembly and thixotropic properties [5].

The results of a recent study show that some of the L-γ-methyleneglutamic acid amides exhibit selective anticancer activity against various breast cancer cell lines, with some compounds showing potency comparable to Tamoxifen or Olaparib, drugs currently used to treat breast cancer [6]. Ethyl or *tert*-butyl esters of L-γ-methyleneglutamic acid amides have potential as novel therapeutics for the treatment of multiple subtypes of breast cancer, glioblastoma, head and neck cancer [7].

On the other hand, 4-(octyloxy)aniline has proven to be a compound with multiple applications in chemistry and material science. Many compounds based on 4-(octyloxy)aniline fragments have found applications in the development of polarizing liquid crystal-based films with good polarization and light absorption characteristics. These materials are used in optical display devices that control the amount of light passing through them. Thus, derivatives of 4-(octyloxy)aniline based on biphenyl, biphenyltetracarboxydiimde, methylthioether or Schiff base moiety reveals promising results for the optoelectronic devices industry [8-13].

Azobenzene-based compounds are synthesized for their photoresponsivity properties, enabling applications in optical storage devices, light shutters, and remote-controllable devices [14].

Pyrazine-2,5-dicarboxylic acid derivatives with different *p*-alkoxy anilines were found to be efficient organogelators, readily forming stable gels in various organic solvents, contributing to advancement in material science [15].

Recently, dyes laterally substituted with *p*-alkoxy-aniline moieties, including 4-(octyloxy)aniline, have been studied for their mesomorphic properties, gelling ability or applications in dyeing [16,17].

Compounds, like *N,N'*-diarylthiourea or thiobenzenanilide derivatives and some chlorinated plastoquinone analogs, are synthesized for their potential anticancer properties, targeting breast cancer cells, leukemia and difficult-to-treat melanomas [18-20]. Other chlorinated plastoquinone analogs, were evaluated for their ability to inhibit microbial growth, including bacteria and fungi [21]. Derivatives containing glutamic acid fragments and 4-(octyloxy)aniline have demonstrated substantial lymphopenic activity *in vivo* in mouse and rat tests [22].

A novel series of gemini surfactants bearing 4-alkoxyphenyl hydrophobic tails with superior surface properties and good antibacterial activity might be good candidates for wastewater and surface treatments [23]. Another research direction where 4-(octyloxy)aniline was successfully employed was in dendrimer chemistry [24-26].

Taking into account the multiple applications of L-glutamic acid and 4-(octyloxy)aniline in a multitude of domains, in this work we aimed to synthesize and analyse by physico-chemical methods the amide resulting from the condensation of these two reactants as a potential ligand in complexation with transition metal ions or as a good compound for the biological studies. In this context, we report a new amide which was prepared following the protocol used for peptide synthesis, i.e. regioselective acylation of the aromatic amine with the anhydride of the *N*-protected amino acid. This new glutamyl amide namely (*S*)-2-amino-5-((4-(octyloxy)phenyl)amino)-5-oxopentanoic acid (**4**) was synthesized in four steps with an overall yield of 42%, in mild condition, which facilitated the preservation of the optical purity both of the intermediates and the final synthesis product.

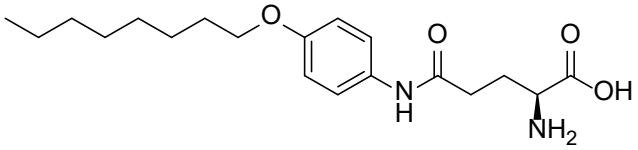

(**4**)

Figure 1. (*S*)-2-amino-5-((4-(octyloxy)phenyl)amino)-5-oxopentanoic acid

RESULTS AND DISCUSSION

A proper method that does not affect the chiral center of the amino acid, consists of the use a mild phthaloylation at the amino group in the first synthesis step. A common compound often used for this purpose is phthalic anhydride, but this produces partial racemization, which cannot be avoided [27,28].

In our earlier work, we identified *N*-ethoxycarbonylphthalimide as being a commercial and easy-to-use reagent, with satisfactory yield in the protection stage, which reacts in mild condition, without racemization at the chiral center [29-31].

Then, the *N*-protected glutamic acid was treated with acetic anhydride, by heating at 80^0C, for a short time under nitrogen atmosphere, and the *N*-phtaloyl-γ-L-glutamic anhydride (**2**) was obtained as an activation form for the carboxylic group, in the second stage of the synthesis. This step occurs with high yield, no racemization.

A regioselective acylation of 4-(octyloxy)aniline with the *N*-protected anhydride in chloroform and catalytic quantity of pyridine under nitrogen atmosphere led to obtaining the *N*-phthaloyl-γ-L-glutamyl amide (**3**), also optically active (see Experimental Section).

After this, we have easily removed the phthaloyl group with hydrazine hydrate in methanol under reflux and the free amide (**4**) was obtained until pH 6-6.5, as a pale grey-blue solid, in the last synthesis step.

The first three steps were monitored by TLC in ethanol:acetone=3:1 (v/v) and visualization in UV at λ=245nm, but for the last step it was necessary to change the system with 1-propanol:acetic acid:water=8:1:1 (v/v/v) and visualization in ninhydrin or I_2 vapor, like in the other cases of amides derived from amino acids, synthesized by us [29-31].

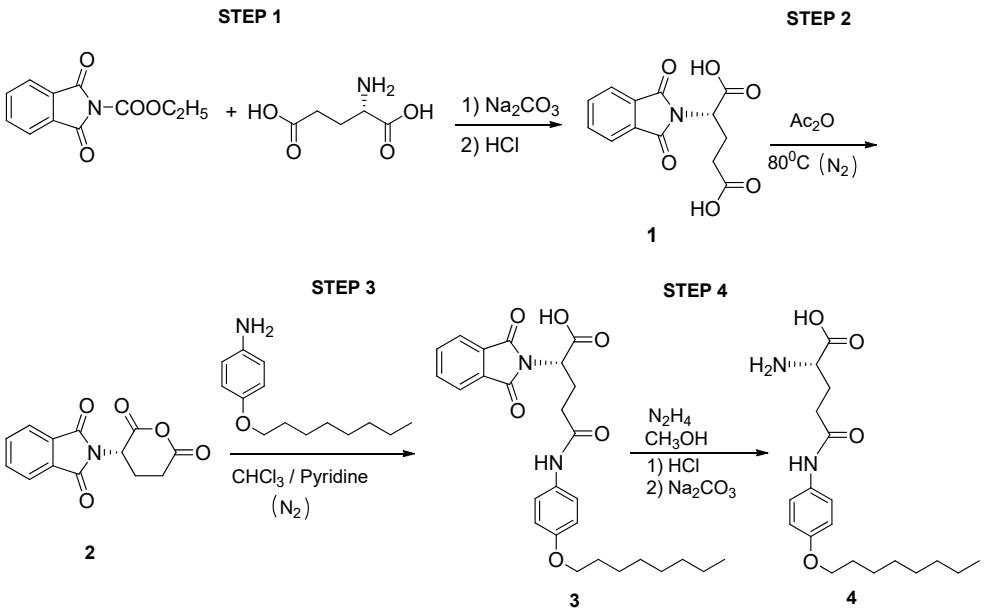

Scheme 1. Synthesis of (*S*)-2-amino-5-((4-(octyloxy)phenyl)amino)-5-oxopentanoic acid

The identitys of the all-synthesized compounds were confirmed by routine analysis such as ^{1}H-NMR, ^{13}C-NMR, HRMS and FT-IR spectra.

The ^{1}H-NMR spectrum for the compound (**4**) was recorded in DMSO+DCl_{aq} at 400MHz. A low-intensity signal at 10.13 ppm was observed, which corresponds to the free carboxylic acid proton of the amino acid residue. This attenuated signal is likely a result of deuterium exchange with the solvent. A multiple signal appears at chemical shift range at 8.65-8.59 ppm due to the NH group, while the aromatic protons of the amine are found at 7.46 ppm and 6.79 ppm, respectively, through distinct doublets and increased coupling constants, which are also found in other cases of 4-(octyloxy)aniline derivatives [12,18,26]. The multisignals within 3.92-3.83 ppm range are assigned to the NH_2 group overlapping with the proton H_2 belonging to the amino acid rest. The aliphatic side chain protons reveal overlapped signals within 2.15-0.79, specific fact for compounds with this aniline derivative (Figure 2a).

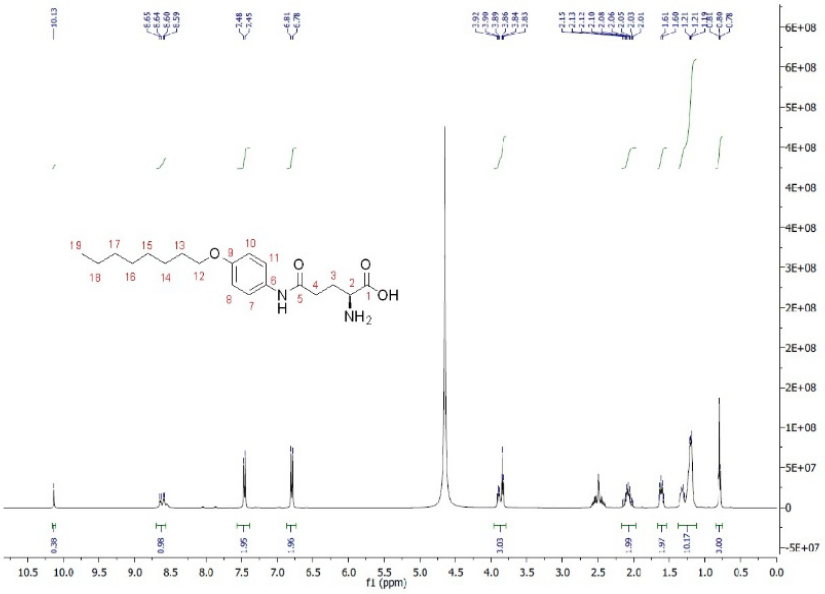

Figure 2a. ^{1}H-NMR spectrum of γ-L-glutamyl amide (**4**)

Regarding the ^{13}C-NMR spectrum, the presence of the signals of the compound and of the solvent can be both identified (see Experimental Section and Figure 2b). On the ^{13}C-NMR were noticed 17 signals. The aromatic part has 6 carbons, but because of symmetry there are 4, carbon C_8 and C_{10} also C_7 and C_{11} are equivalent, respectively (Figure 2b).

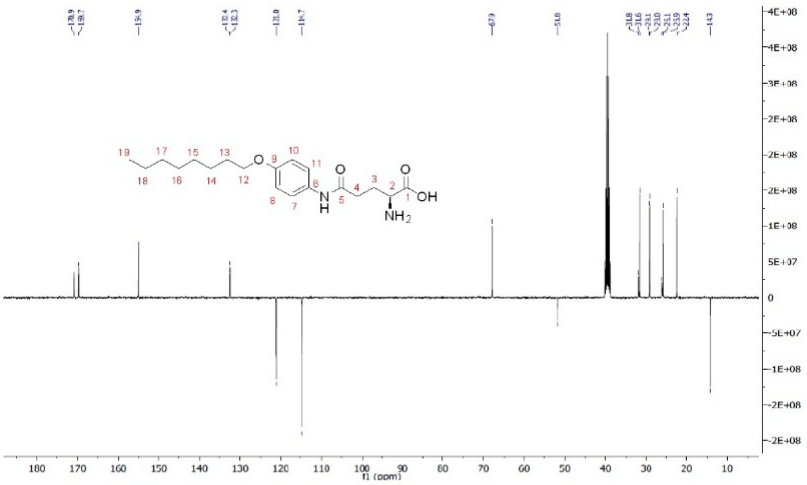

Figure 2b. ^{13}C-NMR spectrum of γ-L-glutamyl amide (**4**)

HRMS spectrum (ESI+) of γ-glutamyl amide (**4**) confirms the presence of the [M+Na], as a molecular peak, at 373.2112 value and [M+H] at 351.2292 value, respectively (Figure 3).

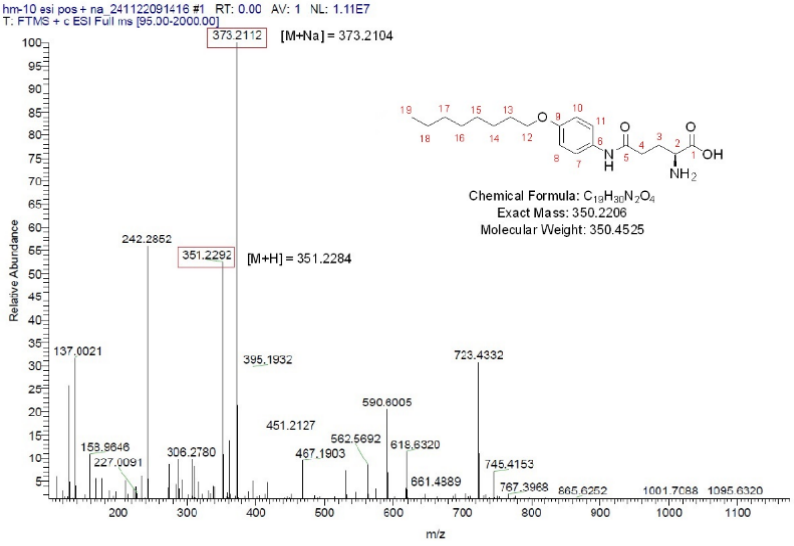

Figure 3. HRMS spectrum (ESI) of γ-L-glutamyl amide (**4**)

FT-IR spectroscopy provided complementary data that confirmed the structural assignment of the synthesized glutamyl amide.

In the spectral region of 3100-2500 cm^{-1} a wide band formed by some overlapped bands is observed, that may be assigned to ν_{O-H} vibration due to intra- and intermolecular hydrogen bonding in the crystalline state [32]. Also, in this area, probably the stretching frequencies from aliphatic and aromatic fragments overlap as well.

Two very sharp bands at 1655 cm^{-1} and 1582 cm^{-1}, could be attributed to the *v(COO⁻as)* and *v(COO⁻sym)* respectively, specific to solid state amide I and II bands [33]. The stretching vibration *v(NH_2)* appears at a strong signal at 3277 cm^{-1} while the *v(NH)* and *δ(NH)* frequencies can be found at 1248 cm^{-1} and 1628 cm^{-1} respectively.

On the other hand, the stretching frequencies *v(CH_2as)* and *v(CH_2sym)* corresponding to the aliphatic residue are very well highlighted at 2932 cm^{-1} and 2852 cm^{-1} respectively [33,34]. Other stretching, bending and combination bands which appear in the "fingerprint" region down to 1500 cm^{-1}, cannot be ascribed with certainty (Figure 4).

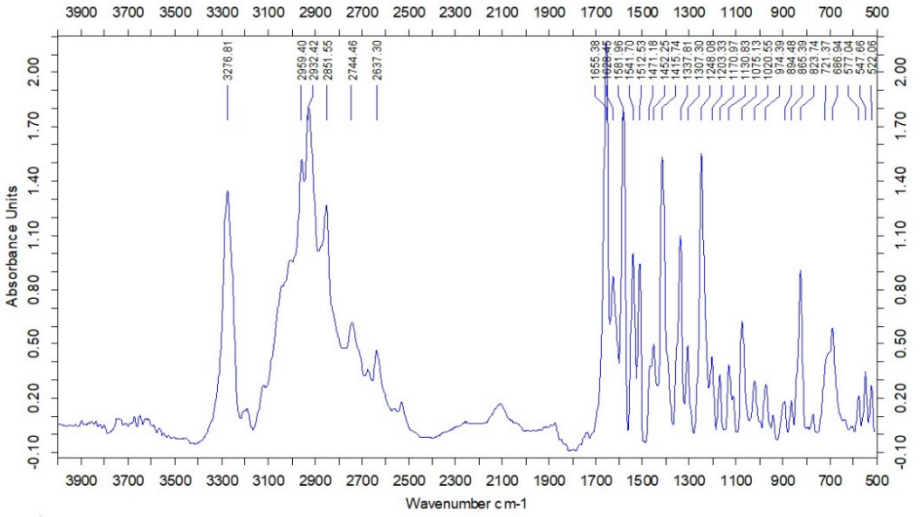

Figure 4. IR spectrum of γ-L-glutamyl amide (**4**)

CONCLUSIONS

The objective of this study was to synthesize a novel γ-L-glutamyl amide from two compounds with extensive application: an important amino acid, L-glutamic acid, and an amine 4-(octyloxy)aniline that has recently been widely used in chemistry and material science.

The amide bond formation process was applied for this purpose, from peptide synthesis starting with an *N*-terminal amino acid, in four steps. In the protection stage, we used *N*-ethoxycarbonylphthalimide, as a proper acylating agent, in order to introduce the phthaloyl group in mild condition, to avoid racemization.

It was established that by maintaining mild conditions throughout all synthesis stages, the compounds in question were able to retain their optical activity and were obtained in relatively good yields.

The compound's identity was confirmed by spectral analysis like NMR, HRMS and FT-IR data.

Finally γ-L-glutamyl amide (**4**), namely (*S*)-2-amino-5-((4-(octyloxy)phenyl)amino)-5-oxopentanoic acid, can be used as a potential ligand to form novel complexes with different metal ions and also for the purpose of conducting biological tests.

EXPERIMENTAL SECTION

Materials and instrumentation

All reagents and chemicals were purchased from commercial sources and used as received. TLC monitoring was performed by using aluminum sheets with silica gel 60 F_{254} (Merck® visualization in UV at λ=254 nm; I_2 vapor or ninhydrin). NMR spectra were recorded on BRUKER® AM 400 instruments operating at 400 and 100 MHz for ^1H and ^{13}C nuclei, respectively. All chemical shifts (δ value) are given in ppm without TMS added. The chemical shifts were measured against the solvent residual peak. Elemental analyses were determined on Thermo Scientific Flash EA 1112 Elemental Analyzer. Melting points were measured on an ELECTROTHERMAL® instrument and were not corrected. Specific rotations were estimated on a Polamat A Karl Zeiss Jena photopolarimeter. Mass spectra were carried out on a LTQ ORBITRAP® XL (Thermo Scientific) instrument which was externally calibrated using the manufacturer's ESI(+) calibration mix. The samples were introduced into the spectrometer by direct infusion. FT-IR spectra were recorded in KBr pellets on a BRUKER® VECTOR 22 Spectrometer which operates with OPUS soft.

*Synthesis of N-Phthaloyl-L-Glutamic Acid **(1)***

To a solution of 6.25g (0.0589 mol) Na_2CO_3 and 25mL distilled water, 3g (0.0204 mol) L-glutamic acid was added at room temperature with vigorous stirring until the amino acid was solved. The solution was cooled at 0-1^0 C and 6.25g (0.0285 mol) of *N*-carbetoxyphthalimide was added gradually, within 1 hour. The mixture was left to stirring overnight at room temperature,

then cooling again and filtrating to remove the ethylureatane. The resultant pH solution was found to be between 8.6 and 9. The remaining solution was acidified with HCl to pH = 1-1.5, when an oily product was formed, which crystallized within 12 hours in the refrigerator. The resulted product was filtrated, followed by a thorough wash with the mother solution and acidified water with HCl, dried 2 days in air, then in a desiccator. The product was purified through a process of dissolution and reprecipitation. Initially, it was dissolved in a 1M Na_2CO_3 solution, followed by reprecipitation with 6N HCl. The resultant solid was then dried under the same conditions.

$C_{13}H_{11}NO_6$ (**1**) white solid; MW = 277.2295; mp = 159-160^{0}C; Yield 76%; TLC analysis: R_f = 0.48 (ethanol:acetone = 3:1 (v/v)) visualization in UV at λ = 254 nm; Elemental analysis (%) calcd(found): C: 56.32(56.47); H: 4.00(4.14); N: 5.05(4.89); HRMS (ESI+) [M+Na]: 300.0472; Exact Mass: 277.0586; $[\alpha]_{546}^{25} = -89\ (c = 1,\ DMF)$.

^{1}H-NMR (DMSO, 400MHz, δ(ppm)): 10.97 (2H, s, 2 COOH groups); 7.92-7.85 (4H, overlapped signal, Ar-H); 4.81 (1H, t, $^3J_{H,H}$=12Hz, CH); 2.39-2.22 (4H, m, 2 CH_2 from aliphatic rest); ^{13}C-NMR (DMSO, 100MHz, δ(ppm)): 173.9 (COOH); 170.5 (COOH); 167.6 (CO); 134.9 (C_{arom}); 131.4 (C_{arom}); 123.5 (C_{arom}); 51.2 (CH); 30.5 (CH_2); 23.8 (CH_2); FT-IR (KBr, cm^{-1}): ν_{max}: 3054(bb); 2911(m); 1777(vs); 1728(vs); 1707(vs); 1690(vs); 1429(m); 1387(vs); 1259(vs); 1203(s); 1168(m); 713(s).

*Synthesis of N-Phthaloyl-L-Glutamic Anhydride (**2**)*

A mixture of *N*-Phthaloyl-L-Glutamic Acid **(1)** 3g (0.0108 mol) and acetic anhydride 10mL (98.5% pure, ρ=1.08g/cm^3, 0.1042 mol) was heated at 90^{0}C for 30 minutes under nitrogen atmosphere. An opalescent solution appears in short time. The mixture was subjected to a cooling process in a freezer, with a duration of 3 hours. Thereafter, the precipitate that had formed was filtered, washed with cold ether and dried in a desiccator for a period of 5 days.

$C_{13}H_9NO_5$ (**2**) white solid; MW = 259.2143; mp = 199-200^{0}C; Yield 93%; TLC analysis: R_f = 0.52 (ethanol:acetone = 3:1 (v/v)) visualization in UV at λ = 254 nm; Elemental analysis (%) calcd(found): C: 60.24(60.01); H: 3.50(3.67); N: 5.40(5.23); HRMS (ESI+) [M+Na]: 282.0366; Exact Mass: 259.0481; $[\alpha]_{546}^{25} = -43\ (c = 3,\ dioxane)$.

^{1}H-NMR (DMSO, 400MHz, δ(ppm)): 7.92 (2H, dd, $^2J_{H,H}$=12Hz, Ar-H); 7.86 (2H, dd, $^2J_{H,H}$=12Hz, Ar-H); 4.81 (1H, dd, $^2J_{H,H}$=12Hz, CH from aliphatic rest); 2.40-2.34 (2H, m, from aliphatic rest); 2.32-2.23 (2H, m, from aliphatic rest); ^{13}C-NMR (DMSO, 100MHz, δ(ppm)): 174.2 (CO from aliphatic rest); 170.8 (CO from aliphatic rest); 167.9 (CO from aromatic rest); 135.2 (C_{arom});

131.7 (C_{arom}); 123.8 (C_{arom}); 51.5 (CH); 30.8 (CH_2); 24.1 (CH_2); FT-IR (KBr, cm^{-1}): v_{max}: 1818(m); 1780(s); 1715(vs); 1392(s); 1225(m); 1117(s); 1034(s); 722(m).

*Synthesis of N-Phthaloyl-γ-L-glutamyl-4-(octyloxy)anilide (**3**)*

A suspension of *N*-Phthaloyl-L-Glutamic Anhydride (**2**) 2.59g (0.001 mol) and an equivalent quantity of pyridine as a catalyst in 20 mL chloroform was heated at 50^0C under nitrogen atmosphere. A solution of 4-(octyloxy)aniline 2.21g (0.001 mol) in 10 mL chloroform was added slowly, dropwise, over a period of 1 hour. The solution was then stirred for 3 hours under reflux. After being kept 24 hours at room temperature, the solvent was removed under reduced pressure. The residue was triturated with ether, filtered off, washed with cold ether and dried in a desiccator.

$C_{27}H_{32}N_2O_6$ (**3**) pale blue solid; MW = 480.5528; mp = 139-140^{0}C; Yield 68%; TLC analysis: R_f = 0.65 (ethanol:acetone = 3:1 (v/v)) visualization in UV at λ = 254 nm; Elemental analysis (%) calcd(found): C: 67.48(67.26); H: 6.71(6.84); N: 5.83(5.98); HRMS (ESI+) [M+Na]: 503.2147 Exact Mass: 480.2260; $[\alpha]_{546}^{25} = -76\ (c = 0.25,\ DMSO)$.

^{1}H-NMR (DMSO, 400MHz, δ(ppm)): 9.66 (1H, s, -COOH); 7.98-7.83 (2H, m, Ar-H); 7.32 (2H, d, $^2J_{H,H}$=8Hz, Ar-H); 6.76 (1H, d, $^2J_{H,H}$=8Hz, NH); 6.61 (2H, dt, $^2J_{H,H}$=12Hz, CH from Ar-H); 6.51 (2H, dt, $^2J_{H,H}$=12Hz, CH from Ar-H); 4.79 (1H, m, CH from Glu rest); 3.85 (2H, t, $^3J_{H,H}$=12Hz OCH_2 octyl rest); 3.77 (2H, t, $^3J_{H,H}$=12Hz, $NCOCH_2$); 2.52-2.33 (2H, m, CH_2 from Glu rest); 1.68-1.58 (2H, m, OCH_2CH_2 from octyl rest); 1.36-1.23 (10H, m, $OCH_2(CH_2)_5$ from octyl rest); 0.83 (3H, t, $^3J_{H,H}$=12Hz, CH_3 from octyl rest) ^{13}C-NMR (DMSO, 100MHz, δ(ppm)): 170.5 (-CONH); 169.6 (-COOH); 167.5 (CO from aromatic rest); 154.5 (=C-O-) 150.3 (=CHN); 141.9 (C_{arom}); 134.8 (C_{arom}); 132.2 (C_{arom}); 131.3 (C_{arom}); 123.4 (C_{arom}); 67.9 (-NCH from Glu); 67.6 (CH_2 from Glu); 51.4 (CH_2 from Glu); 31.3 (-OCH_2 from octyl rest); 28.9 ((CH_2)$_4$ from octyl rest); 25.6 (CH_2 from octyl rest); 22.2 (CH_2 from octyl rest); 14.0 (CH_3 from octyl rest) FT-IR (KBr, cm^{-1}): v_{max}:: 3349 (w); 2923(m); 2853(m); 1709(vs); 1511(s); 1392(s); 1257(m); 1113(w); 829(m); 720(m).

*Synthesis of γ-L-glutamyl-4-(octyloxy)anilide (**4**)*

A suspension of phthaloyl amide (**3**) (1.6 g, 0.0027 mol) in 25mL methanol was treated with 0.6 mL (0.0122 mol) hydrazine hydrate (100%) with vigorous stirring, under reflux for 3 hours. Then the mixture set aside at room temperature for 24 hours. The precipitate was filtered, well washed with cold methanol and suspended 15 mL acetone at room temperature. The suspension was stirred for 30 minutes, after which it was filtered once more, washed with cold acetone and ether. The dried material was suspended in

10 mL 6N HCl, filtered after 15 minutes from phthalylhidrazide, and aqueous layer was adjusted to pH 6-6.5 with 6M Na_2CO_3 when the final product precipitate. Following filtration, the glutamyl anilide can be purified through dissolving in a 1M Na_2CO_3 solution, followed by reprecipitation with 6N HCl at the isoelectric point.

$C_{19}H_{30}N_2O_4$ (**4**); pale grey-blue solid; MW = 350.4525; mp = 204-205^{0}C; Yield 88%; TLC analysis: R_f = 0.58 (1-propanole:acetic acid:water = 8:1:1 (v/v/v)) visualization with ninhydrin ethanolic solution or I_2 vapor; Elemental analysis (%) calcd(found): C: 65.12(65.39); H: 8.63(8.51); N: 7.99(8.12); HRMS (ESI+) [M+Na]: 373.2112 (molecular peak); [M+H]: 351.2292; Exact Mass: 350.2206; $[\alpha]_{546}^{25} = +42\ (c = 0.25,\ \ DMSO + HCl\,0.5N)$.

^{1}H-NMR (DMSO, 400MHz, δ(ppm)): 10.13 (1H, s, -COOH) 8.65-8.59 (1H, bs, NH); 7.46 (2H, d, $^2J_{H,H}$=12Hz, H_7, H_{11}, Ar-H); 6.79 (2H, d, $^2J_{H,H}$=12Hz, H_8, H_{10}, Ar-H); 3.92-3.83 (3H, overlapped signals from NH_2 and H_2); 2.15-2.01 (2H, m, H_3); 1.65-1.58 (6H, m, H_4, H_{12}, H_{13}); 1.31-1.19 (10H, m, $H_{14\text{-}18}$); 0.79 (3H, t, $^3J_{H,H}$=12Hz, H_{19}); ^{13}C-NMR (DMSO, 100MHz, δ(ppm)): 170.9 (C_5); 169.7 (C_1); 145.9 (C_9); 132.4 (C_6); 121.0 (C_8, C_{10}); 114.7 (C_7, C_{11}); 67.9 (C_{12}); 51.8 (C_2); 31.8 (C_{17}); 31.6 (C_4); 29.1, 29.0, 29.0 (C_3, C_{13}, C_{15}); 26.1 (C_{16}); 25.9 (C_{14}); 22.4 (C_{18}); 14.3 (C_{19}); FT-IR(KBr, cm^{-1}): ν_{max}: 3277(s); 2959(s); 2932(vs); 2852(s); 1655(vs); 1628(m); 1582(vs); 1542 (m); 1513(m); 1452(s); 1338(s); 1248(s); 1075(m); 865(m); 687(m).

REFERENCES

1. S. S. Tate; A. Meister; *Methods Enzymol.*,**1985**, *113*, 400-419
2. S. J. Ali; A. A. Bazzaz; A. I. Arif; *Adv. Biosci. Biotechnol.*, **2017**, *8*, 324-341
3. A. Menard; R. Castonguay; C. Lherbet; C. Rivard; Y. Roupioz; J. W. Keillor; *Biochemistry*, **2001**, *40*, 12678-12685
4. M. Kriegelstein; A. Marek; *J. Label Compd. Radiopharm.*, **2022**, *65*, 244-253
5. T. Shirosaki; S. Chowdhury; M. Takafuji; D. Alekperov; G. Popova; H. Hachisako; H. Ihara; *J. Mater. Res.*, **2006**, *21(5)*, 1274-1278
6. M. I. Hossain; A. G. Thomas; F. Mahdi; A. T. Adam; N. S. Akins; M. M. Woodard; J. J. Paris; B. S. Slusher; H. V. Le; *RSC Adv.*, **2021**, *11*, 7115-7128
7. M. I. H. Khan; F. Mahdi; P. Penfornis; N. S. Akins; M. I. Hossain; S. J. Kim; S. P. Sulochana; A. T. Adam; T. D. Tran; C. Tan; P. P. Claudio; J. J. Paris; H. V. Le; *Bioorg. Med. Chem.*, **2023**, *78*, 117137 10.1016/j.bmc.2022.117137
8. D. K. Moon; H. N. Kim; S. H. Park; Y. J. Lee; J. H. Won; M. S. Jung; *Pat. US 9335442 B1 2016-05-10*, **2016**
9. S. A. Al-Zahrani; M. T. Khan; V. Jevtovic; N. Masood; Y. A. Jeilani; H. A. Ahmed; F. M. Alfaidi; *Crystals*, **2023**, *13*, 645

10. J. Y. Al-Humaidi; S. A. Alissa; K. D. Katariya; K. A. Abu Al-Ola; M. Hagar; K. D. Khalil; *Molecules*, **2021**, *26*, 3035
11. A. Z. Omar; M. A. El-Atawy; M. S. Alsubaie; M. L. Alzami; H. A. Ahmed; E. A. Hamed; *Crystals*, **2023,** *13*, 378
12. M. A. El-atawy; M. M. Naoum; S. A. Al-Zahrani; H. A. Ahmed; *Molecules*, **2021**, *26*, 1927
13. A. Z. Omar; M. L. Alazmi; M. S. Alsubaie; E. A. Hamed; H. A. Ahmed, M. A. El-Atawy, *Molecules*, **2023**, *28*, 3804
14. B. N. Sunil; W. S. Yam; G. Hegde; *RSC Adv.* **2019**, *9*, 40588-40606
15. H. Yao-Dong, T. Wei; Y. Yu-Qin; F. Dong-Li; *Tetrahedron*, **2014**, *70(6)*, 1274-1282
16. B. P. Cao; X. W. Shi; X. Ding; Y. M. Wu; K. Matsumoto; H. Okamoto; Q. Xiao; *RSC Adv.* **2022**, *12*, 33589-33597
17. H. A. Ahmed; M. A. El-Atawy; F. A. Alamro; N. S. Al-Kadhi; O. A. Alhaddad; A. Z. Omar; *Molecules*, **2022**, *27*, 8980
18. M. A. El-Atawy; M. S. Alsubaie; M. L. Alazmi; E. A. Hamed; D. H. Hanna; H. A. Ahmed; A. Z. Omar; *Molecules*, **2023**, *28*, 6420
19. M. J. Alvaro-Martins; V. Railean; F. Martins; M. Machuqueiro; R. Pacheco; S. Santos; *Molecules*, **2023**, *28*, 1877
20. N. Bayrak; H. Yildirim; M. Yildiz; M. O. Radwan; M. Otsuka; M. Fujita; H. I. Ciftci; A. F. Tuyun; *Chem. Biol. Drug Des.* **2020**, *95(3)*, 343-354
21. E. M. Kara; N. Bayrak; H. Yildirim; M. Yildiz; B. O. Celik; A. F. Tuyun; *Folia Microbiol,* **2020**, *65(5)*, 785-795
22. G. Evindar; H. Deng; S. G. Bernier; E. Doyle; J. Lorusso; B. A. Morgan; W. F. Westlin; *Bioorg. Med. Chem. Lett.*, **2013**, *23(2)*, 472-475
23. K. Taleb; M. Mohamed-Benkada; N. Benhamed; S. Saidi-Besbes; Y. Grohens; A. Derdour; *J. Mol. Liq.*, **2017**, *241*, 81-90
24. C. Morar; P. Lameiras; A. Bende; G. Katona; E. Gal; M. Darabantu; *Beilstein, J. Org. Chem.*, **2018**, *14*, 1704-1722
25. C. Sacalis; C. Morar; P. Lameiras; A. Lupan; R. Silaghi-Dumitrescu; A. Bende; G. Katona; D. Porumb; D. Harakat; E. Gal; M. Darabantu; *Tetrahedron*, **2019**, *75*, 130486
26. S. Ionescu-Zinca; P. Lameiras; D. Porumb; E. Gal; M. Darabantu; *Studia UBB Chemia*, **2020**, *65(1)*, 39-54
27. H. Gu; Y. Jiang; *Org. Prep. Proc. Int.*, **2004**, *36(5)*, 479-481
28. G. Speranza; M. Rabuffetti; N. Vidovic; C. F. Morelli; *Molbank*, **2020**, *M1147*, https://doi.org/10.3390/M1147
29. I. Cristea; S. Mager; C. Batiu; G. Ple; *Rev. Roum. Chim.*, **1994**, *39(12)*, 1435-1441
30. C. Sacalis; S. Jahiji; A. Avram; *Studia UBB Chemia*, **2022**, *67(4)*, 337-352
31. I. Abdiji; C. Sacalis; A. Shabani; A. Jashari; *J. Nat. Sci. Math.*, **2023**, *8(15-16)*, 72-81
32. C. Sacalis; F. Goga; C. Somesan; *Studia UBB Chemia*, **2018**, *63(4)*, 51-63
33. I. Fleming; D. Williams; Infrared and Raman Spectra, In: *Spectroscopic Methods in Organic Chemistry*, 7th Ed., Springer, Cham, Switzerland, **2019**, Chapter 3, pp. 91-98, 111-118, https://doi.org/10.1007/978-3-030-18252-6_3
34. J. Clayden; N. Greeves; S. Warren; Determining organic structure, In: *Organic Chemistry*, 2th Ed., Oxford University Press Inc., New York, US, **2012**, Chapter 3, pp. 63-69

STUDIA UBB CHEMIA, LXX, 3, 2025 (p. 141-154)
(RECOMMENDED CITATION)
DOI:10.24193/subbchem.2025.3.10

THE ROLE OF VITAMIN B_6 IN THE CHEMICAL SELF-PURIFICATION PROCESSES OF AQUATIC SYSTEMS

Viorica GLADCHI[a], Gheorghe DUCA[b], Vladislav BLONSCHI[a], Maxim CISTEACOV[a], Angela LIS[a,*]

ABSTRACT. Water resources can constantly renew themselves due to their self-purification capacity, but anthropogenic activities reduce the intensity of these self-purification processes. One of the organic substances present in water is vitamin B_6, which is present in surface waters as a result of biological processes in water bodies or as a result of anthropogenic impact. So, the changes in vitamin B_6 were examined using test systems that included substances involved in the self-purification of natural waters: dissolved oxygen, hydrogen peroxide, and copper (II) ions. Analysis of the results obtained shows that vitamin B6 efficiently degrades by reacting with dissolved oxygen in the presence of copper ions. This indicates that the substrate is not persistent and can be easily removed from the aqueous environment.

Keywords: *vitamin B_6; pyridoxine; dissolved oxygen; hydrogen peroxide, copper (II) ions.*

INTRODUCTION

Water is an essential component of the natural environment and the basis of many types of industrial activities. In recent decades, there has been a growing concern about the quality of natural water and various problems associated with the availability, use, and management of water resources.

[a] *Moldova State University, Faculty of Chemistry and Chemical Technology, 60 Mateevici str., MD-2019, Chisinau, Republic of Moldova*
[b] *Moldova State University, Institute of Chemistry, 3 Academiei str., MD-2028, Chisinau, Republic of Moldova*
* *Corresponding author:* angela.lis@usm.md

Water quality assessment has become an important issue, since scientists predict that fresh water will become a scarce resource in the future. Deterioration of water quality is a serious degradation of the environment due to anthropogenic load. The presence of organic substances of various kinds in natural waters is an urgent global problem that requires constant assessment and study. When these substances significantly reduce the self-purification capacity of natural waters, the problem intensifies [1]. Self-purification of natural waters is a complex process that simultaneously includes physical, chemical, and biological processes. Self-purification of water and improvement of its quality are necessary for the self-sustaining of the aquatic ecosystem. Therefore, it is important to study the participation of various substances with reducing properties in the processes of chemical self-purification of water bodies.

Vitamin B_6 (pyridoxine), a biologically active organic compound, can enter surface waters through both natural and anthropogenic pathways. Anthropogenic inputs come from industrial effluents, wastewater discharge, and agricultural runoff, whereas natural sources include phytoplankton, aquatic bacteria, and decomposing plant matter. Despite its low concentration, vitamin B_6 can be found in a variety of chemical forms, including phosphorylated derivatives of pyridoxine, pyridoxal, and pyridoxamine [2].

The concentration of vitamin B_6 in natural waters is generally very low and varies depending on the water source and environmental conditions [3, 4]. Data on vitamin B6 concentrations in various aquatic systems are limited. A study conducted in the Western Atlantic Ocean (at the mouth of the Amazon River) reported vitamin B_6 concentrations ranging from undetectable levels to 36 pM, equivalent to 0–7.4 ng/L [3]. In another study on the Osun River (Nigeria), pyridoxine concentrations ranging from 71.6 to 622.8 µg/L, or approximately $4.26 \cdot 10^{-4}$ to $3.68 \cdot 10^{-3}$ M, were detected. These higher values may be attributed to anthropogenic activities and the presence of specific phytoplankton species [4].

The behavior of vitamin B_6 in aquatic environments is a little-studied topic. However, it is known that vitamin B6 is unstable in water, being readily degraded in the presence of light and oxygen [5-10]. Under aerobic conditions, pyridoxine can be oxidized to form pyridoxal (Scheme 1), a process that is favored by alkaline pH and the presence of transition metals (Fe^{3+}, Cu^{2+}), which catalyze redox reactions [5–8].

Exposure to UV light (260–320 nm) causes cleavage of the pyridoxine side chain, leading to the formation of degradation products such as aldehydes, carboxylic acids, and other compounds. These photochemical products resulting from pyridoxine degradation no longer possess biological activity [9–11].

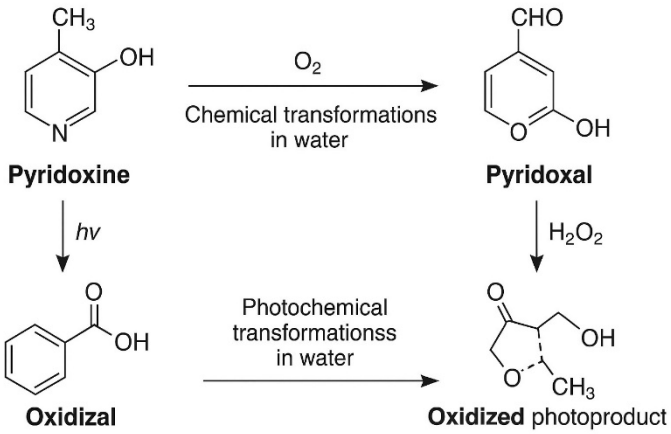

Ehrenshaft et al., 2006, Gregory, 1998, Combs, 2012

Scheme 1. Chemical and photochemical transformations of pyridoxine [7, 9]

Studies have shown that vitamin B_6 exhibits significant antioxidant properties. Therefore, it is important to investigate its role in aquatic environments.

The aim of this study is to evaluate the contribution of vitamin B_6 to the self-purification processes of aquatic systems. We undertook the following tasks to attain this objective:

- to study the efficiency and mechanisms of redox transformations of vitamin B_6 using model systems;
- to determine the kinetic parameters of redox reactions involving vitamin B_6 and assessing its persistence in aquatic systems.

RESULTS AND DISCUSSION

Dissolved oxygen is the most common oxidizing agent in natural waters, typically present at concentrations ranging from 0 to 15 mg/L. However, under normal conditions, it is relatively inert due to its triplet ground state. Therefore, to participate in oxidation processes, it must first be activated—either by sunlight or by interaction with substances possessing reducing properties [11]. Given its constant presence in surface waters, it is of interest to study its interaction with vitamin B_6 in aqueous solutions.

To investigate this, a simplified system (1) was modeled: B_6-$H_2O_{dist.}$-O_2. During the experiments, the concentration of dissolved oxygen in the system was maintained at $3.0 \cdot 10^{-4}$ M. To study the oxidation of vitamin B_6 by dissolved oxygen, five subsystems were modeled in which the initial concentration of the

vitamin varied from $1.0 \cdot 10^{-5}$ M to $5.0 \cdot 10^{-5}$ M, while the oxygen concentration remained constant—corresponding to its saturation level at 20 ºC (approximately $3.0 \cdot 10^{-4}$ M).

Analysis of the kinetic data showed that vitamin B_6 is resistant to oxidation by dissolved oxygen alone. Only a slight decrease in vitamin concentration over time was observed, and the reaction rates were very low ($W_{300} \approx 10^{-10}$ M/s).

Given that natural waters also contain transition metal ions—particularly Cu(II) ions [12]—these were added to the simulated systems at concentrations consistent with those found in natural environments (10^{-7} to 10^{-6} M). To investigate catalytic processes involving dissolved oxygen, the following system was modeled: *vitamin B_6-$H_2O_{dist.}$-O_2-Cu(II)* (system *2)*. In this system, a series of subsystems was created by varying the concentration of one component at a time while keeping the others constant. For determination of partial order with respect to all components of the modeled systems, the method of initial rates using logarithmic transformation was applied. Thus, for determination of partial order with respect to vitamin B_6, in the system 2, the initial concentration of vitamin $(2.48\text{-}8.92) \cdot 10^{-4}$ M was varied, and the concentration of Cu(II) ions was kept constant. The graphical representation of *log W* (initial rate) versus the log of the system's initial vitamin B_6 concentration was used to calculate the partial order with respect to vitamin B_6 (Figure 1). The data for determining the reaction order with respect to vitamin B_6 during catalytic oxidation with dissolved oxygen are presented in the Table S.1.1.

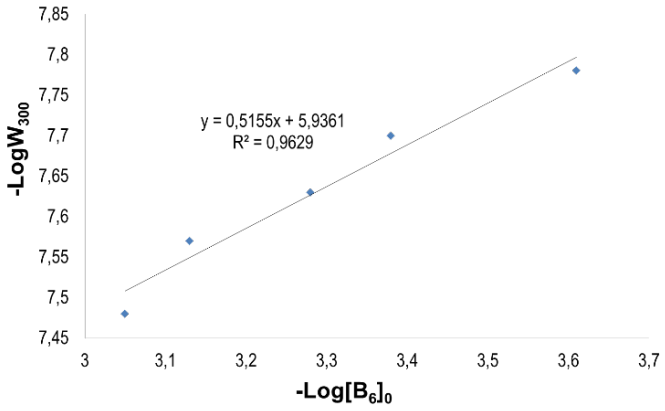

Figure 1. Determination of the partial order (log-log plot of rate vs. [B_6]) for the catalytic oxidation with dissolved oxygen ([Cu(II)]=*const.*=$3 \cdot 10^{-6}$ M, 20ºC, pH=*const.*=7) [own data]

From Figure 1 it was established that the partial order with respect to vitamin B_6 is ≈ 0.5.

In the same way, the partial order of reaction towards Cu(II) ions was determined by varying their concentration in the system and keeping the concentration of vitamin B_6 constant (Figure 2).

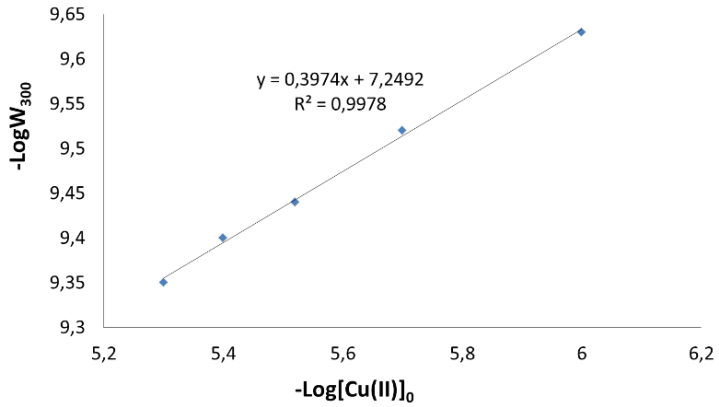

Figure 2. Determination of the partial order (log-log plot of rate vs. [Cu(II)]) for the catalytic oxidation with dissolved oxygen ([B_6]=*const.*=$3 \cdot 10^{-4}$ M, 20ºC, pH=*const.*=7) [own data]

The data for determining the reaction order with respect to Cu(II) ions during catalytic oxidation with dissolved oxygen are presented in the Table S.1.2.

From Figure 2 it was established that the partial order with respect to vitamin Cu(II) ions is ≈ 0.4, and the apparent constant in these systems is $2 \cdot 10^{-5}$ s^{-1}.

Using chemical kinetics methods, a rate equation (equation 1) was derived to express the rate-law dependence of the reaction rate on the concentrations of the system's components:

$$W = k \cdot [B_6]^{0,5} \cdot [Cu(II)]^{0,4} \quad (1)$$

where k is the rate constant (s^{-1}), which is influenced by the temperature, the concentration of dissolved oxygen in the water, and the pH value. Thus, it was found that this is a first-order reaction. Based on the law of first-order reactions, the reaction constant and half-life were calculated.

The average value of the effective constant was also calculated, which is equal to $5.31 \cdot 10^{-5}$ s^{-1}. Based on the obtained value of the effective constant k, the half-life was established to be (218 ± 0.23) min.

Hydrogen peroxide is one of the important oxidizing agents in natural waters, participating in various reactions that influence the redox state of aquatic systems. Numerous studies indicate that average hydrogen peroxide concentrations in surface waters range from 10^{-7} to 10^{-5} M [13–15]. The highest concentrations of H_2O_2 typically occur during the day under solar radiation, while the lowest levels are observed at night in the absence of sunlight. To investigate the transformation processes of vitamin B6, the following system was modeled (3): *vitamin* B_6-$H_2O_{2\,dist.}$-H_2O_2. For this model system, kinetic patterns were established, and a rate equation was derived to describe the dependence of the vitamin transformation rate on the concentrations of the system's components.

Using the calculated partial reaction orders of the system components (Figure 3 (A) and (B)), the following kinetic equation (equation 2) was obtained, reflecting the power-law dependence of the reaction rate on component concentrations:

$$W = k \cdot [B_6]^{0.7} \cdot [H_2O_2]^{0.5} \quad (2)$$

where k is the rate constant (s^{-1}), which is influenced by the temperature, the concentration of dissolved oxygen in the water, and the pH value.

The data for determining the reaction order with respect to vitamin B_6 and H_2O_2 during oxidation with hydrogen peroxide are presented in the Tables S.2.1 and S.2.2.

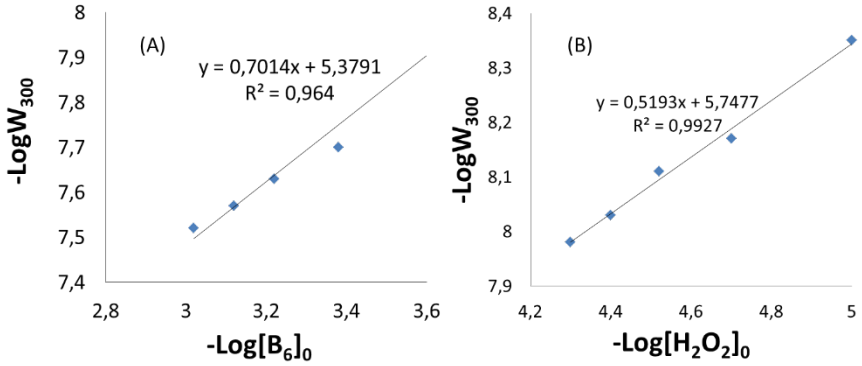

Figure 3. Determination of the partial order in the system *vitamin* B_6-$H_2O_{2\,dist.}$-H_2O_2, for the oxidation with hydrogen peroxide: *A* - log-log plot of rate vs. [B_6], [H_2O_2]=*const.*=$3 \cdot 10^{-5}$ M; B - log-log plot of rate vs. [H_2O_2], [B_6]=*const.*=$3 \cdot 10^{-4}$ M; 20ºC, pH=*const.*=7 [own data]

For the oxidation of vitamin B_6 by hydrogen peroxide, the effective rate constant was calculated to be $3.55 \cdot 10^{-5}$ s^{-1}. Based on this rate constant (k), the half-life ($\tau_{1/2}$) of the process was determined to be (325±0.65) min.

Metal ions with variable valence, particularly Cu(II) ions, play an important role in reactions involving hydrogen peroxide. In the presence of dissolved oxygen, these metal ions remain in an oxidized state and are involved in the activation of both oxygen and hydrogen peroxide. Once activated, these species interact with various substrates, facilitating their transformation and acting as catalysts in oxidation processes [11, 12]. Therefore, it is important to study the oxidation of vitamin B_6 by hydrogen peroxide in the presence of Cu(II) ions.

As in the previous experiments, a system (4) was modeled consisting of the following components: *vitamin B_6-$H_2O_{dist.}$-H_2O_2-O_2-Cu(II)*. The principles of chemical kinetics were applied to this system to determine the partial reaction orders (Figure 4 (A), (B) and (C), derive an expression for the reaction rate, and calculate the effective rate constant.

Thus, the kinetic equation can be expressed as in equation 3:

$$W = k \cdot [B_6]^{1.2} \cdot [H_2O_2]^{0.5} \cdot [Cu(II)]^{0.3} \quad (3)$$

The effective rate constant at different concentrations of components in the systems is $4.22 \cdot 10^{-5}$ s^{-1}, which is influenced by the temperature, the concentration of dissolved oxygen in the water, and the pH value. Based on this rate constant (k), the half-life ($\tau_{1/2}$) of the process was determined to be (274±0.75) min.

The data for determining the reaction order with respect to vitamin B_6, H_2O_2 and Cu(II) ions during catalytic oxidation with hydrogen peroxide are presented in the Tables S.3.1, S.3.2 and S.3.3.

The experimental data can be interpreted as follows. In the presence of copper ions, oxygen oxidizes pyridoxine significantly faster than in their absence. This acceleration occurs because copper ions act as catalysts, facilitating the activation of molecular oxygen and enhancing the transfer of electrons from pyridoxine to oxygen.

Molecular oxygen itself is a relatively weak oxidizing agent under normal conditions. Consequently, the oxidation of pyridoxine proceeds very slowly and typically requires either elevated temperatures or extended reaction times. However, in the presence of copper ions, pyridoxine forms coordination complexes with copper, which can activate molecular oxygen and promote its conversion into more reactive species, such as the superoxide anion (O_2^-•), hydroxyl radical (•OH), and hydrogen peroxide (H_2O_2). These reactive oxygen species efficiently oxidize pyridoxine to pyridoxal or other products [16–19].

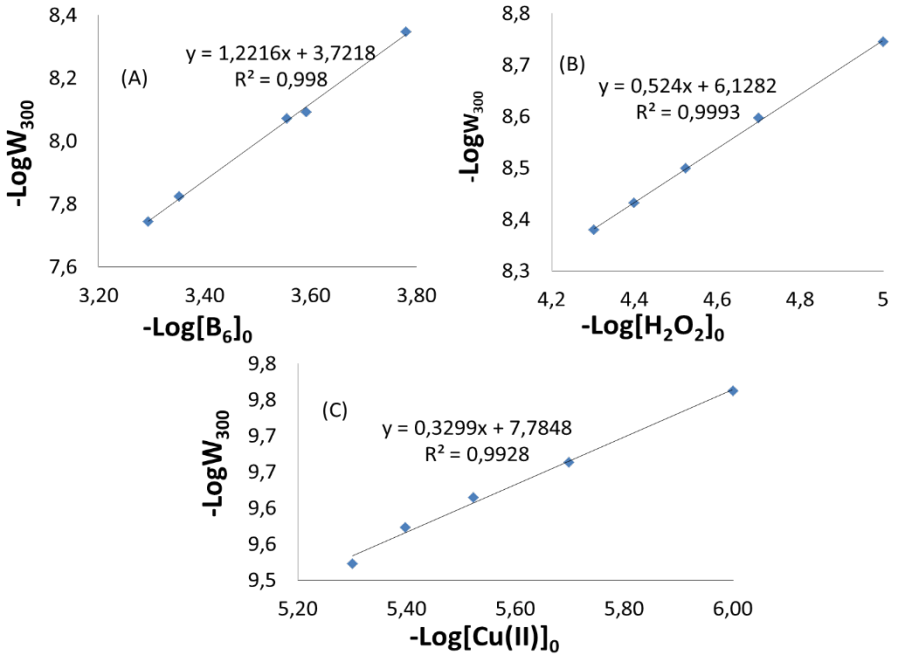

Figure 4. Determination of the partial order in the system B_6-$H_2O_{dist.}$-H_2O_2-O_2-*Cu(II),* for the catalytic oxidation with hydrogen peroxide: *A* - log-log plot of rate vs. [B_6], [H_2O_2]=*const.*=$3\cdot10^{-5}$ M, [Cu(II)]=*const.*= $3\cdot10^{-6}$ M; B - log-log plot of rate vs. [H_2O_2], [B_6] =*const.*= $3\cdot10^{-4}$ M, [Cu(II)]=*const.*=$3\cdot10^{-6}$ M; C - log-log plot of rate vs. [Cu(II)], [B_6]=*const.*=$3\cdot10^{-4}$ M, [H_2O_2]=*const.*=$3\cdot10^{-5}$ M; 20ºC, pH=*const.*=7 [own data]

Taking into account the structural features of pyridoxine and by analogy with similar systems, the following mechanism of its oxidation in the presence of copper ions and oxygen can be proposed:

1. Complexation and reduction of Cu^{2+} to Cu^{+}:

Pyridoxine coordinates with Cu^{2+} ions to form an active complex. When pyridoxine (vitamin B_6) interacts with copper(II) ions (Cu^{2+}), a complexation reaction occurs, resulting in the formation of coordination complexes, reaction 4. These complexes are stable in aqueous solutions and can contain one or two pyridoxine ligands per copper ion:

$$Cu^{2+} + n\ PN \rightleftharpoons [Cu(PN)n]^{2+} \qquad (4)$$

where PN is pyridoxine; *n=1* or *2,* depending on the reaction conditions and *pH* of the medium.

The interaction mechanism includes three main stages [16–18]:

- coordination of donor atoms:
  pyridoxine contains several donor centers: a hydroxyl group, an amino group, and a pyridine ring. Copper(II) ions can coordinate to the nitrogen atom of the pyridine ring and to the oxygen atoms of the hydroxyl groups;
- complex formation:
  the formation of both 1:1 and 1:2 complexes (metal:ligand) in aqueous solution was observed, especially at pH 5–7. This conclusion is supported by spectrophotometric and conductometric data;
- reduction of Cu^{2+} to Cu^{+}, reaction 5:
  pyridoxine can act as a reducing agent by interacting with copper(II) ions, reducing them to copper(I), while itself undergoing oxidation:

$$Cu^{2+}+PN \rightarrow Cu^{+}+PN^{\cdot+} \quad (5)$$

where $PN^{\cdot+}$ is the oxidized pyridoxine cation radical.

2. Oxygen activation:

Further interaction of Cu^{+} with molecular oxygen can lead to the formation of reactive oxygen species, reaction 6:

$$Cu^{+}+O_2 \rightarrow Cu^{2+}+ O_2^{\cdot-} \quad (6)$$

In addition, copper(II) ions can bind with superoxide anions to form superoxide complexes, reaction 7 [20]:

$$Cu^{2+}+ O_2^{\cdot-} \rightarrow [Cu^{2+}(O_2^{\cdot-})]^{+} \quad (7)$$

This process is accompanied by the formation of reactive oxygen species such as hydroxyl radicals (•OH) and hydrogen peroxide (H_2O_2), which participate in subsequent oxidation reactions [21].

3. Substrate oxidation:

The reactive intermediates transfer electrons from pyridoxine to oxygen, resulting in its oxidation to corresponding products such as pyridoxal or pyridoxic acid.

The non-catalytic oxidation of pyridoxine by hydrogen peroxide is a complex process that has not been sufficiently studied in the scientific literature. This reaction proceeds very slowly under neutral conditions and typically requires either highly acidic environments or elevated temperatures [22–23].

However, there are studies focusing on the interaction of pyridoxine with H_2O_2 in the presence of catalysts, as well as general information on the oxidation of pyridine derivatives [24–30].

The catalytic oxidation of pyridoxine by hydrogen peroxide in the presence of copper ions is an intriguing process that may have applications in both biochemical research and environmental chemistry. Although direct studies on this specific reaction are limited, existing data suggest a possible mechanism.

Analogies with the oxidation of other compounds in the presence of copper ions and hydrogen peroxide suggest the following mechanism [27–28]:

1. *Complexation*:

Pyridoxine coordinates with copper(II) ions to form an active complex (4).

2. *Activation of hydrogen peroxide*:

The copper(II) complex reacts with H_2O_2 to form reactive copper-peroxide intermediates, reactions (8) and (9). This step is analogous to the formation of complexes capable of electrophilic or nucleophilic reactions with organic substrates [29–30]:

$$[Cu^{2+}(PN)]+H_2O_2 \rightarrow [Cu^{+}(PN)]+HO_2^{\cdot}+H^{+} \quad (8)$$

$$[Cu^{+}(PN)]+H_2O_2 \rightarrow [Cu^{2+}(PN)]+OH^{-}+{\cdot}OH \quad (9)$$

1. Oxidation of pyridoxine:

The active intermediates transfer electrons from pyridoxine to oxygen, resulting in its oxidation to corresponding products such as pyridoxal, reactions (10) and (11) [31]:

$$PN\text{-}CH_2\text{-}OH+{\cdot}OH \rightarrow PN\text{-}CH^{\cdot}\text{-}OH+H_2O \quad (10)$$

$$PN\text{-}CH^{\cdot}\text{-}OH+{\cdot}OH \rightarrow PN\text{-}CHO+ H_2O \quad (11)$$

2. Catalyst regeneration:

The reduced copper(I) ion is oxidized back to copper(II), completing the catalytic cycle, reaction (12):

$$[Cu^{+}(PN)]+H_2O_2 \rightarrow [Cu^{2+}(PN)]+OH^{-}+{\cdot}OH \quad (12)$$

The experimental data and the key relationship for the catalytic oxidation of the substrate show that Cu (II) ions not only help speed up the reaction but also take part in the changes happening during the process. The partial order of reaction after Cu (II) ions, which is valued at 0.3, indicates its insignificant influence on the transformation of vitamin B_6, but it still exists. In this case, the oxidation proceeds according to a cyclic mechanism, in which the role of the active particle that directly participates in the oxidation of the substrate is played by the metal ion in the oxidized form. In this case, oxygen or hydrogen peroxide mainly helps to turn the metal back into its oxidized form after it has been changed to its reduced form during the oxidation of the substrate.

Schematically, these transformations can be presented as follows [11, 32]:

- oxidation of the substrate and reduction of the transition metal ion (Cu^{2+}):

$$2Cu^{2+} + DH_2 \rightarrow 2Cu^{+} + D + 2H^{+} \quad (13)$$

- regeneration of the oxidized form of the metal:

$$2Cu^{+} + O_2(H_2O_2) + 2H^{+} \rightarrow 2Cu^{2+} + H_2O_2\ (2H_2O) \quad (14)$$

Thus, the copper ion cyclically switches between oxidation states II and I, activating O_2 or H_2O_2 and continuously generating oxidizing radicals that convert pyridoxine to pyridoxal.

CONCLUSIONS

The most efficient process for vitamin B_6 oxidation is the catalytic oxidation by dissolved oxygen in water, which exhibits the highest rate constant and the lowest half-life. The slowest oxidation occurs with hydrogen peroxide, with a half-life of 5 h 25 min 25 s. When copper ions are added to the B_6-H_2O_2 system, the reaction rate increases significantly, confirming the catalytic role of copper ions in surface waters.

The rate of oxidation in the B_6-O_2-Cu (II) system is higher than in the B_6-H_2O_2-Cu (II) system. This indicates that vitamin B_6 is more readily oxidized by catalytically activated dissolved oxygen than by hydrogen peroxide. Considering that the concentration of hydrogen peroxide varies throughout the day and may sometimes be absent in surface waters, while dissolved oxygen is always present, this scenario ensures the continuous catalytic decomposition of vitamin B_6. Consequently, chemical self-purification via redox transformations involving vitamin B_6 occurs both day and night.

Since vitamin B_6 is effectively oxidized catalytically by dissolved oxygen, its degradation in the aqueous medium can lead to the accumulation of additional hydrogen peroxide, which is an active intermediate product of oxygen reduction. The presence of copper ions positively influences the redox processes involving vitamin B_6, with catalytic activity being most pronounced in the B_6-O_2-Cu (II) system.

The analysis of the results indicates that the presence of vitamin B_6 in the aqueous medium can positively influence chemical self-purification processes. The following points support this assertion:

a) vitamin B_6 is effectively degraded by dissolved oxygen in the presence of copper ions, which is beneficial because it does not require additional reagents or special conditions. Moreover, the short half-life suggests that the substrate is not persistent, enabling its easy removal from the aqueous medium.

b) the efficient oxidation of vitamin B_6 by dissolved oxygen produces additional hydrogen peroxide. The accumulation of extra H_2O_2 helps maintain the oxidative state of the water and supports hydrogen peroxide's role in redox reactions involving peroxidase substrates.

c) the fact that hydrogen peroxide and Cu(II) ions do not significantly accelerate vitamin B_6 oxidation is advantageous for the aquatic environment, as these components remain available to participate in other biochemical processes.

EXPERIMENTAL SECTION

To study the kinetics of vitamin B_6 transformations in aqueous solutions using model systems, a direct spectrophotometric method was employed, utilizing a phosphate buffer at pH 7. The optical density of the solution was measured at 328 nm to determine substrate concentrations. Under laboratory conditions, the following redox systems were modeled: *Vitamin B_6-$H_2O_{dist.}$-O_2 (1); Vitamin B_6-$H_2O_{dist.}$-O_2-Cu(II) (2); Vitamin B_6-$H_2O_{dist.}$-O_2-H_2O_2 (3); Vitamin B_6-$H_2O_{dist.}$-O_2-H_2O_2-Cu(II) (4)*. All systems were investigated under aerobic conditions, with dissolved oxygen acting as a key oxidant in the aquatic environment. Hydrogen peroxide (H_2O_2), a naturally occurring oxidant in surface waters, was added in systems (3) and (4). The addition of copper(II) compounds in systems (2) and (4) is justified by their environmental relevance and the catalytic role of Cu(II) ions in the redox transformations of pollutants.

Kinetic regularities were studied for each modeled system by varying the concentration of a single component while keeping the others constant. As a result, partial reaction orders were determined, rate equations were derived,

and effective rate constants and substrate half-life values were calculated. The concentrations of components in the model systems were selected to reflect natural conditions: hydrogen peroxide at approximately 10^{-5} M, Cu(II) ions at 10^{-6} M, and vitamin B_6 at 10^{-5} M, ensuring optimal optical density values.

ACKNOWLEDGMENTS

The results have been obtained in the framework of the project 010603 – *Advanced research in computational and ecological chemistry, identification of technological procedures for treatment, formation of water quality and quantity*, Institute of Chemistry of the Moldova State University.

REFERENCES

1. H. P. H. Arp; S. E. Hale; *ACS Environ. Au*, **2022**, 2, 482–509, DOI: 10.1021/acsenvironau.2c00024.
2. D. G. Sokač; S. Kovač; V. Bušić; C. R. Martin; J. V. Furač. In *B Vitamins and Folate: Chemistry, Analysis, Function and Effects*, ed. V. R. Preedy, RSC Publishing, Cambridge, **2012**, DOI: 10.1039/9781849734714.
3. L. P. Barada; L. Cutter; J. P. Montoya; E. A. Webb; D. G. Capone; S. A. Sañudo-Wilhelmy; Front. Microbiol., **2013**, 4, 25, DOI: 10.3389/fmicb.2013.00025.
4. M. A. Sneineh; Nutr. Res. Food Sci. J., **2021**, 4(1), 1–9, DOI: 10.31038/NRFSJ.2021411.
5. Food and Nutrition Board, Institute of Medicine, *Dietary Reference Intakes for Thiamin, Riboflavin, Niacin, Vitamin B6, Folate, Vitamin B12, Pantothenic Acid, Biotin, and Choline*, National Academy Press, Washington, DC, **1998**, 592 p., DOI: 10.17226/6015.
6. J. E. Leklem; *In Handbook of Vitamins*, 3rd ed.; R. B. Rucker; J. W. Suttie; D. B. McCormick; L. J. Machlin, Eds.; Marcel Dekker: New York, **2001**; 600 p.; ISBN: 0-8247-0428-2.
7. G. F. Combs. *The Vitamins: Fundamental Aspects in Nutrition and Health*, 4th ed., Academic Press, **2012**, 598 p., ISBN: 9780123819802.
8. K. Dakshinamurti; S. Dakshinamurti; M. P. Czubryt. In *Handbook of Famine, Starvation, and Nutrient Deprivation*, ed. V. Preedy and V. Patel, Springer, Cham, **2017**, DOI: 10.1007/978-3-319-40007-5_81-1.
9. C. Bueno; P. Pavez; R. Salazar; M. V. Encinas; *Photochem. Photobiol.*, **2010**, 86(1), 39–46, DOI: 10.1111/j.1751-1097.2009.00643.x.
10. I. R. Calori; L. A. Gusmão; A. C. Tedesco; *J. Photochem. Photobiol.*, **2021**, 7, 100041, DOI: 10.1016/j.jpap.2021.100041.

11. Gh. Duca; Iu. Scurlatov; *Ecological Chemistry*, Publishing Center M.S.U., Chisinau, **2002**, 279 pp., ISBN: 9947-70-172-8.
12. I. Mansilla-Rivera; J. O. Nriagu; *J. Great Lakes Res.*, **1999**, 25(4), 599–610, DOI: 10.1016/S0380-1330(99)70765-3.
13. W. J. Cooper; D. R. S. Lean; J. H. Carey; *Can. J. Fish. Aquat. Sci.*, **1989**, 46, 1227–1231, DOI: 10.1139/f89-158.
14. J. A. Rusak; D. A. Vasconcelos; L. Persaud; P. J. Dillon; *Mar. Freshw. Res.*, **2010**, 61, 650–657, DOI: 10.1071/MF10001.
15. P. E. Garcia; M. Diaz; L. E. Bruna; D. M. Pérez; M. A. Piccolo; *Sci. Total Environ.*, **2020**, 727, 138641, DOI: 10.1016/j.scitotenv.2020.138641. DOI: 10.1016/j.scitotenv.2020.138641.
16. J. S. Casas; M. D. Couce; J. Sordo; *Coord. Chem. Rev.*, **2012**, 256(23–24), 3036–3062, DOI: 10.1016/j.ccr.2012.07.001.
17. M. E. Farago; T. Matthews; *J. Chem. Soc. A*, **1969**, DOI: 10.1039/J19690000609.
18. A. Chylewska; M. Biedulska; L. Chmurzyński; M. Makowski; *J. Coord. Chem.*, **2015**, 68, 1–28, DOI: 10.1080/00958972.2015.1088149.
19. G. N. Weinstein; M. J. O'Connor; R. H. Holm; *Inorg. Chem.*, **1970**, 9, 2104–2112, DOI: 10.1021/ic50091a029.
20. S. Fukuzumi; K. D. Karlin; *Coord. Chem. Rev.*, **2013**, 257(1), 187–195, DOI: 10.1016/j.ccr.2012.05.031.
21. Y. Zhang; J. Fan; B. Yang; W. Huang; L. Ma; *Chemosphere*, **2017**, 166, 89–95, DOI: 10.1016/j.chemosphere.2016.09.066.
22. T. M. Nagiev; *Russ. Chem. Rev.*, **1985**, 54(10), DOI: 10.1070/RC1985v054n10ABEH003152.
23. M. B. Smith; *March's Advanced Organic Chemistry: Reactions, Mechanisms, and Structure*, 8th ed., Wiley, **2020**, 2144 pp., ISBN: 978-1-119-37179-3.
24. C. Y. Zhang; L. J. Peng; G. Y. Chen; H. Zhang; F. Q. Yang; *Molecules*, 2022, 27, 4262, DOI: 10.3390/molecules27134262.
25. F. F. Bamoharram; M. M. Heravi; M. Roshani; N. Tavakoli; *J. Mol. Catal. A: Chem.*, **2006**, 252(1–2), 219–225, DOI: 10.1016/j.molcata.2006.02.059.
26. Y. Kaneda; K. Ohnishi; T. Yagi; *Biosci. Biotechnol. Biochem.*, **2002**, 66(5), 1022–1031, DOI: 10.1271/bbb.66.2723.
27. J. Schubert; V. S. Sharma; E. R. White; L. S. Bergelson; *J. Am. Chem. Soc.*, **1968**, 90(16), 4476–4478, DOI: 10.1021/ja01018a061.
28. G. R. A. Johnson; N. B. Nazhat; *J. Am. Chem. Soc.*, **1987**, 109(7), 1990–1994, DOI: 10.1021/ja00241a015.
29. M. H. Robbins; R. S. Drago; *J. Catal.*, **1997**, 170(2), 295–303, DOI: 10.1006/jcat.1997.1754.
30. T. Y. Lin; C. H. Wu; *J. Catal.*, **2005**, 232(1), 117–126, DOI: 10.1016/j.jcat.2005.01.038.
31. J. M. Matxain; D. Padro; M. Ristilä; Å. Strid; L. A. Eriksson; *J. Phys. Chem. B*, **2009**, 113(29), 9629–9632, DOI: 10.1021/jp903023c.
32. Gh. Duca; Yu. Scurlatov; A. Sycev; *Redox Catalysis and Ecological Chemistry*, Publishing Center MSU, Chisinau, **2002**, 316 p., ISBN: 9975-70-170-1.

STUDIA UBB CHEMIA, LXX, 3, 2025 (p. 155-175)
(RECOMMENDED CITATION)
DOI:10.24193/subbchem.2025.3.11

GROUNDWATER QUALITY ASSESSMENT IN DOMESTIC WELLS OF HODĂI-BOIAN, CEANU MARE COMMUNE, ROMANIA

Nicolae-Leontin PETRUȚA[a,*], Ioana Monica SUR[a*], Ioana PETRUȚA[b], Ramona Bianca ŞONHER[a], Tudor Andrei RUSU[a], Timea GABOR[a], Tiberiu RUSU[a]

ABSTRACT. This study provides a comprehensive chemical assessment of groundwater quality from 37 domestic wells in the rural village of Hodăi-Boian, Ceanu Mare commune, Romania, with emphasis on contamination risks arising from anthropogenic activities. Key water quality parameters—nitrites(NO_2^-), nitrates(NO_3^-), ammonium(NH_4^+), pH, turbidity, and electrical conductivity(EC)—were determined according to standardized analytical protocols and compared against Romanian and European regulatory thresholds. Exceedances of the maximum admissible concentration for NO_2^- were detected in seven wells, indicating recent contamination events likely linked to the proximity of animal shelters and latrines. NO_3^- and NH_4^+ concentrations remained below legal limits, although elevated NH_4^+ levels signal persistent microbiological activity. The findings revealed pronounced mineralization and frequent surpassing of conductivity limits, while pH values below 7.0 in selected wells suggested active organic fermentation processes. Water temperature ranged from 11–13 °C, confirming the shallow aquifer character. Correlative analysis demonstrated strong associations between well proximity to pollution sources, livestock density, and water quality deterioration. The results underscore the necessity of regular water quality monitoring, rigorous enforcement of protective distances, and technical improvements to well construction. Strengthening

[a] *Department of Environment Engineering and Entrepreneurship of Sustainable Development, Faculty of Materials and Environmental Engineering, Technical University of Cluj-Napoca, 103–105 Muncii Avenue, 400641 Cluj-Napoca, Romania.*
[b] *Ceanu Mare Secondary School, 381 Principală Street, 407185 Ceanu Mare, Cluj County, Romania.*
[*] *Corresponding authors: Petruta.Em.Nicolae@student.utcluj.ro; ioana.sur@imadd.utcluj.ro*

public health education and upgrading sanitation infrastructure are imperative to mitigate health risks and safeguard the safety of groundwater resources in vulnerable rural environments.

Keywords: *groundwater, water quality*, *physico-chemical parameters, domestic wells, rural area.*

INTRODUCTION

Worldwide, many communities, especially in rural areas, rely on wells as their primary source of drinking water and irrigation. Access to safe and clean drinking water and sanitation is a fundamental human right, essential for the full realization of life and all other human rights [1].

Freshwater resources are facing growing scarcity due to factors such as population growth, urban expansion, and climate change, all of which intensify water stress in many parts of the world [2].

However, poor water quality from wells can be linked to public health problems, leading to water-related epidemics such as cholera [3]. One way to improve water quality is by using water filters [4], but cost often represents a significant impediment.

Groundwater can be accessed via deep boreholes or shallow wells, with the latter being more common in low-income communities due to their lower construction costs and typical private ownership [5]. Water is extracted from shallow wells using a container and rope, and in some cases, manually operated or improvised pulleys, hand pumps, or electric pumps are employed.

The quality of drinking water is undeniably crucial for society, particularly for maintaining a high standard of public health. It is well known that many wells are situated near potential sources of contamination, such as solid waste landfills, which can lead to disease outbreaks.

Moreover, groundwater can dissolve minerals, resulting in undesirable characteristics such as hardness and contamination with toxicants and microorganisms. The use of untreated groundwater has been linked to waterborne diseases such as gastroenteritis, cholera, hepatitis, typhoid fever, and giardiasis, which are caused by bacteria, viruses, and protozoa [6].

The proximity of pollution sources—such as wastewater treatment plants, landfills, or agricultural fields—also affects the concentration of emerging pollutants in the soil. Their presence in agricultural ecosystems adversely affects soil and environmental health, ultimately impacting both ecological and human well-being [7].

The chemistry of water is a key factor in determining its suitability for various uses. Therefore, chemical analysis is crucial for assessing water quality and identifying potential pollutant pathways. Common chemical contaminants found in well water include nitrates (NO_3^-), nitrites ($NO2^-$), ammonium (NH_4^+), chlorides (Cl^-), sulfates (SO_4^{2-}), and heavy metals [8, 9].

Monitoring NO_3^-/NO_2^- levels is essential to ensure that water meets health and safety standards, such as those set by the World Health Organization (WHO) [10]. High NO_3^- levels in water are dangerous for human health, particularly for infants, causing methemoglobinemia or "blue baby syndrome," which reduces the blood's ability to carry oxygen [11].

Moreover, high NO_3^-/NO_2^- concentrations can lead to eutrophication when groundwater enters surface waters, promoting excessive algal growth and reducing oxygen levels in aquatic ecosystems [12]. Chronic exposure to $NO_3^-/NO_2^-$is also associated with certain cancers and thyroid problems in adults [13].

Heavy metals are important as well, as they significantly affect the suitability of water for both irrigation and drinking purposes [14]. For example, one study evaluated the quality of surface water near Baia Mare by determining the concentrations of several heavy metals and comparing contamination levels and overall water quality using the Heavy Metal Evaluation Index (HEI) for 2021 and 2022.

The findings revealed that the HEI value showed a deterioration in water quality in 2022 compared to 2021, which resulted in human exposure to higher health risks of intoxication with the studied metals.

In Romania, several studies have investigated the use of water from wells. S. Burca et al. [15] reported on the quality of shallow wells from Feleacu village, Cluj County, and Sândominic commune, Harghita County [16].

These papers monitored the physico-chemical parameters of shallow wells to assess their suitability for drinking water. Most samples showed moderate to high mineralization, and some were found to be contaminated by organic substances and NO_3^- ions. C. Roba et al. [17] studied the chemistry of groundwater and its suitability for drinking and irrigation purposes in several urban and rural areas from Cluj, Sălaj, Satu Mare, and Alba counties. They reported that a total of 40% of the private wells were suitable for drinking, while 60% were not recommended for high-quantity or long-term consumption.

Moreover, the calculated ingested dose suggested that regular consumption of water from certain private wells poses a significant health risk due to elevated levels of NO_3^- and NO_2^-.

Similarly, Hoaghia et al. [18] performed a detailed health risk assessment for groundwater consumers in the Mediaș area (Sibiu County), showing frequent exceedances of maximum admissible values for NO_3^- and NO_2^- and highlighting the associated non-carcinogenic health risks, particularly for children.

In our previous paper [19], we conducted a rigorous multidisciplinary evaluation of shallow groundwater vulnerability and rural well water quality in Hodăi-Boian, Ceanu Mare commune. Despite NO_3^- and NH_4^+ levels being within legal limits, all tested wells exceeded the legal threshold for NO_2^- and showed microbiological contamination, including E. coli, posing serious health risks.

The present study aimed to analyze the chemical quality of water from wells used for domestic and agricultural consumption in the commune of Ceanu Mare, with a particular focus on the locality of Hodăi-Boian as an area with potentially higher risks regarding the safety of well water.

For this purpose, 37 wells were selected, distributed throughout the commune, considering the type of water use and the proximity to pollution sources such as stables, latrines, and intensively used agricultural areas.

Other parameters considered in this study included the number of inhabitants and large animals for each well, average daily and monthly water consumption, and water level and depth in the well.

The collected water samples were chemically characterized for NO_2^-, NO_3^-, NH_4^+, pH, turbidity, and electrical conductivity (EC), and were compared with allowable values for drinking water.

RESULTS AND DISCUSSION

Characterization of the Studied Households

To enable a rigorous assessment of the chemical risk associated with the use of water from wells in Hodăi–Boian, a descriptive analysis was conducted of the main usage parameters and the local hydrogeological context.

This section synthesizes data regarding the number of inhabitants served by each well, the number of large animals, water consumption, the water level and depth in the well, as well as distances to potential sources of contamination.

The analysis of these variables allows for the identification of key determinants that may directly influence the chemical quality of the water and provides the foundation for interpreting the laboratory results presented later.

Table 1 summarizes the key data concerning water use from 37 wells, highlighting essential parameters for evaluating both contamination risk and the sustainability of the local water resource.

The variables analyzed include the number of inhabitants served, the number of large animals, daily and monthly water consumption, the water level and depth in the well, as well as distances to potential sources of contamination such as stables and latrines.

For the thorough assessment of chemical risks associated with the use of well water in Hodăi–Boian, a descriptive analysis was undertaken of the main operational parameters and the hydrogeological context.

Considered aspects included the number of inhabitants served, the number of large animals, water consumption, the water level and depth in the well, as well as distances from potential sources of contamination.

These variables represent key determinants of the chemical quality of the water and support the interpretation of the laboratory results presented subsequently.

The number of inhabitants served by each well ranges from 1 to 6 (with an average of 2–4 persons), reflecting the specific characteristics of rural households.

The number of large animals varies between 1 and 9, with maximum values recorded at wells 4, 18, and 30, where livestock farming is more developed. This aspect is directly relevant from a chemical perspective, as the presence of a large number of animals favors the accumulation of organic matter and nutrients (nitrogen (N), phosphorus (P)), compounds that can rapidly reach the water source, especially when the distance to stables or latrines is small.

Figure 1 highlights these variations, indicating areas with an increased potential for chemical contamination. It is noteworthy that in many households, the number of animals equals or even exceeds the number of inhabitants, which further increases the pressure on the quality of the water source.

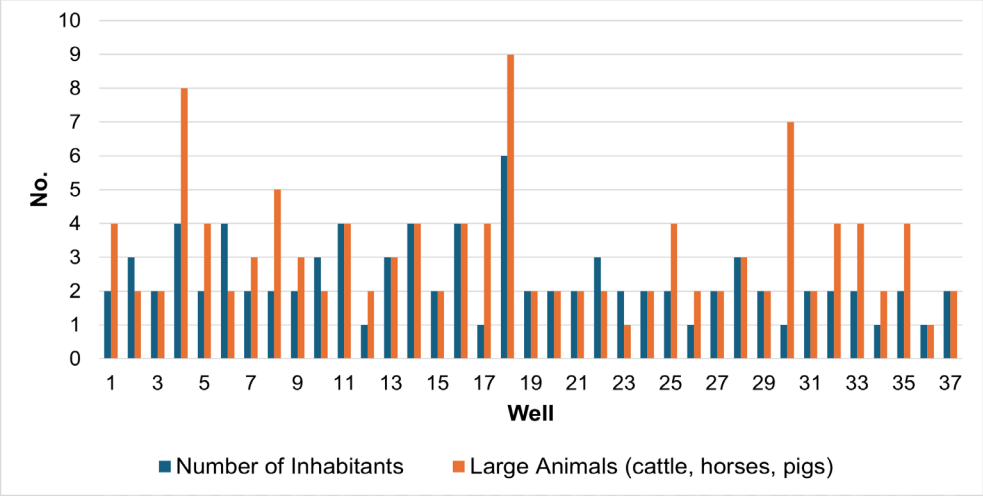

Figure 1. Number of inhabitants and large animals (cattle, horses, and pigs) associated with each well

From a chemical perspective, the simultaneous presence of a large number of animals and short distances to pollution sources represents a major risk factor for the accumulation of NO_2^-, NO_3^-, and NH_4^+ in well water, as well as for the occurrence of high levels of coliform bacteria and other indicators of organic pollution. These effects are often correlated with increased values of electrical conductivity and the total N content in water.

Daily water consumption is relatively constant for most wells (10–60 L), depending on household and livestock needs. Monthly values show significant fluctuations, with maximum levels recorded in households with a higher number of inhabitants and animals (Figure 2).

This pattern can directly influence the chemical dynamics of the water source, accelerating dilution and renewal processes, but also the temporary mobilization of contaminants present in the soil or within the well structure.

In certain hydrogeological contexts, these dynamics favor the transfer of NO_3^-, PO_4^{3-}, or heavy metals into the water mass, increasing risks to human health, especially in households with multiple sources of pollution [20].

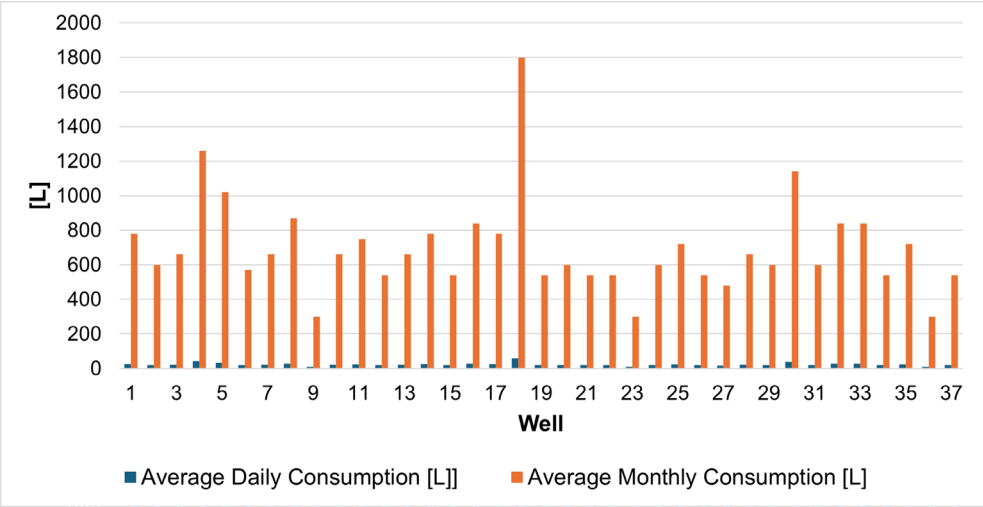

Figure 2. Average daily and monthly water consumption per well

Figure 3 illustrates the variability of water level and the depth of the water column in the analyzed wells. The water level in the wells ranges from 3 to 8 meters, while the depth of the usable water column varies between 1.2 and 3 meters.

Wells with low water levels are more vulnerable to chemical contamination due to their limited dilution capacity and increased sensitivity to external factors such as heavy rainfall or nearby livestock activities.

Under these conditions, there is a high risk of exceeding the permissible concentrations for NO_3^-, phosphates (PO_4^{3-}), and other soluble substances, with a negative impact on water potability [20].

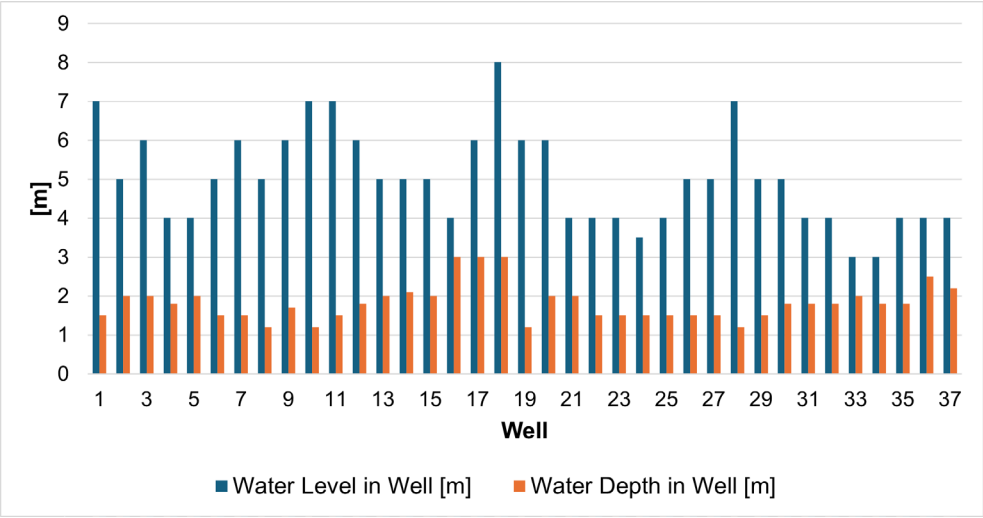

Figure 3. Water level and depth of the water column in each well (m)

Figure 4 highlights the distribution of distances between wells and potential sources of pollution (stables and latrines), showing that the measured distances range from 6 to 22 meters.

A significant proportion of wells are located less than 15 meters from these sources, which facilitates the rapid infiltration of N compounds, bacteria, residues of veterinary pharmaceuticals, and other contaminants resulting from inadequate management of animal waste.

This indicates an increased susceptibility to contamination with highly mobile substances such as NO_2^-, NO_3^-, and NH_4^+. The risk of transfer of these pollutants increases exponentially at shorter distances and is further influenced by factors such as soil structure, land slope, and groundwater level. In addition, the use of pesticides and herbicides in households can amplify contamination through infiltration or surface runoff, representing an additional threat to well water quality [20, 21].

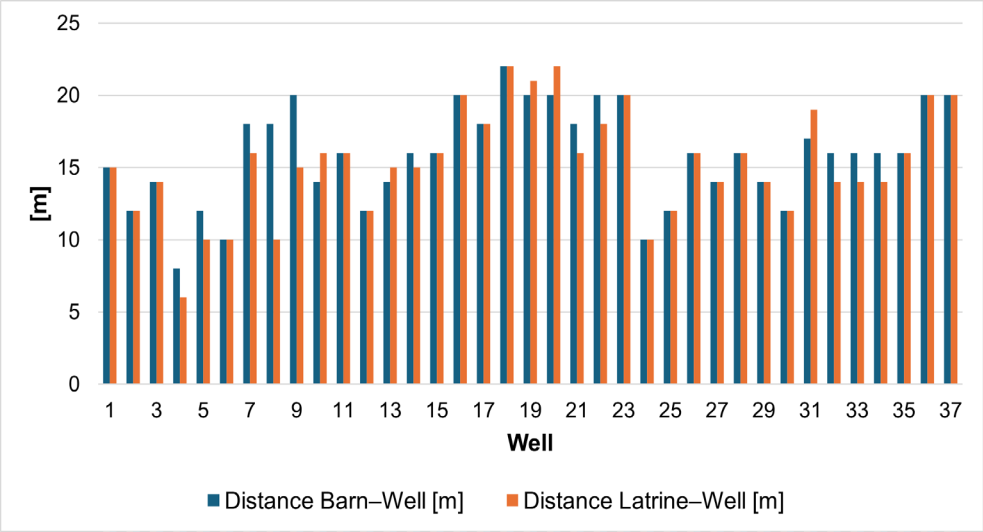

Figure 4. Distance from well to barn and latrine (m)

Chemical Analysis of Water from the Investigated Wells

To assess the potability status and chemical contamination risks associated with the consumption of water from wells in Hodăi–Boian, seven essential chemical and physico-chemical parameters were analyzed: concentrations of NO_2^-, NO_3^-, NH_4^+, pH, turbidity, electrical conductivity, and water temperature.

These analyses enable the identification of potential pollution sources, the degree of mineralization, as well as public health risks, providing a comprehensive overview of local water quality.

The concentrations of NO_2^- (Figure 5) reveal exceedances of the safety limit for drinking water (0.5 mg/L) in seven wells (4, 5, 8, 18, 30, 35, and 31). This finding is indicative of recent pollution with organic matter of animal or human origin, likely correlated with the proximity of pollution sources (latrines, barns) or improper waste management within households.

From a chemical perspective, NO_2^- is a sensitive indicator of acute contamination and poses a serious risk to the health of young children and infants, due to its methemoglobin-forming potential [20].

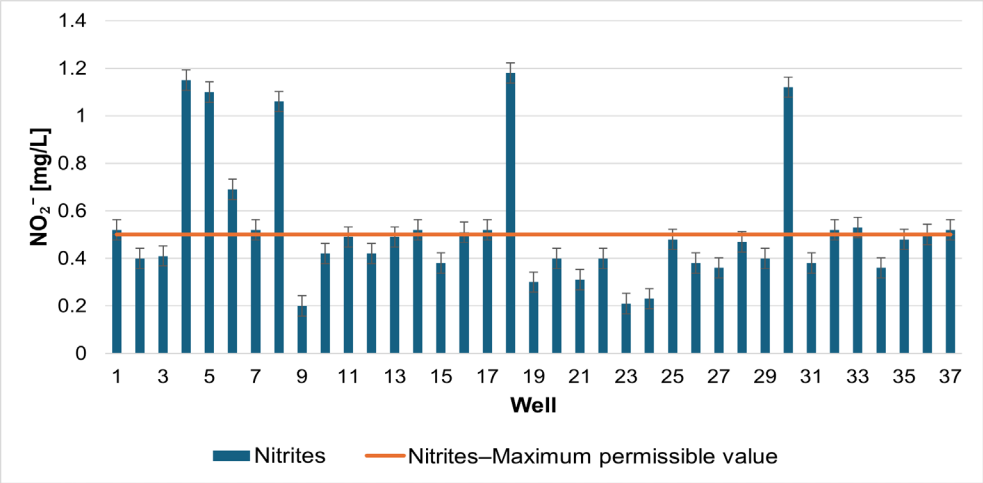

Figure 5. NO_2^- concentration in water from the investigated wells compared to the maximum admissible value

Figure 6 shows a relatively heterogeneous distribution of NO_3^- concentrations, with values approaching the maximum admissible limit in wells 4, 5, 18, 35, 36, and 37.

This pattern reflects a constant input of NO_3^- from diffuse sources, such as the use of chemical fertilizers or infiltration from animal waste.

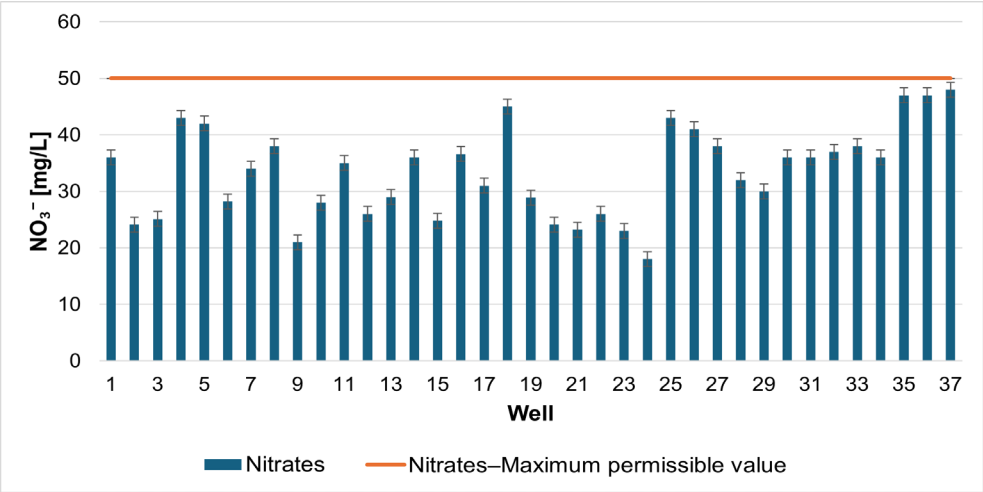

Figure 6. NO_3^- concentration in the water of the investigated wells compared to the maximum admissible value

NO_3^- are stable compounds with high persistence in groundwater, which underlines the importance of regular monitoring and the implementation of preventive measures to reduce the risk of chronic exposure.

All measured NH_4^+ values (Figure 7) remain below the potability threshold; however, the presence of relatively elevated concentrations (close to 0.4 mg/L in wells 4, 5, 8, 18, and 30) indicates recent low-level N input (e.g., manure or latrines) or local anoxic conditions. In oxic environments, NH_4^+ should be converted to NO_3^- [22, 23].

Unlike NO_3^-, NH_4^+ is less stable and reflects more recent pollution, often correlated with household or livestock activities near the wells.

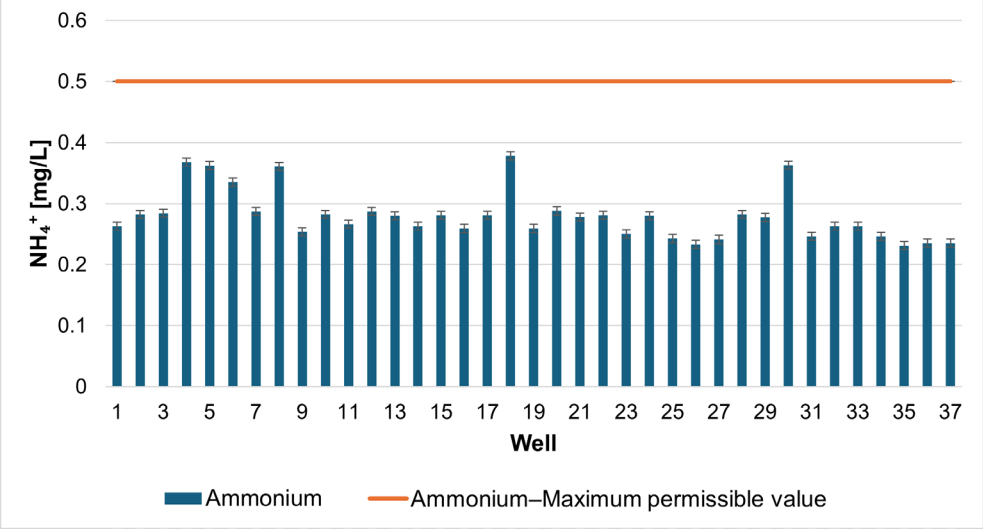

Figure 7. NH_4^+ concentration in well water compared to the maximum admissible value

The pH values (Figure 8) generally fall within the optimal range for drinking water (6.5–9.5), except for a few wells that display slightly acidic pH values (6.8–7.0), suggesting possible fermentation processes or increased microbiological activity. Slightly alkaline pH values, observed in most wells (>8), may reflect the mineral nature of the geological substrate, but also a high degree of mineralization and the presence of inorganic compounds (bicarbonate(HCO_3^-), carbonate(CO_3^{2-}), sodium (Na^+)).

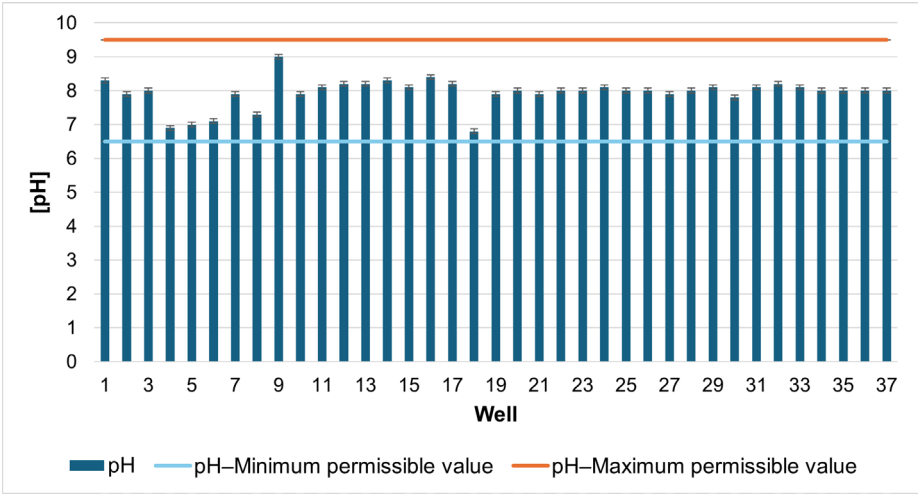

Figure 8. pH values of well water compared to the permissible limits

In Figure 9, turbidity remains below the maximum admissible limit for drinking water (5 NTU); however, values ranging between 2.1 and 4.5 NTU suggest the persistent presence of suspended solids, colloidal particles, or undecomposed organic matter [24, 25]. This phenomenon may result from insufficient filtration, contamination with plant material, or infiltration of rainwater into the well structure—factors that can potentially impact the clarity and microbiological safety of the water.

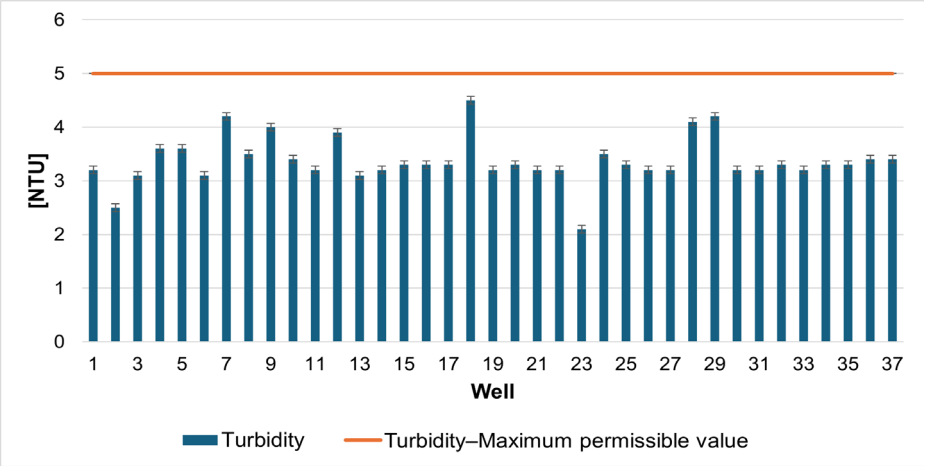

Figure 9. Turbidity of well water compared to the maximum admissible value

No transmitted light optical microscopy images of the most turbid samples (7, 18, and 29) were obtained in this study. The identification of dispersoid nature was based on indirect field evidence, context interpretation, and supporting literature regarding rural well water contamination (e.g., soil particles, organic matter, microorganisms).

Electrical conductivity, presented in Figure 10, frequently exceeds the maximum admissible value of 2500 µS/cm for drinking water, according to Directive (EU) 2020/2184 [26]. Such exceedances indicate either a naturally high mineralization of the water—caused by a geologic substrate rich in salts—or an inorganic input from anthropogenic sources such as animal waste or fertilizers.

From a chemical perspective, this parameter reflects the presence of dissolved ions (sodium(Na^+), potassium(K^+), calcium(Ca^{2+}), magnesium (Mg^{2+}), Cl^-, SO_4^{2-}, NO_3^-), which require special attention when evaluating potability, especially for vulnerable groups [27].

Total dissolved solids (TDS) and salinity were not directly measured in this study. However, the well-established correlation between electrical conductivity and these parameters was considered in the interpretation of the results.

Elevated conductivity values suggest a high level of mineralization (dissolved ions), often associated with mixtures rich in NO_3^-, Cl^-, and HCO_3^-, while correlation with the Cl^-/Br^- ratio may assist in identifying the source of salinity [28].

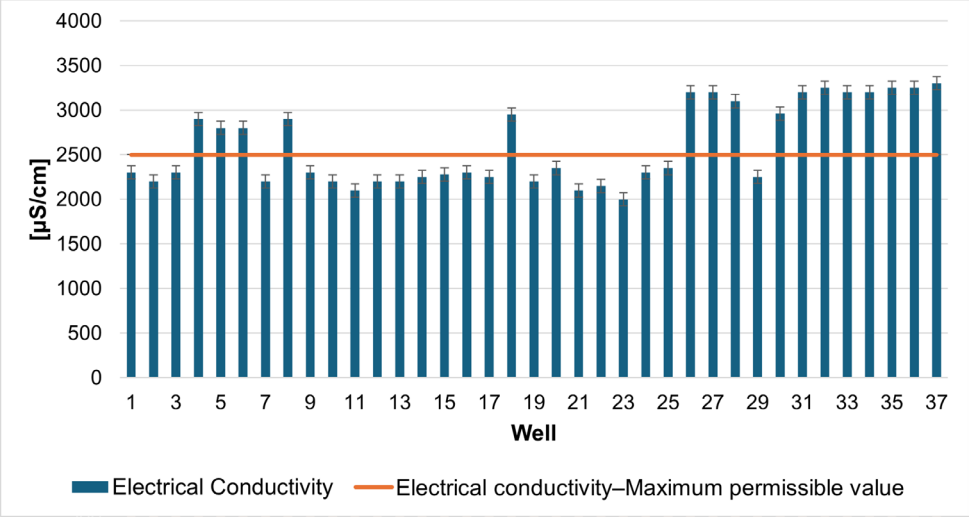

Figure 10. Electrical conductivity of well water compared to the maximum admissible value

The water temperature values (Figure 11) range between 11°C and 13°C, which is typical for shallow groundwater sources in a temperate-continental climate. While these parameters do not significantly influence the chemical quality of water, they can have an indirect impact on microbiological activity and the solubility of certain chemical compounds.

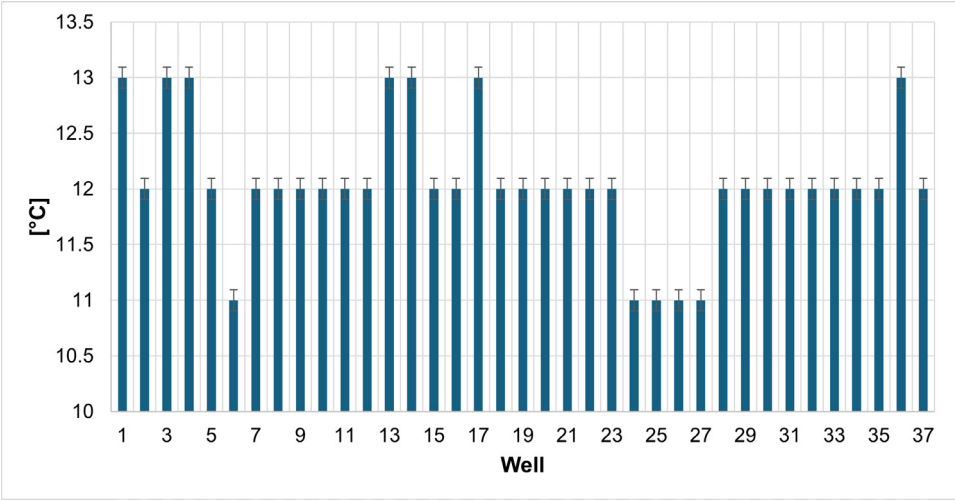

Figure 11. Water temperature in the analyzed wells

The results of the chemical analyses performed on water samples from wells in Hodăi–Boian highlight significant public health risks, mainly due to repeated exceedances of NO_2^- concentrations and high levels of NO_3^-, especially in wells located near potential pollution sources.

The water from wells in the Hodăi–Boian area shows moderate concentrations of NO_2^- (0.20–1.18 mg/L), with values below the maximum permissible limits set by current legislation. The results obtained are comparable to those reported for wells in Feleacu (0–1.61 mg/L) [15], but higher than those determined in wells from Mediaș (0.15–0.85 mg/L) [18], where values frequently approach regulatory thresholds, suggesting an increased risk of chronic NO_3^- exposure.

NO_3^- concentrations determined in Hodăi–Boian (18–48 mg/L) are lower than those reported in studies conducted in Sândominic (11–94 mg/L) [16] and Mediaș (11–130 mg/L) [18], indicating a possible reduction in recent organic pollution inputs.

NH_4^+ levels were within the permissible limits (<0.5 mg/L), ranging between 0.21 and 0.37 mg/L. These values are similar to those found in Sândominic (0–0.38 mg/L) [16], but higher than those in Feleacu (0–0.22 mg/L) [15], and significantly greater than those reported in Mediaș (0.01–0.01 mg/L) [18], suggesting local hydrogeological conditions that favor the retention of NH_4^+ compounds.

The pH values ranged from 6.8 to 9.0, with most samples exhibiting a slightly alkaline character (pH >8). However, some samples with pH below 7.0 were also identified, where the presence of dissolved carbon dioxide and organic fermentation processes may promote the mobilization of potentially toxic compounds (e.g., metals). The range determined is comparable to that reported in Feleacu (6.5–8.43) [15] but differs somewhat from the characteristic values of wells in Sândominic, where pH often falls below 7.0.

Electrical conductivity in water from Hodăi–Boian wells exhibited high values (2000–3300 µS/cm), with the threshold of 2500 µS/cm being exceeded in approximately half of the wells. This suggests pronounced natural mineralization, possibly amplified by inorganic inputs of anthropogenic origin, which may also indicate an increased microbiological risk. In comparison wells, electrical conductivity values were significantly lower, ranging between 671–1792 µS/cm [15] and 573–1532 µS/cm [16].

The elevated values of electrical conductivity and turbidity confirm both pronounced mineralization and the input of solid particles and dissolved substances, reflecting a direct influence of anthropogenic factors and local waste management practices.

The data analyzed reveal a clear correlation between animal density, distances to pollution sources, and the potential for chemical contamination of well water. Regular monitoring of key chemical indicators (NO_2^-, NO_3^-, NH_4^+ and where applicable, pesticides) is essential to prevent risks associated with the consumption of water from vulnerable sources. It is also recommended to strictly observe the minimum distance between wells and pollution sources, by current legislation and best rural management practices.

Overall, the data obtained underscore the necessity of continuous monitoring of these water sources, the implementation of sanitary protection measures, and the adoption of sustainable resource management practices to reduce contamination risks and ensure safe drinking water access for the local community.

Study Limitations

While this study provides a comprehensive chemical assessment of groundwater quality in domestic wells in Hodăi-Boian, certain limitations should be acknowledged. The analysis did not include microbiological parameters or

specific toxic contaminants such as pesticides and heavy metals, which are important for a complete risk evaluation. Sampling was limited to a single period and does not capture seasonal fluctuations in water quality. Additionally, total dissolved solids (TDS) and salinity were estimated indirectly from electrical conductivity, and the nature of suspended particles in turbid samples was inferred from field evidence rather than direct microscopic analysis. Finally, to ensure privacy, precise geographical coordinates were omitted, which may limit the spatial resolution of exposure assessment.

Despite these limitations, the study provides valuable insights into groundwater quality in a vulnerable rural environment and offers a solid basis for future research.

Recommended Monitoring Strategy

To improve the quality of well water for rural inhabitants, it is strongly recommended to implement a systematic groundwater monitoring strategy at the community level. This should include regular testing of key physico-chemical and microbiological parameters (such as NO_3^-, NO_2^-, NH_4^+, pH, turbidity, electrical conductivity (EC), and bacterial indicators) at least twice per year, ideally in both dry and wet seasons.

Monitoring should be coordinated by local public health authorities in collaboration with water management experts and should involve clear protocols for sampling, data recording, and rapid communication of results to well owners.

Additionally, educational campaigns should be organized to raise awareness among local residents about potential contamination sources and the importance of maintaining sanitary protection zones around wells.

Where water quality problems are identified, targeted interventions—such as improving well construction, relocating animal shelters or latrines, and promoting water treatment solutions—should be promptly recommended and supported.

CONCLUSIONS

The chemical analysis of water from the 37 wells in the village of Hodăi-Boian revealed exceedances of the maximum admissible concentration for NO_2^- (0.5 mg/L) in seven cases, indicating possible recent organic or livestock-related pollution.

NO_3^- concentrations (18.0–48.0 mg/L) remained below the 50 mg/L threshold but reached values close to this limit in three wells, suggesting a constant input of nutrients from fertilizers or household infiltration.

NH_4^+ levels (0.23–0.37 mg/L), although below the 0.5 mg/L threshold, indicate microbiological activity and a potential risk of recent contamination.

Physico-chemical parameters (pH 6.8–9.0; turbidity 2.1–4.5 NTU; conductivity 2000–3300 µS/cm) reflect pronounced mineralization and the presence of fine suspended particles, with frequent exceedances of the recommended limits for drinking water, especially about conductivity.

The presence of pH values below 7.0 in three wells indicates organic fermentation processes, while temperatures of 11–13°C confirm the nature of shallow groundwater.

The results highlight a significant influence of anthropogenic activities on groundwater quality, posing potential risks for human consumption, especially in the case of unprotected or inadequately maintained sources.

EXPERIMENTAL SECTION

The village of Hodăi-Boian, located in the southeastern part of Cluj County (Ceanu Mare commune), lies within the low hilly area of the Transylvanian Plain (46°38′26.62″ N, 24°00′35.75″ E).

This rural settlement is characterized by a diverse agricultural landscape, traditional land use patterns, and temperate-continental climate—factors that shape both the local hydrographic network and groundwater resources.

The village's geographical position within the Transylvanian Plain determines not only soil composition and vegetation, but also directly influences the quality and availability of natural water sources of major scientific interest in the context of water supply and environmental monitoring in Central and Eastern European rural areas.

Characterization of the Studied Households

The aim of the present study was to provide a detailed assessment of the chemical quality of water from wells used for domestic and agricultural purposes within the territory of Ceanu Mare commune, with a particular focus on the village of Hodăi-Boian.

To highlight the influence of anthropogenic factors on water quality, the investigation focused on 37 households in Hodăi-Boian, each with its well (Figure 12). The sampling strategy was designed to ensure uniform coverage of the entire village area and to reflect the diversity of water use conditions.

For each household, data was collected regarding the intended use of water (domestic or agricultural), the number of inhabitants and farm animals (cattle, horses, pigs), as well as the average daily and monthly water consumption. In addition, relevant parameters for risk assessment were

determined, including the water level and depth in the well, and the distance to animal shelters and latrines. The water level, depth of the wells, and distances to potential contamination sources (animal shelters, latrines) were measured in situ by the investigators using measuring tapes and field equipment. Information regarding water use and livestock numbers was collected through direct inquiry with well owners.

This integrated approach allowed for the identification of significant correlations between the chemical quality of water, potential sources of pollution, and the socio-economic characteristics of each household, thus providing a comprehensive picture of the risks and vulnerabilities associated with the use of local water sources in rural environments.

Chemical processes relevant in rural groundwater under the influence of agricultural and domestic contaminants

From a chemical perspective, groundwater in rural areas is subjected to complex processes involving the transformation of N compounds, SO_4^{2-}, heavy metals, and other substances originating from fertilizers, animal manure, latrines, as well as the use of pesticides or other plant protection products. Among them, the Ncycle involves reactions where organic compounds and NH_4^+ are gradually oxidized to NO_2^- and then to NO_3^-, under the action of nitrifying bacteria, as follows:

Ammonification and nitrification:

Organic matter → NH_4^+
$NH_4^+ + 1.5\ O_2 \rightarrow NO_2^- + 2\ H^+ + H_2O$ (Nitrosomonas bacteria)
$NO_2^- + 0.5\ O_2 \rightarrow NO_3^-$ (Nitrobacter bacteria)

Denitrification (under anaerobic conditions):

$NO_3^- \rightarrow NO_2^- \rightarrow NO \rightarrow N_2O \rightarrow N_2\uparrow$

These processes are significantly influenced by the water's pH and oxygen content. A slightly acidic or neutral pH and good aeration favor nitrification, while an alkaline environment or lack of oxygen favors the accumulation of NH_4^+ and reduction processes with possible release of nitrogenous gases into the atmosphere [29].

Regarding the pH, if the value is situated below 7 than it favors the solubilization of heavy metals and the occurrence of fermentation reactions. A pH value higher than 8 favors the accumulation of NH_4^+, which is no longer efficiently oxidized to NO_3^- [30].

Degradation processes of pesticides and organics: pesticides may undergo abiotic degradation (hydrolysis, photolysis) or biodegradation under the action of microorganisms [31], generating metabolites with variable toxicity following the reactions of hydrolysis of pesticides and enzymatic biodegradation, respectively:

$$R\text{-}Cl + H_2O \rightarrow R\text{-}OH + HCl$$
$$\text{Organic pesticide} + O_2 \rightarrow \text{Oxidized metabolites} + CO_2 + H_2O$$

These reactions are not specific to each compound but highlight the chemical complexity of contaminants in rural groundwater. Thus, groundwater contamination in wells is determined not only by the amount of infiltrated pollutants but also by the chemical specificity of the subsurface environment and the complex interactions between present compounds, pH, and bacterial activity, which can generate both mobilization and immobilization processes for substances with toxic potential.

Chemical Analysis of Water from the Investigated Wells

Water samples were collected in polyethylene containers, complying with the SR EN ISO 5667/2017 standard [32], transported to the laboratory in a refrigerated box, stored at 4°C, and analyzed within 24 hours from collection. Each sample was analyzed in triplicate, and the average of the values obtained was used to interpret the results. The chemical analysis of the samples aimed to identify the main risk factors for human health and agricultural water use at the local level.

The quality of the water samples collected from the domestic wells was determined by analyzing the following parameters: the concentration of NO_3^- and NO_2^-; turbidity; water conductivity; and the water pH.

The concentrations of NO_3^- and NO_2^- were determined spectrophotometrically using portable colorimeters (HANNA Instruments HI 96728 for NO_3^- and HI 96708 for NO_2^-; Hanna Instruments, USA). For NO_3^-, the cadmium reduction colorimetric method was applied (adapted according to EPA 353.2 [33] and ISO 7890-3:1988 [34]), with the reaction yielding an amber coloration measured at 525 nm. For NO_2^-, the ferrous sulfate colorimetric method was used (adapted from ISO 6777:1984 [35] and EPA 353.2 [33]), generating a greenish-brown tint read at 575 nm. Each measurement was performed using pre-dosed reagents and single-use optical cuvettes, following the manufacturer's instructions. The detection range was 0.0–30.0 mg/L for NO_3^- and 0–150 mg/L for NO_2^-.

NH_4^+ concentrations were determined in the field using a portable colorimeter (HANNA Instruments HI 93700, Hanna Instruments, USA) with salicylate-based reagents, according to the indophenol blue method (adapted from ISO 7150-1:1984 [36] and Standard Methods 4500-NH_3 [37]). The method relies on the reaction of NH_4^+ with salicylate and hypochlorite, forming a blue-green indophenol complex measured photometrically at 655 nm. Pre-dosed reagent packets and single-use optical cuvettes were used, as specified by the manufacturer. The detection range for NH_4^+-N was 0.00–0.80 mg/L.

The pH and electrical conductivity (EC) of water samples were measured using a portable multiparameter meter (HANNA Instruments HI 991301, Hanna Instruments, USA). pH was determined with a combined glass electrode, previously calibrated with standard buffer solutions (pH 4.01, 7.00, and 10.01) as per the manufacturer's protocol. Electrical conductivity was measured in µS/cm, with calibration performed using standard KCl solution. All measurements were conducted in situ, with the probe rinsed with distilled water between samples.

Turbidity was measured using a portable turbidimeter (HANNA Instruments HI 93703, Hanna Instruments, USA), based on the nephelometric method according to ISO 7027:1999 [38]. The instrument was calibrated with formazin standards, and turbidity was recorded in nephelometric turbidity units (NTU). Water samples were measured in optical glass cuvettes, with care to avoid air bubbles and sedimentation.

The results obtained were compared with the maximum allowable concentrations in drinking water, as specified by Directive (EU) 2020/2184 and Law 458/2002: 50 mg/L for NO_3^-, 0.5 mg/L for NO_2^-, and 0.5 mg/L for NH_4^+ [26,39].

In rural areas, where water supply is often provided by individual wells, a general threshold of 5 NTU is applied as the reference limit for potability, in accordance with national legislation and the requirements of European Directives [26–39].

REFERENCES

1. United Nations General Assembly; Resolution 64/292: The human right to water and sanitation; United Nations: New York, USA, 2010
2. W. Musie, G. Gonfa, *Heliyon*, **2023**, *9*, e18685
3. M. Pritchard, T. Mkandawire, J.G. O'Neill, Groundwater Pollution in Shallow Wells in Southern Malawi and a Potential Indigenous Method of Water Purification', Appropriate Technologies for Environmental Management in the Developing World, Springer Publishing, **2009,** ISBN 978-1-4020-9138-4 (Print) 978-1-4020 9139-1 (Online) pp. 169–179

4. O.A. Crisan, M.S. Pustan, C.J. Bîrleanu, A.E. Tiuc, I. Sur, H.G. Crisan, F.M. Serdean, L. Flamand, T. Rusu, *Studia UBB Chemia,* **2020**, *65*, 253-266
5. E.W., Kimani-Murage, A.M. Ngindu*J. Urban Health*, **2007**, *84*, 829–838
6. E.K. Wallender, E.C. Ailes, J.S. Yoder, V.A. Roberts, J.M. Brunkard, *Groundwater*, **2014**, *52*, 886–897
7. M.F. Sardar, X.F. Younas, H. Li, J. Ali, P. Zhu, X. Yu, Z. Cui, W. Guo, *Ecotoxicol. Environ. Saf*., **2025**, 291, 117829
8. F. Alam, *Arab. J. Geosci*., **2013**, *7*, 4121-4131
9. T.Y. Stigter, L. Ribeiro, A.C. Dill, *J. Hydrol.*, **2006**, *327*, 578-591
10. World Health Organization, Guidelines for drinking-water quality, 2nd ed. Addendum to Vol. 2. Health criteria and other supporting information, 1998, Geneva
11. J.M. Elwood, Bert van der Werf, *Cancer Epidemol.,* **2022**, *78*, 102148
12. Council Directive of 12 December 1991 concerning the protection of waters against pollution caused by nitrates from agricultural sources (91/676/EEC)
13. M.H. Ward, B.A. Kilfoy, P.J. Weyer, K.E. Anderson, A.R. Folsom, J.R. Cerhan, *Epidemiology*, **2010**, *21*, 389–395
14. I.M. Sur, A. Moldovan, V. Micle, E.T. Polyak, *Water,* **2022**, *14*, 3118
15. Burcă, C. Indolean, A. Maicaneanu, Studia UBB Chemia, **2015**, *3*, 247-255
16. Burcă, C. Indolean, Studia UBB Chemia, LXVI, 1, **2021**, 115-125
17. C. Roba, R. Bălc, F. Crețа, D. Andreica, A. Pădurean, P. Pogăcean, T. Chertes, F. Moldovan, B. Mocan, C. Roșu, *Environ. Eng. Manag. J.,* **2021**, *20*, 435-447
18. M.-A. Hoaghia, O. Cadar, E. Levei, D. Ristoiu, *Studia UBB Chemia*, **2016**, *3*, 451–460
19. N.-L. Petruța, I.M. Sur, T.A. Rusu, T. Gabor, T. Rusu, *Sustainability*, **2025**, *17*, 6530
20. World Health Organization (WHO). Guidelines for Drinking-water Quality, 4th edition incorporating the 1st and 2nd addenda; WHO Press: Geneva, 2022
21. European Commission. (2021). *Commission Staff Working Document SWD (2021) 1001 final – Report on the implementation of Council Directive 91/676/EEC concerning the protection of waters against pollution caused by nitrates from agricultural sources*
22. C. Rosu, C. Roba, I. Pistea, B. Bâscovan, O. Devian, Studia UBB Ambient. **2020**, 65, 75–85
23. D.E. Canfield, A.N. Glazer, P.G Falkowski, *Science*, **2010**, *330*, 192-196
24. Government Decision No. 971/2023 regarding the approval of the Rules for the surveillance, monitoring and sanitary inspection of drinking water quality, Annex 1, Section 1, Table 1, Note 4
25. U.S. Geological Survey (USGS). *National Field Manual for the Collection of Water-Quality Data — Chapter A6.7: Turbidity.* Techniques of Water-Resources Investigations, Book 9; Reston, VA, 2023
26. European Union. Directive (EU) 2020/2184 of the European Parliament and of the Council of 16 December 2020 on the quality of water intended for human consumption. Official Journal of the European Union L 435, 23.12.2020, 1–62
27. U.S. Geological Survey (USGS). *Chloride, Salinity, and Dissolved Solids.* USGS Water Science School

28. U.S. Geological Survey (USGS). *Using Chloride/Bromide Ratios to Identify Sources of Salinity (septic/road salt diagnostic)*
29. A. Bernhard, *Nature Education Knowledge*, **2010**, *3*, 25
30. T.C Zhang, P.L. Bishop, *Water Environ. Res.*, **1996**, *68*, 1107–1115
31. M. Arias-Estévez, E. López-Periago, E. Martínez-Carballo, J. Simal Gándara, J.-C. Mejuto, L. García-Río, Agri. Ecosys. Environ., **2008**, 123, 247-260
32. SR EN ISO 5667:2017. Water quality. Sampling. Guide to sampling rivers and streams. National Standardization Body of Romania, Bucharest, 2017
33. U.S. Environmental Protection Agency (EPA), Method 353.2: Determination of nitrate-nitrite nitrogen by automated colorimetry, Revision 2.0, Environmental Monitoring and Support Laboratory, Office of Research and Development, Cincinnati, OH, USA, 1993.
34. International Organization for Standardization (ISO), ISO 7890-3:1988. Water quality – Determination of nitrate – Part 3: Spectrometric method using sulfosalicylic acid, Geneva, Switzerland, 1988.
35. International Organization for Standardization (ISO), ISO 6777:1984. Water quality – Determination of nitrite – Molecular absorption spectrometric method, Geneva, Switzerland, 1984.
36. International Organization for Standardization (ISO), ISO 7150-1:1984. Water quality – Determination of ammonium – Part 1: Manual spectrometric method, Geneva, Switzerland, 1984.
37. American Public Health Association (APHA), American Water Works Association (AWWA), Water Environment Federation (WEF), Standard Methods for the Examination of Water and Wastewater, 23rd Edition, Method 4500-NH_3: Ammonia, Washington, D.C., USA, 2017.
38. International Organization for Standardization (ISO), ISO 7027-2:2019. Water quality – Determination of turbidity, Geneva, Switzerland, 2019.
39. Law No. 458/2002 on the quality of drinking water, republished, with subsequent amendments and completions. Official Gazette of Romania, Part I, No. 875 of December 12, 2011.

STUDIA UBB CHEMIA, LXX, 3, 2025 (p. 177-190)
(RECOMMENDED CITATION)
DOI:10.24193/subbchem.2025.3.12

COMPARATIVE FLOW BEHAVIOR OF OIL SLUDGE AND CRUDE OILS FROM ALGERIAN STORAGE TANKS

Farid SOUAS[a*], Abdelhamid SAFRI[a], Abderazak GUECIOUER[b]

ABSTRACT. This study investigates the flow behavior of tank bottom sludge and two crude oil samples by analyzing the variation of viscosity and shear stress with shear rate and temperature. The flow curves reveal that all samples exhibit non-Newtonian, shear-thinning behavior characterized by a distinct yield stress, particularly prominent in the sludge due to its high content of heavy fractions such as asphaltenes, resins, and solid particulates. Viscosity and shear stress consistently decrease with increasing temperature, a result of the thermal disruption of intermolecular forces and breakdown of microstructural networks. At low shear rates, sludge displays more pronounced shear-thinning behavior than crude oils, while at high shear rates, all samples approach Newtonian flow regimes due to molecular alignment and structural degradation. Model fitting shows the Herschel-Bulkley model best describes the sludge's rheology, whereas the Casson model better fits the crude oils under specific temperature conditions. Temperature sensitivity analysis (10–40 °C) indicates that crude oils experience greater viscosity reduction than sludge, with crude 1 showing the highest response due to its thermally labile composition. Yield stress also diminishes with temperature, reflecting the weakening of internal structural rigidity. These findings underscore the critical influence of composition and temperature on the flow properties of petroleum-derived fluids, with implications for pipeline transport and sludge management.

Keywords: *Crude oil, flow behavior, Sludge, temperature, viscosity, yield stress.*

[a] *LEGHYD Laboratory, Faculty of Civil Engineering, University of Science and Technology Houari Boumediene (USTHB), Bab Ezzouar, Alger, Algeria*
[b] *Research Unit Materials, Processes and Environment (UR-MPE), Faculty of Engineering Science, University M'Hamed Bougara, Boumerdes, Algeria*
* *Corresponding author: fa.souas@gmail.com, farid.souas@usthb.edu.dz*

INTRODUCTION

Crude oil remains a cornerstone of the global energy supply, with demand significantly rising in the early years of the 21st century compared to the latter part of the 20th century [1]. Given this persistent and growing demand, crude oil is expected to continue serving as a primary energy source in the foreseeable future. Ensuring the safe and efficient transport of crude oil from subsurface reservoirs to surface facilities is a critical aspect of flow assurance. Among available methods, pipeline transportation stands out as the most economical and efficient means for delivering crude oil and its derivatives. A key factor in the successful transport of petroleum fluids is their rheological behavior. Rheological properties, such as viscosity, play a central role in governing flow dynamics and directly impact the design and operation of pipeline systems [2]. Effective management of these properties allows oil companies to optimize the use of existing pipeline infrastructure while minimizing technical challenges. Crude oil is a complex mixture composed of various hydrocarbon fractions, including saturates, aromatics, resins and asphaltenes. Viscosity, in particular, is influenced by the chemical nature and relative concentrations of these components. Heavy crude oils, characterized by high viscosity, are especially prone to pressure drops during long-distance pipeline transport. This increased flow resistance results in elevated energy consumption for pumping operations [3]. The molecular structure of crude oil constituents has a profound impact on viscosity. Non-polar components such as saturates and aromatics tend to reduce viscosity, whereas polar components such as resins and asphaltenes tend to increase it. Asphaltenes are highly polar due to the presence of heteroatoms and metallic elements. They are prone to self-association, forming viscoelastic nanoaggregates. When their concentration exceeds a critical threshold, these aggregates interact with other polar compounds, leading to a dramatic rise in viscosity [4].

Crude oil often separates into heavier and lighter fractions during storage, with the heavier components settling at the bottom of tanks as sludge. This sludge, a complex mixture of oil, sediment, heavy metals, paraffin, and water, can form a stable water-in-oil emulsion. It causes issues like corrosion, reduced storage capacity, and blocked discharge lines, requiring periodic removal [5]. However, it is valuable due to its high oil content, which can be recycled to improve energy resources. Oil sludge composition varies, but typically contains 4-7% solid sediment and has a higher aliphatic (40-60%) than aromatic (25-40%) content. Technologies like solvent extraction, centrifugation, and microwave irradiation have been developed to treat sludge [6-7]. The stability of sludge, caused by oil adsorption on solid particles and the presence of polar fractions like resins and asphaltenes, increases its viscosity [8].

Rheology, which studies how a material deforms under shear stress, is crucial for understanding oil sludge flow. Oil sludge, with its high solid and water content, exhibits complex rheological behavior. It can be pseudoplastic (shear-thinning) and behave differently based on temperature, shear rate, and chemical additives. Research has shown that surfactants, solvents, temperature, and pressure can significantly reduce sludge viscosity, making it easier to handle and pump. Rheological studies, including those by Hassanzadeh et al. [9] and Jie et al. [10], help optimize the management and treatment of tank bottom sludge.

The purpose of this article is to investigate and compare the flow behavior of oil sludge and various Algerian crude oils under different thermal and shear conditions, with particular focus on their rheological properties such as viscosity, shear stress, and yield stress. Understanding these properties is critical for optimizing the handling, transport, and processing of petroleum products, especially in storage tank management where sludge accumulation presents operational and environmental challenges. By modeling the variation of viscosity and shear stress with both temperature and shear rate, this study aims to offer practical insights into flow improvement strategies and sludge remediation. The comparative nature of this study is especially important for identifying how sludge behavior deviates from that of standard crude oils, thus guiding the development of more efficient mechanical or chemical treatment methods and contributing to enhanced operational efficiency and reduced maintenance costs in the petroleum industry.

RESULTS AND DISCUSSION

Variation of viscosity and shear stress with shear rate at various temperatures

Over extended storage periods, the physicochemical properties of crude oil undergo significant alterations due to factors such as reservoir depletion, pressure fluctuations, temperature variations, climatic conditions, and microbial activity, including the presence of oxidizing bacteria and fungi. Moreover, the volatilization of lighter hydrocarbon fractions leads to compositional changes that affect the polarity, solubility, and density of the crude oil, as well as the ratio of saturated to aromatic hydrocarbons. These transformations promote the sedimentation of heavier constituents such as paraffins, asphaltenes, resins, and inorganic solids at the bottom of storage tanks [9]. Consequently, the flow behavior of the resulting high-viscosity sludge is

modified due to structural rearrangements in asphaltene and wax crystal networks, which can form gel-like matrices, particularly at lower temperatures. A comprehensive understanding of the parameters influencing the rheological behavior of these materials is essential for accurate flow modeling, the characterization of complex flow phenomena, and the design of pipelines and treatment equipment. Such insights are critical for optimizing energy consumption, enhancing operational safety, and achieving economic and processing efficiency within the petroleum industry.

The flow behavior of the oil sludge and crude oil samples, characterized by the variation of viscosity and shear stress as a function of shear rate at selected temperatures (10 °C and 20 °C), is illustrated in Figures 1 and 2. The shear stress versus shear rate plots reveal the existence of a distinct yield stress, below which no flow occurs. Beyond this yield point, a linear relationship emerges, indicating a non-Newtonian, pseudoplastic behavior. This suggests that a finite shear stress is required to overcome internal structural resistance and initiate flow. Experimental observations further show that with increasing temperature, shear stress, viscosity, and yield stress decrease. This reduction is attributed to the thermal weakening of intermolecular interactions, consistent with previous findings [11].

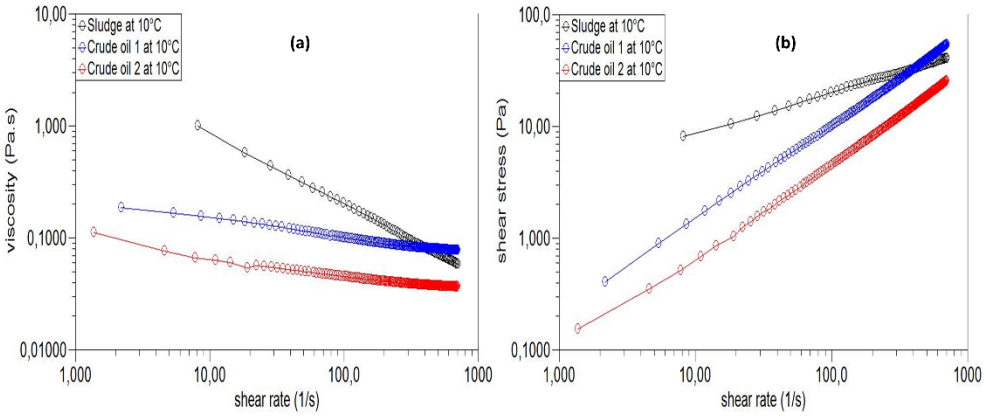

Figure 1. Flow curves of sludge and crude oils at a temperature of 10 °C: (a) viscosity versus shear rate, (b) shear stress versus shear rate.

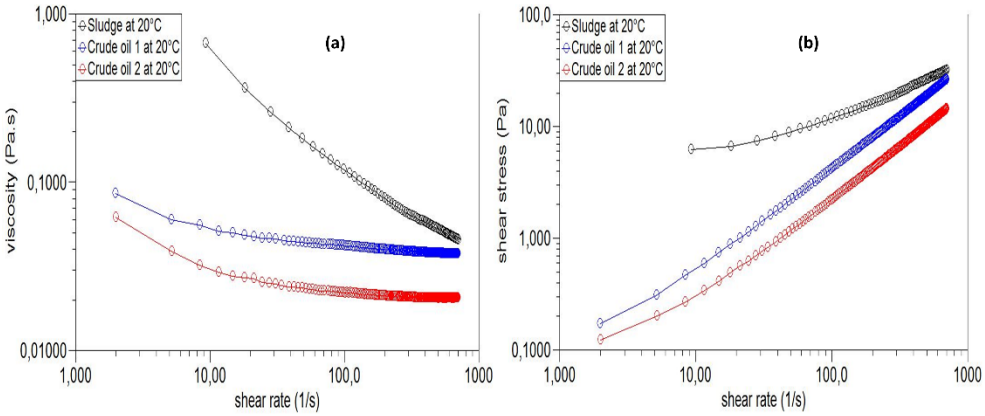

Figure 2. Flow curves of sludge and crude oils at a temperature of 20 °C: (a) viscosity versus shear rate, (b) shear stress versus shear rate.

The viscosity profiles of the sludge and both crude oils reveal two distinct rheological regimes. At low shear rates, the sludge exhibits pronounced non-Newtonian shear-thinning behavior, markedly more significant than that observed in the crude oils. Conversely, at high shear rates, the viscosity curves for all samples converge toward Newtonian behavior, indicating a transition in flow characteristics. Notably, shear rate exerts a substantial influence on viscosity, particularly under low-temperature conditions. This flow behavior can be attributed to compositional differences among the samples and their temperature-dependent structural responses. At elevated temperatures, the samples behave as homogeneous, isotropic Newtonian fluids, where viscosity is primarily governed by temperature. A reduction in temperature increases viscosity at a given shear rate due to decreased molecular mobility. Further cooling promotes the formation of a weak gel network structure, which contributes to a progressive rise in viscosity due to the presence of a nascent dynamic gel phase. Under applied shear, the mechanical energy disrupts this gel network, leading to its deformation and eventual breakdown. This structural degradation under shear results in reduced viscosity, especially at higher shear rates. As illustrated in Figures 1 and 2, viscosity is significantly elevated at low shear rates but stabilizes as shear rate increases. This behavior is attributed to the irreversible disruption and alignment of heavier molecular components, which dominate the rheological response at elevated shear conditions [12].

According to Jie et al. [10], the shear-thinning behavior of tank bottom sludge is more pronounced than that observed in crude oil, primarily due to the sludge's distinct compositional characteristics. As indicated in Table 5,

the sludge contains elevated levels of heavy fractions such as asphaltenes and resins, as well as a substantial amount of solid particulate matter. These components significantly influence the system's rheological properties. An increase in solid particle concentration enhances the shear-thinning response. In water-in-oil (W/O) emulsion systems, strong interactions among particles and between particles and oil molecules lead to the formation of a continuous, space-filling network. This interconnected structure, combined with aggregates formed by high molecular weight substances, contributes to the sludge's elevated viscosity. Upon the application of shear stress, these structural networks begin to break down. As the shear rate increases, the extent of structural breakdown becomes more substantial, resulting in a marked reduction in viscosity. Beyond a certain shear rate, a dynamic balance is established between the rates of structural breakdown and reformation, and molecular alignment along the shear direction leads to a stabilization of viscosity at a constant level [13].

To characterize the flow behavior of various non-Newtonian fluids under diverse flow conditions, numerous rheological models have been developed and reported in the literature. Nonetheless, specific laboratory and field investigations indicate that empirical correlations derived from curve-fitting techniques are sometimes necessary to accurately capture the complex rheological behavior of certain fluids [14]. In this study, four rheological models, namely the Bingham model, the Casson model, the power-law model, and the Herschel-Bulkley model, were evaluated using Equations 1 through 4 to determine the most suitable model for representing the observed experimental data.

$$\tau = \tau_0 + \mu\dot{\gamma} \quad (1)$$

$$\sqrt{\tau} = \sqrt{\tau_0} + \sqrt{\mu\dot{\gamma}} \quad (2)$$

$$\tau = K\dot{\gamma}^n \quad (3)$$

$$\tau = \tau_0 + K\dot{\gamma}^n \quad (4)$$

Where: τ is shear stress (Pa); τ_0 is apparent yield stress (Pa); μ is apparent viscosity (Pa. s); K is the consistency index (Pa.s^n); $\dot{\gamma}$ is shear rate (s^{-1}) and n is the flow behavior index.

The rheological models described earlier were applied to fit the shear stress data obtained at different shear rates for each sample examined in this study. Both the shear stress values predicted by the models and the experimentally measured values were used to compute statistical error parameters. To evaluate the predictive accuracy of the rheological models, the standard error (SE), a statistical measure quantifying the deviation between predicted and observed values, was calculated following the approach outlined by [15]:

$$SE = \left[\frac{\left[\frac{\sum_{i=1}^{n}(x_m - x_c)^2}{n-2}\right]^{\frac{1}{2}}}{X_m^{max} - X_m^{min}}\right] \times 1000 \quad (5)$$

The term x_m represents the observed or measured value, x_c indicates the computed or theoretical value, and n refers to the total count of data points.

Table 1. Standard error values of shear stress for various rheological models.

Sample	Temperature, °C	Bingham (Eq.1)	Casson (Eq.2)	Power law (Eq.3)	Herschel-Bulkley (Eq.4)
Sludge	10	49.17	26.73	8.28	**8.13**
	20	24.20	5.83	20.36	**5.04**
Crude oil 1	10	8.06	**2.10**	5.27	3.15
	20	3.52	**1.31**	2.49	1.71
Crude oil 2	10	6.78	**1.84**	4.14	2.65
	20	1.88	2.32	3.28	**1.80**

The findings from the modeling study, as shown in Table 1, along with the corresponding minimal standard errors, indicate that the Herschel-Bulkley model most accurately characterizes the flow behavior of sludge over a defined range of shear rates and temperatures. For crude oil 1, the flow behavior is best represented by the Casson model. In the case of crude oil 2, the Casson model is the most suitable for describing flow at 10°C, while the Herschel-Bulkley model provides a better fit at 20°C.

Variation of viscosity and shear stress with temperature and variable shear rate

Table 2 presents the relationship between apparent viscosity and shear stress of samples as a function of temperature across various shear rates, highlighting their non-Newtonian behavior. In pipeline systems, pressure drop refers to the energy loss resulting from frictional interactions between the fluid and the pipe walls. This pressure drop is inversely related to viscosity; lower viscosities correspond to reduced energy losses, while higher viscosities are associated with increased friction and consequently greater pressure drops and energy dissipation. Shear stress, which is closely dependent on the viscosity of fluid, reflects the fluid's resistance to deformation under flow

conditions, particularly in regions near the pipe wall where frictional forces are most prominent [16]. It can also be interpreted as an analogue to the pressure required to initiate or maintain the flow of fluid within the pipeline.

The sludge and crude oil samples exhibited the highest sensitivity to thermal variation, particularly within the temperature range of 10°C to 40°C. Within this interval, a pronounced decrease in both apparent viscosity and shear stress was observed, indicating substantial improvements in the flow properties due to temperature elevation.

Table 2. Effect of temperature on the rheological behavior of samples under different shear rates.

		Temperature, °C					
		10°C		**20°C**		**40°C**	
Type	**Shear rate, S^{-1}**	**Viscosity, mPa.s**	**Shear stress, Pa**	**Viscosity, mPa.s**	**Shear stress, Pa**	**Viscosity, mPa.s**	**Shear stress, Pa**
Sludge	100	204	20.16	118.8	11.74	85.51	8.417
	200	130.5	25.9	80.36	15.95	54.93	10.94
	300	97.54	29.19	64.62	19.34	44.5	13.3
	400	81.42	32.49	57.97	23.13	39.13	15.6
	500	71.56	35.68	52.74	26.3	35.82	17.88
	600	64.28	38.46	48.57	29.06	33.33	19.96
	700	58.2	40.68	45.46	31.78	31.44	21.96
Crude oil 1	100	100.9	9.903	42.04	4.119	16.7	1.637
	200	88.96	17.7	39.84	7.92	16.17	3.214
	300	83.7	24.96	38.7	11.53	15.99	4.767
	400	81.11	32.36	38.21	15.24	16.01	6.387
	500	79.48	39.6	37.85	18.85	16.11	8.022
	600	77.86	46.64	37.67	22.56	16.17	9.684
	700	77.26	53.94	37.57	26.22	16.2	11.31
Crude oil 2	100	45.31	4.485	22.08	2.164	10.64	1.05
	200	40.98	8.122	21.12	4.197	10.26	2.03
	300	38.39	11.64	20.79	6.196	10.18	3.04
	400	37.87	15.08	20.59	8.211	10.15	4.039
	500	37.18	18.49	20.45	10.18	10.24	5.106
	600	36.75	21.99	20.5	12.27	10.23	6.117
	700	36.58	25.51	20.51	14.32	10.32	7.209

To quantitatively assess the extent of improvement in flow behavior, specifically the reductions in viscosity and shear stress, the Average Degree of Reduction (DAR) is introduced. The DAR is calculated using the following equation:

$$(\mathrm{DAR})\% = \frac{1}{n}\sum_{i=1}^{n}\left[\frac{\text{initial value} - \text{final value}}{\text{initial value}}\right] \times 100 \qquad (6)$$

The data presented in Table 3 demonstrate that increasing the temperature from 10°C to 40°C significantly reduced the initial viscosity and shear stress at the fluid–pipe wall interface for sludge and crude oils 1 and 2 by approximately 52%, 81%, and 74%, respectively, indicating a substantial improvement in flow behavior. When the temperature was increased from 10°C to 20°C, viscosity and shear stress reductions of 31%, 54%, and 46% were recorded for sludge, crude 1, and crude 2, respectively. Further heating from 20°C to 40°C resulted in additional reductions of 31%, 58%, and 51% for the same samples.

Table 3. Percent decrease in viscosity and shear stress of samples with increasing temperature.

		Temperature, °C					
		10°C - 20°C		20°C - 40°C		10°C - 40°C	
Type	Shear rate, S^{-1}	% Viscosity reduction	% Shear stress reduction	% Viscosity reduction	% Shear stress reduction	% Viscosity reduction	% Shear stress reduction
Sludge	100	41.76	41.77	28.02	28.30	58.08	58.25
	200	38.42	38.42	31.65	31.41	57.91	57.76
	300	33.75	33.74	31.14	31.23	54.38	54.44
	400	28.80	28.81	32.50	32.56	51.94	51.99
	500	26.30	26.29	32.08	32.02	49.94	49.89
	600	24.44	24.44	31.38	31.31	48.15	48.10
	700	21.89	21.88	30.84	30.90	45.98	46.02
Crude oil 1	100	58.33	58.41	60.28	60.26	83.45	83.47
	200	55.22	55.25	59.41	59.42	81.82	81.84
	300	53.76	53.81	58.68	58.66	80.90	80.90
	400	52.89	52.90	58.10	58.09	80.26	80.26
	500	52.38	52.40	57.44	57.44	79.73	79.74
	600	51.62	51.63	57.07	57.07	79.23	79.24
	700	51.37	51.39	56.88	56.86	79.03	79.03
Crude oil 2	100	51.27	51.75	51.81	51.48	76.52	76.59
	200	48.46	48.33	51.42	51.63	74.96	75.01
	300	45.85	46.77	51.03	50.94	73.48	73.88
	400	45.63	45.55	50.70	50.81	73.20	73.22
	500	45.00	44.94	49.93	49.84	72.46	72.39
	600	44.22	44.20	50.10	50.15	72.16	72.18
	700	43.93	43.87	49.68	49.66	71.79	71.74

These findings reveal that while all three fluids exhibit a strong temperature-dependent decrease in viscosity, the extent of this response is governed by their compositional characteristics. Crude 1 showed the greatest reduction, suggesting a higher concentration of thermally sensitive constituents such as waxes and low molecular weight asphaltenes.

Crude 2 also responded significantly to temperature, although to a slightly lesser degree, indicating a somewhat more stable molecular composition. The sludge sample exhibited the lowest total reduction, with identical decreases of 31% observed over both the 10°C to 20°C and 20°C to 40°C intervals. This uniform reduction implies that the sludge contains a broader distribution of heavy components, with viscosity loss occurring more gradually across the full temperature range. Unlike crude oils, where most structural breakdown occurs rapidly at lower temperatures, the sludge matrix may contain a wider range of molecular weights, causing continuous disaggregation and viscosity reduction over both intervals.

The decrease in viscosity across all samples can be attributed to thermal effects on the fluid microstructure. Heating disrupts intermolecular forces within high molecular weight compounds such as waxes and asphaltenes, promoting molecular mobility and reducing resistance to flow. This effect is particularly pronounced between 20°C and 40°C, where wax dissolution typically occurs [17]. Additionally, increased temperature enhances the Brownian motion of dispersed particles, contributing to the breakdown of structured aggregates and further lowering viscosity [10,18]. The differences observed among the samples underscore the influence of composition and molecular architecture on thermal response, with crude oils exhibiting sharper declines in viscosity compared to the more compositionally heterogeneous sludge.

Yield stress

The yield stress represents the critical shear stress at which a material transitions from an elastic (solid-like) response to plastic (flow) behavior. Below this threshold, deformation is primarily reversible and the sample behaves elastically due to its internal structure. Once the applied stress exceeds the yield point, irreversible deformation occurs, initiating flow [19]. Yield stress is typically determined either by extrapolating flow curves to zero shear rate or by fitting data to non-linear rheological models. In the present study, yield stress measurements were conducted under controlled shear rate conditions at two different temperatures, 10°C and 20°C. This method is widely accepted for characterizing yield stress, particularly in complex fluids with non-Newtonian behavior such as sludge and crude oils.

Table 4. Measurement of the yield stress of samples as a function of temperature.

	Yield stress, Pa		
Temperature, °C	**Sludge**	**Crude oil 1**	**Crude oil 2**
10	8.18	0.404	0.153
20	6.22	0.171	0.123

The results in Table 4 demonstrate a pronounced temperature dependence in all samples, reflecting the influence of fluid microstructure on flow initiation. At 10°C, the sludge exhibited a substantially higher yield stress (8.18 Pa) compared to both crude oil 1 (0.404 Pa) and crude oil 2 (0.153 Pa), suggesting a significantly more rigid structure likely dominated by higher contents of heavy components such as asphaltenes and resins. When the temperature increased to 20°C, the sludge yield stress decreased to 6.22 Pa, and corresponding reductions were also observed in crude oil 1 and crude oil 2, with values declining to 0.171 Pa and 0.123 Pa, respectively. This consistent decrease across all samples with rising temperature indicates a reduction in internal resistance to flow, attributed to the thermal softening of structural components, which facilitates molecular mobility and disrupts the elastic network. The comparative analysis reveals that sludge maintains a significantly higher resistance to flow under both thermal conditions, underscoring its more complex or aggregated microstructure, whereas the much lower yield stress values in crude oils 1 and 2 reflect less structural rigidity and a greater intrinsic ability to flow, even at lower temperatures. These findings align with the general rheological understanding that the flow behavior of complex fluids is strongly influenced by the presence and thermal responsiveness of heavy fractions.

CONCLUSIONS

The rheological investigation of sludge and crude oil samples under varying shear rates and temperatures reveals complex, non-Newtonian flow behavior that is highly dependent on both composition and thermal conditions. A key finding is the presence of yield stress in all samples, with sludge exhibiting significantly higher values due to its dense, structured matrix enriched with asphaltenes, resins, and particulate matter. This indicates a strong internal network that must be disrupted to initiate flow.

Shear-thinning behavior dominates across the samples, particularly in sludge, where viscosity decreases markedly with increasing shear rate. This is due to the progressive breakdown of microstructural networks and molecular alignment under applied stress. At low shear rates, the sludge

behaves as a structured gel-like material, while at higher rates, its behavior transitions toward Newtonian as viscosity stabilizes. Crude oils demonstrate similar transitions but with less pronounced structural resistance.

Temperature plays a critical role in modulating rheological properties. As temperature increases, shear stress, viscosity, and yield stress all decline substantially, driven by the weakening of intermolecular interactions and breakdown of structured aggregates. The most significant viscosity reductions occur between 10°C and 40°C, particularly in crude oils, where thermally sensitive components like waxes and low molecular weight asphaltenes contribute to sharper transitions in flow properties. Sludge, with its broader molecular weight distribution, shows a more gradual response to thermal changes.

Modeling results confirm the suitability of the Herschel-Bulkley and Casson models in capturing the observed flow behavior, with the Herschel-Bulkley model best describing sludge rheology across temperature ranges. These insights underscore the importance of compositional and structural factors in determining the flow characteristics of heavy petroleum residues and highlight the critical role of temperature in optimizing their handling and transport.

EXPERIMENTAL SECTION

The oily sludge used in this study was sourced from the bottom of a crude oil storage tank at an oil refinery located east of Algiers, which processes crude oil from various regions of the Algerian desert. Following collection, the viscous sludge was stored in a sealed glass container at ambient temperature. Prior to testing, the sludge was manually stirred and subsequently homogenized using a Heidolph MR 3001k incubator shaker at 250 rpm for 15 minutes at 20 °C to prepare 20 mL samples. Key properties of the sludge are presented in Table 1. Crude oil samples were also obtained from two separate tanks in the Tin Fouye Tabankort (TFT) field in southern Algeria. At 20 °C, the densities of crude oil 1 and crude oil 2 were 840 kg/m³ and 825 kg/m³, with corresponding API gravities of 37 and 40, respectively.

The flow behavior of all samples was assessed using an AR-2000 rheometer (TA Instruments) equipped with a Couette geometry featuring a 14 mm diameter and a 1 mm gap [20-24]. Measurements were conducted at 10, 20, and 40 °C, with temperature control maintained via an external water bath and a cover to limit evaporation. Data were acquired and analyzed using the Rheology Advantage software. The rheometer operated in various modes including controlled rate (CR), controlled stress (CS), and oscillatory (OSC)

testing. Before measurements, samples were subjected to a 30-second pre-shear at 100 s^{-1} to ensure homogenization, followed by a one-minute rest period. Shear rate sweeps were performed across a range from 0.01 to 700 s^{-1}.

Table 5. Characteristics of the sludge sample used in this study [25].

Characteristics	Amount
oil (wt %)	75
water (wt %)	19
solid particles (wt %)	6
Saturates	52.10
Aromatics	25.90
Resins	15.50
Asphaltenes	6.50

REFERENCES

1. M. Ghanavati; M. J. Shojaei; A. R. SA; *Energy Fuels*., **2013**, *27*, 7217–7232.
2. D.E. Djemiat; A. Safri; A. Benmounah; B. Safi; *J. Petrol. Sci. Eng*., **2015**, *133*,184-191.
3. S. K. Al-Dawery; S. K. Al-Shereiqi; *J. Petrol. Explor. Prod. Technol*., **2019**, *9*, 2109–2121.
4. R. Anto; S. Deshmukh; S. Sanyal; U. K. Bhui; *Fuel*., **2020**, *275*, 117873.
5. G. M. Heath; R. A. Heath; Z. Dundr; *Acta Montan. Slovaca*., **2004**, *9*, 184–188.
6. G. Hu; J. Li; G. Zeng; *J. Hazard. Mater*., **2013**, *261*, 470–490.
7. K. Hui; J. Tang; H. Lu; B. Xi; C. Qu; J. Li; *Arab. J. Chem*., **2020**, *13*, 6523–6543.
8. T. M. Lima; A. F. Fonseca; B. A. Leao; A. H. Mounteer; M. R. Tótola; A. C. Borges; J. *Bioremed. Biodegrad*., **2011**, *2*, 10–4172.
9. M. Hassanzadeh; L. Tayebi; H. Dezfouli; *Petrol. Sci*., **2018**, *15*, 634–643.
10. C. Jie; Z. Xiaoyuan; J. Yuqi; M. Xiaojun; Z. Yaogen; *CIESC J*., **2015**, *66*, 4380.
11. R. Sharma; B. Deka; A. Mandal; V. Mahto; *Asia-Pac. J. Chem. Eng*., **2019**, *14*, e2279.
12. J. B. Taraneh; G. Rahmatollah; H. Amini; A. Davarpanah; *Fuel Process. Technol*., **2008**, *89*, 973–977.
13. R. Kumar; S. Mohapatra; A. Mandal; T.K. Naiya; *J. Pet. Sci. Res*., **2014**, *3*, 90-99.
14. N. A. Sami; D. S. Ibrahim; A. A. Abdulrazaq; *Petrol. Sci. Technol*., **2017**, 35, 856–862.
15. K. Benyounes; *SN Appl. Sci*., **2019**, 1,1-8.
16. R.I. Ibrahim; M.K. Oudah; A.F. Hassan; *J. Petrol. Sci. Eng*., **2017**, *156*, 356-365.

17. M.T. Ghannam; N. Esmail; *Pet. Sci. Technol*., **2006**, *24*, 985-999.
18. M.R. Khan; *Energy sources*., **1996**, *18*, 385-391.
19. R. Kumar; S. Banerjee; A. Mandal; T. K. Naiya; *J. Petrol. Sci. Eng*., **2017**, *152*, 353–360.
20. F. Souas; A. Safri; A. Benmounah; D.E. Djemiat; *Pet. Sci. Technol*., **2018**, *36*, 1093-1099.
21. F. Souas; A. Safri; A. Benmounah; D.E. Djemiat; *Pet. Sci. Technol*., **2018**, *36*, 1757-1763.
22. F. Souas; A. Safri; A. Benmounah; *Pet. Sci. Technol*., **2019**, *37*, 443-451.
23. F. Souas; A. Safri; A. S. E. Meddour; *Studia UBB Chemia*., **2025**, *70*, 221-234.
24. F. Souas; A. Gueciouer; *Ovidius Univ. Ann. Chem*., **2024**, *35*, 98–104.
25. F. Souas; *Pet. Res*., **2022**, *7*, 536-544.

STUDIA UBB CHEMIA, LXX, 3, 2025 (p. 191-199)
(RECOMMENDED CITATION)
DOI:10.24193/subbchem.2025.3.13

INVESTIGATION OF THE POTENTIAL OF ENVIRONMENTALLY FRIENDLY NON-IONIC SURFACTANTS FOR EOR

Ditta Adrienn GERBOVITS[a,*], Roland NAGY[a], Sándor PUSKÁS[b]

ABSTRACT. This study investigates the use of non-ionic surfactants synthesized from sunflower oil as sustainable alternatives for enhanced oil recovery (EOR). The bio-based surfactants were evaluated alongside commercial products through physicochemical and performance tests. The results revealed that the renewable formulations demonstrated excellent oil displacement and emulsification capacity, comparable to or exceeding that of conventional surfactants. These findings highlight the potential of plant-derived surfactants to reduce the environmental impact of EOR processes without compromising efficiency.

Keywords: *enhanced oil recovery, sustainability, environmentally friendly, non-ionic surfactant.*

INTRODUCTION

In addition to meeting the increasing global energy demand, environmental protection has become an increasingly critical priority. Balancing these two often conflicting objectives poses significant challenges for professionals in the field of engineering. According to current forecasts, the world's energy supply will continue to rely predominantly on crude oil-based sources, making it essential to develop more environmentally friendly technologies for oil extraction.

[a] *University of Pannonia, Faculty of Engineering, 10. Egyetem str., HU-8200, Veszprém, Hungary.*
[b] *MOL Plc, Group Oil Chemical Technologies, HU-6750, Algyő, Hungary.*
[*] *Corresponding author: gerbovits.ditta.adrienn@mk.uni-pannon.hu*

The continuous growth in global energy consumption has intensified the need for more efficient exploitation of existing petroleum reserves. One of the most effective strategies in this regard is Enhanced Oil Recovery (EOR), a technique employed when conventional primary and secondary recovery methods are no longer capable of extracting the residual oil trapped within the pore spaces of reservoir rocks [1]. In such cases, the injection of auxiliary substances becomes necessary to alter the properties of the reservoir fluids and improve oil mobility and recovery efficiency [2].

The fundamental principle of EOR lies in the ability of the injected agents to disrupt the physicochemical forces that retain oil within the porous matrix of the reservoir. By modifying these interactions, the mobility of the trapped oil increases, enabling more effective displacement towards production wells [3].

A wide range of EOR techniques exists, which are typically categorized based on the type of agent applied. These include thermal methods, gas injection processes, chemical techniques, and other additive-based approaches. The selection of a suitable EOR strategy is influenced by various factors, such as the geological characteristics of the reservoir, the physical and chemical properties of the crude oil, and the composition of formation water [4–6]. A classification of EOR methods is illustrated in Figure 1 [7].

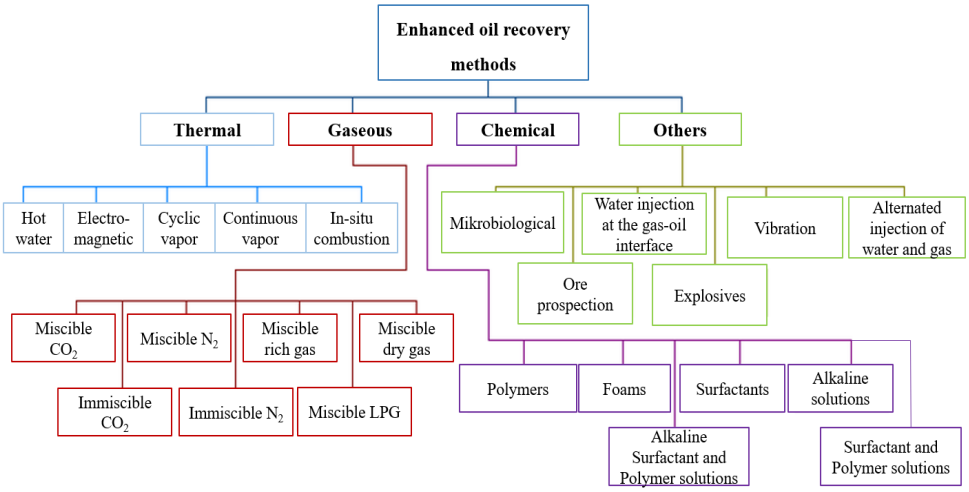

Figure 1. Additives used in enhanced oil recovery processes

The next phase of this research focuses on the investigation of surfactants used in chemical enhanced oil recovery (cEOR) processes. As shown in Figure 1, various chemical agents are commonly employed in cEOR techniques, including polymers, surfactants, alkaline substances, and

foaming agents [8]. While each of these additives can be effective on its own, their combined application may result in synergistic effects, further improving oil recovery efficiency.

This study focuses on the development and comprehensive evaluation of environmentally friendly, plant-based non-ionic surfactants for Chemical Enhanced Oil Recovery (CEOR) applications. The primary objective is to synthesise and evaluate alternative surfactant formulations derived from renewable resources in order to reduce the environmental footprint of EOR operations. In addition to their green origin, these novel surfactants were tested for a wide range of physicochemical properties including solubility, pH, viscosity, pour point and transmittance. In addition, their functional performance was investigated through oil displacement, emulsification and interfacial tension (IFT) tests under reservoir relevant conditions. The aim is to identify sustainable surfactant candidates that can match or exceed the performance of conventional fossil-based products, while offering improved environmental performance and process stability. This work contributes to ongoing efforts to align oil recovery technologies with the principles of green chemistry and sustainable engineering.

RESULTS AND DISCUSSION

In the following, the measured physical and chemical properties of the tested surfactants are presented. The results are summarized in **Table 1.**

Table 1. Physical and chemical properties of the investigated surfactants

Properties/ Sign of surfactant		S1	S2	S3	S4	REF1
Density (g/cm^3)	40°C	0.9800	0.9860	1.2201	1.0032	1.2223
Dynamic viscosity (mPas)	40°C	450	1285	1.6570	0.74264	1.5947
pH value		9.74	not measurable	12.83	11.83	8.89
Pour point (°C)		9	1	-15	-16	<-90*
Solubility		partially soluble	non-soluble	soluble	soluble	soluble
Transmittancy (%)		51	69	23	28	82
Water number (cm^3)		13.5	4.30	13.0	11.65	11.25

*In this case, the pour point was determined on the manufacturer's SDS sheet [9].

In all cases, the acid value was in the alkaline range and in the case where it was not measurable (S2), the acid value in **Table 2** also indicates that the substance is alkaline in nature.

The value of the water number is higher than 10 for all the samples tested, except for S2, indicating that the substance is soluble in water.

Table 2. Results of the impact assessments of the investigated surfactants

Properties/Sign of surfactant	S1	S2	S3	S4	REF1
Oil displacement test, (mm)	12	10	26	20	20
Emulsifying (solubilising) effect test, (V/V% emulsion)	22	23	41	63	100
IFT (mN/m)	8.67	10.2	7.14	5.3	1.82
Acid number	0	7.69	0	0	0.33
Turbidity value	688	>1100	1.93	3.42	11.16

The experimental results revealed that Sample-3 and Sample-4 exhibited favourable physicochemical properties, such as good solubility, high thermal stability (low pour points) and a pH ranging from neutral to alkaline. Their performance in impact-related tests was particularly noteworthy. Sample-3 achieved the highest oil displacement value (26 mm), outperforming both industrial and natural surfactants. Sample-4 demonstrated remarkable emulsifying capacity (63% V/V) and an interfacial tension (IFT) of 5.3 mN/m, lower than that of most of the tested surfactants, except REF1.

The industrial reference surfactant (REF1) demonstrated excellent performance in terms of IFT (1.82 mN/m) and emulsification (100% V/V). However, its environmental credentials could not be verified due to a lack of information on the origin of the raw materials. While partially plant-derived, SPAN80 and Empilan 2502 showed limited performance: SPAN80 had the highest acid number and turbidity, and both commercial biosurfactants displayed significantly lower oil displacement and emulsifying capabilities than the experimental samples.

Ultimately, of the surfactants tested, S2 was inferior to the others in terms of water solubility and in the impact studies. Despite having a pH in the alkaline range and being largely dissolved by mixing, surfactant S1 has a high transmission and turbidity and is also below the reference surfactant in terms of impact studies. The pH of surfactants S3 and S4 is in the alkaline range, and they are soluble in water with minimal mixing, with a water number above 11 in both cases, which is also related to water solubility. In the impact tests, similar or better results than the reference were obtained. Based on the properties tested and the results obtained, I establish the following ranking in **Table 3**.

Table 3. Ranking of the investigated surfactants

Rank	Sign of surfactant	Name of surfactant
1.	S4	Sample-4
2.	S3	Sample-3
3.	S1	EMPILAN 2502
4.	S2	SPAN80

CONCLUSIONS

This study investigated the potential use of environmentally friendly, plant-based, non-ionic surfactants in chemical enhanced oil recovery (CEOR) processes. Five surfactants were evaluated: three commercial products (REF1, Empilan 2502 and SPAN80) and two experimental samples synthesised from sunflower oil (Sample-3 and Sample-4). The evaluation covered a wide range of physical, chemical and performance parameters relevant to the applicability of EOR.

It is important to note that this study did not include a full environmental impact assessment. Therefore, no conclusions can be drawn on the overall environmental impact of the tested surfactants. However, the use of renewable raw materials in the synthesis of Sample-3 and Sample-4 suggests a potential for improved sustainability, pending further life cycle or biodegradability analysis.

In conclusion, the results indicate that the experimental plant-based surfactants, particularly Sample-3 and Sample-4, have competitive physicochemical profiles and functional properties that support their application in EOR. Future work should focus on structural optimisation to further improve performance, as well as conducting core flooding tests, long-term stability evaluations and comprehensive environmental impact assessments to confirm their suitability for industrial use.

EXPERIMENTAL SECTION

Raw Materials

This paper presents the results of an experimental study examining the physical, chemical, and functional properties of several plant-based non-ionic surfactants. The investigated materials include 2,4,7,9-tetramethyl-5-decyne-4,7-diol, which is the active substance in Surfynol 440 [10-12], hereafter REF1; Empilan 2502, derived from coconut fatty acid [13]; SPAN80, an oleic acid-based surfactant supplied by Sigma-Aldrich [14]; and two experimental surfactants synthesized from sunflower oil, designated as Sample-3 and Sample-4.

The REF1 non-ionic surfactant was tested for comparison as it is used in industry. Its raw material is not known to be environmentally friendly.

The surfactants listed in **Table 4** were subjected to a comprehensive set of laboratory tests to assess their physicochemical characteristics and potential applicability in Enhanced Oil Recovery (EOR) processes. All substances under investigation belong to the non-ionic surfactant category.

Table 4. Investigated surfactants and their environmentally friendly base materials

Sign of surfactant	**S1**	**S2**	**S3**	**S4**	**REF1**
Name of surfactant	**Empilan 2502**	**SPAN80**	**Sample-3**	**Sample-4**	**-**
Raw material	coconut fatty acid	sorbitol	sunflower oil	sunflower oil	-
Distributor	Huntsman	SigmaAldrich	University of Pannonia	University of Pannonia	SigmaAldrich

The plant oil-based surfactants developed in this study are non-ionic in nature. The synthesis pathways of the experimental surfactants described below follow a similar approach, with the main difference being the carbon chain length of the connecting spacer molecules. In both cases, a dibromoalkane compound was used for the linkage.

The first step of the synthesis involved the transesterification of vegetable oil with glycerol to produce a glycerol ester intermediate. In the second step, this intermediate was reacted with a dibromoalkane in an alkaline environment using a phase-transfer catalyst. The reactions were carried out at temperatures ranging from 80 to 250°C under atmospheric pressure. The resulting products were dried using anhydrous sodium sulphate [15].

Methodology: To assess the suitability of the investigated surfactants for chemical enhanced oil recovery (CEOR), a comprehensive series of physicochemical and performance evaluations was conducted. These tests aimed to determine key parameters that influence the efficiency, stability, and environmental compatibility of surfactants in reservoir conditions.

pH value: The pH of the surfactant solutions was measured in a 5 g/L aqueous solution prepared with distilled water, using a SevenCompact Duo pH meter (Mettler Toledo). The pH indicates the chemical stability of the surfactant and its potential interactions with reservoir fluids, as extreme pH values can adversely affect formation integrity and equipment.

Density and dynamic viscosity: Density and dynamic viscosity were measured at 40°C using an SVM 3000 Stabinger Viscometer. These parameters affect fluid flow, injectivity, and mobility control during CEOR operations.

Solubility: The water solubility of the surfactants was evaluated in 5 g/L aqueous solutions prepared with distilled water. Solubility was assessed through visual inspection and transmittance measurements. Transmittance was determined in 645 nm, using an Avantes AvaSpec-DUAL spectrophotometer (0% completely cloudy, 100% transparent). Good water solubility and high transparency are indicators of efficient dispersion in brine and reduced risk of phase separation in the reservoir.

Pour point: The pour point of the surfactants was determined using a Koehler automatic pour point and freezing point analyzer. A low pour point is essential to ensure injectivity and operational stability under varying field temperatures.

Water number: This test is used to assess the hydrophilic–lipophilic balance of surfactant compounds, providing insight into their emulsifying capabilities and salt tolerance. The water number was determined by titration. For the measurement, 1 g of surfactant was dissolved in 30 cm^3 of a 4:96 (V/V) cyclohexane–acetone mixture and titrated with distilled water until the onset of turbidity was observed [16].

Oil displacement test: The oil displacement test was performed using a thin film chromatography method. Glass plates coated with Algyő grained rock powder and crude oil droplets were immersed in 5 g/L surfactant solutions prepared with filtered brine. After 3 hours at 60 °C, the displacement distance of the oil was measured to evaluate surfactant efficiency [17]

Emulsifying (solubilising) effect test: The emulsifying capacity of the surfactants was tested using an ADEM automatic emulsibility tester in crude oil–brine systems. Equal volumes (40 cm^3) of 5 g/L surfactant solution and Algyő 892 crude oil were mixed at 1500 rpm, then left to rest for 30 minutes. Emulsion stability and extent were evaluated under controlled conditions [18].

Interfacial tension test: Interfacial tension (IFT) was measured using a Krüss SDT Spinning Drop tensiometer with Algyő 892 crude oil and 5 g/L surfactant solutions in filtered brine. The droplet radius was used to calculate IFT, providing insight into the surfactants' effectiveness in modifying oil–water interfaces for EOR optimization [19]

Acid number: The acid number was determined by titration with standardized KOH solution using phenolphthalein as an indicator. The required KOH volume was used to calculate the acid content (mg KOH/g sample), providing information on the sample's chemical quality and processing suitability [20].

Turbidity value: Turbidity was measured using a WTW Turb 430IR handheld turbidimeter. The turbidity value is expressed in NTU (Nephelometric Turbidity Unit). For each sample I tested a solution of 5g/L in filtered brine from Algyő.

By combining these analyses, a detailed profile of each surfactant's performance and compatibility with reservoir conditions was obtained, ensuring that the most promising candidates could be identified for sustainable CEOR applications.

Table 5 summarises the measurement methods used and their associated standards.

Table 5. Measurements and related standards

Measurement	Method Description	Relevant Standard(s)
pH value	5 g/L aqueous solution, measured with a pH meter (Mettler Toledo)	ISO 10523, ASTM D1293
Density and viscosity	Measured at 40 °C using SVM 3000 Stabinger Viscometer	ASTM D7042 (dynamic), ASTM D445, ISO 12185
Solubility & transmittance	Visual and spectrophotometric assessment (645 nm)	No standard; method based on literature protocols
Pour point	Measured with Koehler automatic analyzer	ASTM D97, ISO 3016
Water number	Titration until turbidity in cyclohexane–acetone mixture	No international standard; in-house/literature-based
Oil displacement test	Thin-film method using rock powder and crude oil on glass plates	No international standard; literature-based protocol
Emulsifying capacity	ADEM automatic tester, crude oil–brine system, 1500 rpm stirring, 30 min settling	Related: ASTM D6084, ISO 6614 (partially applicable)
Interfacial tension (IFT)	Spinning drop method with Krüss SDT tensiometer	DIN 55681 (spinning drop), ASTM D971, ISO 6889
Acid number	Titration with standardized KOH, phenolphthalein indicator	ASTM D664, ISO 6618
Turbidity	Measured with WTW Turb 430IR turbidimeter (infrared method)	ISO 7027, EPA 180.1

ACKNOWLEDGEMENTS

Prepared with the professional support of the Co-Operative Doctoral Program of the University Research Scholarship Program (code: 2024-2.1.2-EKÖP-KDP-2024-00017) of the Ministry of Culture and Innovation financed from the National Research, Development and Innovation Fund.

REFERENCES

1. A. O. Gbadamosi; R. Junin; M. A. Manan; Int. Nano Lett., 2019, 9, 171–202.
2. W.-L. Kong; B.-B. Zhang; M. Issakhov; M. Gabdullin; Pet. Sci., 2022, 19(4).
3. B. N. Barman; V. L. Cebolla; A. K. Mehrotra; C. T. Mansfield; Pet. Coal, 2001, 73, 2791–2804.
4. A. Agi; R. Junin; M. F. Syamsul; A. S. Chong; A. Gbadamosi; Petroleum, 2019, 5(1), 42–51.
5. A. Gbadamosi; S. Patil; M. S. Kamal; A. A. Adewunmi; A. S. Yusuff; A. Agi; J. Oseh; Polymers, 2022, 14, 1433.
6. O. Tavakkoli; H. Kamyab; M. Shariati; A. M. Mohamed; R. Junin; Fuel, 2022, 312.
7. A. Gurgel; M. C. Moura; T. N. D. Castro; E. L. Barros Neto; A. A. Dantas Neto; Braz. J. Pet. Gas, 2008, 2.
8. A. Samanta; A. Bera; K. Ojha; J. Pet. Explor. Prod. Technol., 2012, 2, 67–74.
9. National Center for Biotechnology Information; PubChem Compound Summary for CID 16213030, 2,4,7,9-Tetramethyl-5-decyne-4,7-diol ethoxylate; https://pubchem.ncbi.nlm.nih.gov/compound/2_4_7_9-Tetramethyl-5-decyne-4_7-diol-ethoxylate; accessed May 19, 2025.
10. E. Sansonetti; B. Andersons; I. Andersone; Mater. Sci. Eng., 2016, 111.
11. R. Krishnan; R. Sprycha; Colloids Surf., 1999, 149, 355–366.
12. M. D. Mampaey; Liquid Absorption into Porous Media; Master's Thesis, Eindhoven University of Technology, Netherlands, 2022.
13. J. Perkowski; W. Jozwiak; L. Kos; P. Stajszczyk; Fibres Text. East. Eur., 2006, 59(5), 114–119.
14. K. Kato; P. Walde; N. Koine; S. Ichikawa; T. Ishikawa; R. Nagahama; T. Ishihara; T. Tsujii; M. Shudou; Y. Omokawa; T. Kuroiwa; Langmuir, 2008, 24(19), 10762–10770.
15. N. Pal; N. Kumar; A. Verma; K. Ojha; A. Mandal; Energy Fuels, 2018, 32, 11344–11361.
16. M. Hartyányi; R. Nagy; L. Bartha; S. Puskás; Energies, 2024, 17, 2438.
17. M. Hartyányi; R. Nagy; R. Bejczi; L. Bartha; S. Puskás; Energy Sci. Eng., 2025.
18. M. Hartyányi; R. Bejczi; R. Nagy; N. Demcsák; L. Bartha; S. Puskás; MethodsX, 2024, 12, 102671.
19. R. Nagy; R. Sallai; L. Bartha; Á. Vágó; Adv. Chem. Eng. Sci., 2015, 5, 121–128.
20. A. V. Molnár-Kiss; R. Nagy; Waste Biomass Valor., 2024, 15, 917–921.

STUDIA UBB CHEMIA, LXX, 3, 2025 (p. 201-212)
(RECOMMENDED CITATION)
DOI:10.24193/subbchem.2025.3.14

CELLULOSE AND LIGNIN FIBERS MEDIATED REMOVAL OF THE OIL SPILL POLLUTION

Daniel ARGHIROPOL[a], Tiberiu RUSU[a], Miuța Rafila FILIP[a], Codruța SAROSI[b], Laura SILAGHI-DUMITRESCU[b], Gertrud-Alexandra PALTINEAN[b,*]

ABSTRACT. Vegetal matter like hemp wastes, peat and sawdust have fibrous and porous morphology if they are properly shredded as observed in SEM images. Polarized light microscopy has been used to study the crystalline structure of biomass and FTIR spectroscopy evidences their specific chemical bonds. Hemp wastes reveal porous husk remains of about 50 – 500 µm abundant in lignin and cellulose fibers lint having length of about 5 – 50 µm. Shredded peat reveal finer cellulose fibrous formation of about 50 µm length and lignin shell like particles of about 20 – 200 µm. Saw dust contains mainly cellulose fibers grouped in flake particles of about 700 µm with fringed edges. These samples were subjected to diesel and oil spills. The gravimetric test indicates the best specific absorption for diesel of 1.76 g/g obtained by sawdust and the lower value of 1.48 g/g was measured for hemp waste. The oil spill was better absorbed by sawdust having a specific absorption of 2.28 g/g and the weaker absorption was measured for hemp wastes around 1.66 g/g. The lower values measured for peat are caused by the presence of quartz particles as forest soil impurity.

Keywords: *Petroleum hydrocarbons, vegetal absorbents, Cellulose fibers.*

[a] *Faculty of Materials and Environmental Engineering, Technical University of Cluj-Napoca, 400641 Cluj-Napoca, Romania.*
[b] *Babeş-Bolyai University, "Raluca Ripan" Institute for Research in Chemistry, 30 Fântânele Str., 400294 Cluj-Napoca, Romania.*
[*] *Corresponding author: gertrud.paltinean@ubbcluj.ro*

INTRODUCTION

Petroleum hydrocarbon pollution poses a significant risk to both the environment and human health. They are hazardous chemicals from various activities such as petroleum industry, vehicle traffic, oil drilling processes, accidental spills, volcanic eruptions [1-3]. Petroleum, gasoline and diesel are the most uses fuels which can lead to a significant release of hydrocarbons in aquatic and terrestrial ecosystem. Their infiltration in environment can generate considerable damages such as loss of biodiversity, fertility and productivity [4-7].

To mitigate its harmful effects, natural absorbents have been employed to help restore balance to affected ecosystems. Hydrocarbon absorption is a fast, straightforward, and broadly applicable technique that uses materials capable of capturing and holding pollutants to lessen environmental impact. These absorbents are gaining attention due to their affordability, biodegradability, high oil absorption capacity, high buoyancy, local availability, and low cost [8, 9]. The decontamination of petroleum hydrocarbons using sawdust, peat and hemp fibers as absorbents proved to be beneficial to the environment [10-12].

Wood sawdust is commonly used in the treatment of oil-contaminated water. Its effectiveness varies depending on the type of wood as well as particle size and moisture content. Sawdust is an efficient absorbent due to its porous structure and the presence of carboxyl and hydroxyl functional groups that allows it to capture both volatile and semi-volatile hydrocarbon fractions [13, 14].

Peat is a natural absorbent composed of lignin, cellulose, as well as fulvic and humic acids. Its porous structure offers a large surface area, giving it a high capacity for hydrocarbon absorption. Peat is also highly buoyant and minimizes the risk of secondary pollution during the recovery process [15].

Taking into consideration the actual state regarding the vegetal absorbents used for the oil spills removal, the aim of present article is to evaluate the viability of hemp wastes, shredded peat and sawdust. All these materials are rich in cellulose and lignin having a great potential to be used as absorbents for petroleum wastes.

RESULTS AND DISCUSSION

Vegetal absorbents are known for their textured morphology, which can be properly observed under Scanning Electron Microscopy (SEM). The series of vegetal samples begins with the shredded hemp waste, Figure 1a.

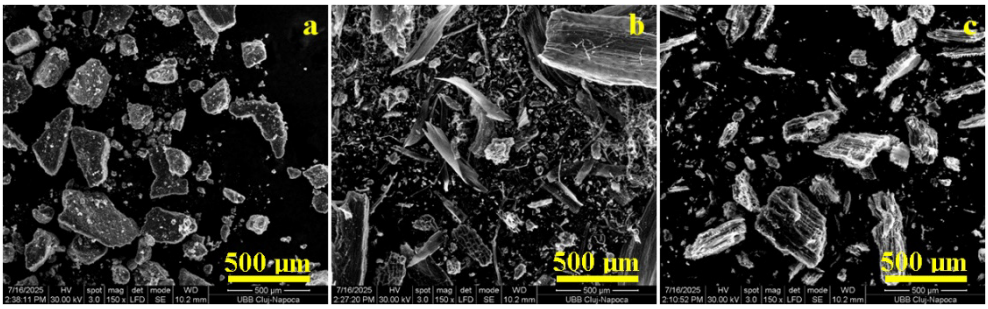

Figure 1. SEM images of the vegetal absorbents samples:
a) Shredded hemp waste, b) Shredded peat and c) Wood sawdust.

This mainly highlights husks from seeds that have a bimodal component formed by the fine fractions predominantly below 20 μm surrounding the coarse fractions that have irregular edges and planar dimensions of 100 – 700 μm associated with a thickness of about 30 – 50 μm.

On the other hand, the shredded peat sample, Figure 1b, contains partially degraded plant material in a wet state, which favors the loosening of the cellulose fibers from the lignified matrix, forming very fine filiform structures with lengths of 500 – 800 μm and thickness of 20 – 50 μm. These surround larger pieces with a still predominantly lignin aspect that gives them cohesion and resistance. We mention that the peat was ground for 30 minutes at 6000 rpm using a blade mill.

The wood sawdust, Figure 1c, is clearly inferior to the peat sample because the cellulose fibers are still strongly bound in the lignified structure, which leads to the predominance of coarse fractions with a chopped appearance (500 – 900 μm) and too few fine fractions to ensure efficient absorption.

Vegetal samples are very abundant in amorphous organic matter which cannot be observed properly in the mineralogical optical microscopy (MOM) but their cohesion is ensured by cellulose fibers and lignin binders which are organic matter with lower crystallinity [15, 16]. Therefore, some of our previous study successfully identifies cellulose fibers having white – yellow appearance and lignin structures predominantly brown under cross polarized light [17, 18]. Thus, the vegetal samples aspect is displayed in Figure 2.

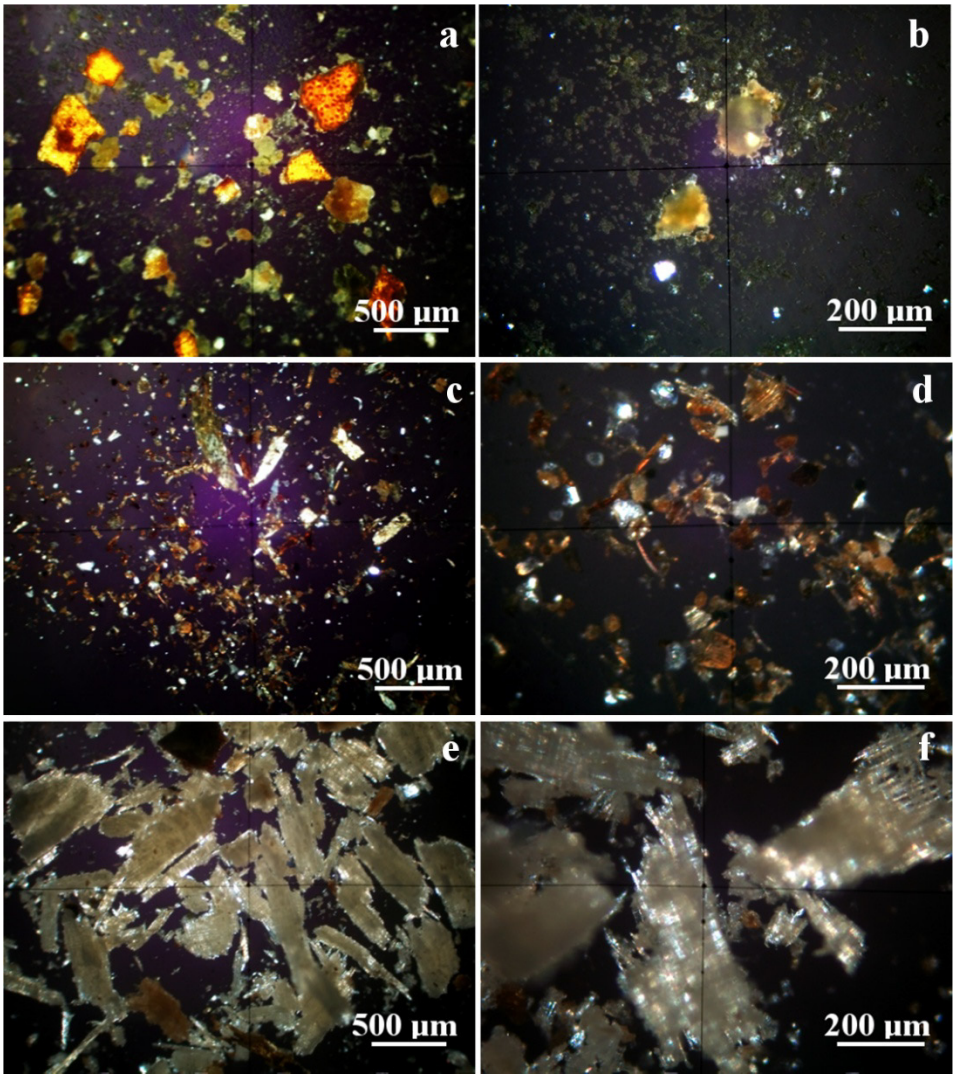

Figure 2. Cross polarized light images of the vegetal absorbents samples: Shredded hemp waste a) overall appearance, b) microstructural detail; Shredded peat c) overall appearance, d) microstructural detail; Sawdust e) overall appearance, f) microstructural detail.

Hemp waste is often a difficult material to naturally biodegrade due to its fibrous texture. The tow can be used as filler such as in the void space between building panels or as a protective coating over certain pipes, but the powdery fractions associated with hemp waste are quite problematic. These,

being ground to a uniform consistency, could act optimally to absorb oil stains. The overall microstructure, Figure 2a, highlights two major components, namely remnants of the husk that covers the hemp fibers. They have a predominantly reddish-brown appearance due to the high lignin content in their structure, which indicates that the stems were harvested at maturity. Their shape is irregular - fringed with planar dimensions varying widely in the range of 50 - 500 μm and the thickness varies between 1 - 5 μm. On the surface of larger shell fragments, circular cell holes with diameters ranging from 5 - 10 μm are observed. These biological reminiscences can be of great use in the absorption and immobilization of petroleum waste due to their high viscosity, which facilitates the retention of liquid in the cell pores.

The second major component of the shredded hemp sample is formed by fine microscopic fiber lint, a fact supported by their cellulose-based composition that appears yellowish white when observed in polarized light with crossed nicols, a fact consistent with data in the literature [17, 18]. The microscopic detail in Figure 2b captures in the central part of the field of view two fragments of hemp husk surrounded by enlarged fiber lint. These have very small dimensions with lengths ranging between 5 – 25 μm and thicknesses ranging between 1 – 3 μm. Their high number correlated with the porous appearance of the husk fragments indicates a high potential for absorption of petroleum waste and oily materials.

Peat has a deep layer with a high degree of carbonization compared to the superficial layers that retain a more pronounced vegetal character [19, 20]. Data from the literature show a significant content of lignin [21] and cellulose [22] of vegetal nature that has not been carbonized. Therefore, it is not surprising that the overall microstructural appearance of the crushed peat sample contains fragments of brown-brown colored lignin and yellowish-white colored cellulose that have a fringed appearance. These are accompanied by compact material particles with a high crystalline character whose nature cannot be detected at such a low magnification as in Figure 2c. The microstructural detail in Figure 2d solves the enigma of mineral particles. These have a boulder-like appearance with rounded edges and the shade is predominantly greenish-gray corresponding to quartz. In fact, these are forest sand particles whose sizes vary in the range of 50 - 100 μm and which are neutral in terms of the absorbing effect (in other words they do not help but do not hinder the absorption process). The particles containing lignin have the appearance of shredded vegetable shells that still retain traces of fibers, the dimensions of these shells vary widely from about 20 μm to 200 μm while the cellulose fibers are rarer and have smaller dimensions, lengths of about 5 - 50 μm and thicknesses of about 5 - 10 μm. Overall, it can be appreciated that such a mixture has a relatively limited ability to absorb petroleum waste due to the large and poorly shredded wood fractions.

Sawdust has an overall appearance of elongated flakes having about 500 – 700 μm length hand 50 – 250 μm width. Their color under cross polarized light is white – yellow due to the dense structure of cellulose fibers and contains moderate amount of brown particles rich in lignin, Figure 2e. Some smaller wood dust particles below 20 μm are also observed surrounding the flakes formations. The microstructural detail in Figure 2f reveal that the flakes formation has their ends featuring a fringe network of crossed cellulose fibers generating meshes below 10 μm which are optimal for the viscous liquid absorption. The microstructural disposal of sawdust cellulose fiber is more proactive than occurs in peat sample making it a better candidate for petroleum absorption.

The gravimetric measurements of diesel and burnt engine oil allow us to calculate each material's specific absorption, Figure 3. The obtained results were analyzed statistically and two relevant groups were found.

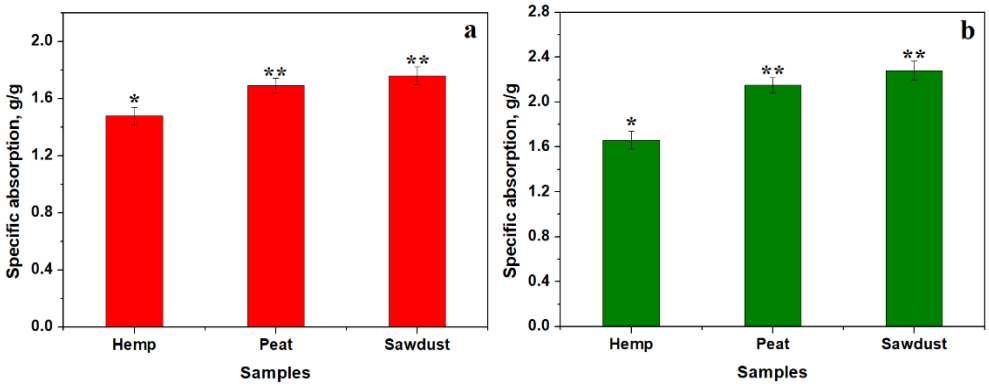

Figure 3. Specific adsorption variation on the vegetal samples tested in: a) Diesel and b) Burnt oil.

At the first sight a major difference is observed between Diesel and burnt oil absorption. The first one is more volatile and therefore the weight uptake is smaller than the one observed for burnt oil within each tested material but the variation tendency is the same in both cases.

The first statistical relevant group is formed by hemp waste sample which ensure a lower specific absorption of both diesel and burnt oil. The second relevant statistical group is formed by the peat and sawdust samples which reveal almost similar specific absorption (peat values being slightly lower). It is perfectly explainable because the wooden fibers within peat samples are partly decayed due to the marsh conditions of the resting ground. The statistical analysis reveals a relevant difference between the identified groups

$p < 0.05$. There must be some microstructural aspect that compromises the hemp waste absorption ability. SEM images taken after absorption, Figure 4, bring light on this aspect.

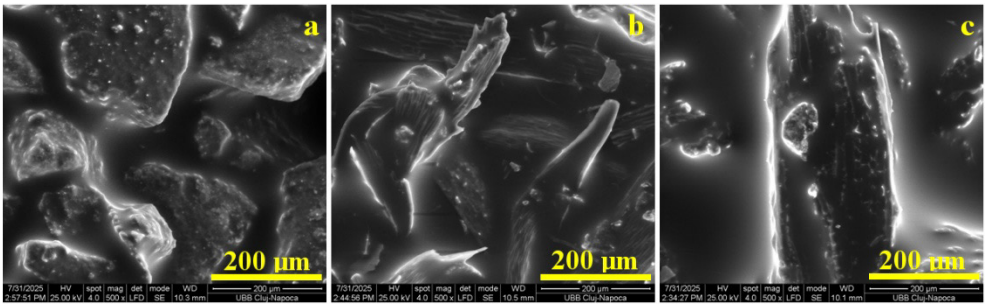

Figure 4. SEM images of the vegetal absorbents after burnt oil absorption: a) Shredded hemp waste, b) Shredded peat and c) Wood sawdust.

Hemp wastes are vey abundant in porous crust formations as observed by both initial SEM and cross polarized light microscopy which were taught to be ideal for absorption. Figure 4a, taken after burnt oil absorption reveal the fast penetration of the oil into the shell - crust pores saturating the bigger particles while the fine microscopic cellulose fiber lint is quickly clogged with oil and looses their individualization ability and become stacked to the shell crusts forming a partly barrier in further absorption. Such obstruction was observed in literature by finest mineral particles onto the vegetal particles within the carwash slurry and particulate matter deposits [23, 24]. Thus, the mechanism fails to rich the best absorption. Perhaps the absorption would be increased if the cellulose fiber lint would have been much more numerous than in the present sample.

The fringed cellulose particles within peat sample, Figure 4b, are prone to absorb the burnt oil into their porous structure becoming soaked reaching their optimal load. Their inter-particle space is filled with a dense pellicle of oil increasing the loaded amount. Figure 4c reveal that the fringed structure of sawdust flake particles is more efficient in absorbing petroleum because of their stabile meshes network which progressively fill with viscous oil reaching the saturation. The flake particles surface after complete soaking still contains a thicker oil film that stack on the large quantity of absorbed petroleum.

FTIR spectra (Figure 5 and 6) reveals the specific absorption bands for cellulose, lignin and some bands corresponding to hydrocarbons (diesel and burnt oil) in all samples: strong broad OH stretching (3300–4000 cm^{-1}), C–H stretching in methyl and methylene groups (2800–3000 cm^{-1}), and a strong broad superposition with sharp and discrete absorptions in the region

from 1000 to 1750 cm^{-1} [25]. The absorption located at ~1730 cm^{-1} is caused by cellulose and indicates the C=O stretch in non-conjugated ketones, carbonyls and in ester groups [26, 27].

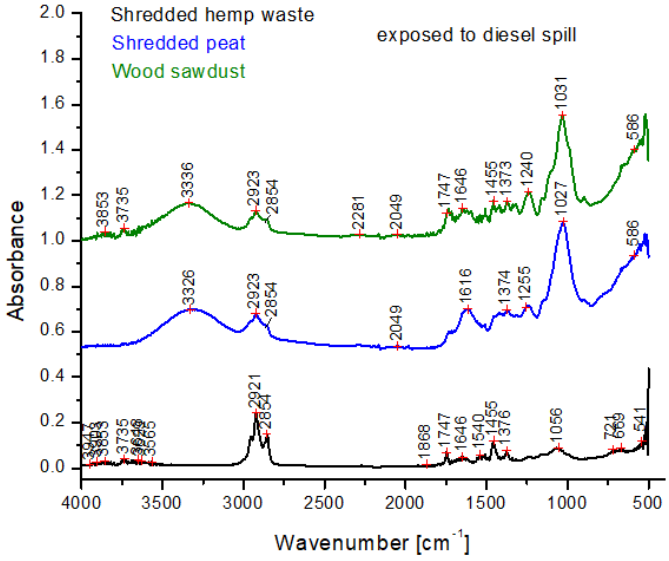

Figure 5. FTIR spectra for vegetal samples exposed to diesel spill.

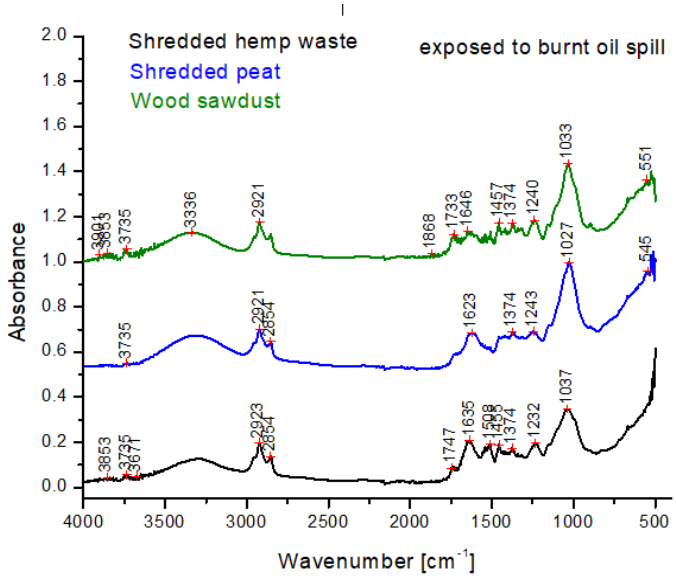

Figure 6. FTIR spectra for vegetal samples exposed to burnt oil spill.

FTIR patterns for peat samples soaked in both diesel and burnt oil reveal absorption bands at 545 cm^{-1} corresponding to O-Si-O bending deformation and 1033 cm^{-1} belonging to the in-plane Si-O stretching within the observed quartz particles [28] that impure the vegetal matter within peat. The other vegetal samples are free of silicates absorption bands.

Band assignments according to the literature and band shifts are listed in Table 1 [25-28].

Table 1. FTIR absorbance bands in vegetable samples (Shredded hemp waste, Shredded peat, Wood sawdust) [25-28].

Wavenumber [cm^{-1}]	**Assignment/functional group**
3700–3100	O–H stretching vibrations
3000–2750	Symmetric and asymmetric C–H stretching vibrations in CH, CH_2, and CH_3 groups
1770–1700	C=O stretching vibrations in carbonyl and carboxyl groups; C=O stretching vibrations in acetyl fragments
1675–1620	C=O stretching vibrations in *p*-substituted aromatic ketones
1470–1460	Asymmetric C–H bending vibrations in CH_2 and CH_3 groups; Scissor symmetric C–H bending vibrations in CH_2 groups
1450–1400	C–C stretching skeletal vibrations of the aromatic ring, combined with asymmetric C–H in-plane bending vibrations in O-CH_3 groups
1380–1370	C–H and O–H bending vibrations
1335–1200	C–H bending vibrations; deformation fan vibrations C–H in CH_2 groups; O–H in-plane bending vibrations
1145–1000	C–H in-plane bending vibrations of the sugar's rings; C–O stretching vibrations in alcohol groups; symmetric and asymmetric C–O–C stretching vibrations;
545	O-Si-O bending deformation;

A limitation of this study lies in the use of vegetable absorbent materials without any specialized pre-treatment. Future research should focus on investigating how the degree of grinding of the raw materials affects absorbency, aiming to identify optimal processing conditions. The current results clearly show that hemp waste exhibits lower absorption capacity due to its suboptimal microstructural properties. However, with more advanced grinding, these properties could be improved, potentially enhancing the absorption capacity to the level anticipated based on initial microstructural evaluations.

Additionally, further grinding of peat and sawdust samples may also lead to increased specific absorbency. Therefore, subsequent studies should emphasize precise control over the grinding process and incorporate a detailed assessment of porosity, including quantitative analysis of specific surface area using BET (Brunauer–Emmett–Teller) measurements.

CONCLUSIONS

The vegetal absorbents are lighter and therefore float on the water surface making them ideal for decontamination of petroleum spills within the aquatic environment. The best absorption was achieved by sawdust followed closely by peat sample. Hemp waste was slightly ineffective due to rapid clogging of the porous structure within the shell-crusts and the lack of significant network of cellulose fibers.

The microstructural aspects reveal that peat and sawdust have fringed structure of cellulose fibers that ensure an optimal absorption of the petroleum spills (e.g. diesel and burnt oil). Lignin rich parts such lignified crusts are less absorbent and diminish significantly the absorption yield.

Thus FTIR-ATR spectroscopy combined with SEM microscopy models offers a technologic tool that can be applied to evaluated the cellulose and lignin fiber's structure used in mediated removal of the oil spill pollution.

EXPERIMENTAL SECTION

The morphology of the samples, both in their initial state and after absorption, was examined using Scanning Electron Microscopy (SEM) with an Inspect S microscope (FEI Company, Hillsboro, OR, USA), operated in low vacuum mode at an acceleration voltage of 30 kV.

Cellulose and lignin components of the samples were examined under cross-polarized light using a Laboval 2 microscope (Carl Zeiss, Oberkochen, Germany). Each powder sample was carefully spread on a glass slide to ensure optimal visualization. Images were digitally captured using a Samsung 10 MPx camera system.

The quantitative absorption experiment was conducted by weighing 100 grams of each vegetal absorbent powder sample, which was then evenly spread over the contaminated surface. The samples were left in contact with the pollutant for 30 minutes, after which they were collected and reweighed. Specific absorption was calculated by relating the post-decontamination weight to the initial absorbent weight, and expressed as grams of petroleum pollutant absorbed per gram of absorbent. Each experiment was performed in triplicate, with standard deviations represented as error bars in the corresponding graphs. Statistical analysis was carried out using ANOVA followed by Tukey's post hoc test at a significance level of 0.05. Data analysis was performed using Microcal Origin Lab software, version 2018b (Microcal Company, Northampton, MA, USA).

Fourier Transform Infrared Spectroscopy (FTIR) was performed using a JASCO 610 spectrophotometer (JASCO International Co., Ltd., Tokyo, Japan) in ATR mode, with a resolution of 4 cm^{-1} and 100 scans per spectrum.

REFERENCES

1. S. S. Shetty; D. D. S. Harshitha; S. Sonkusare; P. B. Naik; S. N. Kumari; H. Madhyastha. *Heliyon*, **2023**, *9*(9), e19496. https://doi.org/10.1016/j.heliyon.2023.e19496
2. M. Rusca; T. Rusu; S. E. Avram; D. Prodan; G. A. Paltinean; M. R. Filip; I. Ciotlaus; P. Pascuta; T. A. Rusu; I. Petean. *Atmosphere*, **2023**, *14*, 862. https://doi.org/10.3390/atmos14050862
3. M. A. Hoaghia; I. Aschilean; V. Babalau-Fuss; A. Becze; O. Cadar; C. Roman; M. Roman; M. Senila; E. Kovacs. *Studia UBB Chemia*, **2021**, *66*(2), 95-104. DOI:10.24193/subbchem.2021.2.08
4. N. N. N. Samsuria; W. Z. W. Ismail; M. N. W. M. Nazli; N. A. A. Aziz; A. K. Ghazali. *Water*, **2025**, *17*, 1252. https://doi.org/10.3390/w17091252
5. E. Lusweti; E. K. Kanda; J. Obando; M. Makokha, *Water Pract. & Technol.,* **2022**, *17*(10), 2171–2185. https://doi.org/10.2166/wpt.2022.104
6. F. Ahmed and A. N. M. Fakhruddin. *J. Environ. Sci. & Nat. Resour*, **2018**, *11*(3), 555811. DOI: 10.19080/IJESNR.2018.11.555811
7. M. Kamranifar; H. Pourzamani; R. Khosravi; G. Ranjbar; K. Ebrahimpour. *Sci. Rep.*, **2025**, *15*, 8459. https://doi.org/10.1038/s41598-025-92512-9
8. R. Olga; R. Viktor; I. Alexander; S. Zinnur; P. Alexandra. *Procedia Chemistry*, **2015**, *15*, 231-236. https://doi.org/10.1016/j.proche.2015.10.037
9. M. R. Pires; M. S. Lorenço; M. C. Dias; L. R. da Silva; I. Petri Junior; F. A. Mori. *Chem. Eng. Technol.*, **2021**, *44*(12), 2269–2278. https://doi.org/10.1002/ceat.202100105
10. D. Zang; F. Liu; M. Zhang; Z. Gao; C. Wang. *Chem. Eng. Res. Des.*, **2015**, *102*, 34-41. https://doi.org/10.1016/j.cherd.2015.06.014
11. C. Cojocaru; M. Macoveanu; I. Cretescu. *Colloids Surf. A: Physicochem. Eng. Asp.*, **2011**, *384*, 675–684. doi:10.1016/j.colsurfa.2011.05.036
12. C. Mongioví; N. Morin-Crini; V. Placet; C. Bradu; A. R. Lado Ribeiro; A. Ivanovska; M. Kostić; B. Martel; C. Cosentino; G. Torri; V. Rizzi; J. Gubitosa; P. Fini; P. Cosma; E. Lichtfouse; D. Lacalamita; E. Mesto; E. Schingaro; N. De Vietro; G. Crini. Hemp-Based Materials for Applications in Wastewater Treatment by Biosorption-Oriented Processes: A Review. Edited by D. C. Agrawal; R. Kumar; M. Dhanasekaran in *Cannabis/Hemp for Sustainable Agriculture and Materials*, Springer Singapore, **2022**, pp. 239-295.
13. E. Meez; A. Hosseini-Bandegharaei; A. Rahdar; A. Thysiadou; K. A. Matis; G. Z. Kyzas. *Biointerface Research in Applied Chem*istry, **2021**, *11(4)*, 11778 – 11796. https://doi.org/10.33263/BRIAC114.1177811796

14. X. Chen; R. Xu; Y. Xu; H. Hu; S. Pan; H. Pan. *J. Hazard. Mater.*, **2018**, *350*, 38-45. https://doi.org/10.1016/j.jhazmat.2018.01.057
15. L. Di Giorgio, L. Martín, P.R. Salgado, A.N. Mauri, *Carbohydr. Polym.*, **2020**, 238, 116187. https://doi.org/10.1016/j.carbpol.2020.116187
16. P.R. Seidl, A.K. Goulart, *Curr. Opin. Green Sustain. Chem.*, **2016**, 2, 48-53. https://doi.org/10.1016/j.cogsc.2016.09.003
17. S.E. Avram, L.B. Tudoran, C. Cuc, B. Borodi, B.V. Birle, I. Petean, *J. Compos. Sci.,* **2024**, 8, 542. https://doi.org/10.3390/jcs8120542
18. M. Filip, M. Vlassa, I. Petean, I. Țăranu, D. Marin, I. Perhaiță, D. Prodan, G. Borodi, C. Dragomir, *Agriculture*, **2024**, 14, 2038. https://doi.org/10.3390/agriculture14112038
19. J. Shen, Y. Qin, J. Wang, Y. Shen, G. Wang, *Minerals*, **2018**, 8, 82. https://doi.org/10.3390/min8030082
20. H.I. Petersen, S. Lindström, H.P. Nytoft, P. Rosenberg, *Int. J. Coal Geol.*, **2009**, 78, 119-134. https://doi.org/10.1016/j.coal.2008.11.003
21. M. Safaei-Farouji, D. Misch, R.F. Sachsenhofer, J. Weitz, I. Kojic, K. Stojanović, S, Tursyngaliyev, M. Junussov, M.; Fustic, *Int. J. Coal Geol.*, **2025**, 306, 104813. https://doi.org/10.1016/j.coal.2025.104813
22. A. Zdravkov, A. Bechtel, K. Stojanović, D. Groβ, J. Weitz, I. Kojić, R.F. Sachsenhofer, D. Misch, D. Životić, *Int. J. Coal Geol.*, **2025**, 104843, https://doi.org/10.1016/j.coal.2025.104843
23. S.E. Avram, L.B. Tudoran, G. Borodi, M.R. Filip, I. Ciotlaus, I. Petean, *Sustainability*, **2025**, 17, 2906. https://doi.org/10.3390/su17072906
24. G.A. Păltinean, I. Petean, G. Arghir, D. F. Muntean, L.-D. Boboş, M. Tomoaia-Cotişel, *Part. Sci. Technol.*, **2016**, *34* (5), 580.
25. S.G. Kostryukov, H.B. Matyakubov, Yu. Yu. Masterova, A. Sh. Kozlov, M.K. Pryanichnikova, A.A. Pynenkova, N.A. Khluchina, *J. Anal. Chem.*, **2023**, *78 (6)*, 718. https://doi.org/10.1134/S1061934823040093
26. Y. Wang, J. Xiang, Y. Tang, W. Chen, & Y. Xu, *Appl. Spectrosc. Rev.*, **2021**, *57(4)*, 300. https://doi.org/10.1080/05704928.2021.1875481
27. R. Javier-Astete, J. Jimenez-Davalos, G. Zolla PLoS ONE **2021**, *16(10)*, e0256559. https://doi.org/10.1371/journal. pone.0256559.
28. S.E. Avram, L.B. Tudoran, G. Borodi, M.R. Filip, I. Petean, *Sustainability*, **2025**, 17, 2077. https://doi.org/10.3390/su17052077

STUDIA UBB CHEMIA, LXX, 3, 2025 (p. 213-226)
(RECOMMENDED CITATION)
DOI:10.24193/subbchem.2025.3.15

MINERAL ABSORBENT EFFIECIENCY ON THE PETROLEUM SPILLS REMOVAL

Daniel ARGHIROPOL[a], Tiberiu RUSU[a], Miuța Rafila FILIP[b], Laura SILAGHI-DUMITRESCU[b], Stanca CUC[b], Gertrud Alexandra PALTINEAN[b*]

ABSTRACT. Mineral absorbents are of great interest for the oil spills removal. Therefore, current investigation tests the removal ability of three commercial products: Zeolit Spectrum, Favisan Clay and professional oil spills removal Adabline II OS. SEM investigation reveals that all compounds relies on small phyllosilicates particles of about 1 – 5 μm accompanied by fewer coarser fractions of 100 – 150 μm. Mineralogical optical microscopy reveals that Zeolit Spectrum and Adabline II OS contains mainly Clinoptilolite while Favisan Clay contains mostly Kaolinite (1 – 10 μm) with some traces of Biotite (5 – 30 μm). These products were tested on diesel and burnt oil spills. The gravimetric measurements reveal the best specific absorption for Clinoptilolite of about 1.26 g/g for diesel and 1.69 g/g for oil while Kaolinite has only 1.04 g/g for Diesel and 1.37 g/g for oil spill. The fact was proved by FTIR spectroscopy revealing the increase of the C=C and C-O. The absorption mechanism was observed by SEM revealing the diesel and oil penetration within the finest mineral clusters, Clinoptilolite being more efficient than Kaolinite which was slightly reluctant because of its hydrophilic nature.

Keywords: *Oil spills, mineral absorbents, zeolite, clays*

[a] *Faculty of Materials and Environmental Engineering, Technical University of Cluj-Napoca, 400641 Cluj-Napoca, Romania*
[b] *Babeş-Bolyai University, "Raluca Ripan" Institute for Research in Chemistry, 30 Fântânele Str., 400294 Cluj-Napoca, Romania*
* *Corresponding author: gertrud.paltinean@ubbcluj.ro*

INTRODUCTION

Industrial and transport activities require a lot of fuel like gas, Diesel and kerosene and the vehicle's engines require proper lubrication ensured by specific oils [1, 2]. Both fuels and oils are hydrocarbons products and therefore they are hazardous for environment especially when are spilled on soil or water [3]. The soil contamination affects plants growth and damages the crops which become un-edible [4, 5]. On the other hand, hydrocarbon wastes on the water environment have toxic effect on the aquatic life forms like fish, shellfish and algae [6, 7]. Therefore, absorbent materials are of great interest to be used for the oil spills mitigation. Their nature should be adapted to the environment conditions: the contaminated soils would require a proper granular absorbent able to catch as more as possible the spilled grease and to preserve the soil structure. Water contamination requires absorbent materials with a good floatability that ensures their concentration over the water surface just like the oil spill. Thus, mineral absorbents are most suitable for the remediation of soil contamination while vegetal absorbents are more indicate to be used for decontamination of water surfaces [8].

An absorbent material requires a high specific surface associated with small particles. There is a mineral class fulfilling these requirements which is widespread in the earth crust. This special mineral class is represented by the phyllosilicates which have a lamellar structure based on the silica tetrahedral sheets interlocked by alumina and various alkaline ions such as K, Na and Li. The silica tetrahedral sheets interconnection through intermediary ions forms several subclasses like: Chlorite (e.g. Clinochlore mineral colored in green shades), Micas (e.g. Muscovite, Biotite and Lepidolite) and Clays (e.g. Kaolinite, Montomrillonite and Sericite) [9-11]. Tectosilicates are very similar to the Phylosilicates being structured on the silica tetrahedra bonded each other on their corners forming a light three-dimensional network the most common Tectosilicate subclass are feldspar and zeolites (e.g. Clinoptilolite). Zeolites are known in literature for their permeable structure allowing liquids to penetrate their interplanar spaces and to exchange ions with the adsorbed liquid [12, 13]. It is also mentioned in literature for its oil spills removal abilities [13, 14].

Literature data reveal that phyllosilicates fragmentation occurs through lateral cleavage of the particles followed by their subsequent breaking under the action of external forces forming very small particles of about 1 μm and even having submicron sizes [15, 16]. Such behavior facilitates increasing of the specific surface which is desired for the absorbent properties. Large amounts of kaolinite are found from natural and anthropogenic sources like sedimentary deposits or industrial sludge [17, 18] having a refined micro-structural distribution.

Local sources are very abundant such industrial sources and natural sedimentary deposits like clays deposited in whole Transylvanian basin as consequence of volcanic eruption of Ciomadu Mare Mountain [11, 19, 20]. Clinoptilolite is found in Dej and Racos volcanic tuff deposits within Transylvanian Basin [20, 21]. Therefore, the local deposits can be easily found and used for development of absorbent materials.

The aim of present research is to investigate the absorbent ability of some commercial materials based on clay and zeolite minerals at different exposure like diesel and burnt oil spills using modern investigation techniques such Scanning Electron Microscopy (SEM) and Fourier Infrared Spectroscopy (FTIR).

RESULTS AND DISCUSSION

The materials considered for use as absorbents for oil waste and oil stains have different natures from minerals to vegetal materials and therefore, they have an electrically insulating character. Therefore, these powdery - granular materials were deposited on double-sided carbon tape and investigated by scanning electron microscopy (Scanning electron Microscopy - SEM) in low vacuum mode so that they do not require metallization and the morphological details are perfectly visible.

Zeolit Spectrum sample has a very fine powdery appearance, with most particles having sizes up to 10 μm but there are some fractions larger than about 100 – 150 μm but not very numerous, Figure 1a.

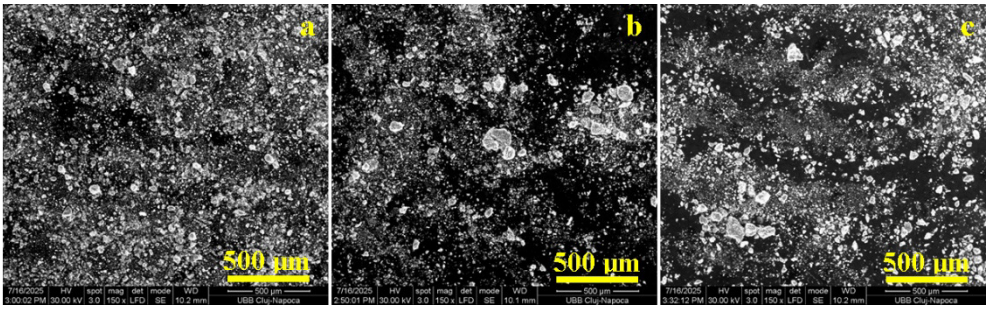

Figure 1. SEM images of the initial mineral absorbents: a) Zeolit Spectrum, b) Favisan Clay and c) Adabline II OS.

Favisan Clay sample is very similar to the previous one having very fine particles predominantly 1 – 3 μm to 10 μm but which tend to agglomerate slowly forming clusters larger than about 50 μm. Some coarse particles

100 – 200 μm with a boulder-like appearance and monolithic texture are also noted indicating an exogenous impurity most likely of a siliceous nature, Figure 1b. The Adabline II OS material has a texture and distribution intermediate between zeolite and clay indicating a mineral component specially conditioned for the absorption of oil and petroleum spills. It has a bentonite look with a high content of montmorillonite, a clay mineral from the smectite category whose crystallographic planes are ideal for liquid absorption, Figure 1c, but the material description indicates the main component as activated Clinoptilolite. It explains the more refined distribution compared to the Zeolit Spectrum's Clinoptilolite featuring coarser fractions.

The targeted absorbing materials have a high content of mineral and/or crystalline material; therefore, each constituent particle must be correlated with the mineral from which it is made. This goal can be achieved by examining the samples with the help of mineralogical optical microscopy that investigates the samples in polarized light with crossed nicols. This method sends a beam of polarized light oriented at 0° that passes through the sample and the analyzer lens (analyzer nicol) is oriented at 90°. Thus, if the sample is missing or if the material is amorphous, then the analyzer nicol does not let any light ray pass and a dark field will be seen in the ocular lens. Crystalline materials cause the plane of oscillation of the polarized light to rotate under a specific angle where colored light maxima will appear in the specific shade of each mineral [18, 22]. Therefore, using this method we can identify the mineral components in the samples to be investigated as well as the dimensional range of the constituent particles, Figure 2.

Zeolit Spectrum sample presents a finely dispersed granular aggregate appearance with an average content of coarse particles with dimensions ranging from 10 to 100 μm as observed in Figure 2a. The microstructural detail in Figure 2b shows that these are surrounded by finer particles with dimensions ranging from 1 to 5 μm. The white-yellowish appearance of the luminous maximum and the greenish-gray extinction are uniform for all particles within the visual field, indicating a high purity of the zeolite. All the observed characteristics indicate its belonging to the Clinoptilolite category according to data from the specialized literature [23, 24]. It has the chemical formula $(Na,K,Ca)_{2\text{-}3}Al_3(Al,Si)_2Si_{13}O_{36}\bullet 12H_2O$ and crystallizes in the monoclinic system. This fact is correlated with the tabular-lamellar appearance of the coarse particles and their angular edges as a consequence of fragmentation by cleavage. Literature data show that the finer the particles in the submicron and nanostructured range, the more capable it is of adsorbing polluting ink stains [24] as well as being effective in desulfurizing crude oil. Therefore, the highlighted microstructure is promising regarding the efficiency of this material in absorbing oil and petroleum stains for the decontamination of solid surfaces.

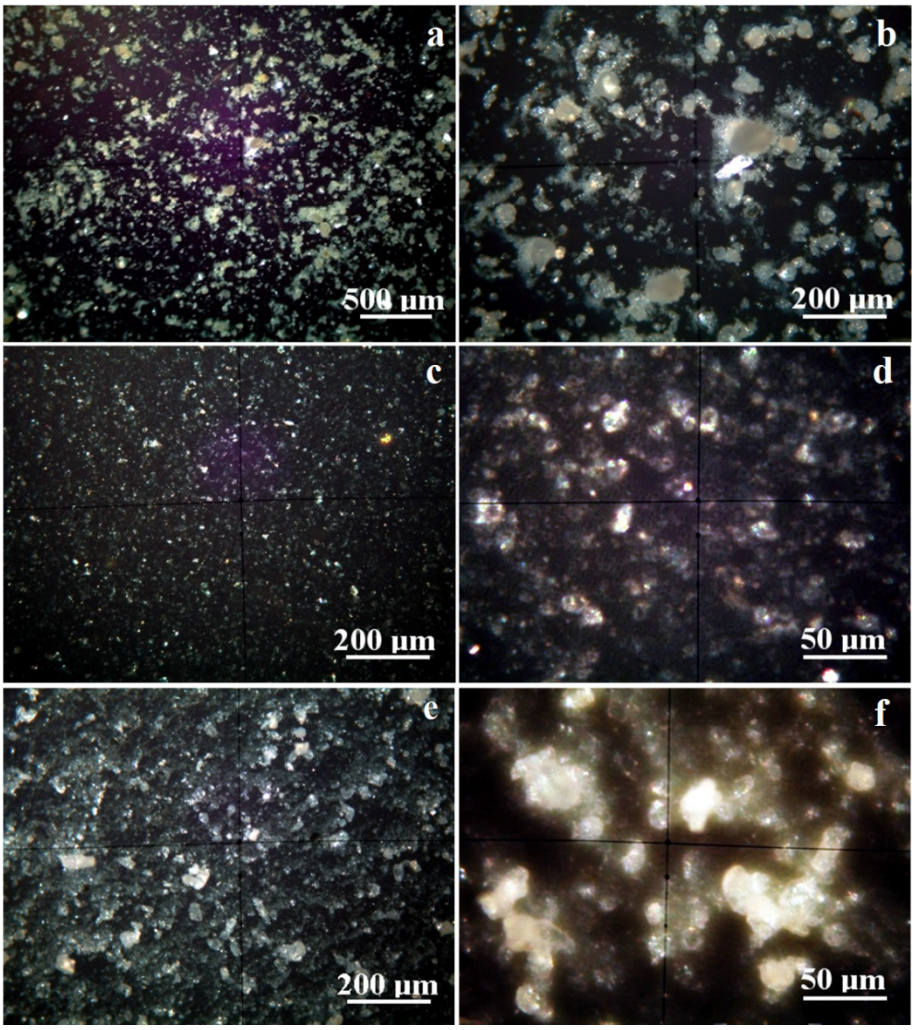

Figure 2. Mineralogical optical microscopy images for the investigated absorbent materials: Zeolit Spectrum a) overall appearance, b) microstructural detail; Favisan Clay c) overall appearance, d) microstructural detail; Adabline II OS e) overall appearance, f) microstructural detail.

Favisan clay is a very fine microcrystalline powder as can be seen in Figure 1c. Most of the particles are extremely fine and have a white hue corresponding to kaolinite which has the chemical formula $Al_2Si_2O_5(OH)_4$ and crystallization in the triclinic system [25, 26]. These are accompanied by some larger fractions having dimensions of about 10 – 50 µm with a tabular lamellar

aspect and reddish brown (orange) hue corresponding to biotite, a mineral in the micas category but where certain K atoms are replaced by Mg and Fe having the chemical formula $K(Mg,Fe)_3(AlSi_3O10)(F,OH)_2$ and crystallization in the monoclinic system [27]. Both minerals have foliated aggregates that cleave very fine fractions. This is proven by the microstructural detail in Figure 1d. Here the lamellar-tabular appearance of the kaolinite particles is very clearly observed, most of which are around 1 μm and some are even finer (they could be nanostructured). However, some particles in the range of 1 – 5 μm are very visible accompanied by some finer orange lamellae of around 2 μm corresponding to biotite. Literature data highlight the ability of kaolinite to absorb liquids by penetrating them between the crystallographic planes formed by SiO2 tetrahedra [25, 26]. It is worth noting that natural forest clays may have, in addition to the kaolinitic mass, traces of muscovite and quartz particles [28] but the sample used does not contain quartz traces. Therefore, it is expected that this powdery material will also have a high efficiency in absorbing oil stains.

The Adabline II OS material is currently used for the decontamination of solid surfaces polluted with petroleum and oleic products. Therefore, it constitutes a benchmark for comparison with other granular materials candidates for the decontamination function. The overall microstructural aspect highlights a very fine granular material with a high tendency to cluster. In general, the microstructural clusters in Figure 2e have a dune shape and predominant dimensions around 40 μm. Their hue is whitish, very similar to kaolinite but which could also be a very finely ground zeolite sample. The overall mineralogic observation confirms SEM microstructure. The detail in Figure 2f highlights very fine particles of about 0.5 – 1 μm that have a high tendency to coalescence, generating the microstructural dune – shaped clusters already observed. The fact that no other colored particles appear indicates the single-phase crystalline constitution of the investigated material. Its great similarity to the zeolite and clay considered gives indications that the latter could be largely as effective in removing oil and/or petroleum stains.

Zeolit Spectrum, Favisan Clay and Adabline II OS material have a deep mineral character generated by the tabular lamellar particles specific to phyllosilicates (clays) and tectosilicates (zeolites). These have a special behavior in the case of fragmentation, namely they cleave very easily under tangential stresses and under axial-perpendicular stresses they show high resistance [15, 17]. Therefore, their current state can be improved by mechanical grinding in a ball mill [18, 19], increasing the specific surface area and activating the liquid penetration sites between the crystallographic planes, improving the absorption of petroleum waste.

All investigated samples have great potential for absorbing petroleum spills but a quantitative measurement is necessary. Thus, 100 grams of each sample was tested gravimetrically against diesel and burnt oil spills revealing their specific absorption, Figure 3.

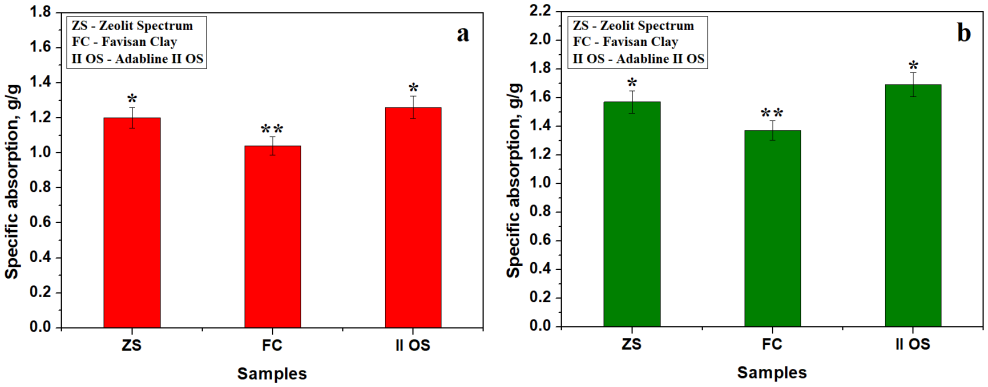

Figure 3. Specific adsorption variation on the mineral samples tested in: a) Diesel and b) Burnt oil.

The specific measured absorption reveals statistical differences between Diesel, Figure 3a, and burnt oil, Figure 3b indicating that the last one is better absorbed by the mineral absorbent comparative to Diesel. The fact is explained by the more viscous nature of oil compared to the significantly volatile behavior of Diesel. Thus, it is expected that the viscous oil adheres better on the absorbent small particles while Diesel favors their relative mobility hindering the formation of removing paste.

There are also found statistical similarities between specific absorption within Zeolite Spectrum and Adabline II OS because of their Clinoptilolite content, thus these samples form the first statistical relevant group. The second statistical group consists in Favisan Clay sample which has a significant lower specific absorption. This behavior is explained by the hydrophilic nature of clays which are prone to absorb aqueous solutions than oily liquids [31, 32]. Avram et.al. evidences the aqueous dispersion ability of the Kaolinite clay withing ceramic slurry being enhanced by the alkaline pH [33]. Wang et.al. reveal that fluoridation of the clay powder switches its hydrophilic behavior into hydrophobic one ideal for oil spills absorption [34]. On the other hand, silanization is also reported to enhance the hydrophobic behavior of the clays [35].

FTIR spectra of mineral absorbents exposed to diesel and burnt oils spills are present in Figure 4 and 5.

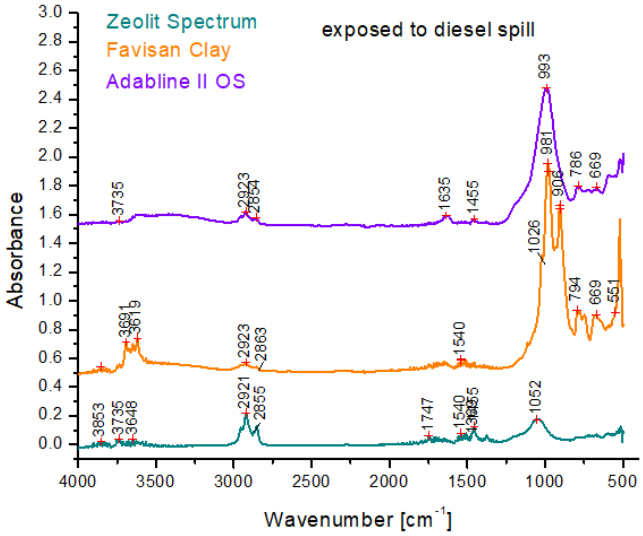

Figure 4. FTIR spectra of mineral absorbents exposed to diesel spill.

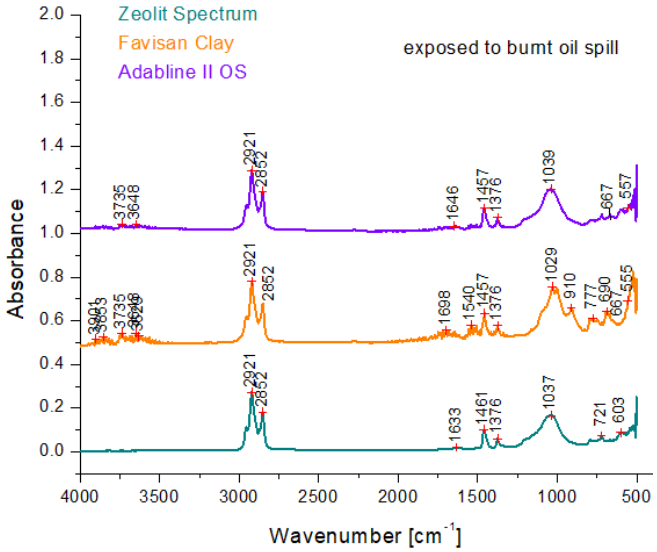

Figure 5. FTIR spectra of mineral absorbents exposed to burnt oil spill.

The absorption bands at 545 cm^{-1} corresponds to O-Si-O bending deformation; 667 cm^{-1} to Si-O symmetrical bending and 1029, 1039 and 1037 cm^{-1} fits the in plane Si-O stretching [36]. These absorption bands are

common for all silicates and are induced by the silica thetrahedra. The clay and zeolite presence are particularly evidenced by the absorption band at 777 cm^{-1} belonging to Al-O stretching [36].

The absorption bands at 2921 cm^{-1} and 2852 cm^{-1} corresponds to CH_2 asymmetric and symmetric stretching within both diesel and burnt oil [37]. The C=O chemical bond within diesel is evidenced by the absorption band at 1635 cm^{-1} while the absorption band at 1540 cm^{-1} belongs to C-C stretching within the burnt oil [38].

FTIR spectrum in Figure 4 reveal the previously mentioned absorption bands which are also observed in the spectra obtained on the mineral samples after diesel adsorption. The intensity of CH_2 and C=O absorption bands increase progressively with the spilled liquid absorption. Thus, Favisan Clay reveals lower intensities for the organic bands while their intensity increases progressively within Zeolit Spectrum and the greatest intensities are observed for Adabline II OS. There is observed a significant increase within absorption bands for Si-O stretching and for Al-O stretching indicating Diesel penetration within the crystallographic planes which causes some local reorientation within the phyllosilicate's sheets.

The FTIR spectra in Figure 5 for burnt oil also reveals absorption bands for CH_2 and C=O but also has the characteristic in C-C stretching. The mineral samples after oil absorption are significantly enriched with its specific bands. Their intensity progressively increases with the absorbed amount. Figure 5 reveal that less oil is absorbed within Favisan Clay and much more onto Clinoptilolite based samples because of better properties of zeolite matter. Beside the oil viscosity, the crystal planes are significantly affected by viscous liquid penetration causing mild increase of the mineral absorption bands in the range of 633 – 1033 cm^{-1}.

These morphological changes should influence the absorbents morphology, fact further investigated by SEM, Figure 6.

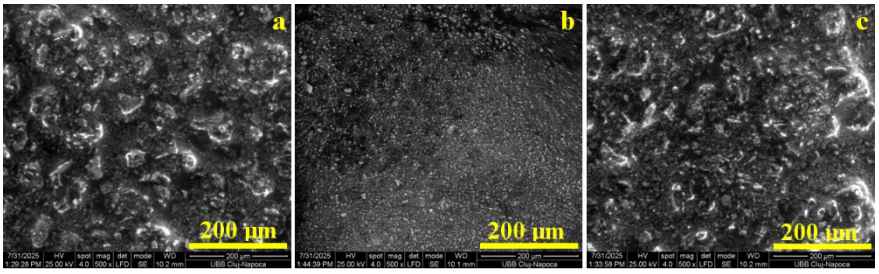

Figure 6. SEM images of the mineral absorbents after burnt oil absorption: a) Zeolit Spectrum, b) Favisan Clay and c) Adabline II OS.

SEM images taken on the absorbent samples after exposure to the burnt oil reveal the spreading of Clinoptilolite particles within Zeolit Spectrum and Adabline II OS within the oil spill absorbing the liquid between the thin crustal sheets, Figures 6a and c, fact in good agreement with FTIR observation regarding enhancing Si-O and Si-O-Si absorption bands intensities. However, the slightly lower absorption of Zeolit Spectrum compared to Adabline II OS is generated by those fewer bigger zeolite particles which do not allow a spread as good as Adabline does. On the other hand, Figure 6b reveals the uneven spreading of the Kaolinite fine particles regarding the oil spill because of the proper modification of their hydrophilicity. It is noteworthy mentioning that the central point of the observation field within Figure 6b and the lower right corner reveal dense areas where clay particles are coalesced through the burnt oil justifying the measured specific absorption.

The physicochemical aspects reveal that the local product Adabline II OS has the best behavior in removing both diesel and burnt oil spills. Zeolit Spectrum is a purified Clinoptilolite destined for human consumption as food supplement and therefore it is very expensive to be used in large quantities for petroleum spills removal. Fortunately, Transilvanian Basin is very rich in volcanic tuff containing both clays (Clinochlore, Muscovite and Kaolinite) but also Clinoptilolite zeolite and can be used for petroleum spill removal with minimal conditioning [39, 40].

Favisan Clay is a pure Kaolinite clay destined for cosmetic usage and therefore it is too expensive for be used for petroleum stains removal. It was used to assess the pure Kaolinite ability in oil spill removal. The lack of fluoridation or silanization treatments to increase its hydrophobicity makes it inferior to the zeolite-based materials. But there are large local clay deposits containing various proportions of Kaolinite and Muscovite which can be easily exploited in Transylvanian Basin generating cost effective oil spill removal agent with good behavior. It is strongly recommended that industrial agents working with large amount of petroleum to have a moderate stock of clay-based absorbent to be used in case of stringent necessity.

The mineral absorbent has a major lack regarding their neutralization after use because they cannot be completely destroyed by burning. They should be deposited in controlled dumps to avoid re-spilling of the absorbed hydrocarbons. The future challenge is how to recover the used mineral absorbents through the progressive filtration or development of a composite byproduct.

This study focused on high-purity, locally sourced materials to evaluate the specific absorption behavior of clinoptilolite and kaolinite with respect to diesel and burnt engine oil. The high cost of products like Zeolit Spectrum or Favisan clay poses a significant limitation to their use as petroleum absorbents.

In contrast, Adabline II OS is a purpose-designed product well-suited for this application. Consequently, a key direction for future research is the in-depth investigation of low-cost local clays, aiming to determine the optimal conditioning methods (such as grinding and/or silanization) needed to achieve effective oil stain absorption.

CONCLUSIONS

The tested local mineral products are effective on the diesel and burnt oil spills removal. The best results are obtained by the Clinoptilolite based materials (Zeolit Spectrum and Adabline II OS) because of their optimal micro porosity and absorption availability generated by the crystal structure. Adabline II OS prove to be very balanced product acting optimally for quick removal of the petroleum spills, while Zeolite Spectrum is not a specific destined product.

Kaolinite sample has slightly lower specific absorption because of its natural hydrophilicity. It requires special treatments to increase its hydrophobicity like silanization. But it can be used as emergency material to mitigate the petroleum spill if the specialized product is missing.

Natural deposit of volcanic tuff within Transylvanian Basin could be a valuable source for production of a cost-effective mixed zeolite/clay mixture to be used for mild spills removal.

EXPERIMENTAL SECTION

The commercial absorbent materials were purchased directly from their supplier as follows: Zeolit Spectrum (Novo Biomedics, Constanta, Romania); Favisan Clay (Favisan, Lugoj, Romania) and Adabline II OS (Adabline, Bucharest, Romania).

The samples morphology in initial state and after absorption was investigated by Scanning Electron Microscopy (SEM) using an Inspect S (FEI Company, Hillsboro, OR, USA) microscope operated in the low vacuum mode at an acceleration voltage of 30 kV.

The crystalline nature of the investigated samples was investigated through the Mineralogical Optical Microscopy (MOM) operated in cross polarized light on a Laboval 2 microscope (Carl Zeiss, Oberkochen, Germany). Each powder was carefully spread on the glass slide allowing its optimal view. The microscopy images were digitally acquired through a Samsung 10 MPx photographic system.

The quantitative absorption experiment was effectuated by weighing 100 grams of each powder samples which was spread on the contaminated surface. They were let to act for 30 minutes and afterward collected and weighed. Reporting the weight after decontamination to the initial absorbent weight results the specific absorption expressed in gram of petroleum pollutant per gram of absorbent used. The experiment was carried out in triplicate and the standard deviation is displayed as error bars in the variation graphs. The values were statistically analyzed using Anova test followed by Tukey post hoc at a significance level of 0.05. The statistical analysis was performed with Microcal Origin Lab version 2018b software (Microcal Company, Northampton, MA, USA).

Fourier Transformed Infrared Spectroscopy (FTIR) was effectuated with JASCO 610 spectrophotometer (JASCO International Co., Ltd., Tokyo, Japan) in ATR method with a resolution of 4 cm^{-1} and 100 scans for each spectrum.

REFERENCES

1. S.H. Pradhan, M. Gibb, A.T. Kramer, C.M. Sayes, *Environmental Research*, **2023**, 231(3),116267. https://doi.org/10.1016/j.envres.2023.116267
2. S.I. Bankole, M.O. Oloruntola, O.O. Bayewu, D.O. Obasaju, *Kuwait Journal of Science*, **2024**, 51, 100133. https://doi.org/10.1016/j.kjs.2023.10.001
3. M. Nie, N. Xian, X. Fu, X. Chen, B. Li, *Journal of Hazardous Materials*, **2010**, 174, 156-161. https://doi.org/10.1016/j.jhazmat.2009.09.030
4. M. Grifoni, I. Rosellini, P. Angelini, G. Petruzzelli, B. Pezzarossa, *Environmental Pollution*, **2020**, 265, 114950. https://doi.org/10.1016/j.envpol.2020.114950
5. M. Abdullah, Z. Al-Ali, A. Abulibdeh, M. Mohan, S. Srinivasan, T. Al-Awadhi, *Environmental Research*, **2023**, 219, 114955. https://doi.org/10.1016/j.envres.2022.114955
6. S. Esterhuyse, N. Redelinghuys, Patricia Charvet, P. Fearnside, V. Daga, R. Braga, W. Okello, J. Vitule, E. Verheyen, M. Van Steenberge, Effects of Hydrocarbon Extraction on Freshwaters, Editor(s): Thomas Mehner, Klement Tockner, Encyclopedia of Inland Waters (Second Edition), Elsevier, 2022, Pages 189-209. https://doi.org/10.1016/B978-0-12-819166-8.00164-X
7. A. Raposo, C. Mansilha, A. Veber, A. Melo, J. Rodrigues, R. Matias, H. Rebelo, J. Grossinho, M. Cano, C. Almeida, I.D. Nogueira, L. Puskar, U. Schade, L. Jordao, *Science of The Total Environment*, **2022**, 850, 157983. https://doi.org/10.1016/j.scitotenv.2022.157983
8. L. Donaldson, Materials Today, 2012, 235. https://doi.org/10.1016/S1369-7021(12)70108-6
9. G. A. Păltinean, I. Petean, G. Arghir, D. F. Muntean, L.-D. Boboş, M. Tomoaia-Cotişel, *Particulate Science and Technology*, **2016**, *34* (5), 580.

10. A. G. Hosu-Prack, I. Petean, G. Arghir, L.D. Bobos, M. Tomoaia-Cotisel, *Studia UBB Chemia*, **2010**, 55(3), 93-104.
11. S.E. Avram, L.B.; Tudoran, G.; Borodi, I.; Petean, *Appl. Sci.* **2025**, *15*, 6445. https://doi.org/10.3390/app15126445
12. Q. Liu, Y. Yu, G. Zhu, H. Liu, C. Jiang, W. Zhang, Y. Li, Q. Xue, Y. Wan, B. Li, X. Zhang, C. Dai, Z. Wang, *Colloids and Surfaces A: Physicochemical and Engineering Aspects*, 2024, 699, 134732. https://doi.org/10.1016/j.colsurfa.2024.134732
13. M. Teymourfamianasl, H. Atakül, *Separation and Purification Technology*,**2025**, 360, 131210. https://doi.org/10.1016/j.seppur.2024.131210
14. L. Bandura, M. Franus, G. Józefaciuk, W. Franus, *Fuel*, **2015**, 147, 100-107, https://doi.org/10.1016/j.fuel.2015.01.067.
15. G. A. Păltinean, I. Petean, G. Arghir, D. F. Muntean, M. Tomoaia-Cotişel, *Revista de chimie*, **2016**, *67* (6), 1118.
16. M. Rusca, T. Rusu, S.E. Avram, D. Prodan, G.A. Paltinean, M.R. Filip, I. Ciotlaus, P. Pascuta, T.A. Rusu, I. Petean, *Atmosphere*, **2023**, 14, 862. https://doi.org/10.3390/atmos14050862
17. S.E. Avram, M.R. Filip, L.B. Tudoran, G. Borodi, I. Petean, *Studia UBB Chemia*, **2023**, 68(4), 57-70. https://doi.org/10.24193/subbchem.2023.4.05
18. S.E. Avram,B.V. Birle, C. Cosma, L.B. Tudoran, M. Moldovan, S. Cuc, G. Borodi, I. Petean, *Materials,* **2025**, 18, 1715. https://doi.org/10.3390/ma18081715
19. K. Sant, D.V. Palcu, E. Turco, A. Di Stefano, N. Baldassini, T. Kouwenhoven, K.F. Kuiper, W. Krijgsman, *Data in Brief*, **2019**, 24, 103904. https://doi.org/10.1016/j.dib.2019.103904
20. A. Leeuw, S. Filipescu, L. Maţenco, W. Krijgsman, K. Kuiper, M. Stoica, *Global and Planetary Change*, **2013**, 103, 82-98. https://doi.org/10.1016/j.gloplacha.2012.04.008
21. A. Maicaneanu, C. Varodi, H. Bedelean, D. Gligor, *Geochemistry*, **2014**, 74, 653-660. https://doi.org/10.1016/j.chemer.2014.02.005
22. M. Shribak, Sci Rep, 2015, 5, 17340. https://doi.org/10.1038/srep17340
23. J.I. Núñez, J.D. Farmer, R.G. Sellar, G.A. Swayze, D.L. Blaney, *Astrobology*, **2013**, 14, 132–169. https://doi.org/10.1089/ast.2013.1079
24. E.S. Elbanna, A.A. Farghali, M.H. Khedr, M. Taha, Journal of Molecular Liquids, 2024, 409, 125538. https://doi.org/10.1016/j.molliq.2024.125538
25. S.E. Avram, L. Barbu Tudoran, C. Cuc, G. Borodi, B.V. Birle, I. Petean, *Sustainability*, **2024**, 16, 1123. https://doi.org/10.3390/su16031123
26. S.E. Avram, L. Barbu Tudoran, C. Cuc, G. Borodi, B.V. Birle, I. Petean, *J. Compos. Sci.*, **2024**, 8, 219. https://doi.org/10.3390/jcs8060219
27. S. Lőrincz, M.; Munteanu, S. Marincea, R.D. Roban, V.M. Cetean, G. Dincă, M. Melinte-Dobrinescu, *Geosciences*, **2025**, 15, 256. https://doi.org/10.3390/geosciences15070256
28. M. Vlassa, M. Filip, S. Beldean-Galea, D. Thiébaut, J. Vial, I. Petean, I. *Molecules*, **2025**, 30, 1959. https://doi.org/10.3390/molecules30091959
29. D.S.D. Lima, I.W. Zapelini, L.L. Silva, S. Mintova, L. Martins, *Catalysis Today*, **2024**, 441, 114842. https://doi.org/10.1016/j.cattod.2024.114842

30. S.R. Hashaikeh, *Materials Chemistry and Physics*, **2018**, 220, 322-330. https://doi.org/10.1016/j.matchemphys.2018.08.080
31. I. Msadok, N. Hamdi, S. Gammoudi, M.A. Rodríguez, E. Srasra, *Materials Chemistry and Physics*, **2019**, 225, 279-283. https://doi.org/10.1016/j.matchemphys.2018.12.098
32. R.J. Sengwa, S. Choudhary, S. Sankhla, Colloids and Surfaces A: Physicochemical and Engineering Aspects, 2009, 336, 79-87, https://doi.org/10.1016/j.colsurfa.2008.11.015
33. S.E. Avram, B.V. Birle, L.B. Tudoran, G. Borodi, I. Petean, *Water*, **2024**, 16, 1027. https://doi.org/10.3390/w16071027
34. Y. Wang, A. Chen, M. Peng, D. Tan, X. Liu, C. Shang, S. Luo, L. Peng, *Journal of Cleaner Production*, **2019**, 217, 308-316. https://doi.org/10.1016/j.jclepro.2019.01.253
35. A.B. Olabintan, T.A. Saleh, *Reactive and Functional Polymers*, **2024**, 195, 105807. https://doi.org/10.1016/j.reactfunctpolym.2023.105807
36. S.E. Avram, L.B. Tudoran, G. Borodi, M.R. Filip, I. Petean, *Sustainability*, **2025**, 17, 2077. https://doi.org/10.3390/su17052077
37. L. Biaktluanga, J. Lalhruaitluanga, J. Lalramnghaka, H.H. Thanga, *Results in Chemistry*, **2024**, 8, 101575. https://doi.org/10.1016/j.rechem.2024.101575
38. A. Wolak, J. Molenda, G. Zając, P. Janocha, Measurement, 2021, 186, 110141. https://doi.org/10.1016/j.measurement.2021.110141
39. Ch. Teas, S. Kalligeros, F. Zanikos, S. Stournas, E. Lois, G. Anastopoulos, *Desalination*, **2001**, 140, 259-264. https://doi.org/10.1016/S0011-9164(01)00375-7
40. W. Li, W. Wang, Y. Qi, Z. Qi, D. Xiong, *Journal of Environmental Management*, **2023**, 341, 118110. https://doi.org/10.1016/j.jenvman.2023.118110

STUDIA UBB CHEMIA, LXX, 3, 2025 (p. 227-241)
(RECOMMENDED CITATION)
DOI:10.24193/subbchem.2025.3.16

AN ENVIRONMENTAL ASSESSMENT OF ENERGY STORAGE USING THE RESTORE CONCEPT: ANALYSIS OF THE GMUNDEN CEMENT PLANT

Alessandra-Diana SELEJAN-CIUBANCAN[a], Letitia PETRESCU[a,*], Stefan Cristian GALUSNYAK[a], Calin-Cristian CORMOS[a]

ABSTRACT. The RESTORE initiative explores an innovative method of energy storage based on the thermochemical cycling of copper sulphate. During periods of surplus renewable electricity, such as for example solar-rich summer months, the system stores energy through the dehydration of copper sulphate. The stored energy is subsequently recovered during colder periods, such as winter, when energy demand increases and renewable availability declines, via the rehydration of the material. The current investigation focuses on the industrial RESTORE application at the Gmunden cement plant in Austria, proposing the integration of Thermochemical Energy Storage (TCES) with an Organic Rankine Cycle (ORC) and a Heat Pump (HP). The sustainability of the system was evaluated through a Life Cycle Assessment (LCA), conducted in accordance with the standard LCA framework, using version 10.8 of the LCA for Experts software. Environmental performance was quantified based on eleven key indicators derived from the ReCiPe 2016 assessment method. The functional unit for this study was set as the generation of 1 kWh of thermal energy, enabling a consistent comparison between the two construction alternatives of storage tanks, relevant to the industrial use case: carbon steel against high-density polyethylene (HDPE). The system boundaries were established to encompass the complete life cycle, segmented into three primary stages: i) Upstream activities; ii) Core operational processes; iii) Downstream operations. The use of HDPE outperformed carbon steel in key impact categories, cutting global warming potential (GWP) by over 55%, while significantly lowering other indicators. However, increased impacts in terms of fossil depletion and freshwater ecotoxicity potential

[a] *Babeş-Bolyai University, Faculty of Chemistry and Chemical Engineering, 11 Arany Janos str., RO-400028, Cluj-Napoca, Romania.*
[*] *Corresponding author: letitia.petrescu@ubbcluj.ro*

are registered, likely due to the petroleum-based nature of HDPE. Several discussions and interpretations of the most relevant environmental key performance indicators are provided, underlining the effectiveness of the proposed concepts.

Keywords: *Life Cycle Assessment (LCA), Thermochemical Energy Storage (TCES), Heat Pump (HP), Organic Rankine Cycle (ORC), District Heating and Cooling (DHC).*

INTRODUCTION

Global efforts to mitigate climate change have intensified in recent years, as the average global temperature continues to rise at a rate of approximately 0.2°C per decade. To address this challenge, international climate targets seek to limit the increase in global mean temperature to below 2°C, and ideally under 1.5°C, above pre-industrial levels [1]. Surpassing these thresholds poses significant risks to human health and the environment, including extreme weather events, rising sea levels, and ecosystem disruptions [2]. One of the primary strategies to combat climate change is the reduction of greenhouse gas (GHG) emissions through improved energy efficiency and the transition to low-carbon energy sources [3]. In this context, domestic heating emerges as a critical sector, representing approximately 78% of the total energy consumption in EU-27 households in 2020 [4]. Currently, around 42% of Europe's energy is still derived from fossil fuels, particularly natural gas. To achieve a sustainable energy transition, the European Commission promotes the adoption of renewable energy sources (RES) such as biomass, solar, wind, and geothermal energy [5,6]. However, the intermittent and seasonal nature of many RES necessitates the development of reliable energy storage technologies to balance energy supply and demand. Among the various storage solutions, Thermochemical Energy Storage (TCES) has gained prominence due to its high energy density and capacity for long-term storage with minimal thermal losses. TCES systems operate by storing heat in thermochemical materials through reversible chemical reactions, making them well-suited both for residential and industrial applications [7]. To facilitate year-round integration of RES, Organic Rankine Cycle (ORC) technology is frequently coupled with TCES. ORC systems are efficient and environmentally friendly technologies that convert low-grade heat, such as waste heat or energy from solar, biomass, or geothermal sources, into electricity [8]. Unlike traditional steam cycles, ORC can effectively utilize low-temperature heat sources, thereby offering a scalable solution for sustainable energy generation in light of dwindling fossil fuel reserves and increasing environmental concerns.

The Renewable Energy-based Seasonal Storage Technology in Order to Raise Economic and Environmental Sustainability of DHC (RESTORE) solution aims to integrate TCES with ORC and HP systems, promoting the large-scale incorporation of RES into District Heating and Cooling (DHC) networks (see Figure 1) [9].

To assess the environmental viability of this integrated system, the project employs Life Cycle Assessment (LCA) as a standardized methodology for evaluating environmental impacts across the full life cycle of a product or technology. LCA enables identification of environmental hotspots and offers guidance for system optimization, thereby supporting sustainable innovation [10].

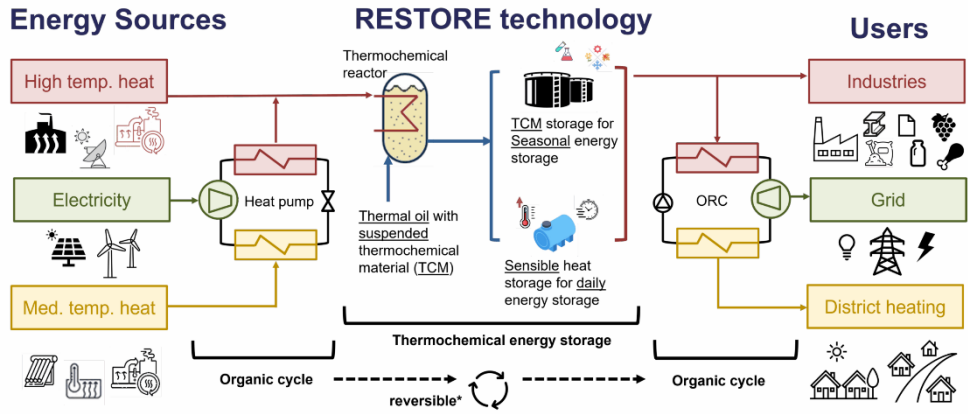

Figure 1. Overview of the RESTORE technology

MATERIALS AND METHODS

The LCA methodology used in this study adheres to ISO 14040:2006 and ISO 14044:2006 standards, which define the principles, framework, and detailed requirements for conducting LCA [11]. The LCA process consists of four interconnected and iterative stages: (1) Goal and Scope Definition, (2) Life Cycle Inventory (LCI), (3) Life Cycle Impact Assessment (LCIA), and (4) Interpretation of Results [12].

This study assesses the environmental performance of the RESTORE technology when integrated into a cement production facility located in Gmunden, Austria. As outlined previously, the proposed RESTORE concept combines TCES with ORC and HP technologies. Two design configurations for the construction of the RESTORE plant are evaluated: in Option 1, the storage tanks for charged and non-charged thermochemical material are constructed

from carbon steel, whereas in Option 2, they are made of plastic. The system aims to enhance the efficiency and sustainability of DHC networks by enabling the seasonal storage of energy from renewable sources. The assessment covers a 25-year operational period and incorporates location-specific conditions for Austria [13].

The Functional Unit (FU) for the study is defined as 1 kWh of thermal energy output, a standardized reference against which all environmental impacts are measured. The study adopts a cradle-to-gate system boundary, covering stages from raw material production (e.g., Therminol V66, copper sulfate, oil, etc.), system assembly, and energy output generation, as illustrated in Figure 2. Notably, the study excludes decommissioning processes, labor activities, rare catastrophic events, and the construction of transport infrastructure.

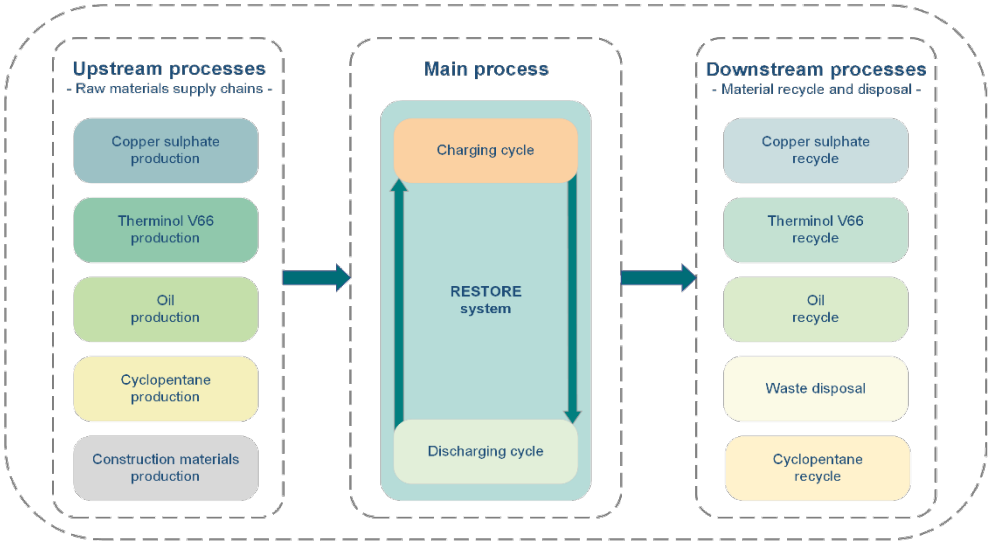

Figure 2. System boundaries for the RESTORE system

Table 1. Assumptions considered in all chemical compound supply chains

Process	Inputs	Value	Unit
Copper Sulphate	Diesel for transportation	10^{-3}	kg/h
	Copper for production	0.39	kg/h
	Sulphuric acid for production	0.61	kg/h
Oil	Diesel for transportation	$1.50 \cdot 10^{-3}$	kg/h
	Rapeseed oil [14]	1.00	kg/h
Cyclopentane	Crude oil	1.02	kg/h
	Electricity	$2.11 \cdot 10^{-4}$	kW/h

During the LCI phase, the study collects detailed data on all inputs and outputs associated with each unit process in the system [15]. Table 1 lists the comprehensive input-output data for the production of 1 kg of each material. Secondary datasets are utilized as they derive from process simulation activities using IPSE GO software, as seen in Figure 3, and a dedicated RESTORE_Lib model developed specifically for the project [16]. IPSE GO is an online process simulation software that features an integrated flowsheet editor for graphically building and connecting process models with advanced numerical methods for fast and precise calculations, and automatically generates reports of results [17]. For the production of specific materials such as Therminol V66, $CuSO_4$, cyclopentane, etc., existing literature and public life cycle databases provided the necessary information [18,19].

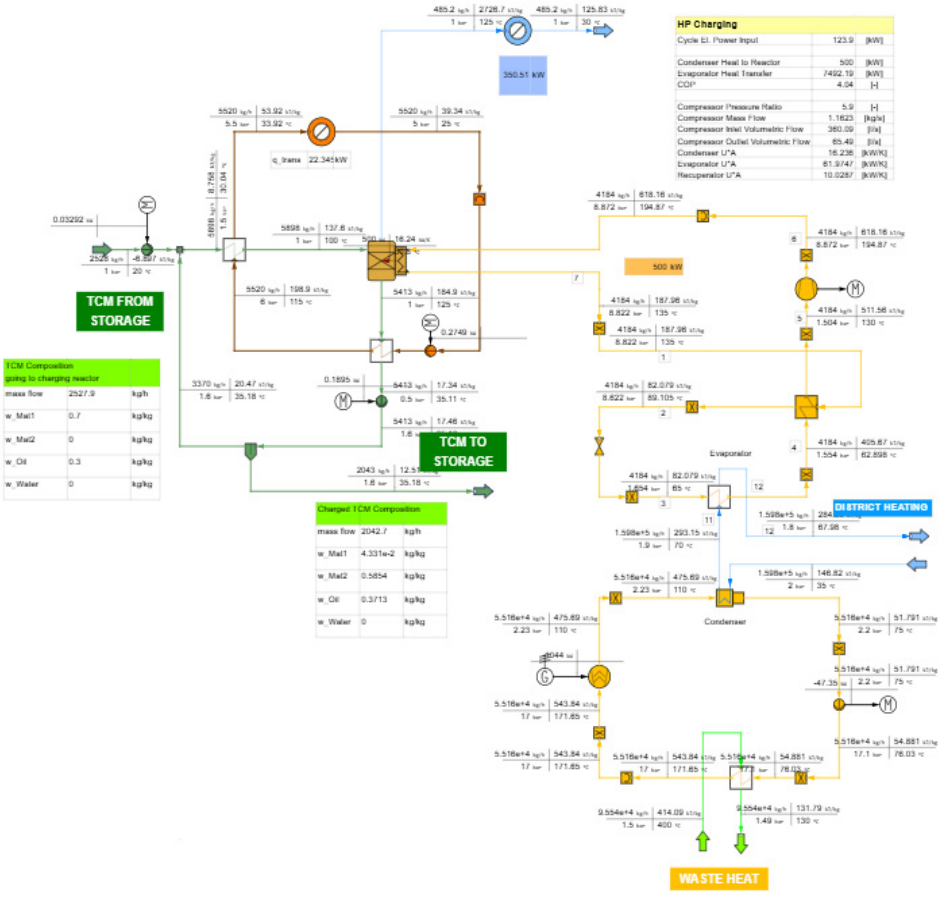

a)

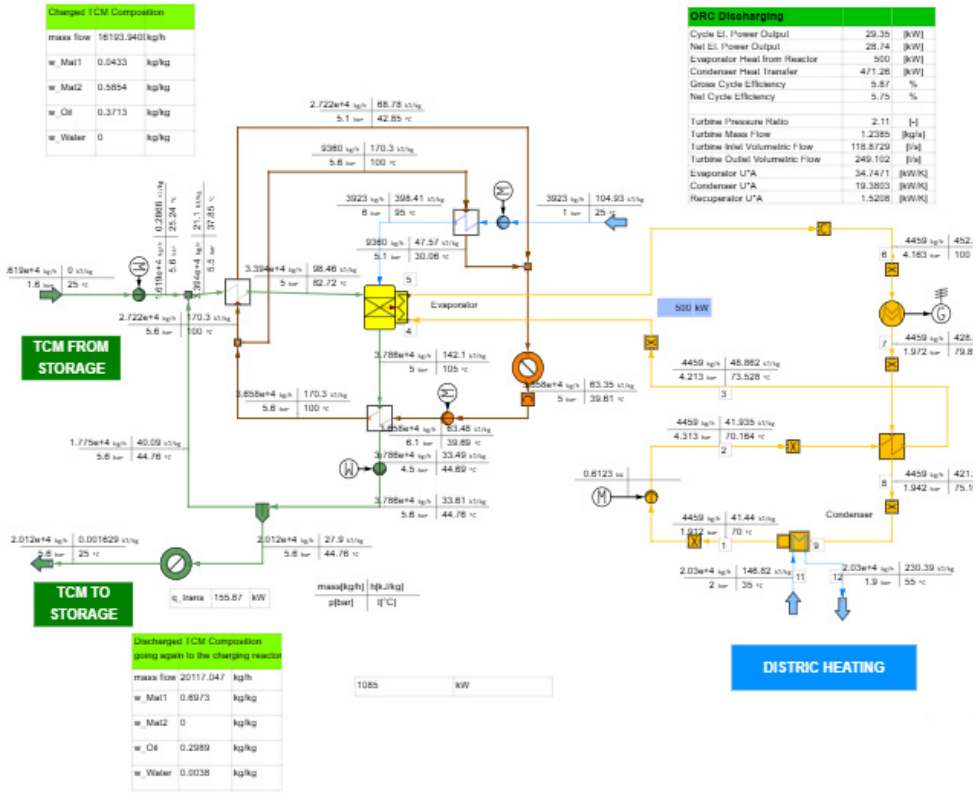

b)

Figure 3. IPSE GO model for the Gmunden (Austria) case:
a) Charging cycle and b) Discharging cycle

In the LCIA stage, the input and output inventory flows are translated into environmental impact categories [10]. This study employs the ReCiPe 2016 methodology, recognized for its capacity to evaluate both midpoint and endpoint indicators through scientifically supported cause-and-effect pathways [15].

The LCA was conducted using the LCA for Experts software [20], a robust platform that supports ISO-compliant assessments and includes extensive databases for modeling material use, energy consumption, emissions, and waste treatment.

RESULTS AND DISCUSSION

Table 2 summarizes the environmental performance of the RESTORE system based on a detailed LCA investigation. The analysis was conducted across three main phases: charging, discharging, and plant construction, which was further analyzed under two alternative scenarios for the storage tank material (carbon steel - Option no.1; and high-density polyethylene - Option no.2), all being reported to the FU of 1 kWh thermal energy output. Part of the LCA plans used for the below-mentioned results are presented in Figure 5 to Figure 7.

Table 2. Environmental key performance indicators (KPIs) according to the ReCiPe impact assessment method

KPIs	Units	Charging	Discharging	Option no.1	Option no.2
GWP	kg CO_2 eq./kWh	$7.68 \cdot 10^{-2}$	$0.92 \cdot 10^{-2}$	$3.21 \cdot 10^{-2}$	$1.35 \cdot 10^{-2}$
FDP	kg oil eq./kWh	$1.90 \cdot 10^{-2}$	$-0.10 \cdot 10^{-2}$	$6.52 \cdot 10^{-3}$	$1.08 \cdot 10^{-2}$
FETP	kg 1,4-DB eq./kWh	$1.53 \cdot 10^{-5}$	$0.12 \cdot 10^{-5}$	$5.44 \cdot 10^{-6}$	$7.63 \cdot 10^{-6}$
FEP	kg P eq./kWh	$1.19 \cdot 10^{-6}$	$0.31 \cdot 10^{-6}$	$1.22 \cdot 10^{-11}$	$1.22 \cdot 10^{-11}$
HTP_{cancer}	kg 1,4-DB eq./kWh	$1.88 \cdot 10^{-4}$	$-1.29 \cdot 10^{-7}$	$1.68 \cdot 10^{-4}$	$1.72 \cdot 10^{-4}$
$HTP_{non\text{-}cancer}$	kg 1,4-DB eq./kWh	$-0.48 \cdot 10^{-3}$	$0.67 \cdot 10^{-3}$	$2.50 \cdot 10^{-3}$	$2.96 \cdot 10^{-3}$
MDP	kg Cu eq./kWh	$1.93 \cdot 10^{-4}$	$3.78 \cdot 10^{-4}$	$9.59 \cdot 10^{-4}$	$1.32 \cdot 10^{-5}$
$POFP_{ecosystem}$	kg NO_x eq./kWh	9.57	0.69	$4.71 \cdot 10^{-5}$	$1.77 \cdot 10^{-5}$
ODP	kg CFC-11 eq./kWh	$2.75 \cdot 10^{-5}$	$3.96 \cdot 10^{-5}$	$1.90 \cdot 10^{-9}$	$2.26 \cdot 10^{-9}$
TAP	kg SO_2 eq./kWh	$2.43 \cdot 10^{-4}$	$1.78 \cdot 10^{-4}$	$4.59 \cdot 10^{-5}$	$1.32 \cdot 10^{-5}$
TETP	kg 1,4-DB eq./kWh	$1.37 \cdot 10^{-2}$	$-3.48 \cdot 10^{-4}$	$2.63 \cdot 10^{-2}$	$1.76 \cdot 10^{-2}$

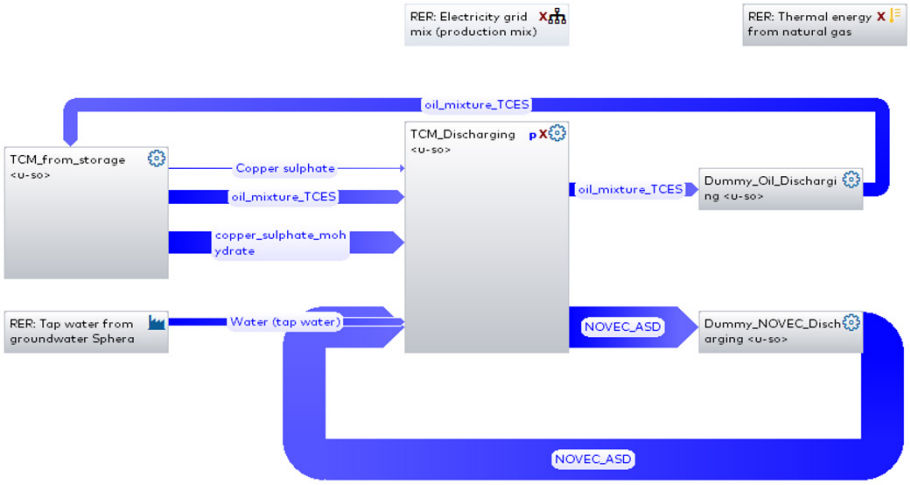

Figure 4. LCA plan for the discharging cycle

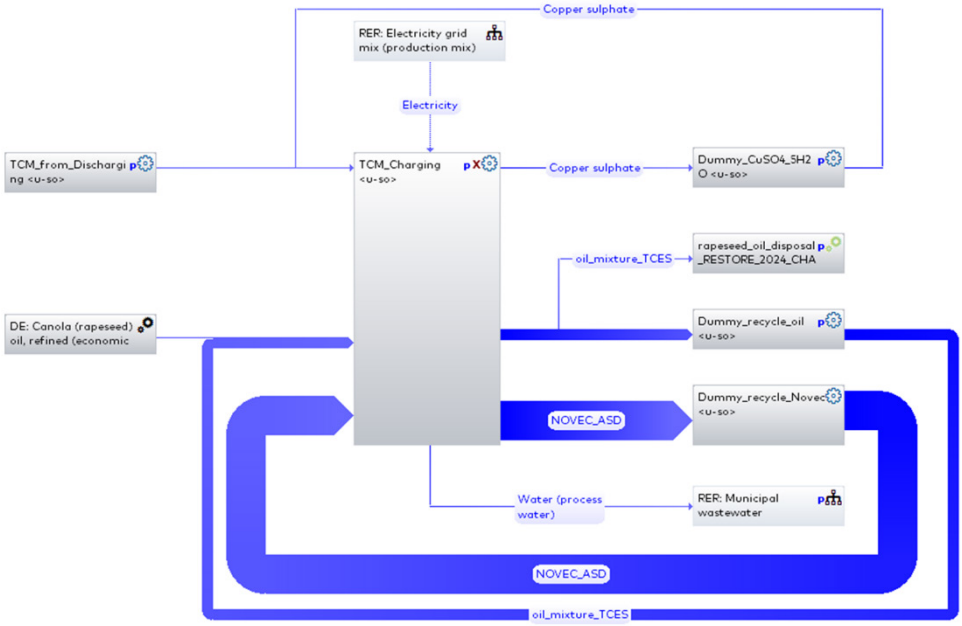

Figure 5. LCA plan for the charging cycle

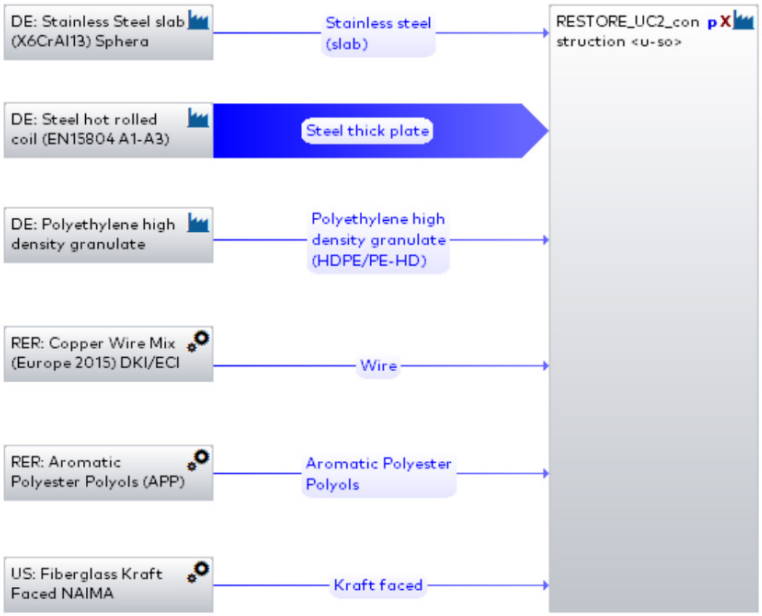

Figure 6. LCA plan for the plant construction

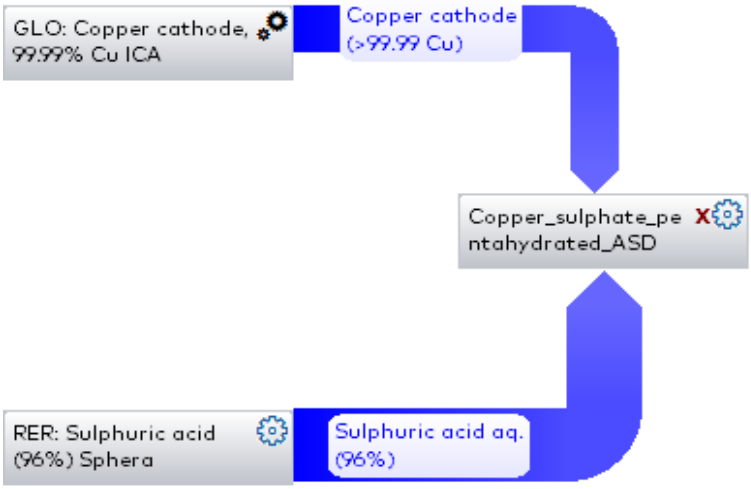

Figure 7. LCA plan for the Copper sulphate production

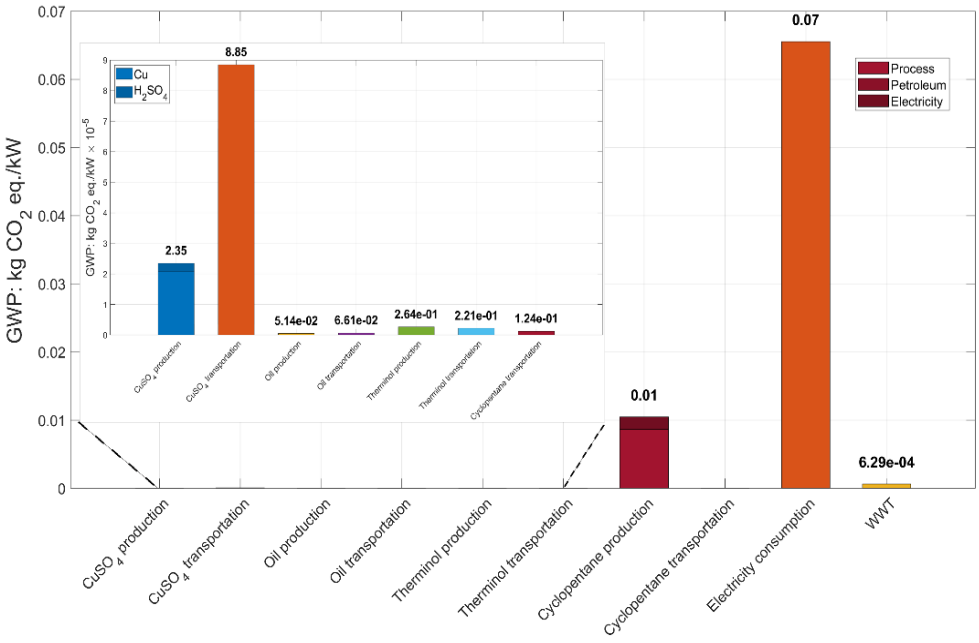

Figure 8. GWP for the Charging phase

During the charging phase, the system exhibited a Global Warming Potential (GWP) of $7.68 \cdot 10^{-2}$ kg CO_2 eq./kWh, significantly higher than that observed during the discharging phase ($9.2 \cdot 10^{-3}$ kg CO_2 eq./kWh), indicating that most of the climate change impact is concentrated in the thermal energy input phase (see Figure 8 and Figure 9). A similar trend was observed for most other impact categories, including Fossil Depletion Potential (FDP), Freshwater Ecotoxicity Potential (FETP), and Terrestrial Acidification Potential (TAP), all of which showed markedly higher values during charging. The FDP and Terrestrial Ecotoxicity Potential (TETP) indicators during the discharging phase registered values of $-1.0 \cdot 10^{-3}$ kg oil eq./kWh and $-3.48 \cdot 10^{-4}$ kg 1,4-DB eq./kWh, respectively. The Human Toxicity Potential cancer (HTP_{cancer}) for charging contributed to $1.88 \cdot 10^{-4}$ kg 1,4-DB eq./kWh, while discharging showed a small negative value ($-1.29 \cdot 10^{-7}$ kg 1,4-DB eq./kWh). Conversely, $HTP_{non\text{-}cancer}$ impacts were higher during discharging ($6.7 \cdot 10^{-4}$ kg 1,4-DB eq./kWh) than charging, suggesting increased exposure to non-carcinogenic toxic agents during this phase.

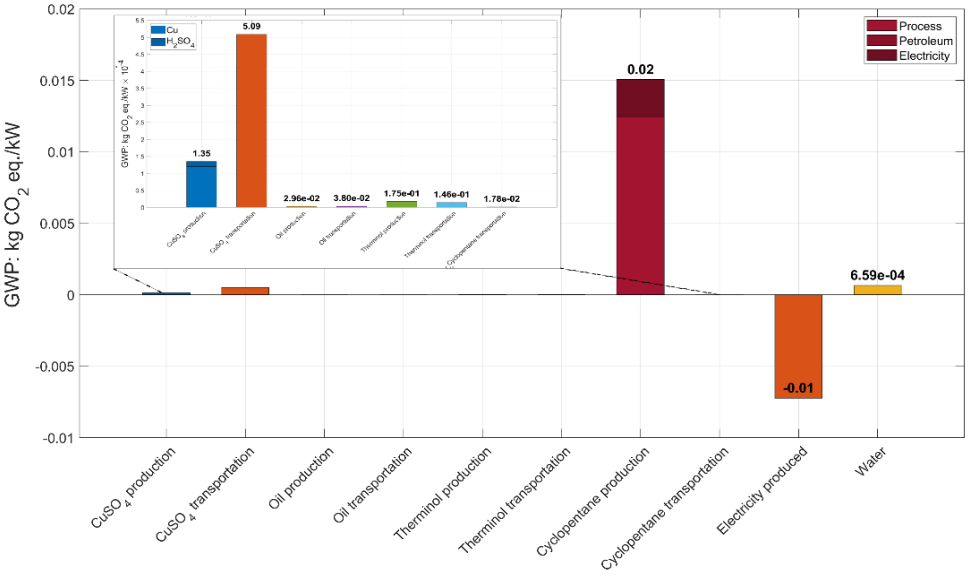

Figure 9. GWP for the Discharging phase

Regarding the environmental impact of plant construction, a notable difference was observed between the two tank material options. Option no.2 (HDPE tanks) consistently showed lower environmental impact across most categories compared to Option no.1 (carbon steel tanks), with the exception of the FEP category, where both options exhibited similar values ($1.22 \cdot 10^{-11}$ kg P eq./kWh). For instance, GWP was reduced from $3.21 \cdot 10^{-2}$ kg CO_2 eq./kWh in Option no.1 to $1.35 \cdot 10^{-2}$ kg CO_2 eq./kWh in Option no.2, indicating a 58% reduction in climate change-related emissions (see Figure 10 and Figure 11).

Similar reductions were evident in categories such as TAP (from $4.59 \cdot 10^{-5}$ to $1.32 \cdot 10^{-5}$ kg SO_2 eq./kWh) and $POFP_{ecosystem}$ (from $4.71 \cdot 10^{-5}$ to $1.77 \cdot 10^{-5}$ kg NO_x eq./kWh), reinforcing the environmental advantage of using HDPE instead of carbon steel. However, some trade-offs emerged since Option no.2 showed a higher impact in categories such as FDP ($1.08 \cdot 10^{-2}$ kg oil eq./kWh vs. $6.52 \cdot 10^{-2}$ in Option no.1), FETP ($7.63 \cdot 10^{-6}$ 1,4-DB eq./kWh vs. $5.44 \cdot 10^{-6}$ kg 1,4-DB eq./kWh), and ODP ($1.90 \cdot 10^{-9}$ kg CFC-11 eq./kWh vs. $2.26 \cdot 10^{-9}$ kg CFC-11 eq./kWh) which reflects the petroleum-based nature of HDPE and the associated toxicity during its production. The most significant divergence occurred in the Mineral Depletion Potential (MDP) category, with Option no.1 exhibiting a substantially higher impact score ($9.59 \cdot 10^{-4}$ kg Cu eq./kWh) compared to Option no.2 ($1.32 \cdot 10^{-5}$ kg Cu eq./kWh), thus highlighting the material intensity and extractive burden of carbon steel manufacturing.

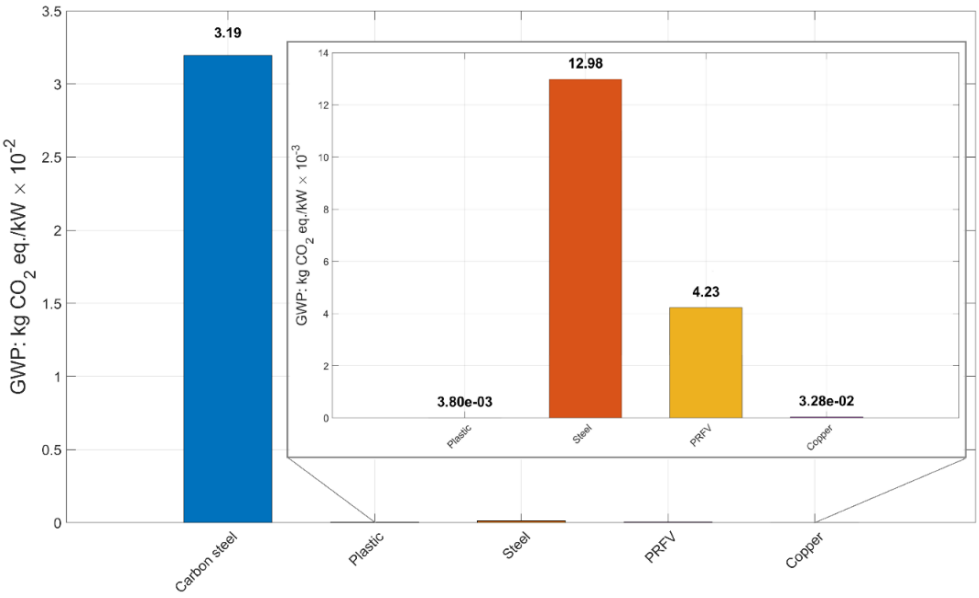

Figure 10. GWP for Plant construction – Option no.1

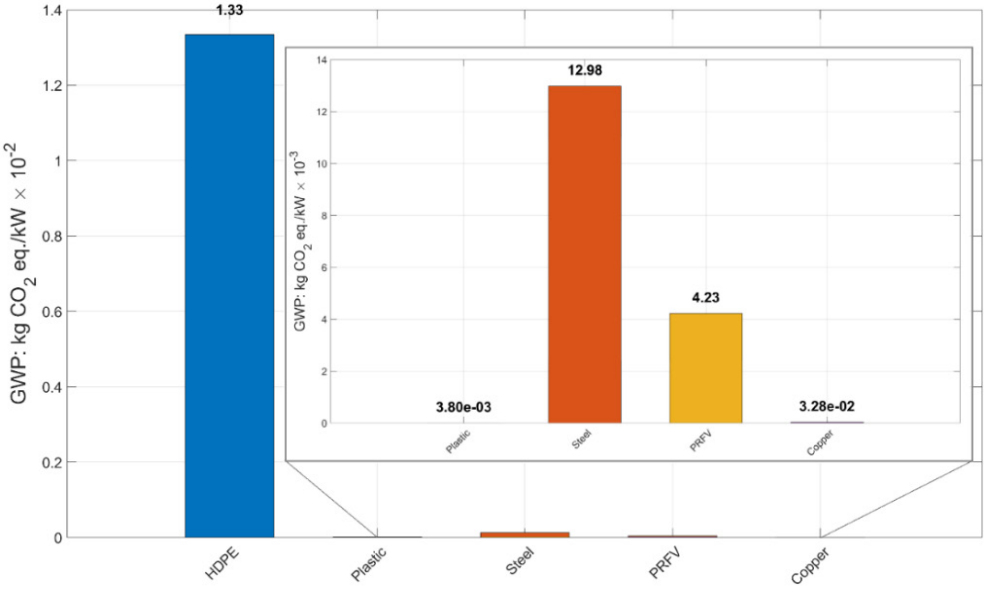

Figure 11. GWP for Plant construction – Option no.2

CONCLUSIONS

This study presented a comprehensive LCA of the RESTORE system, an integrated TCES and ORC/HP solution designed to enhance the environmental sustainability of DHC networks. Conducted over a 25 years operational lifespan and based on a functional unit of 1 kWh of thermal energy output, the assessment focused on three system phases: charging, discharging, and plant construction. Two construction configurations were analyzed, differing in the material used for storage tanks: carbon steel (Option no.1) and high-density polyethylene (HDPE, Option no.2).

The results indicate that the charging phase is the dominant contributor to environmental impacts across most categories, particularly in terms of GWP, FDP, and TAP. In contrast, the discharging phase exhibited considerably lower impacts and even environmental benefits in select categories, such as FDP and TETP.

From a construction perspective, Option no.2 consistently outperformed Option no.1 in several key impact categories. Notably, Option no.2 reduced GWP by approximately 58%, alongside substantial reductions in TAP and POFP. However, trade-offs were observed, as Option no.2 incurred higher impacts in categories such as FDP and FETP, likely due to the petroleum-based origin of HDPE.

These findings underscore the importance of adopting a life cycle perspective in the development of sustainable energy technologies, where both operational performance and construction material selection play critical roles in determining overall environmental outcomes. The RESTORE system, particularly when implemented with HDPE tanks, demonstrates strong potential as a low-impact, long-duration energy storage solution for supporting renewable energy integration in DHC networks. Moreover, this study highlights how combining LCA with performance-based indicators offers valuable guidance for optimizing the design and deployment of TCES technologies in future seasonal storage applications.

ACKNOWLEDGMENTS

The current work has received funding from the European Union's Horizon 2020 research and innovation program under grant agreement No. 101036766.

ABBREVIATIONS

DALY – Disability adjusted life years
DHC – District Heating and Cooling
FDP – Fossil Depletion Potential
FEP – Freshwater Eutrophication Potential
FETP – Freshwater Ecotoxicity Potential
GHG – Greenhouse gas emissions
GWP – Global Warming Potential
HDPE – High-Density Polyethylene
HP – Heat Pump
HTP – Human toxicity potential
ISO – International Organization for Standardization
LCA – Life Cycle Assessment
LCI – Life Cycle Inventory
LCIA – Life Cycle Impact Assessment
MDP – Mineral Depletion Potential
ODP – Ozone Depletion Potential
ORC – Organic Rankine Cycle
POFP – Photochemical Ozone Formation Potential, Ecosystem
PRFV – Reinforced Polyester with Fiberglass
RES – Renewable Energy Sources
TAP – Terrestrial Acidification Potential
TETP – Terrestrial Ecotoxicity Potential
TCES – Thermochemical Energy Storage

REFERENCES

1. E. C. Okonkwo; A. AlNouss; M. Shahbaz; T. Al-Ansari, *Energy Convers. Manage.*, **2023**, *296*, 117687.
2. Causes of climate change - European Commission. https://climate.ec.europa.eu/climate-change/causes-climate-change_en (accessed June 23, 2025).
3. Global and European temperatures 2025. https://www.eea.europa.eu/en/analysis/indicators/global-and-european-temperatures (accessed June 23, 2025).
4. Q. Bian, *Environ. Syst. Res.*, **2020**, *9*, 8.
5. Y. Hao; I. Khan, *Energy*, **2025**, *324*, 135863.
6. K. I. Vatalis; G. Avlogiaris; T. A. Tsalis, *J. Environ. Manage.*, **2022**, *309*, 114713.
7. P. Kalita; D. Kashyap; U. Bordoloi, Thermal Energy Storage Systems for Cooling and Heating Applications. In *Energy Storage*; John Wiley & Sons, Ltd: **2021**; pp 149–199.
8. M. Eyidogan; F. Canka Kilic; D. Kaya; V. Coban; S. Cagman, *Renew. Sustain. Energy Rev.*, **2016**, *58*, 885–895.

9. Luis, H2020 RESTORE Project. https://www.restore-dhc.eu/about-us/h2020-restore-project/ (accessed June 23, 2025).
10. O. Jolliet; S. Shaked; A. Jolliet; P. Crettaz; M. Saadé, *Environmental Life Cycle Assessment*; CRC Press: Boca Raton, **2016**.
11. H.-J. Klüppel, *Int. J. Life Cycle Assess.*, **2005**, *10*, 165–165.
12. S. C. Galusnyak; L. Petrescu; D. A. Chisalita; C.-C. Cormos, *Energy*, **2022**, *259*, 124784.
13. E. Perz; S. Kysela; M. Perz, **2025**, https://doi.org/10.5281/zenodo.15341167.
14. L. Schmieder; S. Kuloglija; K. Ilyina-Brunner; S. Jezernik; F. Winter, *Appl. Therm. Eng.*, **2025**, *258*, 124557.
15. M. A. J. Huijbregts; Z. J. N. Steinmann; P. M. F. Elshout; G. Stam; F. Verones; M. Vieira; et al., *Int. J. Life Cycle Assess.*, **2017**, *22*, 138–147.
16. SimTech GmbH, IPSE GO — The Future of Process Simulation. IPSE GO **2022**. https://about.ipsego.app/ (accessed August 11, 2025).
17. IPSE GO — Mass and Energy Balance Process Simulation Online. https://ipsego.app (accessed August 11, 2025).
18. M. Botejara-Antúnez; J. González-Domínguez; F. J. Rebollo-Castillo; J. García-Sanz-Calcedo, *Sustain. Energy Technol. Assess.*, **2025**, *74*, 104188.
19. S. Katz; A. S. Lindner, *J. Air Waste Manage. Assoc.*, **2003**, *53*, 469–477.
20. *LCA for Experts (GaBi) Software*; Sphera™: **2024**.

STUDIA UBB CHEMIA, LXX, 3, 2025 (p. 243-263)
(RECOMMENDED CITATION)
DOI:10.24193/subbchem.2025.3.17

HYDROTHERMAL CO-LIQUEFACTION OF PROSOPIS JULIFLORA AND POLYPROPYLENE IN CONTINUOUS HIGH PRESSURE SCREW REACTOR: A COMPUTATIONAL AND EXPERIMENTAL ANALYSIS

Chitra Devi VENKATACHALAM[a*], Premkumar BHUVANESHWARAN[a], Mothil SENGOTTIAN[b], Sathish Raam RAVICHANDRAN[b]

ABSTRACT. In advancement over batch reactors for biomass conversion, a continuous high-pressure screw reactor was designed to perform hydrothermal co-liquefaction (co-HTL) under a range of conditions: temperatures of 555–595 K, water-to-biomass ratios (W/B) of 6.3–8.3, and feed rates of 0.005–0.0085 kg/s. *Prosopis juliflora* (PJ) and polypropylene (PP) were used in biomass ratios of 1:4, 1:1, and 4:1. Computational Fluid Dynamics (CFD) using ANSYS Fluent was employed to analyze heat transfer between the reaction chamber and slurry biomass. For 595 K, 8:3 W/B, and 0.007 kg/s, the simulation predicted a maximum temperature of 589.3 K and pressure of 22.1 MPa, showing a 1.3 MPa deviation from experiments due to low-density particles and higher process temperatures. The simulated heat transfer coefficient was 6001 W/m^{2}K, matching experimental data with 94.6% accuracy. Under these conditions, energy recovery reached 70.8%, with biochar and biocrude yields of 34.2% and 48.7%, respectively. A synergistic effect in biocrude and biochar production was observed at a 4:1 PJ:PP ratio, independent of temperature. GC-MS analysis confirmed major aromatic hydrocarbons, including 1-[(E)-2-(4-chlorophenyl)ethenyl]-3,5-dimethoxybenzene, 2-methoxyphenol ($C_7H_8O_2$), and phenol (C_6H_5OH). The optimal conditions of 595 K, 8:3 W/B, and 0.007 kg/s are recommended for maximum energy recovery and efficient heat transfer.

Keywords: *High-pressure screw reactor, Hydrothermal Co-liquefaction, Prosopis juliflora, Polypropylene, heat transfer, energy conversion.*

[a] *Department of Food Technology, Kongu Engineering College, Erode-638060, Tamil Nadu, India*
[b] *Department of Chemical Engineering, Kongu Engineering College, Erode-638060, Tamil Nadu, India*
* *Corresponding author: erchitrasuresh@gmail.com*

INTRODUCTION

Hydrothermal co-liquefaction (co-HTL) is one of the most promising thermochemical conversion processes to understand the synergistic effect of combined biomass. It also provides enhanced conversion rates and divergent bio-energies. Since then, numerous studies have been conducted on various hydrothermal reactors, including Parr micro bench top reactors, high-pressure autoclave reactors and continuous bench scale reactors to determine the quality and energy efficiency of the bioproducts. It is important to upgrade the bench to pilot-scale reactor for commercializing bioenergy without changing its chemical properties [1-4]. Initially, the continuous plug flow reactor is used for pilot scale operation with a capacity of 6-14 kg/h, which gives a maximum biocrude yield of 33 wt.% and also a higher energy recovery than the bench-scale reactor. However, the plugging of slurry biomass is the major reason for uneven radial mixing and pressure drop in the reactor, which also affects the mass flow rate and biomass reactions during the hydrothermal process [5-7]. In addition, a smaller length-to-diameter ratio, rapid mixing of biomass and faster reaction rate are the major drawbacks explored in the continuous plug flow reactors [8]. Therefore, recent studies have given more attention to continuous pilot-scale operations in both screw and non-screw thermal reactors for the co-HTL process.

The Pacific Northwest National Laboratory (PNNL) has developed a continuous flow reactor equipped with a booster pump, a pre-heater, an agitator and a 1L tubular reactor to treat sewage sludge, achieving a flow rate of 1.5 L/h for a continuous operation of 6 to 10 h. It approximately produces 80% of the carbon recovery and 25% of the maximum biocrude yield [4, 9]. Similarly, a small tubular reactor with a capacity of 50 mL was loaded with alkaline pretreated biomass at 475 K and a mass flow rate of 20 kg/h. Then, the biomass was reacted at 675 K and elevated to a high pressure of 30 MPa during 4 hours of continuous operation. It resulted in a 10% higher biocrude yield than the non-pretreated biomass. Additionally, it was found that the higher heating value (HHV) and carbon recovery of bio-crude in continuous tubular operation were comparatively lower than in micro-scale batch operation [10, 11]. A.R. Suesse et al. [12], developed a pilot-scale supercritical flow reactor (SCFR) operated at a maximum temperature and pressure of 725 K and 65 MPa, respectively. It consists of a ten-liter paddle mixer to ensure a homogeneous mixture of slurry biomass, a plunger pump for transporting the mixture to the preheater and a heat exchanger. The optimum biocrude yield of 70% and calorific value of 36.4 MJ/kg were achieved at 575 K similar to the tubular reactor [12]. Instead of a mechanical pump, the feed was also delivered into the inner chamber of the vertical double-tube reactor at

a flow rate of 3 to 7 mL/min using pressurized nitrogen of 16 MPa. The reactor was heated to the maximum temperature of 625 K and placed in the tubular furnace. As a result of the higher heating rate and retention time, the biocrude yield was improved compared to the batch system, and the hotspot regions on the reactor wall were also reduced. [13, 14]. These studies reveal that the mixing of waste sludge and heat transfer rate is not efficient in screwless continuous flow reactors and also not effective to produce a significant amount of bioproduct yield and energy recovery. A longer retention time also leads to thermal cracking.

A pilot-scale reactor was developed with a hydraulic oscillation system having an internal volume of 20 L and a maximum feed rate of 100 L/h to increase the turbulence during the reaction. The oscillation mechanism also supports better mixing and heat transfer, but does not improve the quality of the bioproducts. The average bio-crude yield of 33 wt.% occurred for 5 to 6 h residence time and achieved 80% heat recovery in the heat exchanger. However, a lower HHV of 26-33 MJ/kg was obtained compared to other continuous processes [5, 15]. Two continuous screw reactors of five-liter internal volume were developed for hydrothermal processing of pre-treated lignocellulosic biomass. The compressed hot water was used to heat the reactors to reach the steady state. Thereafter, the slurried biomass replaces the hot water at a flow rate of 9 to 14 kg/h using a high-pressure piston pump (30 MPa) to promote biocrude production. The recirculation of hot water occurs at the end of each batch process, which tends to reduce the yield of bio-crude and causes significant disruption due to fouling during the process [16]. In some cases, deionized water was supplied under pressure to heat the reaction chamber, after which it was replaced by biomass slurry using a feed pump [17]. Mostly, high-pressure feed pumps and piston pumps for continuous feed mechanisms are developed to inject biomass into the reaction medium at a process rate of 16.9% to 17.5%. As a new experimental study, the performance of a high-pressure screw reactor with three pressure development zones was used in the present study to eliminate the mechanisms of preheating, oscillation and recirculation.

An efficient heat transfer is a vital phenomenon to enhance the performance of any thermochemical conversion reactor. Accordingly, some computational fluid dynamics (CFD) models were employed to investigate the heat transfer behaviors between solid-solid and solid-fluid particles. In specific, Moving Mesh Motion (MMM) and Rotating Frame Motion (RFM) are the fluent simulation models used to perform the screw rotation [18-20]. Similarly, Euler-Euler, Euler-granular and Euler-Lagrangian were important cell-based numerical approaches to study the interaction between the different phases using appropriate governing equations such as continuity, momentum and kinetic

energy in continuous multi-phase flow media. Newton's law of motion supports the numerical models for describing the motion and the additional forces acting between the solid and fluid phases during the co-HTL process. These equations ensure homogeneous mixing, mass balancing and smooth transportation of the slurry biomass, depending on the screw diameter, thickness, helix angle and flight length. Further, kinetic energy equations are utilized to predict the thermal properties, including temperature and pressure distribution, viscosity, heat transfer coefficient (HTC) and heat flux during the fluid flow [18, 19, 21, 22].

Most studies have related reactor performance in terms of chemical composition, heating value and energy recovery of the biofuels produced. In particular, the HHV determines the efficient state of any fuel, which can be evaluated using the elemental compositions (C, H, N, S, O) present in the biofuels. The correlations obtained from the prediction model was applied to calculate the HHV [23-26]. The H/C and O/C ratios are estimated from elemental composition and plotted in the Van Krevelen diagram to represent the quality of bioproducts [27]. In addition, the direct HHV of the biomass, biosolids and bioliquids was also measured using the oxygen bomb calorimeter. Hence, the total energy recovery and the mass balance are crucial for describing the energy intensification, thermal degradation of biomass and the performance of the reactor [19, 21, 28, 29].

In the present study, heat transfer analysis was performed on a continuous high-pressure screw reactor using suitable governing equations in the CFD module. Further, the performance of the screw reactor was also investigated based on yield, HHV and energy recovery of bioproduct.

RESULTS AND DISCUSSION

Heat transfer studies

The simulation was performed for a flow duration of 10 s to reduce the complexity of convergence. The steady state condition was observed in the fluent simulation based on the iteration graph, then the CFD results were obtained between cylindrical casing and slurry biomass.

Pressure vs temperature variation

It discloses the maximum temperature occurred at the outer region and decreased radially towards the inner region of the reaction chamber. The experimental observation also confirms that the slurry biomass was highly converted in the outer region and lesser towards the inner region, which shows the uniform heat transfer towards the inner region of the reaction chamber.

Fig. 1 shows that run-8 has the highest simulation temperatures of 589.3 K and 494.3 K at the outer and inner regions of the reaction chamber, which were approximately 10.3 K and 10.7 K deviated from the experimental temperatures for the given process condition. Likewise, the maximum pressure and its deviation from the experimental value occurred in run-8 as 22.10 MPa and 1.3 MPa, respectively. It shows the direct proportionality between pressure and temperature.

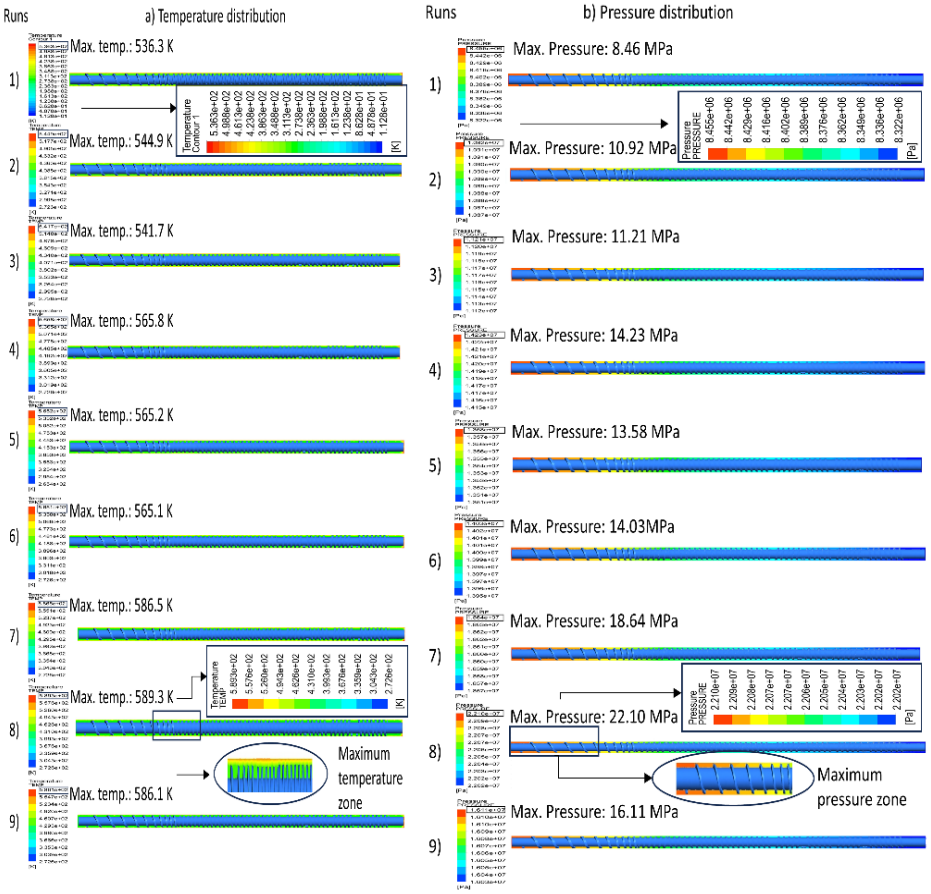

Figure 1. Contour plot for a) temperature and b) pressure distribution after reaching steady state conditions

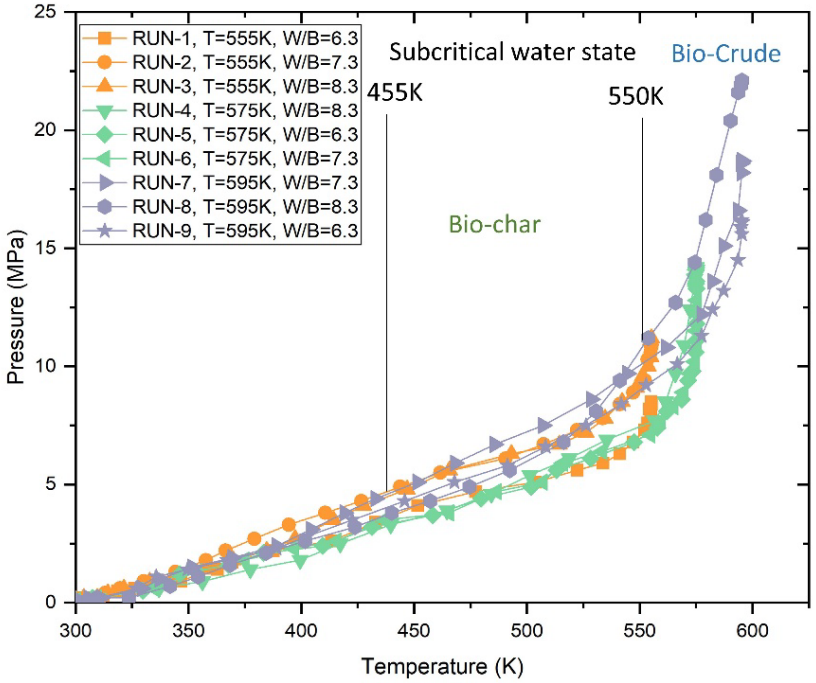

Figure 2. Relationship between temperature and pressure for respective process conditions

The relation between temperature and pressure with respect to water-to-biomass ratio is shown in Fig. 2. The co-HTL process was conducted under temperatures between 555K and 595K at subcritical water state, which provides the fast and efficient reaction medium to developed the autogenous pressure ranges from 8.46 MPa to 22.1 MPa. In addition, Fig. 2 revealed that water-to-biomass ratio plays a vital role in pressure development besides temperature and mass flow rate. The higher pressure was observed particularly for water-to-biomass ratio at 8.3 with their corresponding temperatures. In subcritical condition, the high amount of ionic product from water accelerated the biomass hydrolysis and mostly favor to form the biocrude rather than biochar. It was noticed at the temperature above 575K as given in Fig. 2.

Fluctuations of temperature

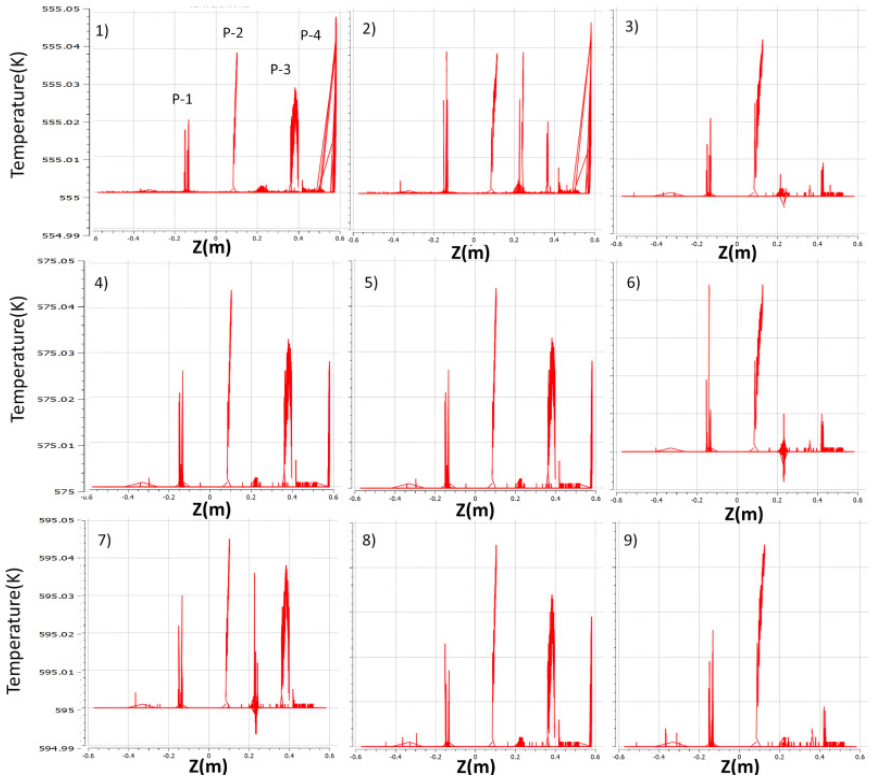

Figure 3. Fluctuation of maximum temperature on the cylindrical casing of the reactor along the axial direction

Fig. 3 confirms the process temperature maintained at the cylindrical casing throughout the length of the reactor. A very slight deviation was observed closer to each compression zone CZ-1, CZ-2 and CZ-3 for flow duration of 1s in fluent simulation. It will be higher for increasing the flow duration in simulation. Runs 1-9 possess a slight deviation of 0.05 K in simulation and a deviation range from 20K to 30K in experiment was noticed that occurs due to the friction caused between the restricted flow in compression zones and the cylindrical casing. The peak temperatures denoted as P-1, P-2, P-3 and P-4 raised at different lengths of the reaction chamber, mentioned as 450 mm, 680 mm, 1000 mm and 1160 mm, shown in Fig. 8. Owing to the high restriction of biomass, the peak P-2 shows the highest deviation that occurs before CZ-2 compared to other peaks observed in each run. In experimental conditions,

a noticeable amount of clogging was observed at the intersection of the expansion and CZ-1 zones. However, the maximum process temperature was maintained in the remaining zones of the reaction chamber.

Actual and Predicted HTC

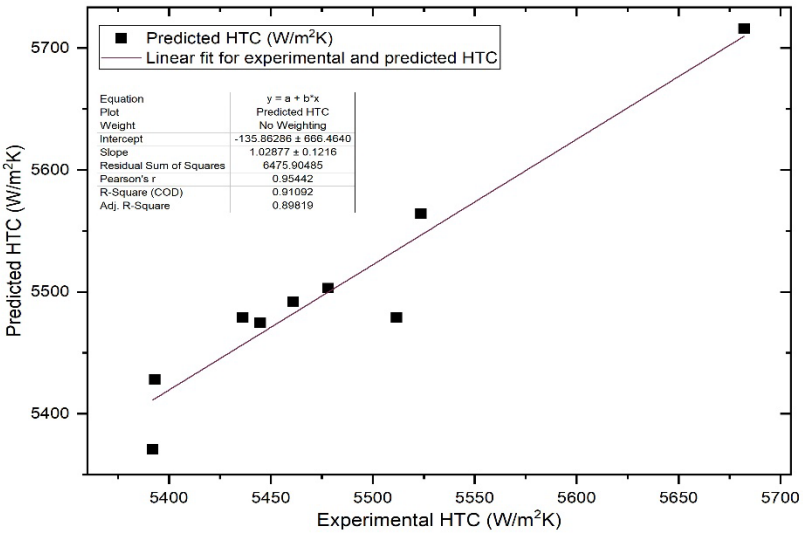

Figure 4. Comparison of HTC between predicted and experimental results

Fig. 4 shows that the predicted results were linearly fitted to the experimental data. It also delivered a wide range of mean deviation between the predicted and experimental results from 4.2% to 6.85%, with a maximum error value of 44 W/m2K. The Root Mean Square Value (RMSE) of the present model was estimated as 33.22 %, which is comparatively less than the Yan et al.[30] correlation for predicting HTC with the RMSE of 64.2%. It is slightly higher than the RMSE of 32 % calculated in the Longo et al.,[31] model, which has 93% accuracy in HTC prediction due to larger data collection [31]. From the adjusted R-squared value, it is observed that the predicted value possessed an average accuracy of 89.8% with the experimental values. The HTC of runs 3, 7, 8 and 9 nearly fitted with the linear regression line and possessed a minimum slope. In contrast, runs 2, 4 and 6 have more deviation from the regression line with a higher slope. The predicted HTC results were always higher than the experimental results due to significant heat loss among cylindrical casing, slurry biomass and ambient conditions. In addition, the variation in biomass thermal properties due to their temperature difference led to a decrease in the experimental HTC during the reaction.

Reactor Performance Analysis

The bioproduct yield, HHV and energy recovery are the vital response parameters considered to analyze the performance of the high-pressure screw reactor. In addition, the co-liquefaction effect was calculated to understand the effect of biomass mixture in the reactor and GC-MS was carried out to investigate the thermal degradation of volatile compounds present in the biocrude.

Bioproducts yield

The HTL of PJ in a 250 mL auto batch reactor provided the maximum bio-crude yield of 42.5% at 700 K. The higher conversion of biogas was observed for further increasing the temperature [32]. A similar operation was performed in a 600 mL autoclave batch reactor, which delivered the maximum biochar and biocrude yield of 45.7% and 45.82% at 525 K [33]. In subcritical temperature (below 625 K), the highest yield of biochar 58.6 % was obtained with bio-crude residue of 15.2 % at 615 K [34, 35]. Chen et al.,[36] found that the optimum yields of 37.5% and 58.6% were attained for corresponding bio-crude and biochar at supercritical temperatures of 695 K and 655 K, respectively [36]. The Liquefaction of PP at 625 K provides the highest biochar yield of 92% with a slight biosolid residue of 6%. Meanwhile, further temperature increases, abruptly decreased the bio-crude and biochar yield to 36% and 2% [34].

The present study compares the bioproduct yield attained from the co-liquefaction of PJ and PP with the optimum yield from HTL of PJ and PP, as depicted in Fig. 5. The highest biochar yield of 45.3% and bio-crude of 53.2% were attained for the corresponding water-to-biomass ratio of 6.3 and 8.3 at 555 K. Run-8 possesses a biochar and bio-crude yield of 35.2% and 48.7 % at 595 K. It stated that the bio-crude yield was comparatively higher than the yield of PP liquefaction at a temperature between 625 K and 700 K resulting in Swathi Mukundan et al.,[32] and Biller et al., [15]. Due to the higher pressure in the current process, the aforementioned bio-crude yields were significantly higher than the optimum yield (46.5%) achieved from the co-liquefaction of PJ and 25% of PP at 695 K in the batch reactor [32]. The biochar yield of 39.4% at 555 K was slightly higher than the yield obtained from the liquefaction of PJ at the supercritical condition of 695 K. In contrast, the biochar yields obtained from the co-liquefaction of PJ and PP at respective temperatures were not as high as the optimum yield from PP liquefaction at 625 K as well as PJ liquefaction at the subcritical condition of 615 K. Likewise, a lower amount of biochar was attained from the co-liquefaction of PJ and PP than from the liquefaction of PJ, but it favored the bio-crude yield. In the continuous co-liquefaction process, the quantity of biogas and AqP was

slightly higher than the liquefaction of PJ and PP. It can be gradually decreased by increasing the temperature and pressure of the co-HTL process. The further increase in temperature led to higher pressure generation of 40 MPa, which may affect the system parts and hydraulic fluid tubes in the present hydrothermal reactor. So, the process halted at 595 K.

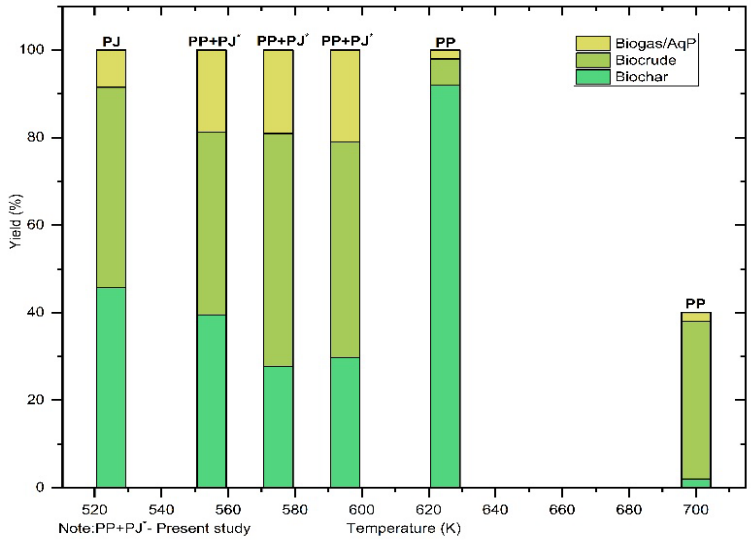

Figure 5. Comparison of maximum yield obtained from co-HTL of PJ and PP at temperatures 555 K, 575 K and 595 K with optimum yield from HTL of PJ and PP

Energy recovery

Figs 6a and 6b illustrate the fluctuation of energy recovery for respective temperatures and biomass ratios. The energy recovery of biochar and biocrude was estimated using corresponding Eqs. (6) and (7). It suggested that the higher energy recovery of biochar and bio-crude was attained at a lower PP ratio in biomass mixture and higher temperature as discussed in the HHV section. The highest energy recovery of 35.16% and 35.64% was calculated for biochar and bio-crude for the corresponding process condition given in run-8. The overall energy recovery was estimated as 70.8% with the standard deviation of 7.8% at similar conditions of biomass ratio and temperature mentioned as 4:1 and 595 K. The lowest overall energy recovery of 54.7% with 8.3 % of deviation was obtained for lower temperature of 555 K and 1:1 biomass ratio. It was observed that the overall energy recovery increased with increasing temperature at a smaller PP ratio in biomass mixture. Similarly, the gradual increase in overall energy recovery was noticed, when increasing the operating

temperature at 1:1 biomass mixture as shown in Fig. 6b. The biochar possessed significantly higher energy recovery than biocrude due to its presence of stable carbon and lower oxygen content.

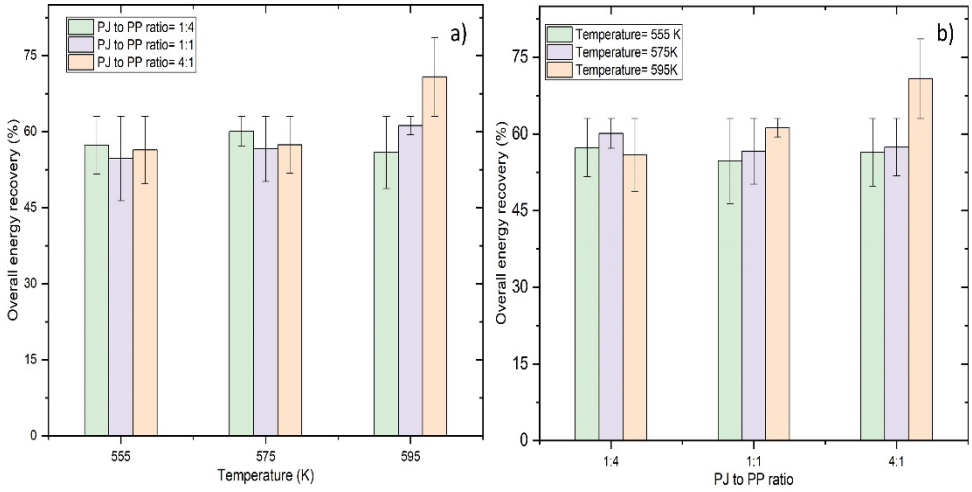

Figure 6. Effect of a) temperature and b) biomass ratio on overall energy recovery of bioproducts

Co-liquefaction effect of PJ with PP

The variation of the co-liquefaction effect related to its temperatures and biomass ratios is depicted in Figs 7a and 7b. The synergetic effect of biochar was observed at lower and moderate temperatures of 555 K and 575 K, respectively and an antagonistic effect was estimated for biochar at a 4:1 PJ to PP biomass ratio irrespective of temperatures. The synergetic and antagonistic effects ranging from 1.37 to 3.53 and -1.11 to -1.14 were noticed in biochar. Run-5 possessed the maximum synergetic effect of 3.53 at 575 k and 1:4 biomass ratio. The lower PP biomass mixture drastically reduced the co-liquefaction value of biochar and showed an antagonistic effect regardless of temperatures. In contrast, the bio-crude has a synergetic effect ranging from 0.6 to 4.78 for given process conditions. Especially, the highest synergistic effect of 4.78 and an antagonistic effect of -1.14 were observed for corresponding bio-crude and biochar at similar process conditions of temperature 595 K and lower PP biomass mixture, as shown in Fig. 7a and 7b. It was slightly higher than the synergetic effect of bio-crude obtained from the co-liquefaction of a 4:1 biomass mixture of sawdust/polyolefin plastic, pistachio hull/polyethylene terephthalate and pistachio/Nylon, which was estimated as 0.7, 3.98 and 3.63, respectively [37-39].

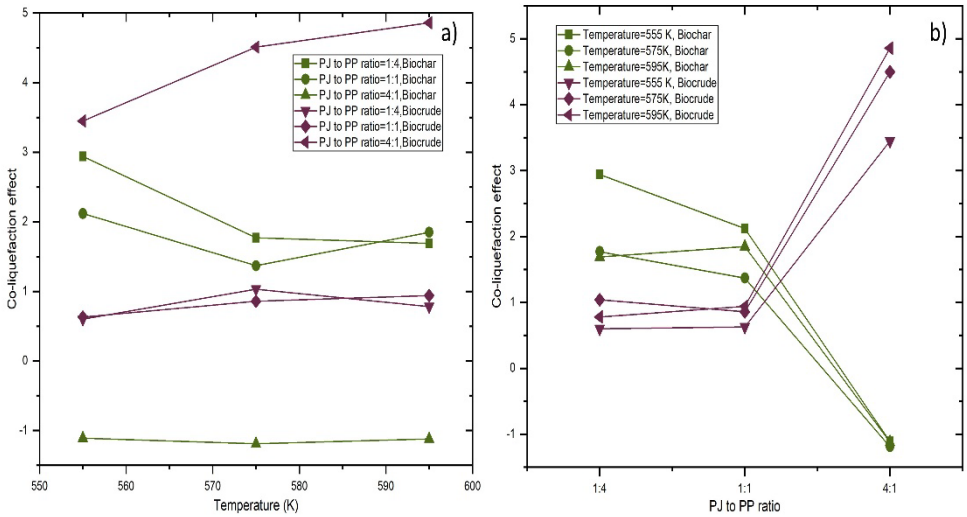

Figure 7. Influence of temperature and biomass ratio on the co-liquefaction effect of biochar and bio-crude

GC-MS analysis

The peak area percentage of selective chemical compounds occupied in the optimal bio-crude. A wide range of aromatic hydrocarbons, ketones and aldehydes were observed in the form of C5 to C17 carbon chains from GC-MS data. The chemical compounds present in the bio-crude were 1-[(E)-2-(4-chlorophenyl) ethenyl]-3,5-dimethoxybenzene ($C_{16}H_{15}ClO_2$), Phenol (C_6H_5OH), 2,3-Dimethoxyphenol ($C_9H_{10}O_4$), 3-Hydroxy-4-methoxy benzaldehyde ($C_8H_8O_3$), Cyclotene (C6H8O2), Cyclohexane 3-ethyl-5-methyl-1-propyl ($C_{12}H_{24}$), 4-Methyl-4-heptanol ($C_8H_{18}O$), Aminocarb ($C_{11}H_{16}N_2O_2$). 2-methyl hexane, Methylcyclohexane and cyclohexane 3-ethyl-5-methyl-1-propyl, which had also been reported by S. Mukundan et al.,[32] and Xiaojuan Zhang et al.,[40]. From the mentioned chemical compounds, aromatic hydrocarbons, Carboxylic acid, oxygenated aromatic hydrocarbons, light oxygenates and a few amino groups were predominantly occupied in the bio-crude. 1-[(E)-2-(4-chlorophenyl) ethenyl]-3,5-dimethoxybenzene, Fenirofibrate and 3-Iodo-L-thyronine are the major chemical compounds with higher area percentage of 15.83 % and a small contribution from amino groups of 2.91%.

CONCLUSIONS

The co-HTL process was performed for various process conditions proposed by Taguchi's method. The simulation results were predicted in terms of contour plot for pressure, temperature, HTC and heat flux distribution and compared with the experimental results. The maximum temperature and pressure of 589.3 K and 22.1 MPa were developed in run-8, which shows the corresponding deviation of 8.55 K and 1.3 MPa with experimental values. A wide range of temperature variation between casing and slurry biomass was observed from 1.9 to 3.4% in simulation and 1.3 to 1.5% in experimental values. The lower particle density and higher process temperature were two main reasons for the minimum temperature difference and led to effective heat transfer in run-8. Likewise, runs 8 and 1 delivered the maximum and minimum HTC of 6001 W/m^2K and 5760 W/m^2K in simulation, which have respective deviations of 5.6% and 4.2% with experimental values. Hence, the lower particle density, higher water-to-biomass ratio, mass flow rate and process temperature are suitable process conditions for efficient heat transfer between the reaction chamber and biomass slurry.

The overall energy recovery of 70.8% was attained at higher process temperature, mass flow rate and the water-to-biomass ratio of 595 K, 0.007 kg/s, 8.3 and lower PP biomass mixture of 4:1. Similar process conditions were recommended to obtain higher HHV of 45.9 MJ/kg and 32.69 MJ/kg for corresponding biochar and bio-crude. It also provided a higher H/C ratio for biochar and biocrude of 1.13 and 1.93, respectively. The predicted HHV revealed the maximum deviations of 15.7% and 12.6% from the actual HHV for respective biochar and bio-crude. In the case of bioproduct yield, the moderate temperature of 575 K provided the maximum yields of biochar as 45.3% and biocrude as 53.2% at their respective water-to-biomass ratios of 6.3 and 8.3. In addition, the biochar exhibited a synergetic effect up to 575 K at a 4:1 biomass mixture and the higher temperature led to an antagonistic effect. Likewise, the synergetic effect in bio-crude was noticed at a lower PP biomass ratio irrespective of process temperatures. Based on percentage selectivity, bio-liquids attained from run-5, run-8 and run-9 proceeded for GC-MS analysis, run-8 had a higher proportion of light oxygenated compounds as 17.2% and aromatic hydrocarbons of 10.34%. 1-[(E)-2-(4-chlorophenyl) ethenyl]-3,5-dimethoxybenzene, 2-Methoxyphenol ($C_7H_8O_2$) and Phenol (C_6H_5OH) were the major aromatic hydrocarbons found in bio-crude. In both heat transfer and performance studies, it is recommended that the process conditions given in run-8 were suggested to recover the maximum energy from the biomass and to attain effective heat transfer.

In the future, the hydraulic pump with a capacity of 40 MPa can be utilized to operate under high process temperature and pressure. It will also assist in improving thermal degradation and expect better conversions of bioproducts.

MATERIALS

Table 1. Proximate and ultimate analysis of dried PJ and PP (textile packing waste)

Feed stock	H (%)	C (%)	N (%)	S (%)	O (%)	HHV (MJ/kg)	Volatile matter (%)	Moisture (%)	FC (%)	Ash (%)
PJ	7.1	48.3	0.4	1.6	42.6	20.5	77.4	7.9	13.2	1.5
PP	14.7	85.3	-	-	-	46.1	87.2	10	2.8	-

Table 2. HHV in MJ/kg for different ratios of PJ and PP (dry basis) using a bomb calorimeter

PJ to PP ratio	1:0	1:1	1:4	4:1	0:1
HHV in MJ/kg	21.8	42.28	51.18	44.64	45.52

The co-liquefaction of Prosopis juliflora (PJ) and textile packaging waste (containing 98% polypropylene) was utilized in the hydrothermal process. The PJ was obtained from wasteland and chopped into fine mesh sizes of 60-80 in the local sawmill. Table 1 shows the characterization analysis of both PJ and PP performed in an elemental analyzer and tubular furnace. Similarly, the HHV of PJ and PP at different ratios was calculated using temperature differences obtained from the oxygen-type bomb calorimeter, as given in Table 2. The highest HHV of 51.18 MJ/kg was estimated for a 1:4 PJ to PP biomass ratio and the lowest HHV of 21.8 was obtained for PJ biomass. As a result of incomplete combustion in PP, the HHV of the biomass mixture at 1:4 was higher than the HHV of polypropylene (45.52 MJ/kg). Zhiwei Wang et al.,[30] confirmed that the presence of PJ could enhance the combustion efficiency and leading to the complete combustion of the volatile components in PP. The PP has attained the heat of fusion state and undergoes phase changes during the combustion. When it was mixed with PJ, the heat released from these phase changes and the combustion of PJ can be contributed to a higher HHV. The interaction between the melting PP and the combusting PJ can lead to more efficient heat transfer and higher overall energy release [30].

EXPERIMENTAL SECTION

Experimental setup

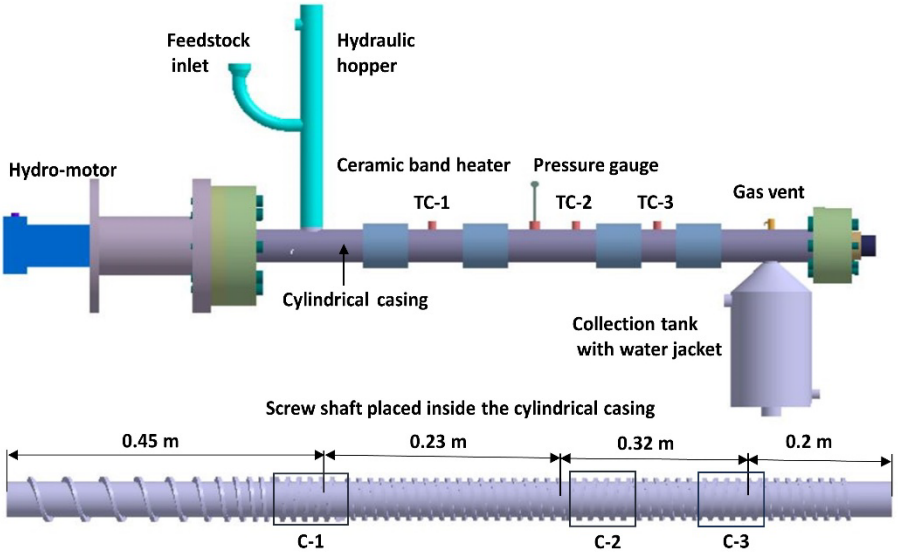

Figure 8. 3D model of hydraulically actuated continuous high-pressure screw reactor

The co-HTL process was carried out in a high-pressure Archimedes screw reactor with a 3L internal volume and heated using two ceramic band heaters, as shown in Fig. 8. The screw shaft was designed for optimal design parameters such as a screw diameter of 58 mm, helix angle of 6.8°, pitch and flight length of 29 mm and 1200 mm, respectively. It is enclosed within a stationary cylindrical casing having a thickness of 16 mm. TC-1, TC-2 and TC-3 are the thermocouples fixed at three different locations on the casing, shown in Fig. 7 to measure the temperatures of slurry biomass inside the reactor. The high torque hydraulic motor (H15) was attached to the screw shaft, which rotates at a speed ranging from 60 to 90 rpm. The piston-type hydraulic hopper was fixed to the inlet side of the reactor for injecting the biomass. It also prevents back pressure from developing at the beginning of the first compression zone. The storage tank was integrated with the water-cooling jacket and coupled at the outlet end of the reactor. Similarly, the sample collection ports were available at the bottom of each compression zone. Finally, the reaction pressure was measured at the mid-section of the reactor with the help of a pressure gauge.

Experimental Procedure

The ideal combinations of process parameters, including temperatures, feed rates and water-to-biomass ratios, were obtained from Taguchi's experimental design, as given in Table 3. Initially, the feedstock was prepared for three different biomass ratios of PJ and PP including 4:1, 1:1 and 1:4. A wide range of water-to-biomass ratios were selected, from 6.3 to 8.3 for preparing 1kg of biomass slurry. Then, the prepared biomass was loaded into the reaction chamber at atmospheric condition with a feed rate ranging from 20 to 30 kg/h. The additional deionized water was injected through the water nozzle to avoid clogging near the compression zones during the flow of biomass. The continuous process took a retention time of 60 to 120 minutes to reach the biomass in the collection tank. The retention time was varied for each run due the restricted flow in the compression zone. The biomass was heated after passing the first compression zone for 363 K and the reaction temperature has been maintained between the second and third compression zones of the reactor. Finally, the processed material was collected in the storage tank and cooled for around 45 minutes to attain the atmospheric temperature.

Product separation technique

After the collected samples had cooled down to ambient conditions, acetone (50 mL) was added to the 200 g of samples. The vacuum filtration method was conducted for the separation of liquid and solid phases from the collected kerogen. Then, the solid residue was dried in the hot air oven at 333K for 8h to remove the presence of acetone and the dried solid product was weighed. Further, the aqueous phase (AqP) was separated from the organic phase (oil + solvent) using a separating funnel, thereby the rotary vacuum evaporator was introduced to separate the required biocrude from the acetone present in the organic phase. Finally, the recovered acetone was reused for other product separation processes. The yields of biosolid, biocrude and AqP were calculated under dry conditions using the given equations (1), (2) and (3). These values can also be applied to determine the co-liquefaction effect of biomass using Eq. (5).

$$Biosolid\ yield, Y_{BS}\ (\%) = \left(\frac{Mass\ of\ biochar}{Mass\ of\ combined\ feedstocks}\right) \times 100 \quad (1)$$

$$Biocrude\ yield, Y_{BC}\ (\%) = \left(\frac{Mass\ of\ biocrude}{Mass\ of\ combined\ feedstocks}\right) \times 100 \quad (2)$$

$$Biogas\ and\ AqP, Y_{BG,AqP}\ (\%) = 100 - (Y_{bs} + Y_{bc}) \quad (3)$$

Table 3. Experimental process parameters for co-HTL process from Taguchi's method

Runs	Temperature (K)	Feed rate (kg/h)	Water-to-biomass ratio	Biomass ratio (PJ/PP)	Capacity of water in mL, weight of PJ and PP in grams (g)	Additional water added (L)
1	555	20	6.3	04:01	733:213.6:53.4	0.95
2	555	25	7.3	01:01	1100:200:200	1.82
3	555	30	8.3	01:04	1466:106.8:427	2.97
4	575	20	8.3	01:01	733:133.5:133.5	1.48
5	575	25	6.3	01:04	1100:80:320	1.42
6	575	30	7.3	04:01	1466:427.2:106	2.43
7	595	20	7.3	01:04	733:53.4:213.6	1.22
8	595	25	8.3	04:01	1100:320:80	2.22
9	595	30	6.3	01:01	1466:267:267	1.89

Analytical methods

The direct gross calorific value or HHV of biomass mixtures, biochar and biocrude was evaluated using the oxygen bomb calorimeter. The 1g test sample was placed in the stainless-steel chamber and it was filled with pressurized oxygen at 300 bars. Thereafter, the initial and final temperature differences were observed to calculate the gross calorific value of the samples by applying equation (4).

The gross calorific value or HHV of biosolid (BS) and bio-crude (BC) was estimated using the given equation,

$$HHV_{BS\ or\ BC} = (3326.248 \times temperature\ difference) - [(60 \times 0.355) + (30 \times 4.18)] \quad (4)$$

The co-liquefaction effect of combined biomass based on biochar and biocrude yield was calculated by,

$$Co - liquefaction\ effect, (E_{CL}) = Y_{co-HTL} - \Sigma\, y_j \times x_j \quad (5)$$

Y_{co-HTL}= yield of biochar or biocrude from the co-liquefaction process; y_j= yield of individual biomass; x_j= mass fraction of respective biomass from the feedstock mixture.

The energy yield of biosolid and bio-crude was calculated according to Eqs. (6) and (7),

$$Energy\ yield\ of\ biosolid,\ EY_{Bs}\ (\%) = \frac{HHV_{Bs}}{HHV_{biomass}} \times Y_{Bs} \quad (6)$$

$$Energy\ yield\ of\ biocrude,\ EY_{BC}\ (\%) = \frac{HHV_{BC}}{HHV_{biomass}} \times Y_{BC} \quad (7)$$

The Dulong equation for calculating HHV of bioproducts is given by [27],

$$HHV = 0.338\,C + 1.44\,H - 0.18\,O + 0.095\,S \quad (8)$$

Simulation process condition

The bulk density, specific heat capacity, thermal conductivity and heat generation are the important thermal properties given in Table 4, which were used in the respective governing equations during CFD analysis. After fitting the initial values in the simulation, it computes the temperature and pressure distribution and HTC.

Table 4. Thermal properties of mixed biomass and process conditions applied in CFD simulations

Runs	Temperature (K)	Mass flow rate (kg/s)	Bulk density (kg/m^3)	Specific heat at constant pressure, Cp (J/kg-K)	Heat generation (W/m^3)	Thermal conductivity (W/mK)
1	555	0.005	933	3378	10840	0.5
2	555	0.007	899	3433	10840	0.5
3	555	0.0085	933	3270	10840	0.5
4	575	0.005	1052	3433	11230	0.5
5	575	0.007	899	3752	11230	0.5
6	575	0.0085	872	3378	11230	0.5
7	595	0.005	1080	3270	11620	0.5
8	595	0.007	872	3400	11620	0.5
9	595	0.0085	899	3433	11620	0.5

The continuity equations of fluid and solid phases based on mass balance are given by,

$$\frac{\partial}{\partial t}\varphi_f \rho_f + \nabla.\left(\varphi_f \rho_f u_f\right) = 0 \tag{9}$$

$$\frac{\partial}{\partial t}\varphi_s \rho_s + \nabla.\left(\varphi_s \rho_s u_s\right) = 0 \tag{10}$$

The momentum equations of fluid and solid with shear stress tensor and drag force are given by,

$$\frac{\partial}{\partial t}\varphi_f \rho_f u_f + \nabla.\left(\varphi_f \rho_f u_f u_f\right) = -\varphi_f \nabla p + \nabla \tau_f - \beta(u_f - u_s) + \varphi_f \rho_f g + \frac{N_p}{V} F_d \tag{11}$$

$$\frac{\partial}{\partial t}\varphi_s \rho_s u_s + \nabla.\left(\varphi_s \rho_s u_s u_s\right) = -\varphi_s \nabla p - \nabla p_s + \nabla \tau_s - \beta\left(u_f - u_s\right) + \varphi_s \rho_s g + \frac{N_p}{V} F_d \tag{12}$$

The thermal energy equation of fluid and solid phases is described as follows,

$$\frac{\partial}{\partial t}\left(\varphi_f \rho_f C_{Pf} T_f\right) + \nabla.\left(\varphi_f \rho_f C_{Pf} T_f u_f\right) = \nabla. q_f + h_{fs}\left(T_s - T_f\right) - \Delta H_f + h_{casing\ wall}\left(T_{casing\ wall} - T_f\right) \quad (20)$$

$$\frac{\partial}{\partial t}\left(\varphi_s \rho_s C_{Ps} T_s\right) + \nabla.\left(\varphi_s \rho_s C_{Ps} T_s u_s\right) = \nabla. q_s + h_{sf}\left(T_f - T_s\right) - \Delta H_s + h_{casing\ wall}\left(T_{casing\ wall} - T_s\right) \quad (21)$$

Whereas, conductive heat flux, $q_s = \varphi_s k_s \nabla T_s$

ACKNOWLEDGMENTS

This research article is based on CFD and performance analysis of continuous high-pressure screw reactors under various process conditions carried out by the authors. The authors would like to thank all the researchers who contributed to the research work. Throughout this study, the authors acknowledge Kongu Engineering College for their support of the research facility. The authors also thank IIT, madras and SAIF, cochin for their contribution to the respective GC-MS and elemental analysis on the test samples.

REFERENCES

1. J. Yang, Q. He and L. Yang, *Appl. Energ.*, **2019**, 250: 926-45.
2. F. Cheng, J.M. Jarvis, J. Yu, U. Jena, N. Nirmalakhandan, T.M. Schaub and C.E. Brewer, *Bioresource Technol.*, **2019**, 294: 122184-93.
3. I.A. Basar, H. Liu, H. Carrere, E. Trably and C. Eskicioglu, *Green Chem.,* **2021**, 23(4): 1404-46.
4. R.F. Beims, Y. Hu, H. Shui and C. Xu, *Biomass Bioenerg.*, **2020**, 135: 105510-24.
5. A. Aierzhati, J. Watson, B. Si, M. Stablein, T. Wang and Y. Zhang, *Energ. Convers. Man.-X*, **2021**, 10(1): 100076-86.
6. C. Jazrawi, P. Biller, A.B. Ross, A. Montoya, T. Maschmeyer and B.S. Haynes, *Algal Res.*, **2013**, 2(3): 268-77.
7. J. Ni, L. Qian, Y. Wang, B. Zhang, H. Gu, Y. Hu and Q. Wang, *Fuel*, **2022**, 327: 125135-49.
8. M. Tabatabaei, M. Aghbashlo, M. Dehhaghi, H.K.S. Panahi, A. Mollahosseini, M. Hosseini and M.M. Soufiyan, *Prog. Energy Combust. Sci.*, **2019**, 74(1): 239-303.

9. D.C. Elliott, T.R. Hart, G.G. Neuenschwander, L.J. Rotness, G. Roesijadi, A.H. Zacher and J.K. Magnuson, *ACS Sustain. Chem. Eng.,* **2013**, 2(2): 207-15.
10. I.M. Sintamarean, I.F. Grigoras, C.U. Jensen, S.S. Toor, T.H. Pedersen and L.A. Rosendahl, *Biomass Convers. Biorefin.,* **2017**, 7(4): 425-35.
11. D.W.F. Brilman, N. Drabik and M. Wądrzyk, *Biomass Convers. Biorefin.,* **2017**, 7(4): 445-54.
12. A.R. Suesse, G.A. Norton and J. van Leeuwen, *Energ. Fuel.*, **2016**, 30(9): 7379-86.
13. J.L. Wagner, C.D. Le, V.P. Ting and C.J. Chuck, *Fuel Process. Technol.,* **2017**, 165: 102-11.
14. W.T. Chen, M.A. Haque, T. Lu, A. Aierzhati and G. Reimonn, *Curr. Opin. Environ. Sci. Health,* **2020**, 14: 63-73.
15. K. Anastasakis, P. Biller, R. Madsen, M. Glasius and I. Johannsen, *Energies*, **2018**, 11(10): 2695-718.
16. T.H. Pedersen, I.F. Grigoras, J. Hoffmann, S.S. Toor, I.M. Daraban, C.U. Jensen, S.B. Iversen, R.B. Madsen, M. Glasius, K.R. Arturi, R.P. Nielsen, E.G. Søgaard and L.A. Rosendahl, *Appl. Energ.,* **2016**, 162: 1034-41.
17. C.U. Jensen, J.K. Rodriguez Guerrero, S. Karatzos, G. Olofsson and S.B. Iversen, *Biomass Convers. Biorefin.*, **2017**, 7(4): 495-509.
18. X. Shi, F. Ronsse, J. Roegiers and J.G. Pieters, *Renew. Energ.,* **2019**, 143: 1465-76.
19. X. Shi, F. Ronsse, R. Nachenius and J.G. Pieters, *Renew. Energ.,* **2019**, 143: 1477-87.
20. S. Aramideh, Q. Xiong, S.-C. Kong and R.C. Brown, *Fuel*, **2015**, 156(1): 234-42.
21. S. Jalalifar, R. Abbassi, V. Garaniya, F. Salehi, S. Papari, K. Hawboldt and V. Strezov, *Fuel*, **2020**, 273: 117782-96.
22. F. Qi and M.M. Wright, *Powder Technol.*, **2018**, 335: 18-34.
23. C. Sheng and J.L.T. Azevedo, *Biomass Bioenerg.,* **2005**, 28(5): 499-507.
24. Q. Liu, R. Xu, C. Yan, L. Han, H. Lei, R. Ruan and X. Zhang, *Bioresour. Technol*., **2021**, 340: 125630-40.
25. B. Li, T. Yang, R. Li and X. Kai, *Energy*, **2020**, 200: 117524-33.
26. H. Li, Z. Zhu, J. Lu, J. Watson, D. Kong, K. Wang, Y. Zhang and Z. Liu, *Fuel*, **2020**, 280: 118605-18.
27. A. Mathanker, D. Pudasainee, A. Kumar and R. Gupta, *Fuel*, **2020**, 271: 117534-44.
28. D. Mahesh, S. Ahmad, R. Kumar, S.R. Chakravarthy and R. Vinu, *Bioresour. Technol*., **2021**, 339: 125537-47.
29. J.S. dos Passos, S. Chiaberge and P. Biller, *Energ. Fuel,* **2021**, 35(13): 10630-40.
30. Z. Wang, Y. Chen, G. Chen, T. Sun, M. Zhang, Q. Wang, M. Wu, S. Guo, S. Yang, T. Lei, K.G. Burra and A.K. Gupta, *J. Energy Resour. Technol.*, **2023**, 145(8): 1-8.
31. X. Tao and C.A. Infante Ferreira, Int. J. Heat Mass Tran., **2019**, 135: 996-1012.
32. S. Mukundan, J.L. Wagner, P.K. Annamalai, D.S. Ravindran, G.K. Krishnapillai and J. Beltramini, *Fuel Process Technol.,* **2022**, 238: 107523-32.

33. C.D. Venkatachalam, M. Sengottian, S.R. Ravichandran, K. Subramaniyan and P. Kalappan Thangamuthu, *Period. Polytech. Chem. Eng.,* **2020**, 65(1): 105-15.
34. M.S. Seshasayee and P.E. Savage, *Appl. Energ.*, **2020**, 278: 115673-85.
35. J.S. dos Passos, M. Glasius and P. Biller, *Process Saf. Environ.,* **2020**, 139: 371-79.
36. W.-T. Chen, K. Jin and N.-H. Linda Wang, *ACS Sustain. Chem. Eng.,* **2019**, 7(4): 3749-58.
37. S. Hongthong, S. Raikova, H.S. Leese and C.J. Chuck, *Waste Manage.,* **2020**, 102: 351-61.
38. N. Li, H. Liu, Z. Cheng, B. Yan, G. Chen and S. Wang, *J. Hazard Mater.,* **2022**, 424: 127460-72.
39. J.A. Onwudili and P.T. Williams, *J. Clean. Prod.*, **2023**, 430: 139733-46.
40. X. Zhang, L. Zhang and A. Li, *Bioresource Technol.*, **2019**, 294: 122113-22.

STUDIA UBB CHEMIA, LXX, 3, 2025 (p. 265-279)
(RECOMMENDED CITATION)
DOI:10.24193/subbchem.2025.3.18

SPECTROSCOPIC AND THERMAL ANALYSES OF THE INHIBITORY MECHANISM OF *OKANIN* ON *XANTHINE OXIDASE*

Meng-Rong LI[a], Mu-Xin LIU[a,*], Wei LIU[a], Rui HE[a], Shan-Bin JIANG[a], Shen-Qiang LI[a]

ABSTRACT. Okanin was identified as a xanthine oxidase inhibitor, and for the first time, the thermodynamic parameters of the interaction—including entropy change (ΔS), enthalpy change (ΔH), and Gibbs free energy (ΔG)—were calculated by combining fluorescence spectrometry and differential thermal scanning. It can be inferred that there exists a hydrogen bond between okanin and XO, with the van der Waals force being the predominant intermolecular force between them. Nuclear Magnetic Resonance Hydrogen Spectroscopy (^{1}H-NMR) not only confirmed the presence of hydrogen bonding but also provided initial predictions of the specific binding location of the inhibitor and enzyme. Three-dimensional and synchronous fluorescence demonstrated that okanin induces structural modifications in the enzyme, leading to inhibition. Molecular docking directly revealed the binding pattern between inhibitor and enzyme, which aligned with the aforementioned experiments. The findings indicated that inhibitors were competitively bound to the enzyme's active site primarily through intermolecular forces such as hydrogen bonding, conjugation, and van der Waals forces. These interactions facilitate the formation of a stable intermediate, inducing structural changes in the enzyme, and enhancing the inhibitory ability of okanin. Antioxidant experiments showed that okanin further inhibits the generation of O_2^- free radicals by simultaneously promoting the reduction of XO molecules and suppressing the production of uric acid. Hence, okanin shows promise as a novel natural product that inhibits the activity of xanthine oxidase, making it highly significant to investigate its potential anti-gout properties.

Keywords: *Okanin; differential thermal scanning; Nuclear magnetic.*

[a] *Bengbu University, School of Materials and Chemical Engineering, Longzi Lake District, 233030, Bengbu, China.*
[*] *Corresponding author: limr@bbc.edu.cn*

INTRODUCTION

Elevated levels of uric acid in the bloodstream are widely recognized as a leading cause of hyperuricemia. Progressive hyperuricemia leads to the deposition of monosodium urate crystals, which can trigger gout pathogenesis. The presence of these crystals within the joints can stimulate the synovial membrane, resulting in joint swelling, deformity, and pain for affected individuals. In severe cases, this can also impede joint mobility. Si et al. [1] discovered a positive correlation between uric acid levels and the incidence of type 2 diabetes in many patients. The body normally maintains stable uric acid levels, but an imbalance in uric acid metabolism can lead to hyperuricemia. Current pharmacological interventions, including xanthine oxidase inhibitors and uricosuric agents, while effective in reducing uric acid production and enhancing excretion, are frequently associated with adverse effects [2]. Therefore, it is crucial to investigate the effects and mechanisms of natural plant-derived active ingredients with pharmacological properties on uric acid synthesis and the activity of related enzymes in order to develop new and safe drugs for lowering uric acid levels.

Xanthine oxidase (XO), is present in various organisms and is commonly found in the liver and kidney of mammals, bacteria, insects, and birds. It facilitates the conversion of purine to uric acid [3]. The crystal structure of xanthine oxidase consists of 1330 amino acids with a 90% similarity in sequence between mice and humans. It is composed of two symmetrical structural units known as homologous dimers, each weighing 145 kDa. The catalytic center includes one molybdenopterin center, two iron-sulfur centers, and one flavin adenine dinucleotide. Among these components, the molybdenopterin center plays a key role in catalyzing the production of uric acid from xanthine [4].

Natural products have emerged as a significant research focus for some scholars due to their attributes of safety, non-toxicity, abundant availability, and strong biological activity. They play a crucial role in the food and biomedicine industries, providing essential guidance for current research on plant active ingredients. Okanin, a principal bioactive flavonoid constituent of Coreopsis tinctoria (Asteraceae family), represents a promising candidate for therapeutic development [5]. Studies have demonstrated its anti-inflammatory, antioxidant, and vascular growth promotion effects in mice [6]. Shi et al investigated okanin's inhibitory effect on two metabolic subtypes of CYP3A4 and CYP2D6 enzymes, suggesting its potential use as a diabetes treatment drug [7]. However, the interaction mechanism between okanin and XO remains unclear; therefore, this experiment selected okanin as an inhibitor to study its inhibition mechanism on XO.

Various methods were employed for the first time to investigate the inhibitory activity and interaction of okanin on XO. The binding constant and interaction force between inhibitor and enzyme were quantitatively analyzed using various spectral methods and differential thermal scanning, which also revealed conformational changes in enzyme structure. ^{1}H NMR could infer hydrogen bond formation and binding sites through variations in hydrogen displacement, while molecular docking provided a direct visualization of the binding diagram between inhibitor and enzyme. This study is valuable for investigating the intermolecular interactions between the okanin and xanthine oxidase, offering a promising approach to exploring the mechanism of inhibitor inhibition on the enzyme, ultimately leading to the discovery of a novel and efficient XO inhibitor.

RESULTS AND DISCUSSION

Experiment of okanin inhibiting enzyme activity.The experimental data of inhibition of enzyme activity demonstrated that okanin exhibited a stronger xanthine oxidase (XO) inhibitory activity than allopurinol, as indicated by its lower IC_{50} value (2.30 μM) in comparison to allopurinol (7.36 μM). This suggests the potential for further exploration of okanin as a new inhibitor. The enhancement of inhibition may be due to the hydroxyl group contained in the benzene ring structure being bonded to the XO active cavity by hydrogen bonding. This interaction appears to movement of hydrogen atoms in the propylene group towards the benzene ring and reduction in electron cloud density of the carbon atoms within the propylene group, thereby achieving highly efficient enzyme inhibition. It was also possible that the enzyme activity was reduced by inhibiting the O_2^- free radicals, the product of xanthine catalyzed by XO.

Inhibition mechanism, inhibition principle. The inhibitory mechanism of okanin on xanthine oxidase was evidented from the Figure 1(A), which shows a linear plot passing through the origin of coordinates. The slope of the curve is inversely proportional to the concentration of the inhibitor. The concentration-dependent decrease in slope confirmed okanin as a reversible inhibitor of XO [8]. The type and inhibition constant of okanin on XO could be determined using the Lineweaver–Burk plot as depicted in Figure 1(B), where four lines intersect at the Y-axis. This indicates that okanin competes with xanthine for binding in the active cavity of XO. Therefore, it is a competitive XO inhibitor [9]. Furthermore, based on the relationship between slope and concentration in Figure 1(C), a K_{IS} value of 0.16 μM suggests that okanin competitively binding to allopurinol at the active center of enzyme, significantly reducing enzymatic activity.

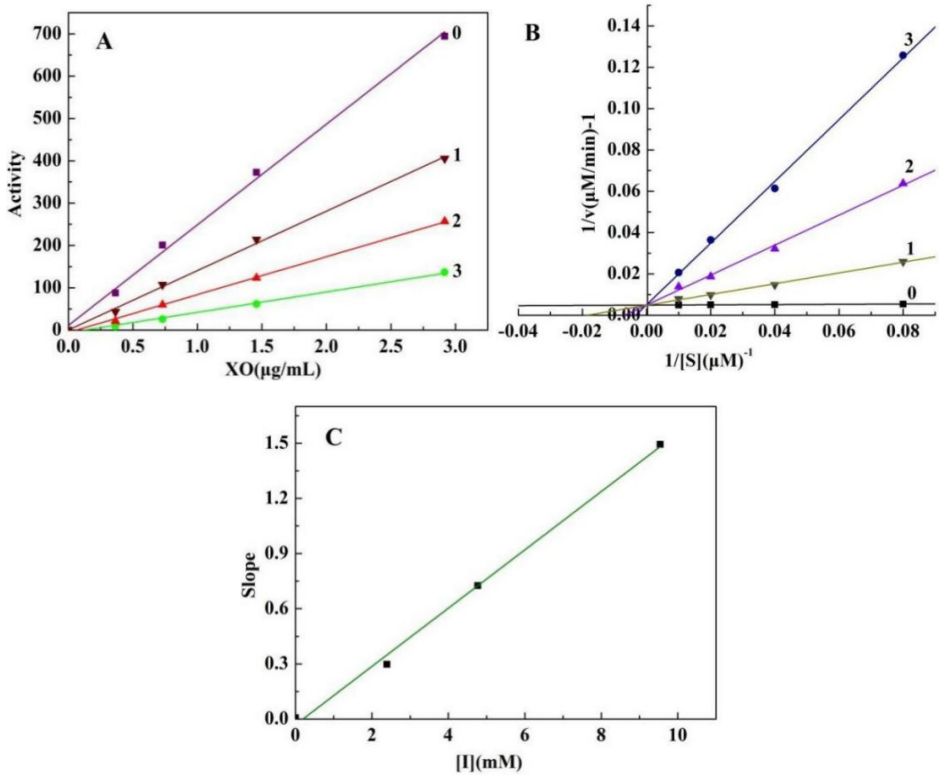

Figure 1. The inhibitory effects of okanin on XO (A). The concentration of curve 0-3 for okanin were 0, 2.39, 4.77, 9.54 mM, respectively; Lineweaver–Burk plots of okanin on XO (B). The concentration of xanthine were 0.02, 0.04, 0.08, 0.15 mM, respectively. The plot of the slope for okanin (C).

Fluorescence quenching. The technique of fluorescence quenching had been commonly utilized to investigate ligand-protein interactions. The fluorescence emission spectra of each solution were depicted in Figure 2(A). It was evident that the fluorescence intensity of XO in aqueous solution at 400 nm was significantly higher than at other wavelengths. Progressive addition of okanin resulted in concentration-dependent quenching of XO fluorescence, which proved that okanin could quench the fluorescence intensity of XO. Stern-Volmer curves at different temperatures revealed two quenching patterns: static quenching and dynamic quenching. As can be seen from the Figure 2(B), The Stern-Volmer curve was divided into two linear intervals, suggesting both dynamic and static modes of fluorescence quenching between okanin and XO. As compound concentration increased, the Stern-Volmer curve approached

the Y-axis, indicating a shift towards more dynamic quenching for XO compounds with higher concentrations. By using a compound concentration of 32.10 μM as the cut-off point, the corresponding Ksv was determined through piecewise linear fitting of Stern-Volmer curves. The Table 1 results presented in the table indicate that the apparent quenching constant significantly exceeds the maximum diffusion impact quenching constant (2.0×10^{10} $L.mol^{-1}.S^{-1}$) [10]. The above results are summarized that the interaction between the compound and enzymes is primarily attributed to static quenching. However, with increasing compound concentration, the influence of dynamic quenching became more prominent. It is evident from the table that both okanin and XO exhibit similar apparent binding sites and binding constants, with an apparent binding constant below 0.08 mol/L indicating non-covalent complex formation through interactions such as hydrophobic interaction and hydrogen bonding [11].

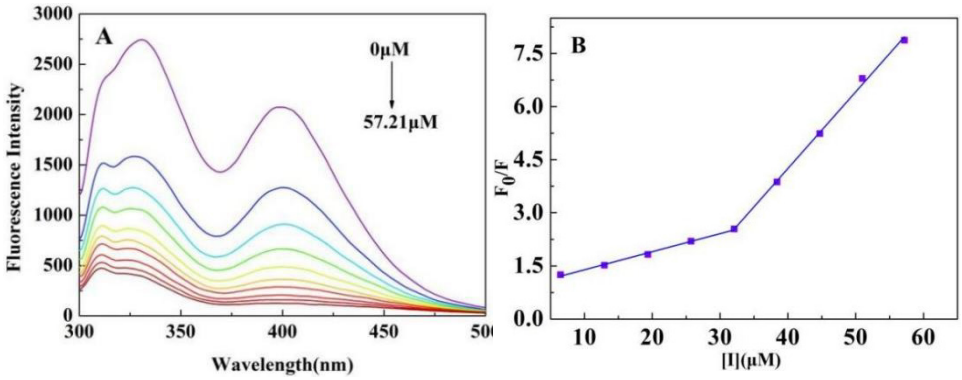

Figure 2. Fluorescence mapping of the interaction between okanin and XO (A) and the Stern–Volmer plot (B). Concentrations for curves were 0-57.21 μM, respectively. The temperature was 303 K.

Table 1. Apparent extinction constants of 303 K interactions between okanin and XO.

Complex	C(μmol·L^{-1})	K_{SV}(10^4L·mol^{-1})	Kq(10^{12}L·mol^{-1}·S^{-1})
Okanin-XO	≤32.1	0.05	0.05
	>32.1	0.22	0.22

The binding constant (Ka) of the inhibitor to the enzyme is obtained by the following formula [12]:

$$\lg\frac{F_0 - F}{F} = \lg K_a + n\lg[Q]$$

Analyzing the data in table 2, When the temperature changed from 298 K to 303 K, there was a significant increase in the Ka value, indicating that the binding affinity of the inhibitor to the enzyme and the formation of hydrogen bonds are closely related to the hydrophobic effect. Subsequently, temperature further increased from 303 K to 308 K, the disruption of hydrogen bonds led to a significant decrease in Ka value, indicating that okanin and enzyme predominantly bond through hydrogen bonding.

Analysis of differential scanning calorimeter test results. Differential scanning calorimeter (DSC), as an experimental tool of differential scanning calorimetry, is widely used in thermal analysis. In this experiment, a dynamic model was employed where the temperature of the sample pool and the reference pool increased simultaneously at a set heating rate to analyze the thermal behavior of the sample under external heating conditions. The system exhibited a progressive decrease in heat flow from 298 K to 308 K, resulting in a gradual decline in the DSC curve. Within this temperature range, software automatically calculates ΔH to be -3.821 J/g, indicating an energy change between okanin and XO leading to complex formation.

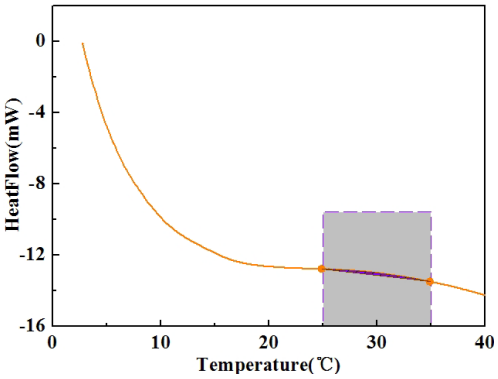

Figure 3. DSC curve of heat flow rate with temperature in okanin and XO mixed system.

Measurement of thermodynamic parameters. On the basis of fluorescence and differential thermal scanning experiments, the Thermodynamically related data during the formation of the complex were calculated according to the formula [13], and the interaction force between okanin and XO was judged successively.

$$\lg K_a = -\frac{\Delta H}{2.303RT} + \frac{\Delta S}{2.303R}$$
$$\Delta G = \Delta H - T\Delta S$$

Table 2. Bind constants and thermodynamic parameters for the interaction of XO with okanin at different temperatures.

Complex	Temperature (K)	K*a* (10^4L.mol^{-1})	ΔH (KJ.mol^{-1})	ΔG (KJ.mol^{-1})	ΔS (KJ.mol^{-1})
Okanin-XO	298	1.09	-13.28	11.19	-37.58
	303	5.15		11.40	
	308	0.44		11.59	

Analysis of the thermodynamic parameters in Table 2 revealed negative values for ΔG, ΔH, and ΔS. A negative Gibbs free energy change (ΔG < 0) indicated that acarbose spontaneously binds to XO. A negative enthalpy (ΔH < 0) and entropy change (ΔS < 0) indicated that van der Waals forces and hydrogen bonds were the main forces for acarbose binding to the enzyme. These thermodynamic findings, combined with the results of fluorescence quenching experiments, concluded that okanin forms a stable complex with the enzyme through these two forces.

Synchronous fluorescence experiment. XO contains fluorescein groups tyrosine and tryptophan residues, and their fluorescence peaks could reflect the conformational changes of XO. Spectral analysis revealed a 2 nm red shift (Δλ=15 nm) in the Tyr emission maximum. This phenomenon indicated a change in the enzyme microenvironment, with implications for enhanced hydrogen bonding force around hydrophilic amino acid residues such as tyrosine. These findings further corroborated the presence of hydrogen bonding forces in the interaction between okanin and XO. The synchronous fluorescence quenching rate (RSFQ) could be determined by substituting the experimental synchronous fluorescence data into the following formula [14]: $\mathrm{RSFQ} = 1 - \mathrm{F}/\mathrm{F}_0$, where F represents the fluorescence intensity of XO and F_0 represents the fluorescence intensity of inhibitor and enzyme binding [15]. As shown in figure 4(C), it was evidented that at the same concentration of okanin, the RFSQ values for tryptophan (∆λ=60 nm) were notably higher than those for tyrosine (∆λ=15 nm). This observation suggests that tryptophan residues may have a greater impact on the fluorescence quenching of XO compared to tyrosine residues, possibly due to their closer proximity to okanin.

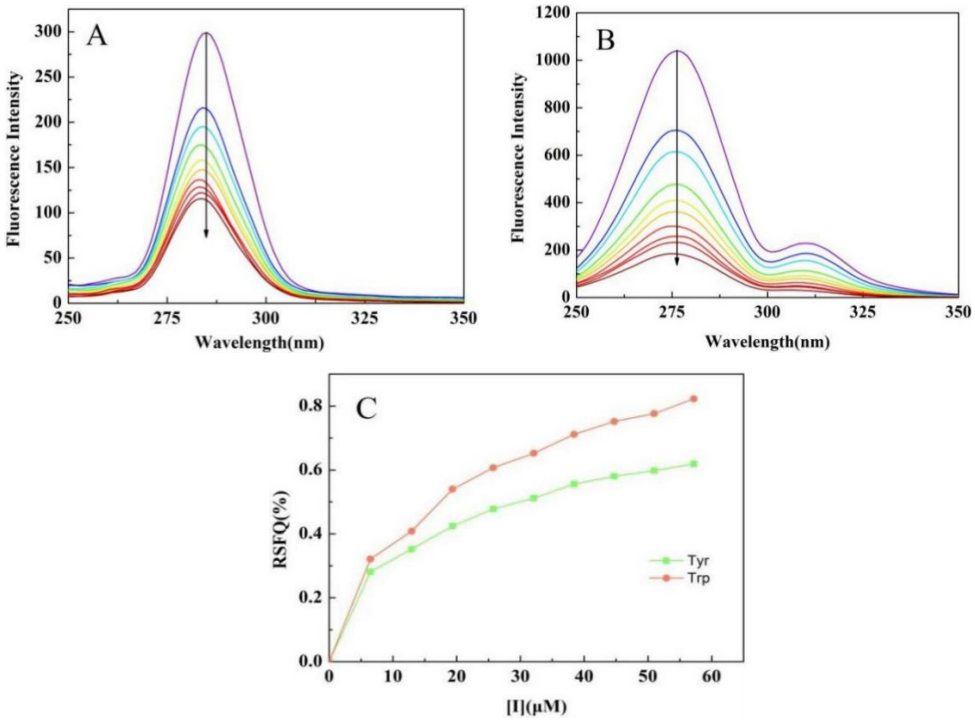

Figure 4. The synchronous fluorescence spectra. Δλ=15 nm (A) and Δλ=60 nm (B), and RSFQ values of Tryptophan and tyrosine residues are present in XO structures (C). Concentrations for curves were 0-57.21 μM, respectively.

Three-dimensional fluorescence. Three-dimensional fluorescence spectroscopy was utilized for investigating alterations in protein structure and microenvironment [16]. Figure 5 displayed four distinct fluorescence emission peaks, including the Rayleigh scattering peak (peak 1), tyrosine residue fluorescence emission peak (peak 2), tryptophan residue fluorescence emission peak (peak 3), skeleton structure of XO (peak 4) [17]. Each peak was represented by a different color-filled region in the figure, with colors deepening from the outside to the inside and corresponding to an increase in fluorescence intensity. Compared to the blank XO (Figure 5A), the enclosed region of each peak in the three-dimensional fluorescence (Figure 5B) resulting from the addition of a certain concentration of okanin was reduced, with a noticeably lighter color indicating decreased fluorescence intensity. The identical conclusion was reached through fluorescence titration experiment. However, there was a stronger impact on the change of tryptophan residues at peak 3 compared to tyrosine residues at peak 2, This certificated that tryptophan residues more

significant impact than tyrosine residues in the binding of the inhibitor to XO. This phenomenon may be attributed to the formation of a complex between okanin and XO, which alters the spatial conformation of XO.

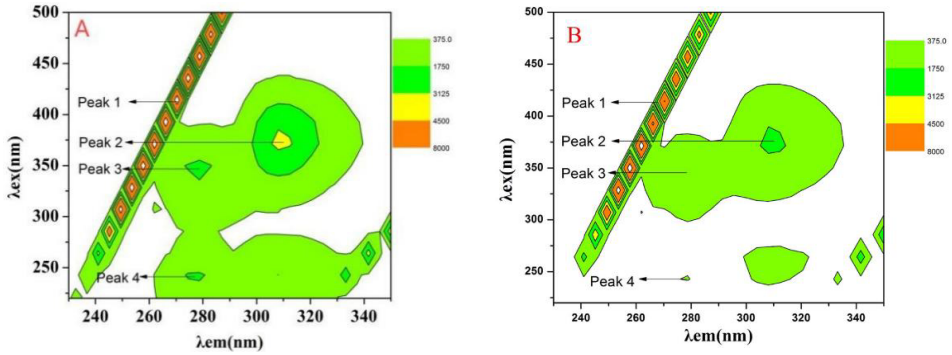

Figure 5. Three-dimensional fluorogram of XO (A) and okanin added in XO (B)

Nuclear Magnetic Titration. Nuclear magnetic titration was a method used to predict the binding site of small molecules on large molecules by analyzing the change in chemical shift of hydrogen atoms within small molecules when they interact with large molecules [18]. As shown in Figure 6, the hydrogen atoms (13.59, 10.09, 9.75, 9.10, 8.60 ppm) on all hydroxyl groups of okanin structure disappear immediately while the CH protons suffer no change in position or in intensity after the addition of a small amount of enzyme solution.

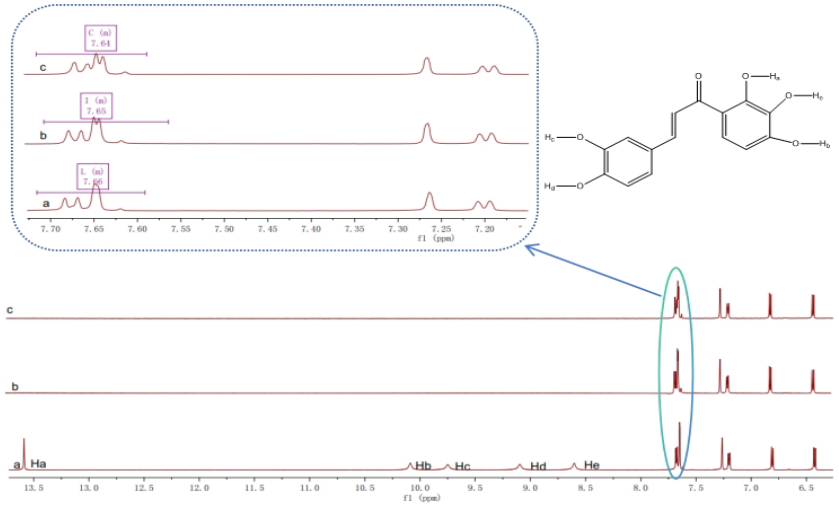

Figure 6. ^{1}H NMR titration of okanin with XO in DMSO-d_6.
Concentrations of XO for curves a-c were 0, 0.2, 0.4 mg/μL.

This could be explanation may be that the OH protons of okanin have been exchanged with deuterium. Figure 6 also indicated that due to the peak splitting of olefin groups, the electron could density increases. This could be attributed to the oxygen atoms within the carbonyl group in okanin's structure forming hydrogen bonds with the enzyme, induced electron cloud density enhancement, thereby enhancing the inhibitory ability of okanin.

Molecular docking. To comprehend the precise binding site and interaction force of inhibitor with XO, molecular docking of okanin was conducted using Accelrys Discovery Studio 4.2 software [19]. Figure 7 clearly illustrated okanin occupies the catalytic center of XO with a potential energy of -28.49 kcal/mol. Purple representing the donor and green representing the receptor. The cavity was identified as a hydrogen bond cavity, indicating the presence of hydrogen bonds. Additionally, a 2D diagram in Figure 7(B) demonstrated that okanin forms hydrogen bonds with amino acid residues such as THR1083, SER1080, LYS1045, GLY1039, GLY797, PHE798 to facilitate its combination with XO. Furthermore, okanin may enhance cavity stability by forming van der Waals forces with ALA1258, ASP1084, VAL1081, SER1082, ALA1078, GLY799, GLY796, GLN1194, GLY1260, and VAL1259. The enzyme-inhibitor primary intermolecular forces was hydrogen bonds and van der Waals forces, which aligned with experimental results from fluorescence and nuclear magnetic titration studies.

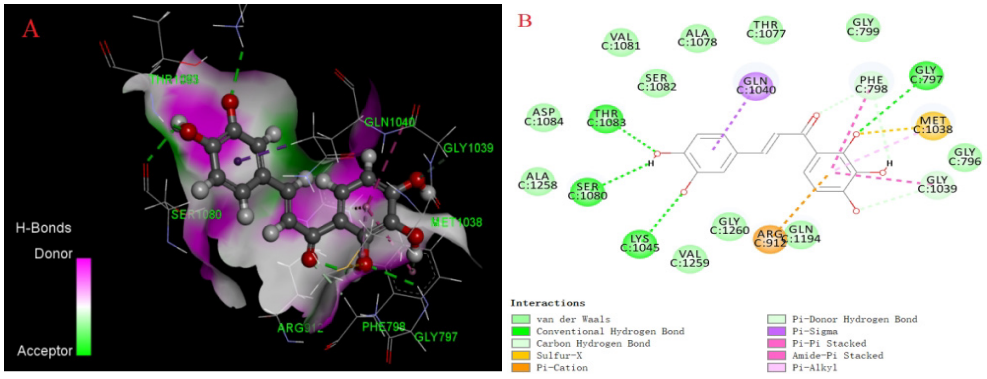

Figure 7. Molecular docking diagram(A) and 2D structure diagram(B).

Antioxidant experiment. The antioxidant experiment could obtain the inhibitory ability of okanin on the generation of O_2- free radicals by XO catalysis. Figure 8 showed the antioxidant activity of okanin in the XO reaction system. It could be seen from Figure 8(A) that the experimental system had obviou absorption at 560 nm. The absorbance of XO decreased significantly after

gradually adding okanin, indicating that okanin could inhibit the O_2- free radical in the product of the XO reaction system. Figure 8(B) proved that O_2- radicals could be inhibited when the concentration of the inhibitor was within the range of 0.81μM, and subsequently the change in inhibitory activity was not obvious. The above results indicated that the reduction of O_2- radicals catalyzed by XO was due to the inhibitory effect of okanin. The IC_{50} value of okanin in inhibiting the generation of O_2- free radicals is 2.25μM, which was similar to the IC_{50} value for inhibiting the production of uric acid. It indicated that okanin further inhibited the generation of O_2- free radicals by simultaneously promoting the reduction of XO molecules and inhibiting the production of uric acid [20].

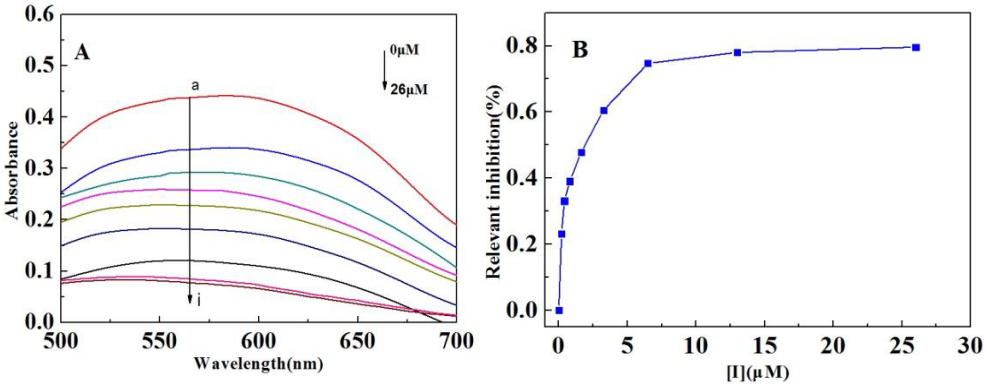

Figure 8. UV spectrum of the reaction between okanin and the O_2- radical catalyzed by XO (A); The inhibition rate of okanin on the O_2- radical of the XO catalytic product (B).

CONCLUSIONS

This study utilized UV spectroscopy, fluorescence spectroscopy, differential thermal scanning, ^{1}H NMR, and molecular docking to systematically investigate okanin's inhibition mechanism against xanthine oxidase. The results showed that okanin competitively bound in the active center of enzyme as indicated and proved that okanin could inhibit the production of O_2- radicals by promoting the reduction of XO molecules by ultraviolet spectroscopy. Fluorescence spectroscopy confirmed that static quenching dominance. Differential thermal scanning provided enthalpy change data for okanin and enzyme binding within the experimental temperature range. More precise thermodynamic parameters obtained through combination with fluorescence spectra. The findings indicated that hydrogen bonding and van der Waals

forces played crucial roles in facilitating the interaction between inhibitor and enzyme, leading to the inhibition of enzyme activity. ^{1}H NMR and molecular docking technology could support this conclusion. In summary, okanin and xanthine competitively bind in the core of XO, forming stable intermediates through hydrogen bonding, van der Waals force, conjugation, and other forces, inducing structural changes of the XO. As a potential new xanthine oxidase inhibitor, okanin presents a promising avenue for further research into gout and hyperuricemia treatment strategies.

EXPERIMENTAL SECTION

Reagents and Materials. Xanthine oxidase (EC 1.2.3.2, from bovine milk, US, Sigma), Xanthine (US, Sigma), Dimethyl sulfoxide (Tianjin, Damao Chemical Reagent), $NaH_2PO_4.2H_2O$ (Nanchang, Xilong Chemical), $Na_2HPO_4.12H_2O$ (Nanchang, Xilong Chemical), Okanin (Chengdu, Reifensi Biotechnology), Ethanol absolute (Tianjin, Damao Chemical Reagent Factory). The reagents used in the experiment were all analytically pure.

Enzyme activity. The experiment method was modified on the basis of previousreference slightly [21]. This activity assay system was incubated one minute at 30℃, contains 0.85 mL 0.05 M PBS buffer (Na_2HPO_4-NaH_2PO_4, pH=7.5), 2 mL 0.15 mM xanthine, 0.05 mL okanin solution and 0.1 mL XO. Among them, xanthine was substrate. The absorbance value of the product was measured at 285 nm, The enzyme activity value could be read directly through the software interface, and inhibit 50% of the enzyme activity (IC_{50}) was calculated by IBM SPSS Statistics software. The formula for calculating the inhibition rate is:

$$\text{Inhibition rate } (\%) = \frac{OD_2 - OD_1}{OD_2} \times 100\%$$

Where OD_1 and OD_2 are the enzyme activity values of the activity assay system in the presence and absence of inhibitors.

Dynamic mechanism experiment. The concentration of XO was varied while keeping the substrate concentration fixed in this assay. Different concentrations of okanin solution were mixed into systems, which containing different concentrations of enzymes and substrates. A series of correlation curves between enzyme concentration and activity value were then generated to judge the inhibitory principle of the inhibitor-XO. The opposite approach to the inhibition mechanism involved maintaining a constant XO concentration while varying the substrate concentration. The inhibition type can be characterized using the Lineweaver-Burk equation [14]:

$$\frac{1}{v} = \frac{K_m}{V_m}\left(1 + \frac{[I]}{K_I}\right) + \frac{I}{V_m}\left(1 + \frac{[I]}{K_{IS}}\right)$$

V represents velocity and K represents a constant. V_m denotes the maximum reaction rate;K_I is the binding constant of okanin with the free enzyme; K_{IS} is the binding constant of okanin with the complex in the solution system, and K_m is Michaelis constant; [*I*] is the inhibitor concentration.

Fluorescence quenching assay. The experimental method was conducted by making slight modifications to a previous article [22]. In the experimental setup, a base solution consisting of 1.8 mL phosphate buffer and 0.2 mL XO solution was utilized. Okanin solution was then titrated into the system using a micropipette, with the final concentration reaching 57.21 μM. The fluorescence intensity of the inhibitor was measured at an excitation wavelength of 278 nm and emission wavelength of 300-500 nm. Three different temperatures (298 K, 303 K, and 308 K) were selected for the experiment. To correct for UV absorption at this wavelength, the following formula was utilized [23]:

$$F_{corr} = F_{obs} e^{(A_1 + A_2)/2}$$

F_{corr} represents the precise fluorescence intensity value, while F_{obs} denotes the fluorescence intensity value measured. A_1 and A_2 stand for the absorbance values at the excitation and emission wavelengths respectively.

The Stern-Volmer equation is as follows [24]:

$$\frac{F_0}{F} = 1 + K_q \tau_0 [Q] = 1 + K_{SV}[Q]$$

F represents the fluorescence intensity of the enzyme; F_0 denotes the fluorescence intensity of the system upon addition of the inhibitor. K signifies the constant; where K_q stands for the rate constant, K_{SV} is the quenching constant; τ_0 indicates the average fluorescence lifetime of the enzyme, and [*Q*] denotes the concentration of the inhibitor.

Experimental study of differential scanning calorimetry. The DSC131 Evo differential scanning calorimeter produced by SETARAM, France, was used in this experiment. High purity nitrogen was used as a purge gas. And a drying gas with a purge rate was 30 mL·min^{-1} while a drying gas rate of 100 mL·min^{-1}. The heating rate is 5K·min^{-1}, these instrument should be calibrated before the experiment. The reference pool and the sample pool were placed in the instrument at the same time. The mixed solution of okanin and XO was placed in the sample pool, and the experimental temperature was set to 0-40℃.

Three-dimensional fluorescence. The reaction system was composed of 1.8 mL of PBS buffer solution, 0.2 mL of xanthine oxidase solution, and 5 μl of 1 mM inhibitor added step by step. The excitation and emission wavelengths must be configured. For this experiment, the excitation wavelength is set to begin at 200 nm, while the emission wavelength range is 200-350 nm, and using a slit width of 5 nm.

Synchronous fluorescence. The solution was prepared following the same procedure as for the three-dimensional fluorescence experiment. Excitation and emission wavelengths were set within the ranges of 200-350 nm and 200-500 nm, with intervals of 15 and 60, respectively. The slit widths were set at 5nm to scan the synchronous fluorescence spectrum.

Nuclear Magnetic Titration. A solution of 2.5 $mg \cdot mL^{-1}$ okanin in DMSO-d_6 was prepared and titrated with a 0.2 $mg \cdot \mu L^{-1}$ xanthine oxidase solution using a micropipette. The 1H NMR spectrum was recorded after each addition of xanthine oxidase, and the perturbation of hydrogen atoms in the spectra was assessed for comparison.

Molecular simulation experiment. In this study, Accelrys Discovery Studio 4.2 software was used to interface okanin with the Mo-pt active center of XO. The X-ray crystal structure of XO (PDB ID: 1FIQ) is available from the RCSB protein database (http://www.rcsb.org/pdb). All water and excess ligands need to be removed from the crystal structure before docking. The docking procedure based on CHARMm was used to dock the small molecule conformation in the receptor active site region, and finally optimize it to obtain the most accurate docking results. The docking structure with the highest score was selected to analyze its combination mode.

Antioxidant experiment. The mixed solution of NBT and xanthine (1:5), 2mg/μL XO solution and different concentrations of okanin (0-26 μM) solution were incubated in a 37 ° C water bath for half an hour. 1mL of standby mixture, 0.1mL XO solution and 0.75mL PBS ((Na_2HPO_4-NaH_2PO_4, pH=7.5)) buffer solution were added to the cuvette. Then, introduced different concentrations of okanin solution and measured the wavelengths-dependent absorbance changes of the system at range of 500 to 700 nm.

ACKNOWLEDGMENTS

This work was supported by the Anhui Provincial universities natural science research key project (KJ2021A1123), Anhui Province excellent young teacher training project (YQZD2023082), Quality Engineering Project of Anhui Province “Material Science and Engineering Teaching Innovation Team” (2023cxtd106) and Bengbu University Natural Science Research Project (2023ZR01). Their support was instrumental in the completion of this research.

REFERENCES

1. N van der Schaft; A Brahimaj; K Wen; OH Franco; A Dehghan; *PloS one*, **2017**, 12, e0179482.
2. S Gong; J Song; L Wang; S Zhang; Y Wang; *Eur J Gastroen Hepat,* **2016**, 28, 132-138.
3. J Gao; X Liu; B Zhang; Q Mao; Z Zhang; Q Zou; X Dai; S Wang; *Eur J Med Chem*, **2020**, 190, 112077.
4. R Rullo; C Cerchia; R Nasso; V Romanelli; ED Vendittis; M Masullo; A Lavecchia; *Antioxidants*, **2023**, 12, 825.
5. Q Yang; Y Sun; L Zhang; L Xu; M Hu; X Liu; F Shi; *J Herb Med*, **2014**, 6, 103-109.
6. Y Mi; J Xu; R Shi; Q Meng; L Xu; Y Liu; T Guo; D Zhou; J Liu; W Li; N Li; Y Hou; *Food Funct*, **2023**, 14, 369-387.
7. Y Shi; J Xie; R Chen; G Liu; Y Tao; Y Fan; X Wang; L Li; J Xu; *Biomed Chromatogr*, **2021**, 35, e5039.
8. C.M. Hu; Y.Y. Zheng; A.T. Lin; X Zhang; X.Z. Wu; J Ling; X.T. Xu; Z Xiong; *J Mol Struct*, **2023**, 1271, 134124.
9. Y Wang; G Zhang; J Pan; D Gong; *J Agr Food Chem*, **2015**, 63, 526-534.
10. L Liu; M Yuan; S Huang; J Li; D Li; L Zhao; *Appl Sci*, **2018**, 8, 158.
11. B Pan; B Xing; W Liu; G Xing; S Tao; *Chemosphere*, **2007**, 69, 1555-1562.
12. X.K. Su; Z.C. Sun; C.Y. Zhao; H Yang; T.M. Zhao; C Ma; G.F. Zhu; *J Spectrosc*, **2024**, 9923310.
13. K Rajeshwari; P Vasantha; B Shekhar; PV Anantha Lakshmi; *Appl Biochem Biotech*, **2022**, 194, 2650-2671.
14. M Li; Y Yu; J Liu; Z Chen; S Cao; *J Mol Struct*, **2018**, 1159, 23-32.
15. N Zeng; G Zhang; X Hu; J Pan; Z Zhou; D Gong; *J Funct Foods*, **2018**, 50, 172-182.
16. Y Gao; Z Wang; Y Li; H Luo; Z Zhou; *Spectrochim Acta A*, **2021**, 248, 119230.
17. L Chen; M Zhu; X Hu; J Pan; G Zhang; *J Sci Food Agr*, **2022**, 102, 3835-3846.
18. J Xu; J Liu; X Zhu; Y Yu; S Cao; *Food Chem*, **2017**, 221, 1530-1538.
19. R.K. Chaudhary; S.S. Karoli; P.S.R. Dwivedi; R Bhandari; *J Diabetes Metab Dis*, **2022**, 21, 445-454.
20. N Masuoka; I Kubo; *BBA-MOL BASIS DIS*, **2004**, 1688, 245-249.
21. N Zeng; G Zhang; X Hu; J Pan; D Gong; *J Funct Foods*, **2019**, 58, 1-10.
22. C Koffler; K Rohde-Brandenburger; *Int J Life Cycle Ass*, **2019**, 24, 397-399.
23. S Bi; Y Sun; C Qiao; H Zhang; C Liu; *J Lumin*, **2009**, 129, 541-547.
24. J Xie; H Cui; Y Xu; L Xie; W Chen; *FQS*, **2021**, 5, fyaa038.

Corrigendum

Correction Note:

Article GERBOVITS, D. A., NAGY, R., & PUSKÁS, S. (2025). INVESTIGATION OF THE POTENTIAL OF ENVIRONMENTALLY FRIENDLY NON-IONIC SURFACTANTS FOR EOR | Studia Universitatis Babeș-Bolyai Chemia, *Studia Universitatis Babeș-Bolyai Chemia*, *70*(3), 191–199. https://doi.org/10.24193/subbchem.2025.3.13 has been corrected in the Platform (Volume 70, No. 3, 2025 | Studia Universitatis Babeș-Bolyai Chemia).
Date: Friday, March 13, 2026 12:36 PM
Subject: Request for Article Correction from Gerbovits Ditta Adrienn <gerbovits.ditta.adrienn@mk.uni-pannon.hu>.
The changes include:
Request for adding funding acknowledgement to published article.
Other parts of the article were left untouched.
No changes were made that would compromise the integrity and content of the article.

Editors' Note: The article was corrected on March 13, 2026 2:15 PM. The pdf file of the volume also includes a *Corrigendum*.